# An Archaeomagnetic Study of Hangi Stones in New Zealand

by

Rimpy Kinger

A thesis

submitted to the Victoria University of Wellington

in fulfilment of the requirements for the degree of

Doctor of Philosophy

in Physics

Victoria University of Wellington

2017

# Abstract

Burnt or fired archaeological artefacts often retain a record of the magnetic field in which they were last heated and cooled. Over the past four years we have collected oriented hangi stones from 10 archaeological sites spread across the North and South Islands of New Zealand. The stones vary in lithology from andesites, originating from the central North Island volcanoes, favoured by Maori for their durability and with remanent magnetization up to 30 A/m, to sandstones and schists from the main axial ranges, with magnetizations as weak as $10^{-4}$ A/m. Radiocarbon dating of charcoal fragments retrieved from amongst the stones indicates that the sites span from ca. 1400 AD to the present.

In all cases, we have independently oriented and retrieved several stones, and we have made several samples from each stone, either by drilling (standard cylindrical samples) or sawing (pseudo-cubes) in the laboratory. We have calculated site mean palaeomagnetic directions (Dec between 1.5° and 19.6° and Inc between -52.2° and -68.3°) from principal component analysis of thermal demagnetization and alternating field demagnetization data, discarding the data of stones that show evidence of disturbance after cooling. The directions are in good agreement with recently published palaeosecular variation records from lake sediments. We have carried out palaeointensity experiments using the Coe/Thellier method with pTRM and tail checks, and with selection criteria modified to the situation. Palaeointensities range from 50µT to 77µT. Rock magnetic experiments contribute to our understanding of the mineralogy, domain state and blocking temperature spectra.

We compare our data with predictions of the global field models ARCH3k and *gufm*1, and suggest that the addition of our new data will improve these models for the SW Pacific region for the most recent time period. Archaeomagnetic measurements are also used to date hangi sites by matching the palaeo-direction to an established archaeomagnetic dating model, NZPSV1k. Archaeomagnetic dating is used to resolve ambiguities in the calibration of radiocarbon dates, and shows up inconsistencies due to unreliable source material for radiocarbon dating. Archaeomagnetic dating and radiocarbon dating results are combined to give the best estimates of the best age of the hangi sites.

# Acknowledgements

iv

# Table of contents

# Table of Figures

# List of tables

# Abbreviations

| | |
|---|---|
| AD | Anno Domini |
| AFD | Alternating field demagnetization |
| ARCH3K | Continuous global geomagnetic field model for 3000 years based archaeomagnetic data |
| BC | Before Christ |
| BP | Before Present |
| CALS3K | Continuous global geomagnetic field model for 3000 years based archaeomagnetic and paleomagnetic data |
| ChRM | Characteristic remanent magnetization |
| CRA | Conventional Radiocarbon Age |
| CRM | Chemical remanent magnetization |
| GAD | Geocentric Axial Dipole |
| GMI | Great Mercury Island |
| HRM | Hangi remanent magnetization |
| IGRF | International Geomagnetic Reference Field model |
| IRM | Isothermal remanent magnetization |
| MAD | Maximum angular deviation |
| MD | Multidomain |
| NRM | Natural remanent magnetization |
| NZ | New Zealand |
| NZPSV1K | New Zealand Palaeo Secular Variation record for 1000 years |

| | | |
|---|---|---|
| OP | | Opihi River |
| PSD | | Pseudo single domain |
| PSV | | Palaeosecular variation |
| pTRM | | Partial thermoremanent magnetization |
| RL | | Riverlands |
| SD | | Single domain |
| SP | | Superparamagnetic |
| SV | | Secular variation |
| SW | | South west |
| THD | | Thermal demagnetization |
| TM | | Titanomagnetite |
| TRM | | Thermoremanent magnetization |
| VADM | | Virtual Axial Dipole Moment |
| VFTB | ` | Variable field translation balance |
| VGP | | Virtual geomagnetic pole |
| VRM | | Viscous remanent magnetization |
| VSM | | Vibrating sample magnetometer |
| WP | | Weld Pass |
| WT | | Whitianga |

# Symbols

$\mu_o$         Vacuum permeability ($= 4\pi \times 10^{-7} H/m$)

$\alpha$         Angular difference between anchored and non-anchored solution

$\alpha_{95}$         Semi-angle of cone of 95% confidence

B         Magnetic field (T)

$B_c$         Coercivity force (T)

$B_{cr}$         Coercivity of Remanence (T)

D, Dec         Declination

$\delta_{CK}$         Relative check error

$\delta_{pal}$         Cumulative check difference

$\delta t^*$         true tail of a pTRM

$\delta_{TR}$         Intensity difference between first and repeated steps

F         Magnetic field Intensity (T or T)

f         Fraction of NRM

M         Magnetization (A/m or $Am^2/kg$)

$M_r$         Remanent magnetization ($Am^2/kg$)

$M_{rs}$         Saturation remanent magnetization ($Am^2/kg$)

$M_s$         Saturation magnetization ($Am^2/kg$)

q         Quality factor

$T_b$         Blocking temperature

$T_c$         Curie temperature

$T_{ub}$         Unblocking temperature

$T_N$         Néel temperature

# 1. Introduction

## 1.1. Earth's Magnetic Field

Earth has a magnetic field due to a self-sustaining dynamo action in its iron-rich fluid outer core. The convective motion of the electrically conductive fluid in the magnetic field generates electric currents, which in turn sustain the field.

The magnetic field of Earth can be defined using a rectangular coordinate system (Figure 1.1). At any location, the declination (Dec) is the angle between geographic north and magnetic north. The inclination (Inc) is the angle of the magnetic field direction below the local horizontal plane. F, the total magnetic field vector, can also be described in terms X, Y and Z, the components in the northerly, easterly and downward directions. Mathematically, X, Y and Z are related to Dec, Inc and F by equations 1.1 to 1.6.
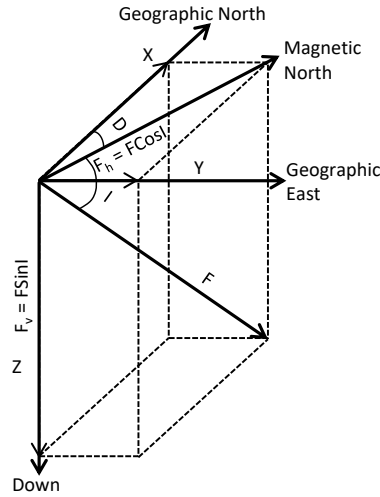


Figure 1.1. Geometrical representation of elements of Earth's magnetic field. X is geographic north, Y is east and Z is downward. Dec, Inc and F represent the magnetic elements declination, inclination and total magnetic intensity. In above figure Dec and Inc are labelled as D and I.

$$X \ = \ F \ cos \ (Dec) \ cos \ (Inc) \qquad (1.1)$$

$$Y = \ F \ sin \ (Dec) \ cos \ (Inc) \qquad (1.2)$$

$$Z = \ F \ sin \ (Inc) \qquad (1.3)$$

$$F = (X^2 + Y^2 + Z^2)^{\frac{1}{2}} \qquad (1.4)$$

$$Dec = tan^{-1}(Y/X) \qquad (1.5)$$

$$Inc = tan^{-1}(Z/(X^2 + Y^2)^{\frac{1}{2}}) \qquad (1.6)$$

Although Earth's main field is due to a self-sustaining dynamo in its outer core, minerals in the upper crust often contain a natural remanent magnetization, sometimes large enough to affect the local magnetic field. Time-varying fields originating from electric currents in the ionosphere and magnetosphere also contribute to Earth's total magnetic field. These external fields vary with both the time of day and the strength of the solar wind, and are much smaller in comparison with the main field (Rikitake & Honkura, 1985).

### 1.1.1. Geocentric Axial Dipole Model

A geocentric axial dipole (GAD) is the simplest first-order approximation to describe the main geomagnetic field. According to this model, Earth's magnetic field is the field of a single dipole at the centre of Earth aligned along its rotational axis. However, a better fitting dipole at Earth's core is tilted ~10° from its rotational axis; this is the inclined geocentric dipole (Figure 1.2). Lines drawn through the axis of the inclined geocentric dipole cut the surface of Earth at the geomagnetic poles, presently at latitudes 80.0° N/S and longitudes 72.2°W/107.8°E. (Roberts & Turner, 2013).
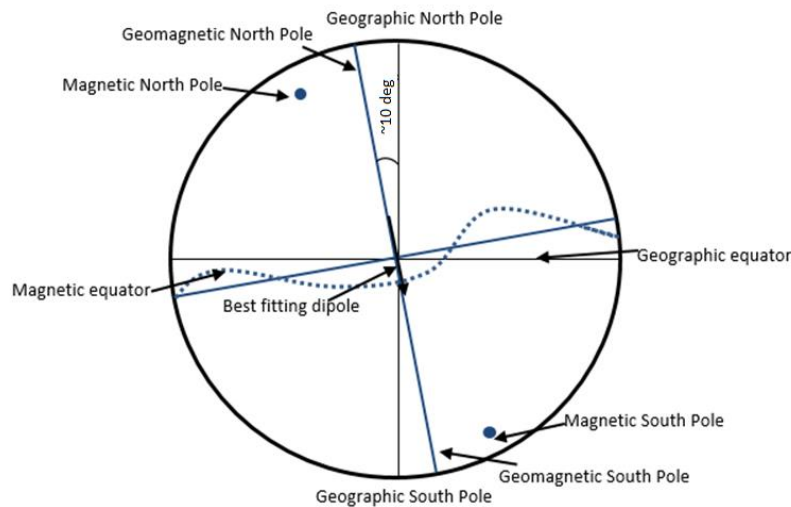


Figure 1.2. Earth's best fitting dipole, indicated by the line between the geomagnetic north and south poles).

2

The inclined geocentric dipole accounts for 80-90% of the observed surface field. The remaining 10-20% of the field cannot be described by a dipole and is known as the non-dipole field. Earth's geomagnetic poles and magnetic poles (the points on the surface of Earth where the field is vertical) are not the same as a result of the non-dipole field.

## 1.1.2. Spherical Harmonics

Carl Friedrich Gauss provided a full mathematical description of Earth's field in 1839, using spherical harmonic analysis (SHA). The Gauss's spherical harmonic equation is the solution to Laplace's equation:

$$\nabla^2 U = 0 \tag{1.7}$$

This results in an expression for the geomagnetic potential, $U$, which contains terms describing both internal and external sources. The following equation gives the full spherical harmonic representation of the geomagnetic potential:

$$U = a \sum_{l=1}^{\infty} \sum_{m=0}^{l} \left(\frac{r}{a}\right)^{l} (b_l^m \cos m\varphi + c_l^m \sin m\varphi) P_l^m (\cos\theta)$$

$$+ a \sum_{l=1}^{\infty} \sum_{m=0}^{l} \left(\frac{a}{r}\right)^{l+1} (g_l^m \cos m\varphi$$

$$+ h_l^m \sin m\varphi) P_l^m (\cos\theta) \tag{1.8}$$

The first term of the right-hand side accounts for sources external to Earth, and the second term for the internal sources of the geomagnetic field. The symbol $r$ is the distance from the centre of Earth, $\theta$ is colatitude and $\varphi$ is longitude in spherical polar coordinates. $r$ is normalized to $a$, i.e. the mean radius of Earth, and $b_l^m$, $c_l^m$, $g_l^m$ and $h_l^m$ are Gauss coefficients with dimensions of magnetic field B. Each $P_l^m (\cos\theta)$ term is an associated Legendre polynomial of degree $l$ and order $m$.

The term $P_l^m (\cos\theta) \sin m\varphi$ (or $\cos m\varphi$) varies with $\theta$ and $\varphi$ and defines surface harmonics. It shows the symmetry of the various contributions to the geomagnetic field on the surface of Earth. Any given $P_l^m (\cos\theta)$ has $(l - m)$ zeros and thus yields $(l - m)$ circles of latitude at which the value is zero. Similarly, $\sin m\varphi$ and $\cos m\varphi$ have $2m$ values of $\varphi$ at which the function is zero.

When $m = 0$, the surface harmonics are simply Legendre's polynomials and are called zonal harmonics. Since there is no dependence on longitude $(\sin m\varphi = \sin 0 = 0, \cos m\varphi = \cos 0 = 1)$, these functions are axisymmetric.

When $l > m$, the surface harmonics are referred to as terrestrial harmonics with $l - m$ lines of latitude on which $U = 0$; when $l = m$ they yield sectorial harmonics.

The International Geomagnetic Reference Field (IGRF) is a spherical harmonic model of the global field calculated to $l = m = 13$ from the observatory and other data. This model is updated every five years.

### 1.1.3. The Present-Day Field

A picture of the spatial variation of the geomagnetic field around the world at any one time is shown by isomagnetic charts (Figure 1.3), which include the contours of equal magnetic field elements such as declination, inclination and intensity. Charts (a) to (c) in Figure 1.3 show declination, inclination, and intensity as given by the 2010 IGRF. At present in New Zealand, the proximity of the south magnetic pole to the southwest causes an easterly-directed declination. As can be seen from Figure 1.3, the influence of the non-dipole field means the magnetic poles are not antipodal to each other. The influence of the non-dipole field also means that intensities vary around Earth asymmetrically.



(a)

(b)



(c)
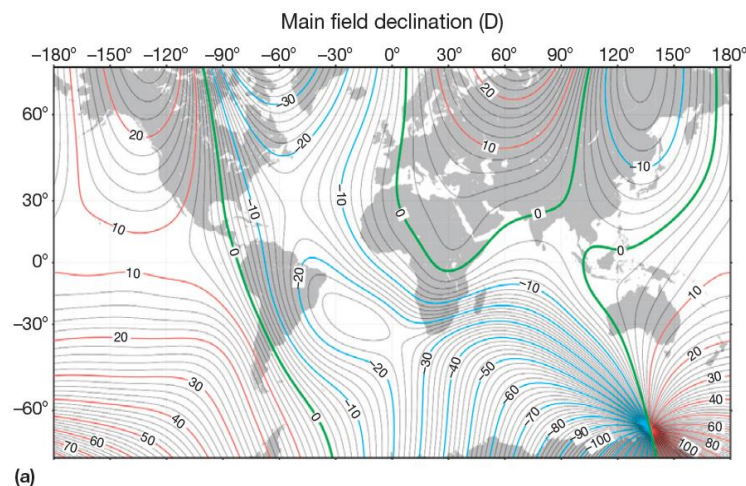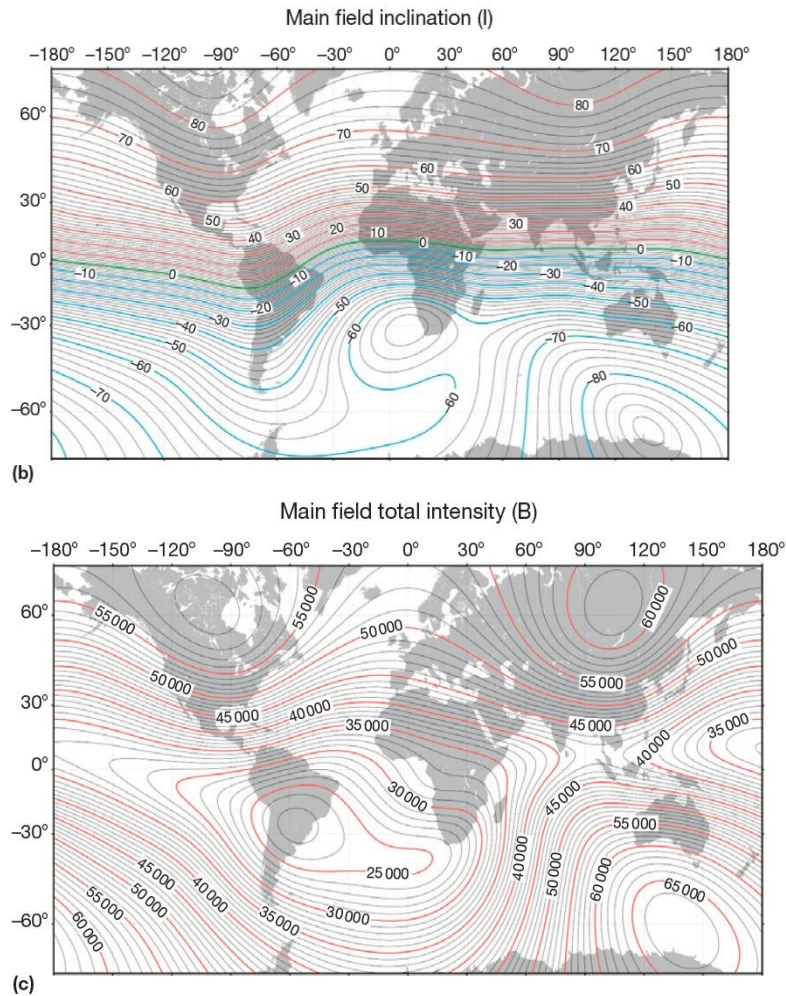
Figure 1.3. Isomagnetic charts (a)-(c). Isogonic, isoclinic and isodynamic charts of the geomagnetic field at the surface of Earth, calculated from the IGRF for the year 2010. (a) Declination in degrees; the green contour is agonic (zero declination), with the red and blue contours indicating eastward and westward declinations respectively. (b) Inclination in degrees; the green contour is the magnetic equator (zero inclination), with the red and blue contours indicating downward and upward inclinations respectively. (c) Intensity in 1000 nT contour intervals; intensity generally rises with increasing latitude. The maps are plotted in Mercator projection (www.ngdc.noaa.org.) (Roberts & Turner, 2013)

## 1.2. Secular Variation

Secular variation refers to the continuous and gradual changes in the geomagnetic field's intensity, declination and inclination over time. Secular variation can be observed on time scales of years to millennia. On longer timescales of ~500,000 years, the field polarity also reverses. There are also shorter-term variations due to external factors like magnetic storms, substorms and pulsations.

Internal changes in the geodynamo result in long-term secular variation. Regular observations of Earth's magnetic field since 1540 AD show significant changes in declination and, later, in inclination. Secular variation curves for Australia (Barton & Barbetti, 1982; Constable & McElhinny, 1985), UK (Turner & Thompson, 1981), Canada (Turner, 1987), and other regions of the world (Turner & Lillis, 1994) show the variation of the geomagnetic field over the past few thousand years. These curves contain data from palaeomagnetic measurements made on lake sediment cores. New Zealand palaeosecular variation curves (NZPSV) are modelled from the sedimentary records of Lake Pounui in the southern North Island and Lake Mavora in the southwest South Island. The sedimentary record from Lake Pounui is for the last 2500 years (Turner & Lillis, 1994), and from Lake Mavora for the last 10 000 years (Turner et al., 2015).

Based on spherical harmonic analysis of historical and palaeomagnetic data, global models of secular variation such as *gufm*1 (Jackson et al., 2000) and CALS3K (Korte et al., 2009) can be used to calculate continuous models of the geomagnetic field at particular locations. However, in general, such models do not include much data from the southern hemisphere. The work described in this thesis is aimed at gathering more high-quality data from New Zealand to supplement both local and global models of secular variation.

## 1.3. Archaeomagnetism

To understand the geomagnetic field of prehistoric times (the time before direct measurements were available), high-quality palaeomagnetic data are needed. Using archaeological materials for palaeomagnetic measurements is known as "archaeomagnetism" (Gose, 2000). Archaeomagnetic work uses fired archaeological artefacts such as baked clays, ceramics, bricks, pottery, and kilns to determine Earth's magnetic field at the time when those artefacts last cooled. The materials contain small amounts of ferri- or ferromagnetic iron oxide minerals. Such minerals may have been in the materials originally or may have formed during the heating. Grains of ferri/ferromagnetic minerals are capable of acquiring a remanent magnetization, which may remain stable for a long time (Néel, 1955). On heating the minerals to a certain temperature, called the Curie temperature, they lose their remanent magnetization.

During cooling, the minerals acquire a new remanent magnetization parallel to the ambient field of that place. This magnetization is called a thermoremanent magnetization (TRM) (Butler, 1992). Consequently, heated or burnt archaeological materials keep a record of Earth's magnetic field. These artefacts can be studied in the laboratory to retrieve recorded information of the ancient geomagnetic field. Once an archaeomagnetic direction and/or intensity have been obtained, they may be compared with regional geomagnetic field models or archaeomagnetic master curves to determine the date when the artefact was last heated. This method of dating is known as archaeomagnetic dating and is a valuable alternative to other dating methods such as radiocarbon dating.

Most of Asia, the Middle East and Europe have a rich cultural heritage. Hence, plentiful archaeomagnetic data from burnt clays and ceramics have extended secular variation curves into the period before observatory records were kept. Archaeomagnetic secular variation curves from Western Europe and the Eastern Mediterranean show sharp variations in the magnetic field over the past three millennia (Gallet et al., 2003). Data from Roman kilns in northeast Spain have contributed to extending the palaeosecular variation curve of Iberia (Gómez-Paccard et al., 2012). Schnepp and Lanos (2005) have developed a secular variation curve of 2500 years for Germany using well-dated archaeological structures. Furthermore, Barbetti (1983) has worked on baked clays from southeast Australia and compiled secular variation records for the last 3000 years. Recent archaeomagnetic work on fragments of Lapita pottery from the southwest Pacific Islands has shown regional variability in intensity data when compared with global field models for the same location (Stark et al., 2010). This suggests that the geomagnetic field in this part of the world is significantly affected by local or regional non-dipole features. To understand these features better, and to better constrain global field models, more palaeomagnetic and archaeomagnetic data is required from the southern hemisphere and the southwest Pacific in particular.

## 1.4. New Zealand archaeology

### 1.4.1. The colonization of New Zealand

New Zealand was one of the last major land masses to be settled by human beings. Polynesians discovered New Zealand during voyages of exploration (Wilson, 2009) from Eastern Polynesian islands in the South Pacific. There have been many theories about the date of early Polynesian settlement of New Zealand, based on genealogical information, orthodox archaeological models (Wilmshurst et al., 2008), forest disturbance, and radiocarbon dating of Pacific rat bones (Davidson, 1987; Wilmshurst & Higham, 2004). Radiocarbon dating of non-native rat bones, for example, initially suggested the arrival of people in New Zealand between 50-150 AD (Irwin & Walrond, 2012). An orthodox archaeological model, however, set the date of initial colonization at about 800 AD. Reassessment of radiocarbon dates using a strict acceptance criterion (Anderson et al., 1991), and radiocarbon dating of rat-gnawed seeds, now puts initial colonization between 1250-1300 AD. (McFadgen, 2007,  Wilmshurst et al., 2008, Wilmshurstet al., 2011). This date is now most widely accepted, and is supported by many of the earliest dated deforestation records (Wilmshurst et al., 2008).

### 1.4.2. Prehistory and development

New Zealand's history is described in two periods of occupation. The prehistoric period is the time between the first arrival of Polynesians in the country and its rediscovery by Europeans in 1769 AD. (Davidson, 1987). Knowledge of the prehistoric period is based on Maori culture and traditions and archaeology. Traditional and cultural knowledge was passed from elders to younger members of the community by oral communication (McFadgen, 2007). The prehistoric period has two main archaeological phases: an early phase called the "Archaic", beginning with the initial settlement by Polynesians, characterized by hunting of the moa, a large flightless bird, and by an assemblage of distinctive artefacts. The later phase, called "Classic Maori", was characterized by  the absence of moa hunting, the emergence of warfare and fortifications,  and a significantly different assemblage of artefacts including weapons (Davidson, 1987). The Polynesians first settled in coastal areas where they extensively hunted fish, seals, and birds. Coastal forests provided easy access to wood, fruits and other useful plants.

Abel Tasman, in 1642, was the first recorded European to sight New Zealand, but he did not land and does not appear to have influenced the prehistoric culture. Lieutenant James Cook arrived in New Zealand in 1769, after which the archaeological record of New Zealand's cultural development is supported by writings and drawings. Europeans have influenced Polynesian culture in New Zealand from that time, with many changes taking place following the arrival of culturally different migrants in New Zealand (Davidson, 1987). An important field of research in New Zealand archaeology is to explain the cultural change between the early (Archaic) and late (Classic Maori) prehistoric periods. There have been various explanations ranging from the introduction of the kumara (Duff, 1956), climate change (Leach & Davidson, 2000), population growth and pressure on food resources (Anderson, 1991), and catastrophic tsunami striking the coast (McFadgen 2007).

Accurate dating of archaeological sites is important to better understand the chronology of New Zealand prehistory and for dating important events since settlement. Radiocarbon dating is most commonly carried out on charcoal and wood. Dating of two different types of material from the same archaeological context sometimes results in differences of hundreds of years (Anderson et al., 1991). Erroneous dates can sometimes be attributed to inbuilt age: i.e. the age of the wood at the time it was burned. In other cases, the calibration from radiocarbon to calendar years introduces problems. The non-linear shape of calibration curves can amplify the uncertainty in age estimates, ambiguous calibrated ages, and anomalous distortions in the distribution of suites of calibrated ages (McFadgen et al., 1994). These issues are discussed further in Chapter 2.

Archaeomagnetic dating offers both a complementary absolute dating technique that can improve extensive chronologies and an alternative technique in situations where suitable materials for radiocarbon dating are not available (Stillinger et al., 2015).

### 1.4.3. Traditional Maori cooking method

The Polynesians brought with them vegetables like kumara, taro and yam. Among these kumara were extensively grown and root vegetables became a major food source. Moa were heavily hunted during the first 100-200 years of settlement and soon became

extinct. There was no pottery in New Zealand, and root vegetables and big birds like moa were cooked by long, slow steaming in earth ovens, a common cooking practice throughout Polynesia. The ovens are called *umu* or *hangi* and were the traditional cooking method of the New Zealand Maori people (Leach, 1982). A traditional style hangi is usually prepared by digging a pit in the ground and filling it with stones and firewood. The fire is kindled and the stones are heated until they are red hot. The heated stones are covered with layers of food packed in baskets and mats. After this, the hangi is sprinkled with water and covered with a thick layer of soil. The food is left for several hours to steam-cook. When the food is cooked and removed from the hangi, the stones are usually left in place for cooling (Nicholas, 1817; Leach, 1982).

## 1.4.4. Archaeomagnetism in New Zealand

The remaining undisturbed hangi stones (and burnt soil if suitable for sampling) can be used for archaeomagnetism in New Zealand. Volcanic rocks and boulders are readily available in much of North Island and were preferred for hangi by Maori as they are good heat retainers and do not fracture easily. Radiocarbon dating is possible where there is a suitable material, such as charcoal, for example. Archaeomagnetic data can also be used for dating by comparing the directions and/or intensities recovered with secular variation curves such as NZPSV1k (Turner et al., 2015).

Before starting this project work, an experimental hangi was constructed at Waiwhetu Marae (Figure 1.4, (a)-(c)) during the Maori Matariki (New Year) festival, with the help of Te Kawa a Māui / the School of Maori Studies (Victoria University of Wellington) (Turner et al., 2012), and using a range of volcanic and sedimentary rocks. A thermocouple was used to check the temperature of the inner parts of the stones (Figure 1.4, (d)). The stones were sampled and their magnetic remanence was studied in the laboratory. The remanence direction and palaeointensity obtained were comparable to the present-day field. The experiment proved that hangi stones are useful for archaeomagnetic experiments. They are the only key source for archaeomagnetism in New Zealand. This thesis describes the sampling of, and some of the first archaeomagnetic results from, New Zealand hangi sites
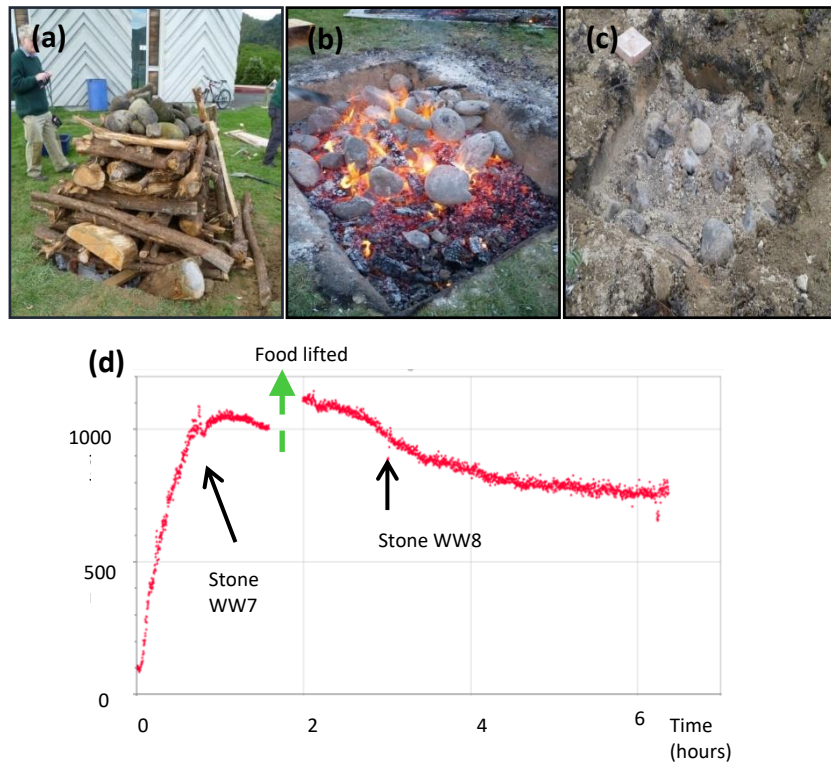
Figure 1.4. Experimental hangi (a)-(d). (a) Cooking stones arranged within a wooden pyre above a hangi pit. (b) Red-hot stones in the hangi pit prior to covering with food and soil. (c) Hangi stones left in place to cool and remagnetize after the lifting of food. (d) Change in temperature of the stones at different stages. (Photos and graph by Dr. Gillian Turner)

## 1.5. Thesis main objectives

The primary aims of this research are:

- To sample a range of archaeological hangi and to investiagte the palaeomagnetic records carried by hangi stones.

- To develop archaeomagnetic records of the variation of the geomagnetic field intensity and direction over the past 1000 years in New Zealand. These data will contribute to global field models for the southwest Pacific region and to modelling studies of the geodynamo.

- To carry out thermo-magnetic and rock magnetic experiments on the hangi stones studied, in order to better understand their magnetic mineralogy and the stability of their magnetic remanence.

- To construct a well-constrained and robust archaeointensity curve for New Zealand.

- To develop archaeomagnetic dating as an archaeological technique in New Zealand.

## 1.6. Thesis structure

The structure of this thesis is as follows. Chapter 2 describes the sites sampled, the method of sampling hangi stones, the experiments performed, and statistical and analytical techniques. Chapters 3-7 deal with each site in turn. Each chapter has a similar format including information about the archaeological setting, the sampled stones, the rock magnetic and palaeomagnetic measurements, the results and a discussion of these results. Chapter 8 discusses the overall results and summarizes the outcomes of the project.

# 2. Fieldwork and Palaeomagnetic Methods

## 2.1. Fieldwork and sampling

The remanent magnetization of rocks, sediments and archaeomagnetic materials can provide a record of the palaeomagnetic field. Study of these materials may give us information on how the strength and direction of Earth's magnetic field have varied with time. When ferro/ ferrimagnetic minerals are heated above their Curie temperature they lose their remanent magnetization, while during cooling they acquire magnetization in the direction of the ambient field. The acquired magnetization is called Thermoremanent Magnetization (TRM). TRM in uniformly magnetized (single domain) grains may remain stable for geological periods of time.

In this study we work with archaeomagnetic fired rocks, or "hangi stones", up to 600-700 hundred years old. These stones are oriented before sampling to obtain reliable and useful directional data. Radiocarbon dating of charcoal fragments from the hangi sites can provide an age range of its last use. High-quality palaeodirections and palaeointensity data may then be determined.

The hangi sites studied here were investigated by archaeologists during excavations for the study of Maori occupation, roadside construction work, and subdivision of land for development.

## 2.1.1. Sites sampled

Field work was carried out at five different archaeological sites from the North and South Islands of New Zealand (Figure 2.1). From the Great Mercury Island, Whitianga, Weld Pass, and Riverlands sites we collected oriented stones. Archaeologist Gerard O'Regan provided us with non-oriented hangi stones from the Opihi River site. Hangi stones from a sixth site, Bob's Bay, in Picton, could not be measured as the stones were very fragile and hence drilling cores from the stones was not straightforward. Consolidating the stones using water glass solution was tried (in accordance with Schnepp et al., 2008), but this was not successful. The stones were therefore stored for possible future

experimentation. Four non-oriented stones from an archaeological site at Lake Kohangatera collected by Dr. Bruce McFadgen did not produce coherent data, possibly because the stones were not heated sufficiently to high temperatures to begin with and thus did not acquire a reliable TRM. All the sites are listed in the New Zealand Archaeological Association's database Archsite (www.archsite.org.nz) and have Archsite reference numbers (Table 2.1). A detailed description of the sites sampled is included in Chapters 3-7. Details of each hangi sampled are given in Table 2.1.



Figure 2.1. Map of New Zealand: red dots indicate the archaeological sites at which hangi have been sampled.

Table 2.1. Description of hangi stones sampled from each site, site name, site ID, and archaeological site numbers.

| Name of place | Site ID | Hangi sites with Archsite number | Number of stones |
|---|---|---|---|
| Great Mercury Island | GM | GM1 (T10/914) | 11 |
| | | GM2 (T10/1114) | 10 |
| | | GM3 (T10/1114) | 4 |
| Lake Kohangatera | LK | LK (R28/30) | 4 |
| Opihi River | OP | OP (J38/75) | ~10 |
| Riverlands | RL | RL (P28/149) | 7 |
| Weld Pass | WP | WP1 (P28/145) | 4 |
| | | WP2 (P28/146) | 4 |
| | | WP4 (P28/145) | 4 |
| Whitianga | WT | WT1 (T11/914) | 10 |
| | | WT2 (T11/914) | 4 |
| | | WT3 (T11/914) | 4 |
| | | WT4 (T11/914) | 4 |

## 2.1.2. Sampling method

Archaeologists first investigate the hangi sites before reporting to us. The sand or soil from the top of the excavated stones should be removed very carefully so that the stones remain undisturbed. The features of each hangi such as the size, pattern of stones, and traces of food cooked in the hangi should be noted. We search suitable charcoal pieces for radiocarbon dating. Several stones (4-10) of appropriate size and shape are collected from each hangi. The field equipment includes:

- non-magnetic shovel and brush for removing soil and cleaning of stones and measuring sticks;
- plaster of Paris, bowl, water, spoon or spatula for mixing and making plaster paste, Perspex sheets, and a bubble level for surface leveling;
- magnetic compass and sun compass, accurately set to watch for orientation;
- colored marker pens, notebook, knife or scissors;
- paper towels, newspapers and boxes for packing.

The sampling method comprises the following steps:

- Select a reddened stone of appropriate size with minimum cracks for sampling;

- Brush the sand from stone softly, then clean with water;

- Mix plaster of Paris (poP) with water in a bowl to make a viscous paste;

- Cover top of stone with poP paste (Figure 2.2 (a)) and level with the help of a perspex sheet and bubble level (Figure 2.2 (b)). Wait until poP paste is dry and ready for marking.

- Label the stone on the dried poP cap.

- Mark sun direction and magnetic north on the levelled poP top (Figures 2.2 (c), (d)). For sun direction, place the sun compass on its flat top, allowing sun rays to pass through two slits of the compass. Mark a line along the base of the compass towards Sun as shown in Figure 2.2 (c). Record the time of marking the sun direction accurately.

- Remove the oriented stone without disturbing other stones in the hangi.

- The minimum number of stones collected from each site is 4, but more is preferable, especially if the stones are small.



Figure 2.2. Sampling method. (a) Hangi stone covered with plaster of Paris. (b) Levelled poP on top of stone with the help of bubble level and Perspex. (c) Sun compass placed on levelled top for marking sun-direction. (d) Compass needle to mark magnetic north direction.

## 2.1.3. Naming of stones and specimen preparation

Hangi stones are named according to the locality or site, the number of pits sampled at the site (if more than one), and the number of stones collected from the pit. Generally, a two-letter abbreviation indicates locality, followed by a number indicating the hangi pit sampled from the site. Stone, core and specimen numbers are then hyphenated (Figure 2.3). Stones are numbered in the order they were excavated from the hangi pit. Hence, GM1-1 indicates the first stone excavated from the first hangi pit sampled on Great Mercury Island. This naming scheme is used throughout for naming specimens in excel sheets and other files. However, for sites where only one hangi pit was sampled (OP and RL), the number following the locality abbreviation is the stone number: for example, RL2 indicates the second stone from the single pit sampled at Riverlands.

For the preparation of specimens, stones were set in wooden boxes with the help of either concrete or expanding foam and leveled with a bubble level on the flat poP surface on the top of the stone. The sun direction marked on the poP is kept parallel with one side of the rectangular box to retain the orientation of the stone in case the poP top breaks during the drilling process (Figure 2.4). Once the concrete or foam is set, a vertical drill press is used to drill cylindrical cores 2.5 cm in diameter and perpendicular to the poP surface (Figure 2.4 (b)). After this the cores are cut into 2.0 cm-long specimens, using a saw machine. The sun direction marked on the stone in the field can be transferred as a X-direction to the core. The Y-direction is at a 90° angle to the X-direction in a clockwise direction and Z is in the downward direction (Figure 2.4 (c)).
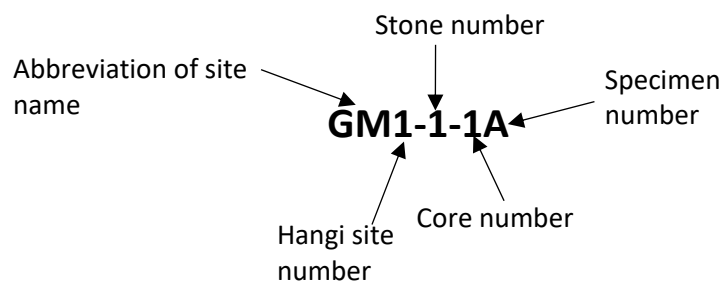


Figure 2.3. Specimen labelling.

Ideally, four cores are drilled out of one stone, but sometimes, with smaller stones, only one or two cores can be drilled. The cores are named in numerical order of drilling, with small specimens named in alphabetical order from top to bottom (Figure 2.3). As the sun direction is marked with a record of the date and time, and the latitude and longitude of the site are also recorded, the azimuth of each stone can be calculated from online sun calculators: (http://www.esrl.noaa.gov/gmd/grad/solcalc /azel.html).
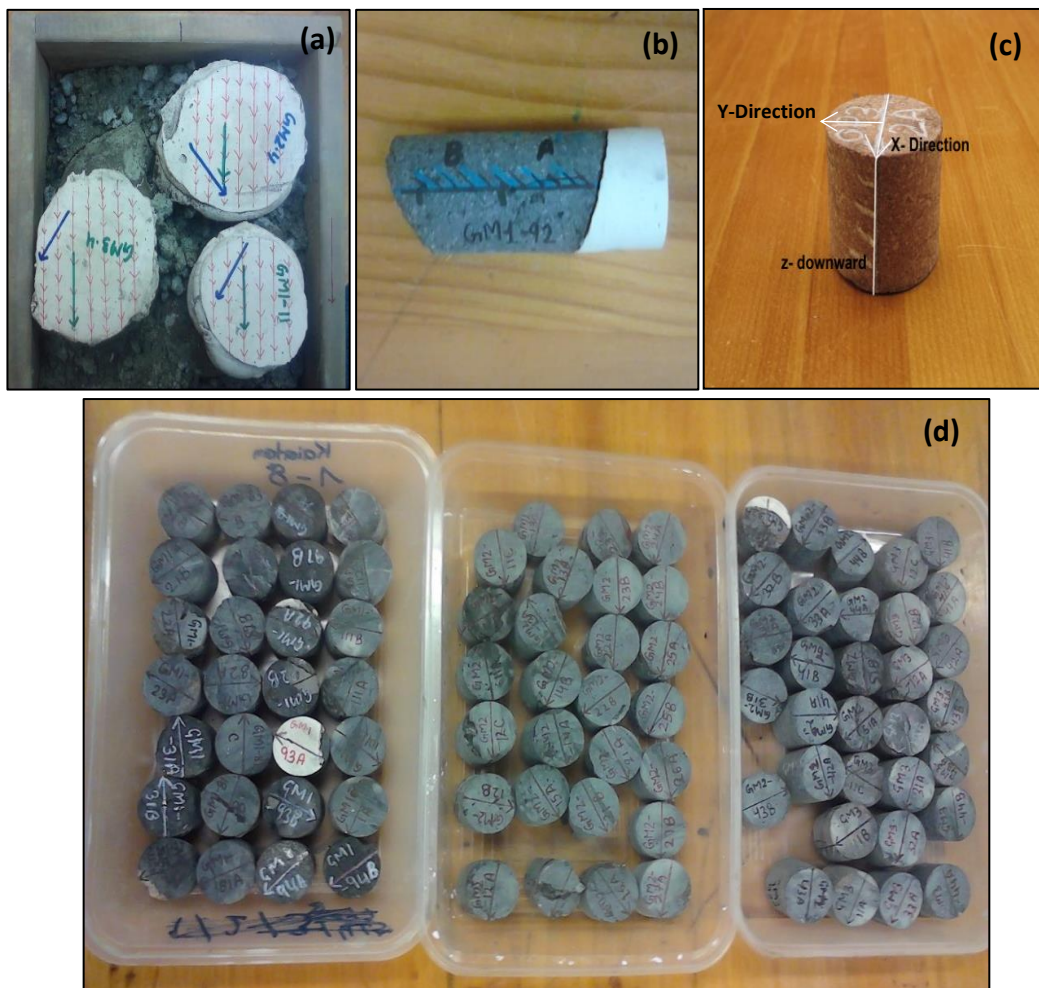


Figure 2.4. Specimen preparation. (a) Hangi stones settled in the wooden box. (b) A drilled core of GM1-9 core. (c) Orientation marks transferred to the specimen. (d) Specimens cut from drilled cores.

## 2.2. Radiocarbon Dating

Carbon has three naturally occurring isotopes: $^{12}C$, $^{13}C$ and $^{14}C$. Of these, $^{14}C$ is radioactive. $^{14}C$ in the atmosphere forms by the action of cosmic ray-induced radiation on atmospheric nitrogen.

$$^{14}N + n \rightarrow {^{14}C} + p$$
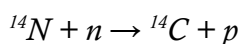
$^{14}C$ in the atmosphere combines with oxygen to form radioactive carbon dioxide, which is then taken up by living organisms and plants through breathing, eating or photosynthesis. When the organism or plant dies, the uptake of $CO_2$ stops and the $^{14}C$ starts to decay at a constant rate given by the half-life of radiocarbon. The half-life of $^{14}C$ was originally determined by W.F. Libby (1955) to be 5568 years (Libby, 1955). Although this was revised in 1962 (Godwin, 1962), the original value is still used (Jull & Burr, 2015), and a correction routinely applied to the age measurements. The time since death can thus be determined by measuring the level of $^{14}C$ left in the remains of the organism. The method of determining the time since death is called radiocarbon dating.

### 2.2.1. Measurement Method

All the charcoal samples collected from archaeological hangi sites for this project were radiocarbon dated using Accelerator Mass Spectrometry (AMS). This technique uses samples considerably smaller than either gas counting, previously used at the Rafter Laboratory of GNS Science, or liquid scintillation, currently used by Waikato University.

The abundance of $^{14}C$ remaining in the sample, compared with $^{12}C$ and $^{13}C$, is used to calculate a Conventional Radiocarbon Age (CRA). This can be expressed as $^{14}C$ years BP (Before Present, where Present is defined as 1950 AD), and its measurement error (±σ, one standard deviation).

### 2.2.2. Calibration from $^{14}C$ to calendar years

The calculation of a CRA assumes that the concentration of $^{14}C$ in the atmosphere is constant over time. The cosmic ray flux entering Earth's atmosphere, and therefore $^{14}C$ production, are affected by Earth's magnetic field, particularly its strength, and the sun's

activity. Therefore, calibration of CRAs is necessary to compensate for the variation of $^{14}$C concentration in the atmosphere over time. A calibration curve for terrestrial samples in New Zealand has been developed by measuring $^{14}$C in annual tree rings from the southern hemisphere (Hogg et al., 2013). There is a difference in the radiocarbon ages of tree rings formed at the same time in the northern and southern hemispheres. The southern hemisphere calibration curve is about 40 years older than northern hemisphere calibration curve. The southern hemisphere radiocarbon calibration curve, SHCal13, for the period of 950 AD-1950 AD, is shown in Figure 2.5 (Hogg et al., 2013).
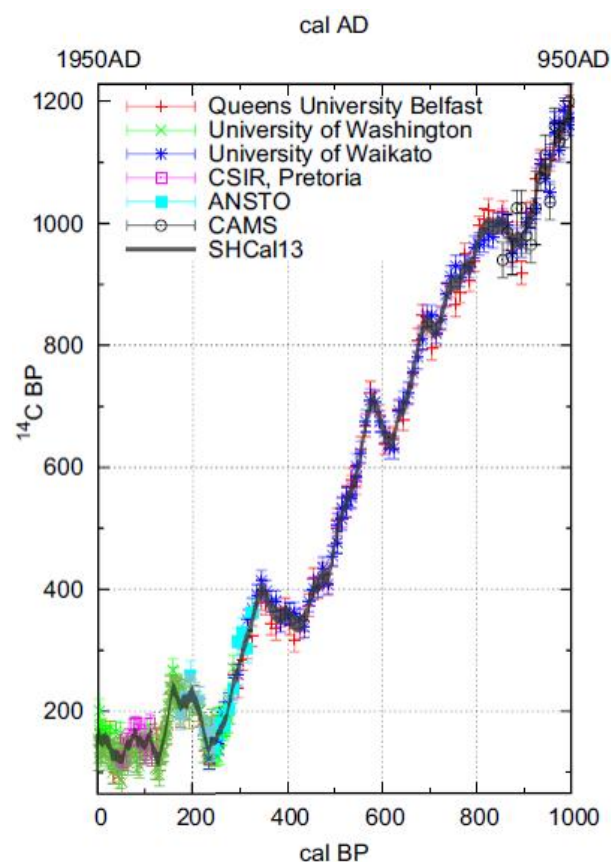


Figure 2.5. SHCal13 terrestrial calibration curve for the archaeological period: data with one standard deviation uncertainty (Hogg et al., 2013).

Radiocarbon age can be converted to calendar years by reflecting $^{14}$C years through the calibration curve as shown in Figure 2.6. The calendar years (years in AD) and radiocarbon years (years in BP) are represented along the x-axis and y-axis respectively of Figure 2.6. The normal distribution curve on the y-axis displays a mean CRA value and its standard deviation, σ. The probability of the date being within ±2σ of the CRA is 95%. Radiocarbon age can be converted into a calendar date by drawing a horizontal line from

the calculated $^{14}$C year to intercept the calibration curve. From this point, a vertical line is dropped to the x-axis (McFadgen, 2007). An example of a charcoal sample from hangi site GM3 is shown in Figure 2.6. The calibration curve used for comparison in the graph is SHCal13 (Hogg et al., 2013).

## 2.2.3. Interpretation of the calendar year and errors

The calibration process described above does not always yield a straightforward, unambiguous calendar year age estimate. Measurement errors in the CRA and wiggles in the calibration curve may give rise to considerable uncertainties and distort the calendar year age. As can be seen in Figure 2.5, after about 1700 AD the calibration curve has more wiggles since, from about this time, $^{14}$C in the atmosphere started varying due to human activities such as the burning of coal and oil, and nuclear bomb testing (Prior, 2012). The radiocarbon age (CRA) for the GM3 sample is 242 ± 16 BP. The probability density function on the x-axis represents a 95% confidence interval containing two main age ranges: 1650 AD-1675 AD (31.6% of area) and 1750 AD-1798 AD (63% of area). The graph does not, however, determine which calendar year range the sample falls within.
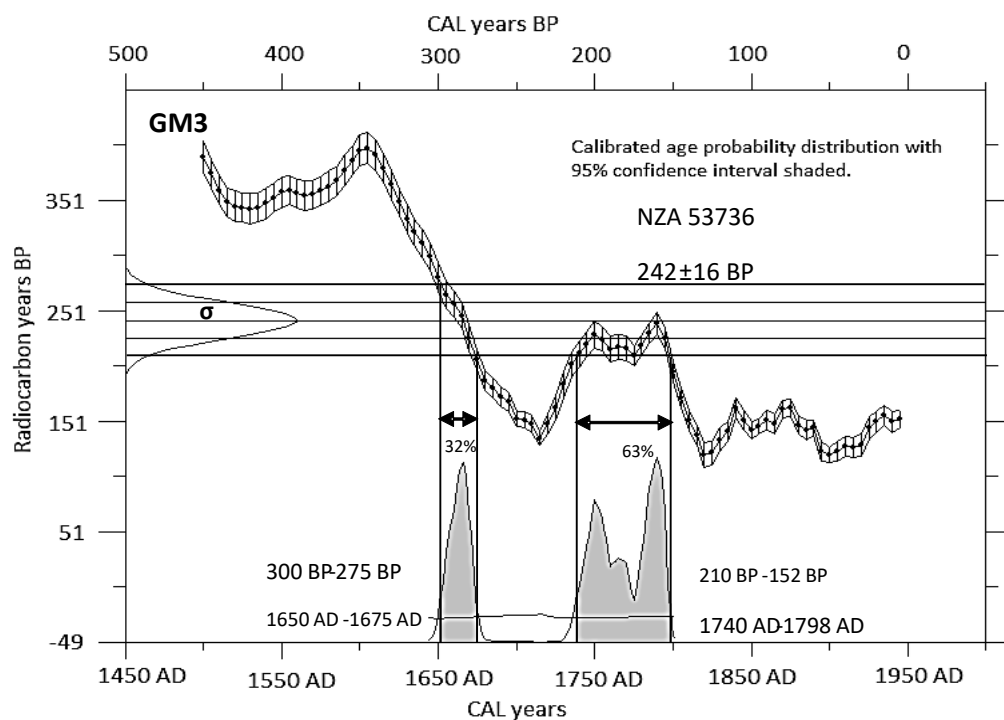


Figure 2.6. Radiocarbon age and calibrated date representation using SHCAL13 calibration curve (Hogg et al., 2013b). Graph produced with the help of program WINSCALX 5.1 (Spark et al., 2011).

Independent archaeological factors and archaeomagnetic data may on the other hand, help to determine the narrow calendar year age range.

Uncertainties in calibration results arise for two main reasons. First, measurement errors of CRA are large in comparison with the timespans of the wiggles. Second, the timespan of a wiggle in radiocarbon years is smaller than its timespan in calendar years (and vice versa for the intervals between wiggles). Another possibility is that for the sample whose true CRA falls within/outside a wiggle, its measured CRA may fall outside/within the wiggle (McFadgen, 2007). When some CRAs are measured, different timespans show spreading and clumping, known as calibration stochastic distortion (CSD). This distortion is due to wiggles of the calibration curve having more calendar years than radiocarbon years, and the intervals between wiggles having more radiocarbon years than the calendar year (McFadgen et al., 1994).

Another important factor which may affect $^{14}$C age estimates is the inbuilt age of the material. Inbuilt age is the difference between the date of death of a sample and the time of the event of interest (in this project, the time of last use of the hangi from which the charcoal was sampled). For a tree, inbuilt age is the sum of its growth age (the age of wood in a tree which may be several hundred years old when the tree dies) and its storage age (trees may last for hundreds of years after they die before being used as firewood) (McFadgen 1982). For this reason, we sent charcoal samples for identification before dating. Short-lived wood and twigs provide reliable dating results.

Occasionally, even though the CRAs have small measurement errors from 16-20 years, there may be spreading and clumping in the distribution of calendar years. In some cases, the radiocarbon age corresponds to several regions of the calibration curve. In such a situation, other, independent information is needed to obtain an unambiguous age estimate. For the hangi sites of Weld Pass and Riverlands, the charcoal was of long-lived species (matai), and provided erroneous radiocarbon ages of around 769±21 BP and 881±21 BP. These dates have significant and unwanted inbuilt age components (McFadgen, 1982). As New Zealand's prehistory is very short (not older than 1250 AD), these are important factors to be considered when interpreting dates.

## 2.3. Laboratory Methods

### 2.3.1. Thermomagnetic Properties

Susceptibility (χ) versus temperature plots

Susceptibility (χ) versus temperature curves help to determine the Curie temperatures of magnetic minerals. Different minerals have different Curie temperatures (see Appendix 1). We can also detect thermally-induced changes to the magnetic mineralogy that affect susceptibility by comparing heating and cooling curves. Curie temperature helps to estimate the mineralogy of the palaeomagnetic samples. The blocking temperature spectrum helps in deciding what steps we should choose for thermal demagnetization (Butler, 1992).

Bartington's MS2 susceptibility apparatus was used to measure magnetic susceptibility as a function of temperature. For this experiment, a piece of rock is crushed into small pieces using a pestle and mortar and weighed. The sample is then heated from room temperature to 700°C. A thermocouple inside the sample holder measures the temperature and the MS2 meter records the susceptibility. The susceptibility is measured at 10°C intervals during heating and cooling. Data is saved, and a plot, which shows the change in susceptibility with the rise in temperature, is drawn on the screen of the computer. The data are transferred to an Excel spreadsheet for calculations and plotting (Figure 2.7). Two curves are plotted: the red plotted during the heating process, and the blue plotted during the cooling process. In Figure 2.7, the heating and cooling curves are almost reversible, meaning little thermal alteration took place in the mineral upon heating. In some cases, irreversibility indicates a thermal alteration in the magnetic minerals. This alteration can indicate the growth of a magnetic mineral at high temperature, giving different values of susceptibility on cooling. Therefore, the heating and cooling curves are useful to check the thermal stability of the magnetic carriers.

In some cases, the experiment is repeated several times, decreasing the maximum temperature until we get reversible heating and cooling curves. From here, we can determine the temperature at which thermal alteration took place in the mineral. In Figure 2.7, sample GM1-9 show two peaks in the heating and cooling curves. Such plots can provide information about the presence of different magnetic mineral phases. Sample GM1-9-2 has shown magnetic mineral phases of low (~250°C, titanium rich titanomagnetite) and high (>600°C, poor titanium titanomagnetite) Curie temperatures.
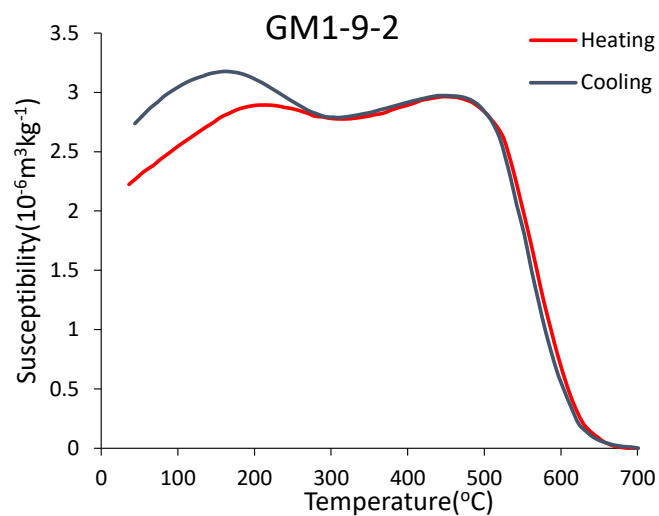


Figure 2.7. A susceptibility versus temperature curve of a sample from hangi stone GM1-9. This experiment was carried out using the Bartington apparatus at Victoria University.

Saturation magnetization ($M_s$) versus temperature plots

Thermomagnetic properties of samples from hangi stones are also studied by using a vibrating field translational balance. The $M_s$ vs. T curves also give us information on the magnetic mineralogy of samples. Similar to the χ vs. T experiment, the sample is heated to 700°C and then cooled to room temperature.  The change in saturation magnetization with temperature is recorded and a graph plotted as shown in Figure 2.8. This plot also gives us information about the magnetic phases and thermal alteration taking place in the sample with a change in temperature (Dunlop & Özdemir, 1997). The experiments for samples of hangi stones were conducted in a constant magnetic field less than 1T. The temperature at which saturation magnetization drops i.e. Curie temperature, is used to get information about the magnetic mineralogy of the sample.
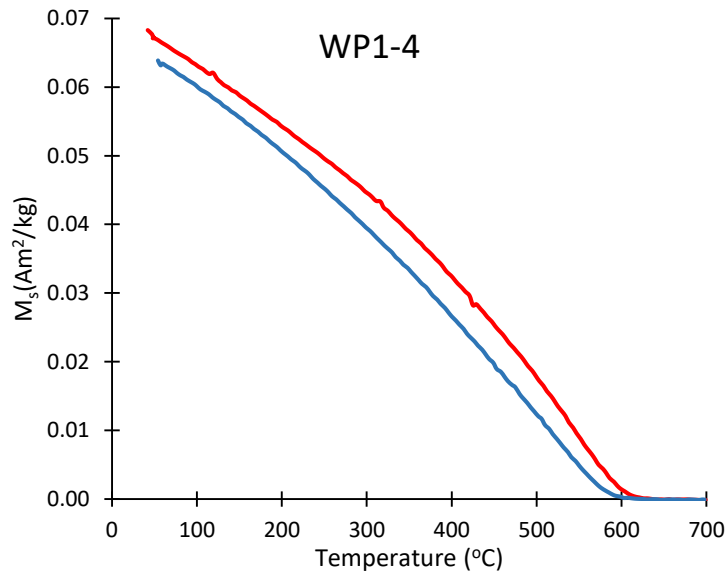
Figure 2.8. Saturation magnetization versus temperature curve of a sample from hangi stone WP1-4.

## 2.3.2. Methods of calculation of Curie temperature

The most challenging task is to choose an accurate method to estimate the Curie temperature from these graphs. Most commonly, four methods can be used for the calculation of Curie temperature: the two tangents method, the inverse susceptibility method, the second derivative method, and the Moskowitz method (Petrovský & Kapička, 2006). For susceptibility versus temperature experiments the inverse susceptibility method was chosen, and for saturation magnetization versus temperature experiments, the second derivative method has been selected. These methods are described below with examples.

(Definition: In χ-T experiments, as the temperature of the grain reaches blocking temperature, susceptibility will increase until the Curie temperature is reached. Then susceptibility will drop inversely with temperature. A sharp peak in susceptibility below the Curie temperature is known as the Hopkinson peak (Tauxe et al., 2007)).
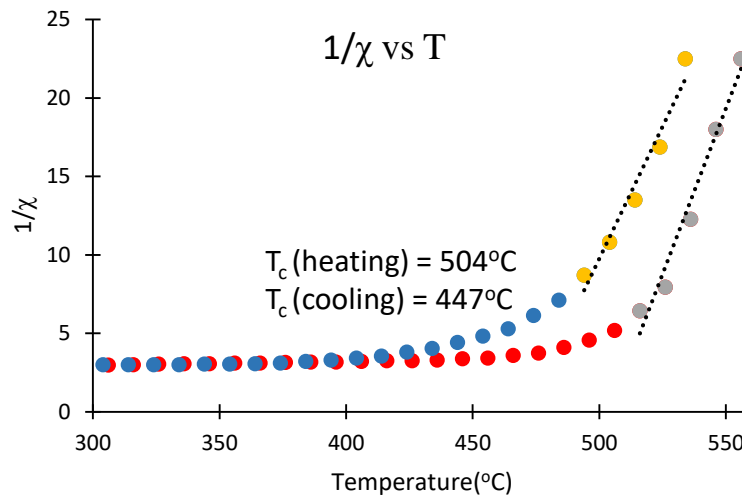
Figure 2.9. Inverse susceptibility versus temperature plot of a sample from stone WP2-2. Red is a heating curve and blue is a cooling curve.

In the **inverse susceptibility method**, Curie temperature can be calculated from the graph plotted between $\chi^{-1}$ and temperature (Figure 2.9) (Petrovský & Kapička, 2006). A tangent from higher values of $\chi^{-1}$ to the point where tangent line meets the temperature axis is the Curie temperature. Errors in this method can occur due to deviation from linearity at temperature near to transition temperature, and also if we have a wide maximum in the susceptibility curve followed by gradual decay over a large temperature range (Petrovský & Kapička, 2006).

Another approach is the **double derivative approach (**Figure 2.10) (Tauxe, 2003). This method can be used to determine Curie temperature from $M_s$ versus temperature plots. The maximum curvature part of the whole curve can be used for calculations. Derivatives $dM_s/dT$ and $d^2M/dT^2$ are calculated for each temperature step of the selected section. The plot of $d^2M/dT^2$ vs. T then shows a maximum temperature which is Curie temperature. The data obtained from a Variable Field Translational Balance was transferred to an Excel spreadsheet and calculations were done to determine the Curie temperature (Figure 2.10). To reduce uncertainty, we can choose four points around the maximum and find the average of these points. In this method, the maximum point selected to calculate the Curie point may amplify significantly, resulting in a wrong

interpretation (Leonhardt, 2006). From RockMagAnalyzer 1.0 software, we can calculate $T_c$ by applying the second derivative method (Tauxe, 2003) and the Moskowitz method (fourth method) (Moskowitz, 1981) (Figure 2.11 (a) & (b)).
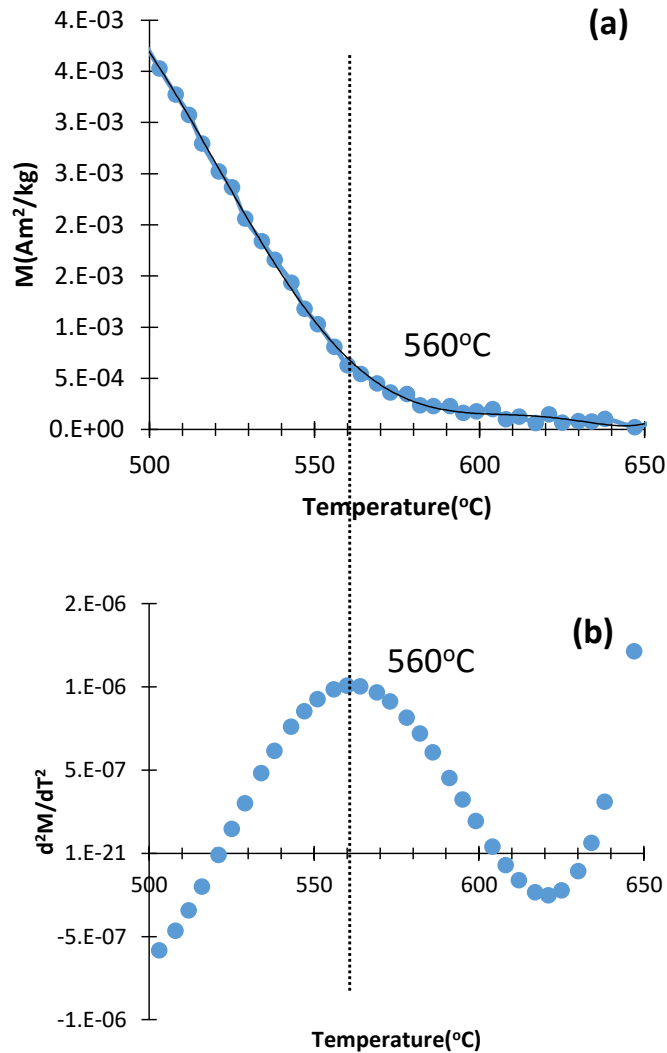


Figure 2.10. Double derivative method. (a) Saturation magnetization versus temperature graph of sample WP2-2 from temperature 500-650°C (heating curve). (b) $d^2M/dT^2$ versus temperature plot.

The results of Curie temperature determined from calculations done on an Excel spreadsheet and Rockmag Analyzer 1.0 using the second derivative method are similar (Figure 2.10 (a) & (b)). Therefore, this software can be utilized throughout to calculate the Curie temperature of samples that have $M_s$ versus T data. From the observations and information provided by Leonhardt & Petrovský in 2006 (Petrovský & Kapička, 2006b), we decided to use the inverse susceptibility method for calculation of $T_c$ for susceptibility versus temperature plots and the two tangents method for M versus T plots.
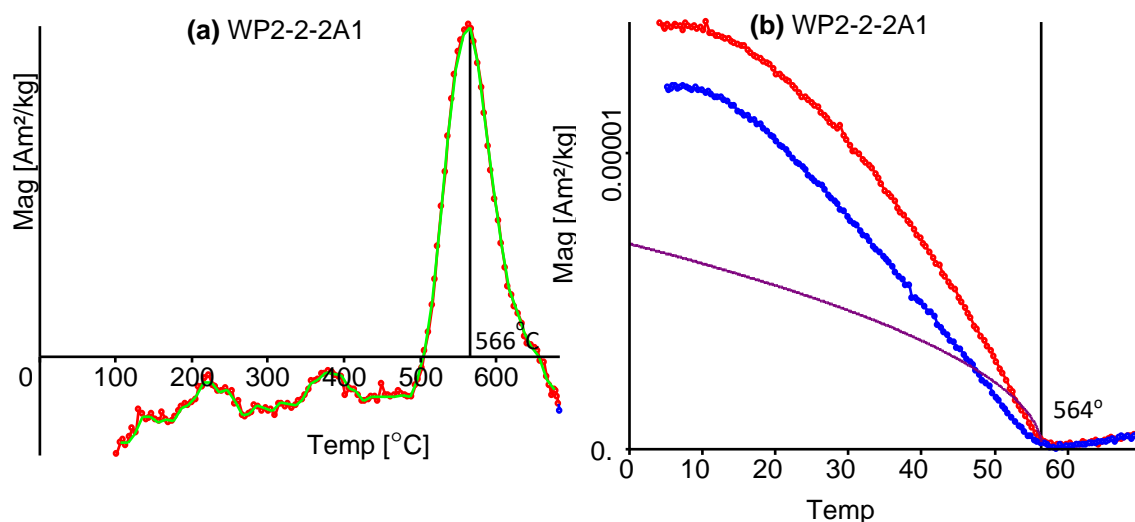
Figure 2.11. Use of Rockmag Analyzer 1.0. to calculate Curie temperature. (a) Double derivative approach. (b) Moskowitz method.

Note: A detailed investigation was done to find the accuracy of Curie temperature measured from Bartington's susceptibility apparatus. We found that a difference of 10-15°C in the $T_c$'s of heating and cooling curves is due to a temperature lag between the thermocouple and the sample. Therefore, a difference of 10-15°C in heating and cooling $T_c$ can be ignored as an instrumental error. Anything above that should be considered as a real alteration in the magnetic mineralogy of the sample.

In titanomagnetite ($Fe_{3-x}Ti_xO_4$), most commonly found in geological rocks, Curie temperature is affected by an increase in the fraction, x, of titanium. An increase in x weakens the ferrimagnetic exchange coupling and decreases the Curie temperature linearly with x (Butler, 1992).

### 2.3.3. Isothermal remanent magnetization (IRM) and Hysteresis loops

Instruments

Modern instruments like the Vibrating Sample Magnetometer (VSM) and the Variable Field Translational Balance (VFTB) are highly sensitive and can be used for plotting hysteresis curves, isothermal remanent acquisition plots, remanence coercivity, and thermomagnetic graphs. These instruments facilitate the calculation of saturation magnetization $M_s$, saturated remanence $M_{rs}$, coercivity, $B_C$ and remanence coercivity,

28

and $B_{cr,}$ of magnetic minerals. These parameters help in understanding the domain state of minerals.

The data presented here are obtained from micromagnetic experiments performed on hangi stone samples using the VSM at the palaeomagnetic laboratory at Australian National University, and the VFTB at the University of Liverpool.

## Hysteresis and IRM plots

Hysteresis curves have been plotted for samples from most of the hangi sites. The results, after paramagnetic correction, show that most of the samples are ferro- or ferri-magnetic. There are significant differences between data from various samples.

First, the magnetization of the sample is measured, then the sample is exposed to an external magnetic field B. The instrument records the change in magnetization as B first increases, then decreases, reverses, and finally returns to zero. This may be shown as a characteristic loop (Figure 2.12). The applied field is $\pm$ 1.0 T. $M_s$ is the saturation magnetization – the value at which the magnetization of the mineral saturates in an applied magnetic field. After saturation when the field reduces to zero the remaining magnetization is called the saturation remanent magnetization ($M_{rs}$) (Tauxe et al., 2010). The coercivity $B_c$ is the intensity of the applied magnetic field required to reduce the magnetization of the sample to zero. Thus coercivity is the resistance of a ferromagnetic material to be demagnetized.
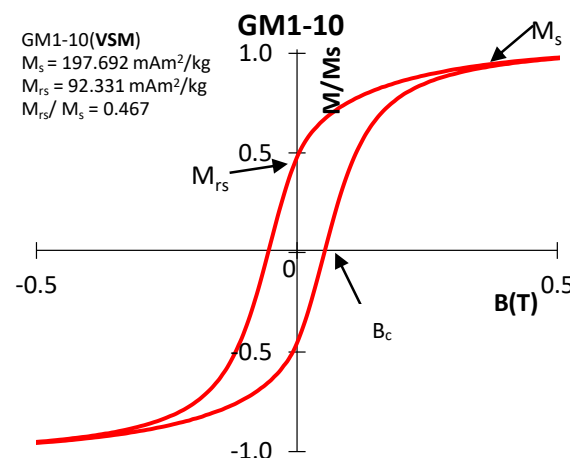


Figure 2.12. Hysteresis loop of sample GM1-10 from Great Mercury Island.

The isothermal remanent magnetization (IRM) can be used to illustrate remanent magnetic properties of the samples, particularly $M_{rs}$ and $B_{cr}$ (Figure 2.13). The instrument measures the remanence of the sample after the application of an applied field.

The maximum remanent magnetization acquired by the sample is called the saturated isothermal remanent magnetization ($M_{rs}$). The sample is then turned around and exposed to an applied backfield until $M_{rs}$ decreases to zero. The field at which the remanence reduces to zero is called the coercivity of remanence $B_{cr}$ (Tauxe et al., 2010).
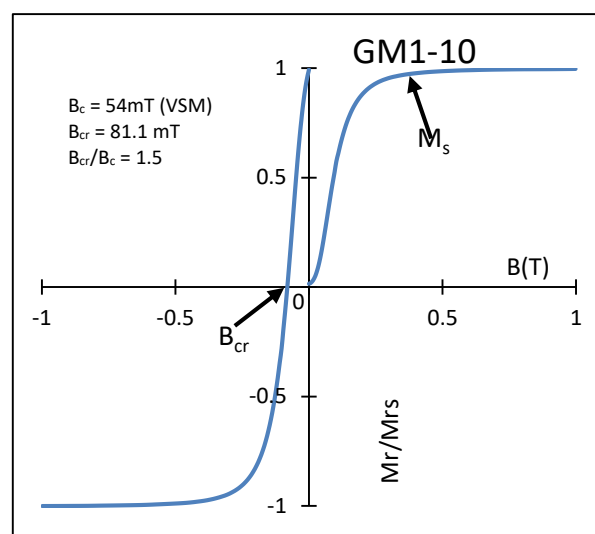


Figure 2.13. Isothermal remanent magnetization acquisition plot and backfield curve of a sample from Great Mercury Island.

The remanent magnetization and coercivity of a sample can be used to plot a graph $M_{rs}/M_s$ vs. $B_{cr}/B_c$, known as a Day plot (Day et al., 1977). This plot is helpful to distinguish the single domain (SD), multidomain (MD), pseudo-single domain (PSD) and superparamagnetic (SP) behaviour of magnetic minerals. For a random distribution of uniaxial SD grains, $M_{rs}/M_s$ should be equal to 0.5, and $B_{cr}/B_c$ should be equal to 2.0. Samples which fall in between the MD and SD regions have a PSD or may contain mixtures of grains of different domain states (SD, PSD, MD, and SP) (Figure 2.14).
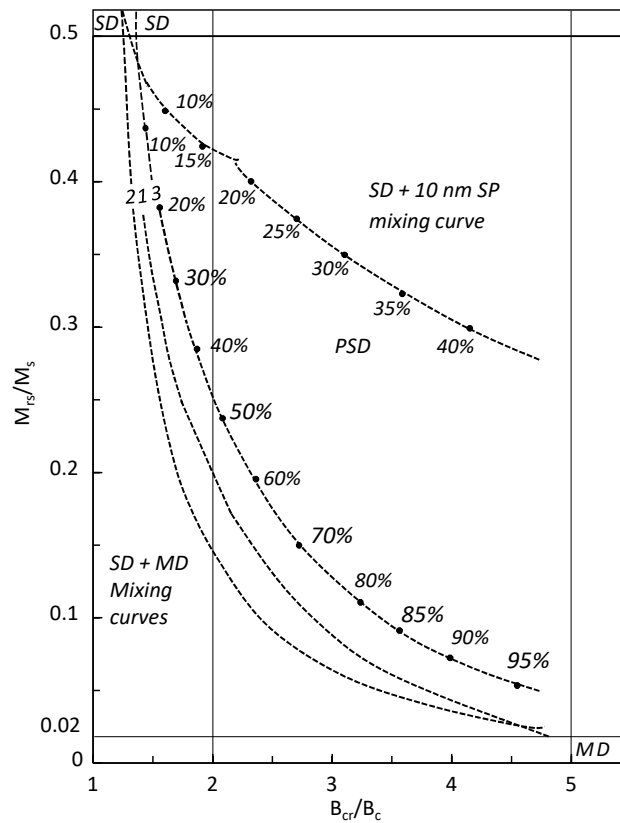
Figure 2.14. Mixing curves of Dunlop (2002) for single domain, multidomain and superparamagnetic grains.

The ratios $M_{rs}/M_s$ versus $B_{cr}/B_c$ of hangi stones can be compared with the theoretical mixing (SD+MD and SD + 10nm SP) curves 1, 2 and 3 in Figure 2.14 (Dunlop, 2002). Curves 1 and two are plotted using data from (Day et al., 1977) and (Parry, 1965). Curve 3 has been drawn using data from Parry (Parry, 1980;. The numbers along the curves are volume fractions (for MD or SP) of the soft magnetic component. The equations used to calculate all parameters are explained in detail by (Dunlop, 2002a; Dunlop, 2002b).

Thus, from $\chi$-T plots and rock magnetic data we can determine both the magnetic mineralogy and domain state of the hangi stones.

Hysteresis of mixtures

We can have a variety of magnetic minerals or grain sizes in samples. Distortion of the hysteresis loop or two different features in the loop indicates the presence of two phases of different coercivities. These may be SD, MD, PSD, SP or a mixture. Most of the time we observed a common mixture of SD plus small amounts of MD with a slightly pot-bellied hysteresis loop (Figure 2.15, (a)-(d)). In some samples, a mixture of SD and SP is seen. Such samples show a so-called 'wasp-waisted' hysteresis curve (Figure 2.15 (e)).
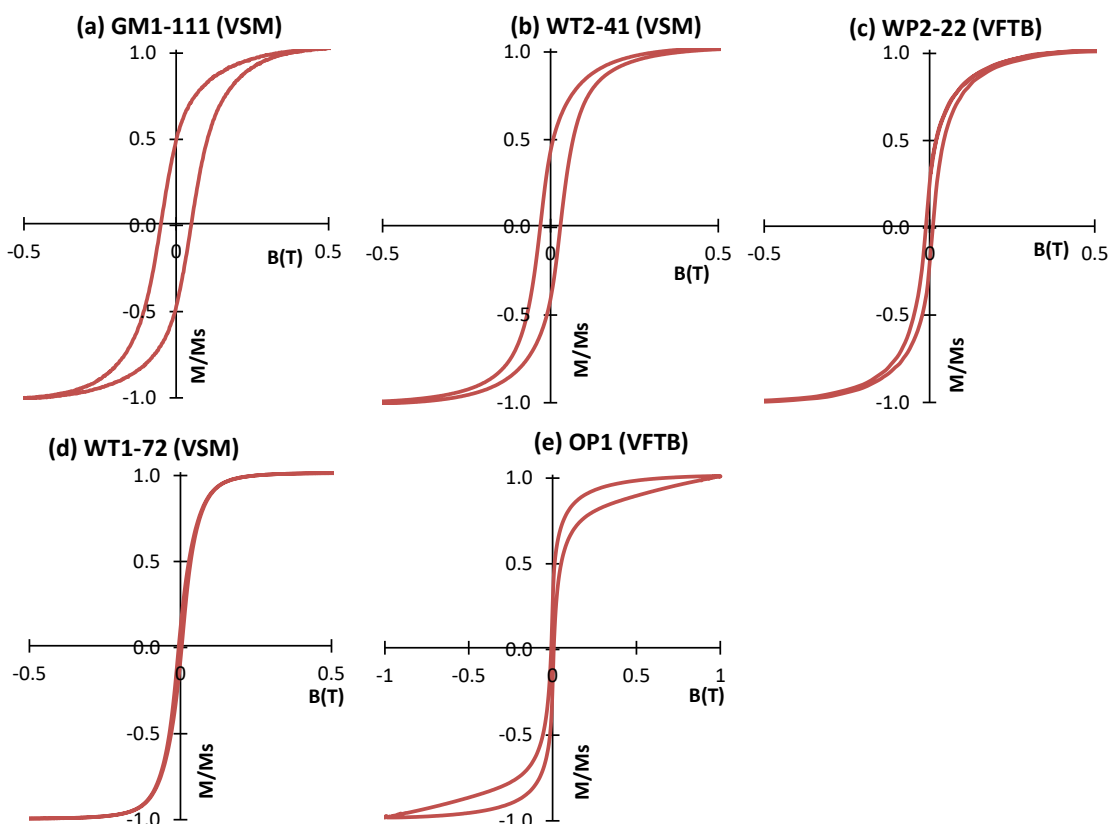


Figure 2.15. Examples of hysteresis showing SD (a), PSD (b), PSD (c), SP (d) and SD+SP (e) behaviour. These plots are obtained from hangi stones experimented on using the VSM (ANU) and the VFTB (Liverpool).

## 2.4. Palaeomagnetic measurements

Before applying any laboratory treatment to specimens, their natural remanent magnetization (NRM) and susceptibility are measured with the use of a JR6A spinner magnetometer and Bartington MS2 susceptibility meter at Victoria University of Wellington.

## 2.4.1. NRM of hangi stones

By the NRM of hangi stones, we mean the magnetization of the stones when sampled and before any laboratory treatment. NRM is a combination of the magnetization retained by the stones after their last heating and any magnetization remaining from its previous history, including its formation. If, in the hangi, the stones were heated above the Curie temperature, then upon cooling, they would acquire a new magnetization parallel to the ambient field of that time, thereby erasing any previous magnetization (Figure 2.16 (a)-(d)). The intensity of the magnetization is also proportional to the field strength. This magnetization is called Thermoremanent Magnetization (TRM) (Butler, 1992)



**(a)** Magnetic moments of ferri-magnetic grains inside a hangi stone before heating

**(b)** Above their blocking temperature, magnetic moments are unstable and change direction randomly

**(c)** Above the Curie temperature there is no magnetic exchange interaction and the mineral is paramagnetic

**(d)** On cooling, the grain magnetic moments stabilize in the direction of the external field
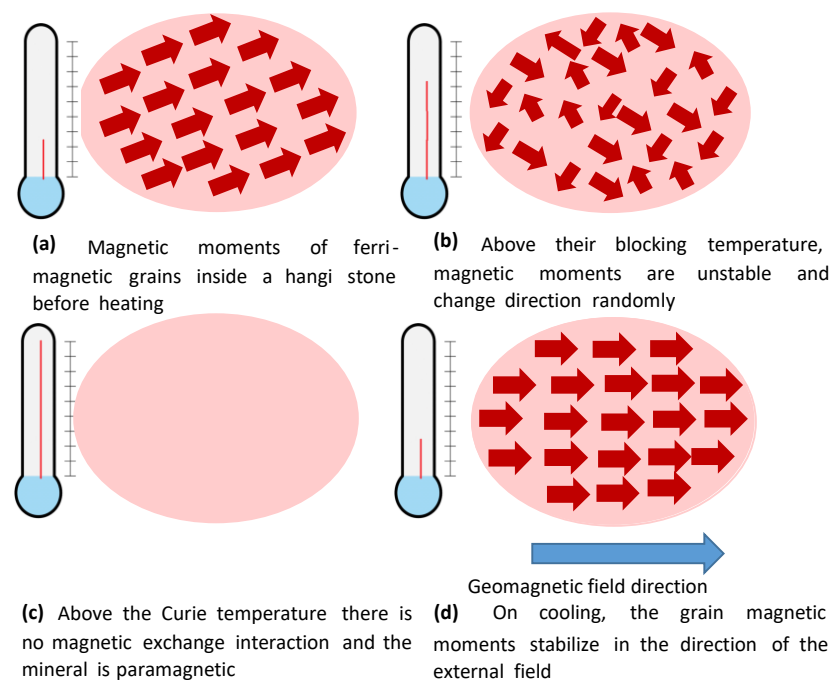
Figure 2.16. Acquisition of thermoremanent magnetization in ferro/ferrimagnetic grains.

If the temperature did not exceed the Curie temperature, then the stones may have a combination of magnetizations, comprising the stone's initial magnetization (which could be geologically present) and a new partial thermoremanent magnetization (pTRM) (Figure2.17). Such stones have more than one component of magnetization (Figure 2.17 (b)). The stones may also have acquired more than one new component of magnetization if they were disturbed during cooling or were heated more than once to

different temperatures in the hangi. Hence, it is crucial to carefully investigate the components of magnetization acquired during cooling. Thus, in hangi stones, the primary component of magnetization is acquired upon cooling after being heated up to the Curie temperature or through geological magnetization. The secondary component is present if the stones were heated or reheated to a temperature lower than the Curie temperature. This secondary component may have also been acquired by the stone after being disturbed. The secondary component is useful and should not be neglected in the case of hangi stones. However, if the primary component acquired during cooling from higher temperature steps is then disturbed, we have no idea of directions present at that time.
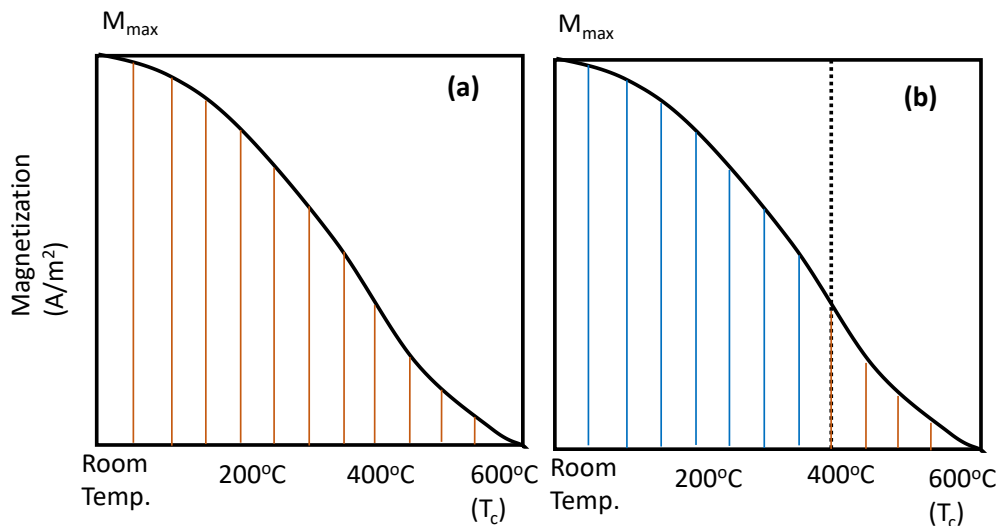


Figure 2.17. (a) Thermoremanent magnetization acquired by a ferro/ferrimagnetic material, when heated up to Curie temperature. The sample is entirely demagnetized upon heating and remagnetized on cooling. (b) When the same material is reheated to 400°C, only the grains whose blocking temperature is less than or equal to 400°C are demagnetized and the remaining magnetization of the sample is not changed. The sample has a combination of magnetizations: partial thermoremanent magnetization and its primary magnetization.

## 2.4.2. Demagnetization Methods

Progressive demagnetization allows us to determine the magnetization carried by specimens of hangi stones in each interval of the blocking temperature or coercivity spectrum. This process helps identify different TRM components and we can deduce the thermal history of each stone. By comparing the demagnetization results from each

stone, we can investigate whether the stones were *in situ* or disturbed during or after the cooling process. The demagnetization results of the stones *in situ* can be included in the calculation of a mean archaeomagnetic direction for the site. Stones whose secondary component of magnetization is consistent with the results of stones *in situ* may also be included in the average calculations. The average result of a site may be interpreted as the geomagnetic field direction acquired by the stones during the time of cooling. Two different methods used to demagnetize hangi specimens are thermal demagnetization (THD) and alternating field demagnetization (AFD).

The thermal method has been used for almost all samples, as it uses blocking temperatures and gives information about the thermal history of the stone. Alternating field demagnetization is an alternative method of demagnetization. Since there is not a simple relationship between blocking temperature and coercivity, AFD sometimes but not always separates out the same components of magnetization.

Step-by-step demagnetization helps separate primary, secondary and viscous components of remanent magnetization. Thermal and AF demagnetization experiments were performed using the thermal and AF demagnetizer at the Victoria University of Wellington.

## 2.4.3. Data presentation and analysis

Progressive demagnetization measurements enable us to get directional data and a magnetization decay plot (Figure 2.18).  The decaying magnetization vectors can then be plotted as projections onto the horizontal and vertical planes. Such plots are called Zijderveld plots (Zijderveld, 1967) or vector component diagrams (Butler, 1992).

## 2.4.4. Principal component analysis (PCA)

The progressive demagnetization data was analyzed with the help of Remasoft software (Chadima & Hrouda, 2006). The magnetic field direction acquired by a specimen can be analyzed by a best-fit line through the data set of high stability components, as shown in Figure 2.18, or through multicomponent data. This direction can be determined either by anchoring the line to the last data point or allowing it to pass through the origin. The

line can also freely pass through the last selected data point. In some cases, there is scatter in data points. The maximum angular deviation (MAD) helps in deciding the precision of directional results and the extent to which scattering in data points is acceptable. In Figure 2.18, the data points corresponding to demagnetization temperatures below 100°C are unstable. This component is a low blocking temperature viscous remanent magnetization, removed at 100°C. From 100°C to 550°C, the direction remains stable and the data points trend toward the origin. The stable component is now isolated, and its direction can be calculated. The example in Figure 2.18 is from specimen RL7-3A from the Riverlands hangi site. PCA, using Remasoft yields the result: Dec = 25.9°, Inc = -68.7° and MAD = 1.6°. The decay in magnetization with a step-by-step increase in temperature can also be seen in the inset of Figure 2.18.
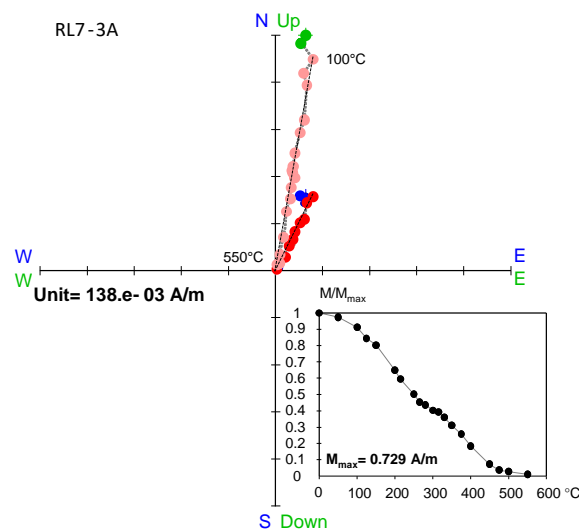


Figure 2.18. Zijderveld plot of thermal demagnetization data from specimen RL7-3A, including projection on horizontal (green and pink) and vertical plane (blue and red) (Chadima and Hrouda, 2006). Red and pink coloured dots indicate the data points included in PCA.

## 2.4.5. Data analysis of samples with more than one component

Cooking food on hangi stones is a repeatable activity. Obviously, then, the stones could be reheated to a temperature below Curie temperature and disturbed during and after cooling. Zijderveld plots show such cases clearly. In Figure 2.19, a sharp angle at the temperature step 400°C indicates the separation of two components. The low blocking temperature component is stable up to temperature 400°C. This component is

calculated as: Dec = 5.2°, Inc = -61.5° and MAD = 1.6°. It is a secondary component of magnetization in stone GM1-9.

Points in the high blocking temperature range, from 450°C-575°C, give Dec = 272.8°, Inc = 42.5°, and MAD = 5.4°. In some cases, a curve is observed instead of a sharp angle, indicating an overlapping of blocking temperature spectra. In this case, the secondary component is comparable with the directional data obtained from *in situ* stones of the same site and New Zealand's historic field directions. The high blocking temperature component gives unknown values so that we can neglect the high $T_b$ component. The high $T_b$ component has also given greater angular deviation, due to a scattering of data points in that range (Figure 2.19). The figure also includes a demagnetization curve and a stereo plot presenting directional data points at each demagnetization step (Dunlop, 1979; Hoffman & Day, 1978).
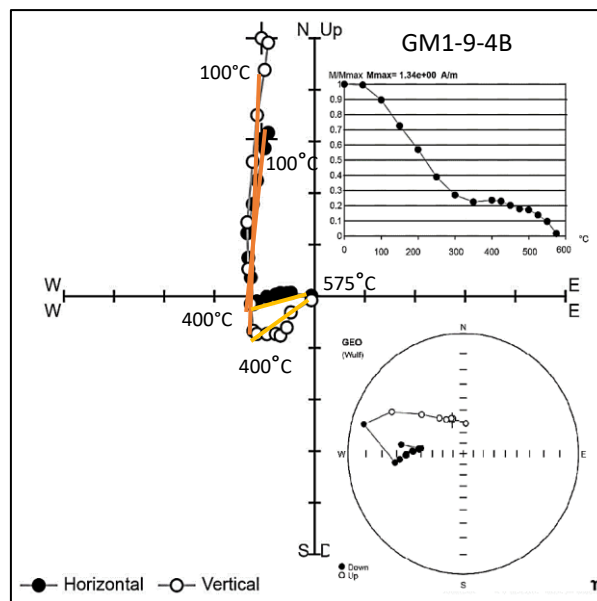


Figure 2.19.  An example of a specimen of stone GM1-9 from Great Mercury Island hangi 1. The Zijderveld plot, thermal decay plot and great circle show the presence of two main components of magnetization.

## 2.4.6. Statistics

Once the directions of individual specimens are calculated from a hangi site, it is important to calculate the average direction from the site. The directions of all experimented specimens from the same stone can be calculated to give the direction of the stone, and then a hangi site's directional data calculated by taking the mean of all

experimented stones. Fisher's statistical parameters help us interpret the quality of directional data calculated for a stone and site.

The parameters calculated by Fisher (Fisher, 1953; Fisher et al., 1987) are:

- Precision parameter "k". The larger the value of k, the less the scatter in data unit vectors. Also, if k tends to infinity, scattering approaches zero.
- Resultant vector "R" of (X, Y, Z) components.
- The number of data points included for direction estimation of a specimen, the number of specimens used to calculate the average of stone, and the number of stones used to derive site's mean direction.
- The semi angle of the cone of 95% confidence around the mean direction, usually called "$\alpha_{95}$".

Fisher's parameters as applied to six specimens of stone GM3-1 are shown in Figure 2.20 (Fisher, 1953; Fisher et al., 1987).



(b) GM3-1 mean direction Dec = 4.9°, Inc = -58.2°, $\alpha_{95}$ = 2.6°, N = 6 specimens
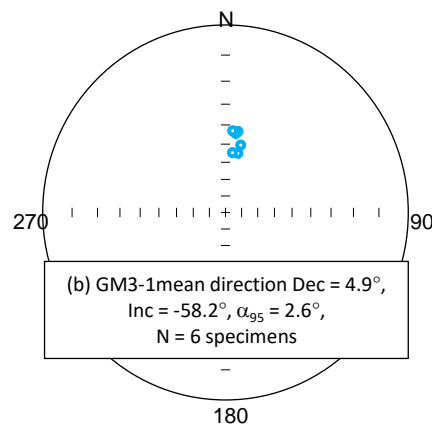
Figure 2.20. Group statistics of six specimens from stone GM3-1 of hangi site 3 from Great Mercury Island.

## 2.5. Palaeointensity determination

There are several methods for determining palaeointensities from rocks, sediments, and archaeological materials. For palaeointensity determination of hangi stones, Thellier's method (Thellier & Thellier, 1959) and the Coe protocol (Coe, 1967) was used.

### 2.5.1. Thellier-Thellier method

The Thellier-Thellier method involves a comparison of the TRM ($m_i$) of hangi stones and a pTRM acquired ($m_{i'}$) during the remagnetization of a sample in a laboratory field. NRM is first measured using the JR6A spinner magnetometer. The specimens are thermally demagnetized at a selected temperature and cooled in a zero-magnetic field. The increase in temperature randomizes magnetic moments with blocking temperatures up to the chosen temperature. The sample is then demagnetized again at the same temperature but cooled in a known magnetic field so the specimen gains pTRM in the laboratory. In this way, the original TRM of a specimen is progressively replaced by a laboratory pTRM at increased temperature steps and in a constant magnetic field. The process is repeated until the specimens either lose all their original magnetization or up to a temperature after which thermal alterations start in the minerals. The palaeointensity method makes several assumptions, described below (Thellier & Thellier, 1959):

- All specimens have well-behaved single domain magnetic grains, and these grains may have a range of different blocking temperatures from room temperature to the Curie temperature.
- The magnetic moment of each grain has the same blocking and unblocking temperature.
- The pTRM gained by the grains in each interval of the blocking temperature spectrum is independent of those carried by other grains in other parts of the spectrum.
- The total thermal remanent magnetization is the vector sum of the pTRMs over the whole blocking temperature spectrum.
- For each interval of blocking/unblocking temperature, spectrum $pTRM_{anc}$ is directly proportional to $B_{anc}$ (the palaeointensity).

- A thermoremanent magnetization grown in a specimen in a known laboratory magnetic field will similarly consist of pTRMs for which pTRM$_{lab}$ is directly proportional to B$_{lab}$. This lab pTRM enables a normalizing procedure to be carried out for each interval of the blocking temperature spectrum (Nagata, 1943).

$$B_{anc} = \frac{m_i}{m'_i} B_{lab}$$

Apart from thermal palaeointensity methods, the microwave palaeointensity method (Tauxe et al., 2010) and the Pseudo-Thellier method (Tauxe et al., 1995) are alternatives for palaeointensity experiments.

### pTRM and tail checks

Step-by-step heating and cooling of samples may cause the thermal alteration of magnetic minerals. To check whether the remanence carriers of a specimen are affected during experiments, infield steps are repeated at regular intervals for lower temperatures. These steps are called pTRM checks (Coe, 1967). For PSD and MD grains, specimens' blocking temperature and unblocking temperature may alter during the experiment. Therefore an additional zero field heating step should be performed before the pTRM check to remove the pTRM gained in the previous step (Riisager & Riisager, 2001). This additional zero field step is called a pTRM-tail check. The difference between the NRMs left after a zero-field heating/ pTRM step and pTRM-tail check/pTRM-check steps at the same temperature can be calculated to understand the alteration level.

An example is shown in Figure 2.21 (a). The data obtained from the palaeointensity experiment on specimen WP1-22A was transferred to the master palaeointensity Excel spreadsheet and a graph plotted between NRM remaining and pTRM gained (Arai plot) (Nagata et al., 1963). The horizontal and vertical arrows on the plot show the pTRM checks. The gradient of the graph gives a palaeointensity of 59.6 ± 1.0 µT.

Another graph, for the same data, is plotted using ThellierTool4.0 (Leonhardt et al., 2004). This software gave an intensity value of 59.4 ± 1.8 µT (Figure 2.21b). The results calculated using the Excel spreadsheet and ThellierTool4.0 are consistent within uncertainties, so the Thellier Tool software was subsequently used for most of the calculations.
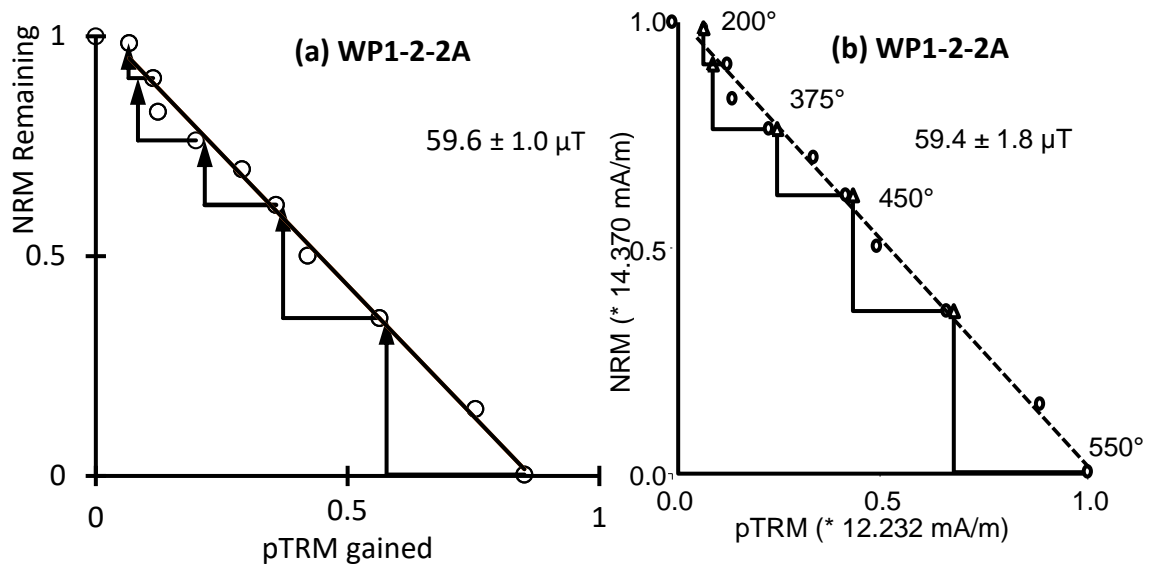
Figure 2.21. Arai plot for specimen WP1-22A from hangi site WP1. (a) Using a palaeointensity spreadsheet in Microsoft Excel; (b) Using Thellier Tool 4.0 (Leonhardt et al., 2004).

Some samples carry multiple components of magnetization: their archaeointensities are calculated using Yu and Dunlop's multivectorial palaeointensity determination method (Yu & Dunlop, 2002) (Figure 2.22 (a) & (b)). From Zijderveld plots, the temperature at which the components of magnetization separate can be clearly seen. The magnetization vector at this temperature (say at temperature $T_i$, where the components separate) is subtracted from all magnetization vectors of temperature steps less than $T_i$, and an Arai plot is plotted between the corrected magnetization and pTRM gained. No changes are necessary on pTRM gained at different steps. For the temperature range $T_i$ to the Curie temperature, the gradient is calculated from a plot between NRM remaining and the scalar subtraction of pTRM at temperature $T_i$ from pTRM of all temperature steps. Intensities were also calculated by using ThellierTool4.0 and selecting low blocking temperature components; these intensities were weaker than the values calculated using the multivectorial palaeointensity method. This approach has also provided improved statistical parameters. Figure 2.22 shows two examples from specimen GM1-9-2A. The intensities are calculated using both methods. The multivectorial palaeointensity method has provided higher intensity, comparable with the values calculated from other specimens of the site. Hence, this method is applied to the specimens which have two or more components of magnetization.
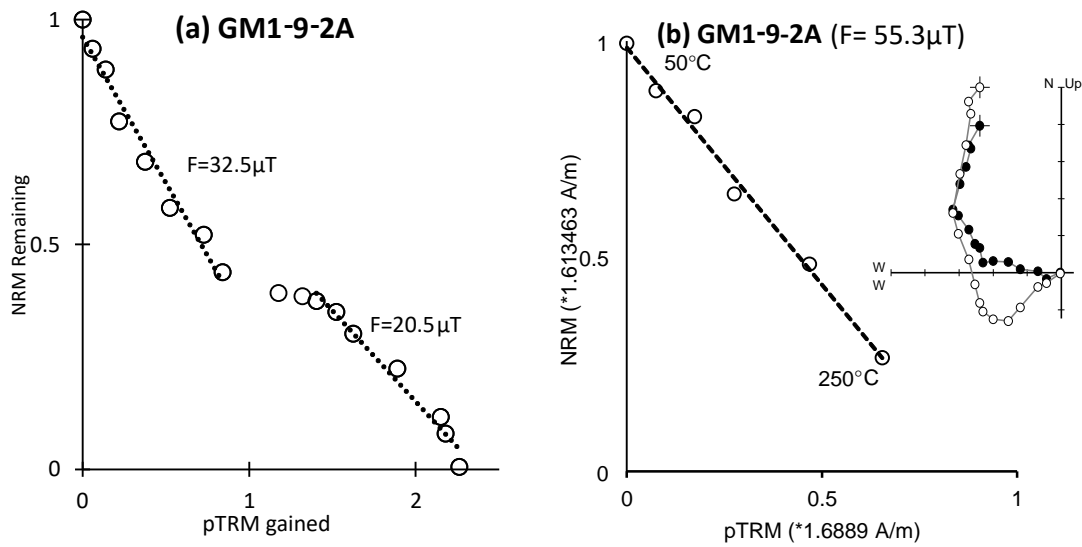
Figure 2.22. Multivectorial palaeointensity determination. (a) Arai plot of a specimen from hangi site GM1, showing two components of magnetization resulting in weak palaeointensities. (b) Calculation of intensity of magnetization of low blocking temperature, using multivectorial palaeointensity determination method (inset is the Zijderveld plot for the same specimen).

## 2.5.2. Data analysis

The whole data presentation comprises four graphs shown in Figure 2.23. If the directional data of the specimens used for palaeointensity experiments is compatible with the data from progressive demagnetization experiments, conducted on other specimens from the same stone, then directional data of the specimens used in palaeointensity experiments can be included in the calculation of mean directional data for the site.

Selection criteria such as SELCRIT2 (Kissel & Laj, 2004), PICRIT03 (Biggin et al., 2007) and TT(A/B/C) (Leonhardt et al., 2004) are essential for the reliable analysis of palaeointensity data. These criteria have been modified to improve data selection so that useful data are not discarded, and to obtain accurate and low scatter palaeointensity estimates (Paterson et al., 2014). The modified criteria allow some relaxation in acceptance of palaeomagnetic data. It is important to have a knowledge of the statistical parameters before we use selection criteria. The main parameters are defined and calculated as described by Paterson et al. (2014) and Coe et al. (1978). The

example shown in Figure 2.23 has a stable single component of magnetization with a blocking temperature spectrum between 400 and 550°C.
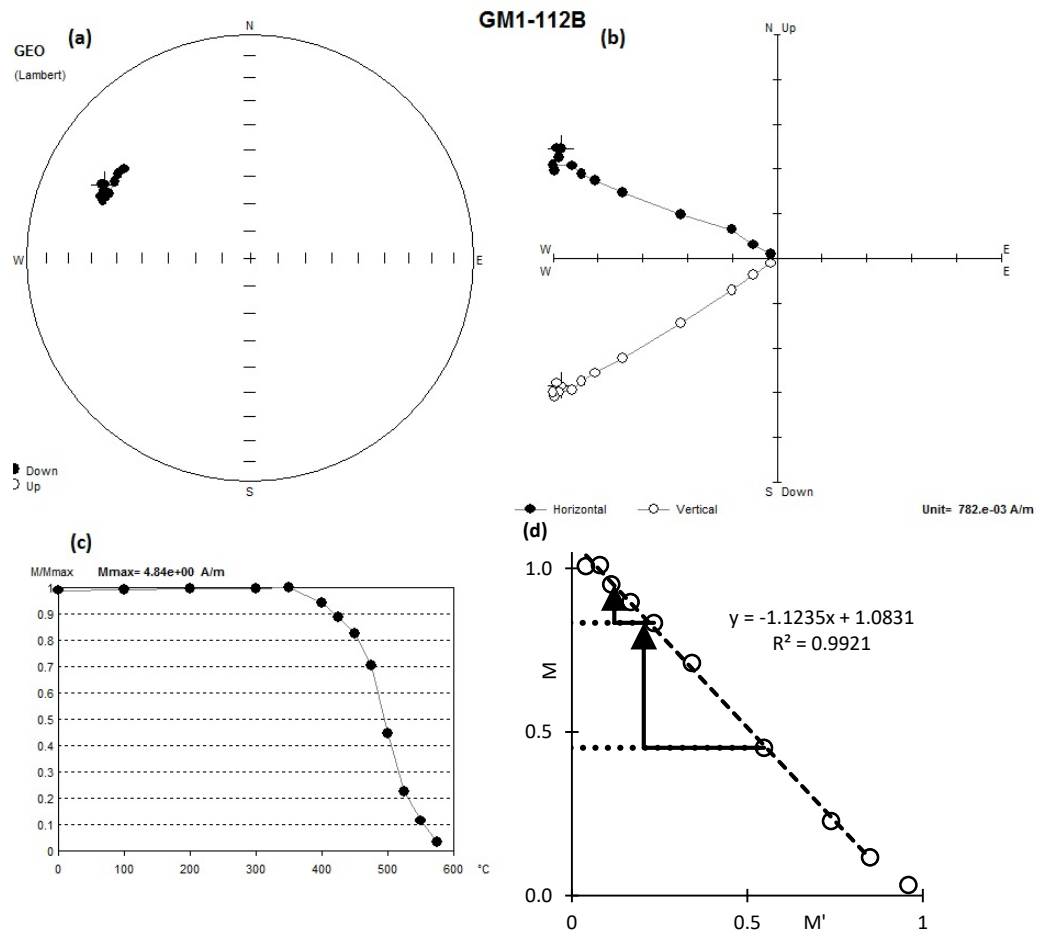


Figure 2.23. Palaeointensity data presentation for specimen GM1-11-2B from GMI hangi site GM1. (a) Stereo plot, (b) Zijderveld plot, and (c) decay plot, all produced with Remasoft software. (d) Arai plot produced with Excel spreadsheet.

## 2.5.3. Statistical parameters for palaeointensity

Statistical parameters show whether the data selected to calculate the average field of a site is accurate or inaccurate. Threshold values of parameters also help us in deciding the quality of results. During calculation of data from each specimen, statistical parameters should lie within the predefined selection criteria so that the calculated results are accurate, reliable, and of high quality.

The main statistical parameters used in this project for data analysis are:

- 'N': the number of data points used in the calculation of palaeointensity.

- 'b': the gradient of the best-fit line to the selected points on the Arai plot (Coe et al., 1978).

- 'σ' or '$\sigma_b$': standard error in the gradient

- 'β': the ratio of the standard error to the absolute value of the gradient, giving a measure of the relative scatter of the data around the best-fit line.

- NRM fraction 'f': the fraction of total extrapolated NRM spanned by the selected segment of the Arai plot (Coe et al., 1978).

- 'g' : The average spacing of selected data points on an Arai plot along the best fit line is called the gap factor (Coe et al., 1978).

- 'q' : The overall quality of the estimated palaeointensity and relative uncertainty in the slope of the best-fit line can be measured with the help of the quality factor. $q = \frac{fg}{\beta}$

- The weighing factor 'w' (Prévot et al., 1985).

- 'α or alpha' : The angular difference between an anchored and a non-anchored direction(Leonhardt et al., 2004).

- '$\delta_{CK}$ or d(CK)' : The difference between the pTRM-check and pTRM acquisition, normalized to thermoremanent magnetization (Leonhardt et al., 2004).

- 'DRAT ' : The maximum absolute difference from a pTRM check normalized to the length of selected best-fit line (Selkin & Tauxe, 2000).

- '$\delta_{pal}$ or D(pal)' : The cumulative difference of checks from the minimum temperature to maximum temperature steps of selected data points of the best-fit line (Leonhardt et al., 2004).

- '$\delta_{TR}$ or D(TR)': The difference in the intensity of a demagnetization step and a repeated demagnetization step normalized by the NRM of the best-fit line of selected portion.

- '$\delta_{t*}$ or D(t*)' **:** The relative extent of the actual tail (Leonhardt et al., 2004).

- 'D(θ) or δ(θ)' : The angle between the NRM of a specimen and applied field.

These are the main parameters calculated during estimation of palaeointensities. Analyzing data using ThellierTool4.0 gives these values (Leonhardt et al., 2004).

Statistical parameters were also calculated using a Microsoft Excel spreadsheet to verify results from ThellierTool4.0.

## 2.5.4. Selection Criteria

Figure 2.23 shows the palaeointensity data for specimen GM1-11-2B, while the statistical parameters, calculated with ThellierTool4.0, are in Table 2.2. The threshold values for statistical parameters from the selection criteria of Leonhardt et al. (2004), and the modified criteria of Paterson et al. (2014) are tabulated in Table 2.3. The calculated palaeomagnetic results for this specimen are:  F = 58.2 ± 0.7 µT, Dec = 293.8° and Inc = 30.3°. These results meet the modified TTA criteria of Table 2.3, and are therefore considered high quality.

Table 2.2. The statistical parameters calculated for specimen GM1-11-2B with ThellierTool4.0.

| ID | N | $\beta$ | f | q | $\delta_{CK}$ | $\delta_{pal}$ | DRAT | $\alpha$ | MAD | $\delta_{TR}$ | $\delta_{t*}$ |
|---|---|---|---|---|---|---|---|---|---|---|---|
| GM1-11-2B | 8 | 0.012 | 0.81 | 52 | 3.1 | 3.9 | 2.48 | 1.6 | 1.2 | 0.5 | 3.2 |

Table 2.3. Selection criterion of Leonhardt et al. (2004) with modified values of Paterson et al. (2014). (For full table see Paterson et al. (2014).)

| Criterion | TTA | TTA(Modified) | TTB | TTB(Modified) |
|---|---|---|---|---|
| Parameters | | | | |
| N | ≥5 | ≥5 | ≥5 | ≥5 |
| f | ≥0.5 | ≥0.35 | ≥0.3 | ≥0.35 |
| $\beta$ | ≤0.1 | ≤0.1 | ≤0.15 | ≤0.15 |
| q | ≥5 | ≥5 | ≥0 | ≥0 |
| MAD | ≤6 | ≤6 | ≤15 | ≤15 |
| $\alpha$ | ≤15 | ≤15 | ≤15 | ≤15 |
| DRAT | - | - | - | - |
| $\delta_{CK}$ | ≤5 | ≤7 | ≤7 | ≤9 |
| $\delta_{pal}$ | ≤5 | ≤10 | ≤10 | ≤18 |
| $\delta_{TR}$ | ≤10 | ≤10 | ≤20 | ≤20 |
| $\delta_{t*}$ | ≤3 | ≤9 | ≤99 | ≤99 |

Other selection criteria, PICRIT03, SELCRIT2 and their modified forms are more relaxed in comparison to Leonhardt et al. (2014), while we used stricter, modified TTA and TTB selection criteria for data analysis.

A specimen from RL5-2A is shown in Figure 2.24. From the Arai plot and the NRM decay plot it is clear that this specimen did not pass pTRM checks and tail checks, as the repeated steps (arrows in Arai plot and solid squares in decay plot) do not coincide with their previous steps. The data points in the Arai plot are also scattered but still follow a decaying trend. Using a temperature range of 100 to 375°C to calculate palaeointensity gives a huge uncertainty in palaeointensity. Also, the statistical parameters do not meet either the TTA or TTB criteria (Table 2.4). The directions are almost stable after the 275°C step and are calculated as: Dec = 15.0°, Inc = -68.2 and MAD = 1.8°. The palaeointensity of this specimen is 53.0 ± 11.7 µT. This kind of behaviour is commonly seen in specimens with either coarse grains or multi-domain character. Some specimens' results have large uncertainties, failed pTRM checks and tail-checks, but provide intensity and directional data comparable to the results of specimens meeting TTA or TTB criteria. Such results can sometimes be accepted as exceptional cases with suitable reasoning.
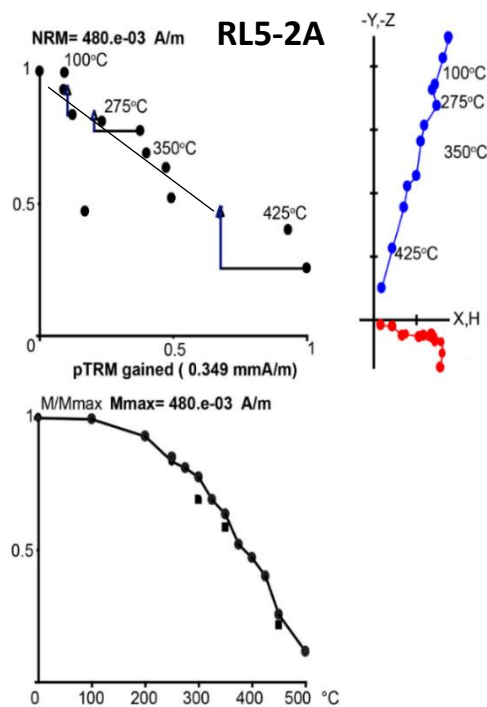


Figure 2.24. Data of specimen from RL5-2A, plotted using Thellier Tool. The arrows in the Arai plot show pTRM checks, solid squares in the decay plot are tail-checks, which do not overlie the original data points.

Table 2.4. Statistical parameters of specimen RL5-2A.

| ID | N | β | F | q | $\delta_{CK}$ | $\delta_{pal}$ | DRAT | α | MAD | $\delta_{TR}$ | $\delta_{t^*}$ |
|---|---|---|---|---|---|---|---|---|---|---|---|
| RL5-2A | 11 | 0.2 | 0.67 | 2 | 40.8 | 77.3 | 1.6 | 2.8 | 8.6 | 4.9 | 11 |

# 3. Opihi River Hangi site

## 3.1. Archaeological Setting

The Opihi River archaeological site (Archsite J38/75) is in an area of sandy limestone with local occurrences of tuff and calcareous sandstone below a limestone bluff (Figure 3.1). It is on the south side of the Opihi River (at latitude/longitude: 44°11'48.1" S/ 171°01'28.4" E), South Canterbury (see map in Figure 3.2).



Legend

Sandy limestone, locally with tuff layers, and calcareous, glauconitic sandstone.

Calcareous sandstone, siltstone and mudstone with bioclastic limestone and local interbedded conglomerate

Weathered greywacke-clast conglomerate with interbedded sandstone, siltstone and mudstone; local lignite.

Weathered gravel, sand, silt and mud of alluvial and colluvial origin.

Windblown silt with interbedded paleosols and peat.

Olivine basalt and hypersthene basalt flows with basal tuff.

Semischist (TZIIA) derived from quartzofeldspathic sandstone, siltstone, mudstone and conglomerate.

Figure 3.1. Geological map of area south of Opihi River. Downloaded from GNS geology website (http://data.gns.cri.nz/geology/).

A Ph.D. student at the University of Auckland, Gerard O'Regan, excavated the hangi during his archaeological work on a large limestone rock shelter (Archsite # J38/75) containing examples of Maori rock art (Figure 3.3). Augustus Hamilton first mentioned the rock art in the shelter in 1897 and later Dr. R. S. Duff, Tony Fomison, and others surveyed the site. The wall and roof of the rock shelter bear traces of ancient Maori paintings, including a famous figure of a Taniwha with an open mouth (McCulloch & Trotter, 1971). The hangi was on a colluvium-covered slope outside a nearby cave (Figure 3.3) (O'Regan pers. comm.). It was visible in the east-west transect of a T-shaped excavated area (Figure 3.4 (a)). The hangi was 1.9m in diameter and 0.7m deep, measured from the ground surface. The details of the hangi and its location are shown in Table 3.1.
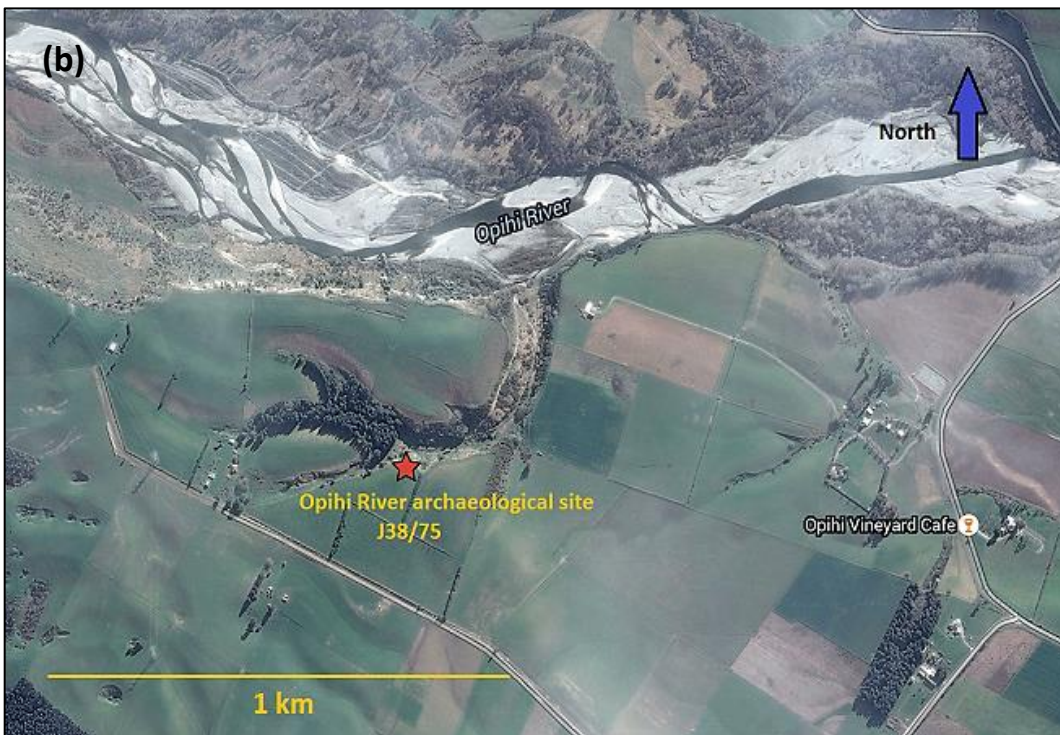
Figure 3.2. (a) Topographic map (http://maps.marlborough.govt.nz/viewer/). (b) Aerial photo of archaeological site near Opihi River (photo downloaded from Google Earth, date of image 2010).

The hangi site contained mostly intact, reddened stones, with charcoal in the top layer, and fire-cracked stones with charcoal at the bottom. The state of the hangi may be due to one of the following reasons. First, it is possible that the heat in the lower part of the hangi was more intense than at the top, cracking the stones. Alternatively, the stones may have been used several times for cooking, with the reheating causing the stones to crack. The intact stones from the top part of the hangi may be younger than the fractured stones at the bottom. The bottom stones may also be the remains of bigger stones which could have been used in an earlier period and remained there when the site was used again as a hangi at a later time. There were no signs that any animal or bird had been cooked in the hangi (O'Regan pers. comm.). The calcareous rocks around the rock shelter and sandstones near Opihi River bed could have provided the stones for the hangi.
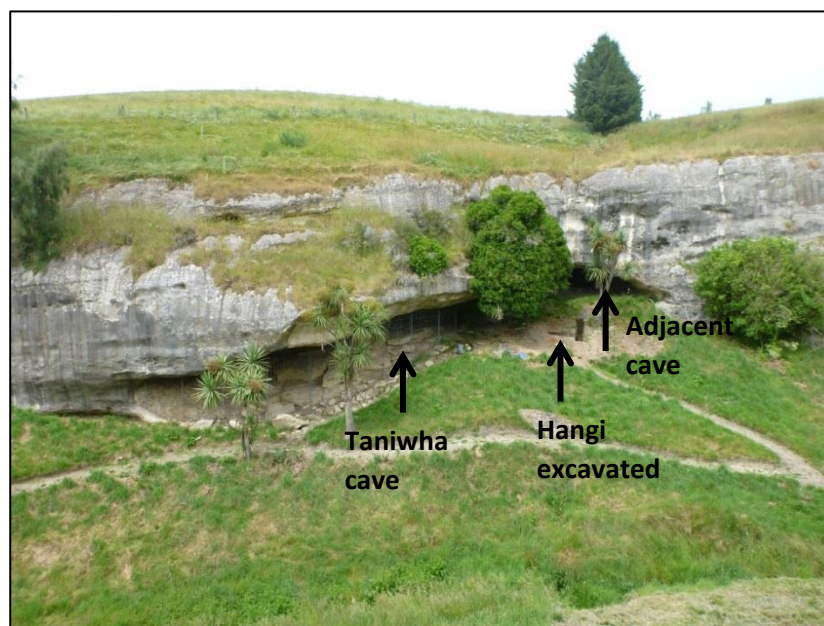


Figure 3.3. Photo of rock shelter near Opihi River. Arrows show the locations of the Taniwha cave, the excavated area and the adjacent cave (photo by Gerard O'Regan).

Table 3.1. Features of Arch site J38/75. GPS coordinates converted to NZTM.

| VUW label/Archsite | O'Regan's feature label | Age control | Features and comments | NZTM coordinates |
|---|---|---|---|---|
| OP (J38/75) | Square 3 | 382±20BP Wk-37506 See Table 3.3 | A hangi, 1.9m diameter × 0.69m depth, containing fire-blackened soil, fire-cracked stones, and some charcoal. | N5104382 E1442144 |

## 3.2. Samples and specimens

We did not visit this site for fieldwork. Gerard O' Regan sent us ten non-oriented hangi stones (OP1 to OP10). Figure 3.4 (a) shows the trenches dug. According to O'Regan, the stones provided were extracted from the top part of the hangi (see arrow in Figure 3.4 (b)), and were tightly packed with fire-blackened sand. To the right-hand side, the lower part of the hangi was soft (Figure 3.4 (b)) with fire-cracked stones loosely laid in blackened sand mixed with charcoal. Charcoal samples were collected from the top and bottom of the hangi for $^{14}$C dating (O'Regan pers. comm.).

Eight hangi stones, identified as calcareous and lithified sandstones, were used for archaeomagnetic experiments. OP3, the largest stone, was about 20cm in size and round in shape. The remaining seven stones were smaller, with fractured and angled faces. Cylindrical specimens were prepared as described in Chapter 2 and detailed in Table 3.2.



Figure 3.4. Opihi River hangi site (a) Excavated area of the hangi. The scale is at the far end of the right-hand trench. Each segment of the scale rod is 10cm in length. (b) A close-up picture showing a section of hangi after the removal of stones. Arrow shows the area from which the stones were taken. Photos provided by Gerard O' Regan.

Table 3.2. Detail of cores and specimens from each stone experimented.

| Stone | Number of cores | Number of specimens |
|---|---|---|
| OP1 | 3 | 5 |
| OP2 | 2 | 4 |
| OP3 | 4 | 5 |
| OP4 | 2 | 2 |
| OP5 | 2 | 2 |
| OP6 | 4 | 7 |
| OP7 | 2 | 3 |
| OP8 | 2 | 3 |
| Total = 8 | 21 | 31 |

# 3.3 Age control

The charcoal sample collected from the top of the hangi was identified as matai, a long-lived species which can achieve a lifespan of some 1000 years (http://terranature.org/bigTrees.htm) and hence unsuitable for $^{14}$C dating because of its likely inbuilt age (McFadgen et al., 1994). The charcoal sample from the bottom of the hangi was identified as bracken fern, a short-lived species, and which provided a conventional radiocarbon age of 382 ± 20 (2$\sigma$) BP, measured using Accelerator Mass Spectrometry (Table 3.3). With 95% confidence, the calibrated date lies between 1465 and 1627 AD (Figure 3.5 & Table 3.3).
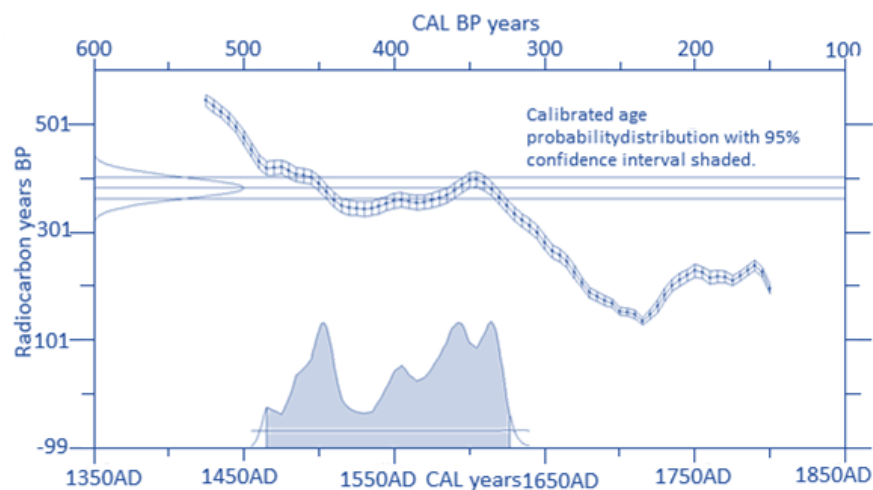


Figure 3.5. Radiocarbon dates calibration using SHCAL13 calibration curve for site J38/75 (Hogg et al., 2013). Dates have been determined using AMS at Waikato University. Figure created using program WINSCALX 5.1 (Sparks, R.J., and Manning, M.R. pers. com., version 5.1. GNS Science, 2011).

Table 3.3. Radiocarbon age estimation of Opihi River hangi site.

| Site Name | Material | Lab No. | $^{14}$C age | Calibrated age range (95% confidence) |
|-----------|----------|---------|-----------|---------------------------------------|
| OP | Bracken | WK-37506 | 382±20 BP | 1465 AD -1627AD |

# 3.4 Rock Magnetism

Measurements of the rock magnetic properties of Opihi River hangi stones are described below (Table 3.4 & Figure 3.6).

## 3.4.1 Thermomagnetic properties

To determine the Curie temperature and the change in susceptibility after being heated to high temperature, susceptibility versus temperature experiments were conducted on samples from the Opihi River hangi stones (Figure 3.6). The room temperature susceptibility of the stones lies in the range of 0.03 to 13.0 X $10^{-06}$ m$^3$/kg. The initial magnetic susceptibilities of the samples have a difference of 3-4 orders of magnitude. The difference may be due to variability in the mineralogy and chemical composition of the stones (Yang et al., 2013). The susceptibility of stones OP1 and OP2 increased with rises in temperature up to 300°C, and, in the other stones, increased with rises in temperature up to 500°C. In the graphs of samples OP3, OP4, and OP6, sharp Hopkinson peaks (Hopkinson, 1890) indicate that the stones have a fairly uniform grain size. In all other samples, there is no sharp Hopkinson peak, suggesting that these stones may contain a spectrum of grain sizes. The heating and cooling curves of OP3, OP4, and OP6 are almost reversible (Figure 3.6 (a), (c), (d) & (f)). OP1, OP2, and OP8 also have reversible heating and cooling curves, but a bigger range of blocking temperatures and grain sizes. OP5 and OP7 are relatively weak, with a significant difference between heating and cooling curves, indicating a thermal alteration in the minerals during the heating process. As mentioned in Section 3.1, the Opihi River hangi stones were calcareous and lithified sandstones which cannot bear extreme heat. Consequently, the stones could not be heated as much in the hangi and underwent thermal alteration during laboratory heating (Hrouda et al., 2003). Repeated experiments (to only 400°C) for stones OP5 and OP7 showed almost reversible heating and cooling curves (Figure 3.6 (j) & (k)). OP2 was slightly altered during heating but showed a single magnetic phase

during cooling measurements. The experiment was repeated for OP1 to a lower maximum temperature, resulting in the same small change in susceptibility (Figure 3.6 (i)). The principal Curie temperatures of the samples lie between 537 and 603°C (Table 3.4), suggesting that these stones carry varying, but small, percentages of (titano) magnetite (with Ti < 10%) and possibly cation-deficient (oxidized) titanomagnetite (Dunlop & Özdemir, 1997).
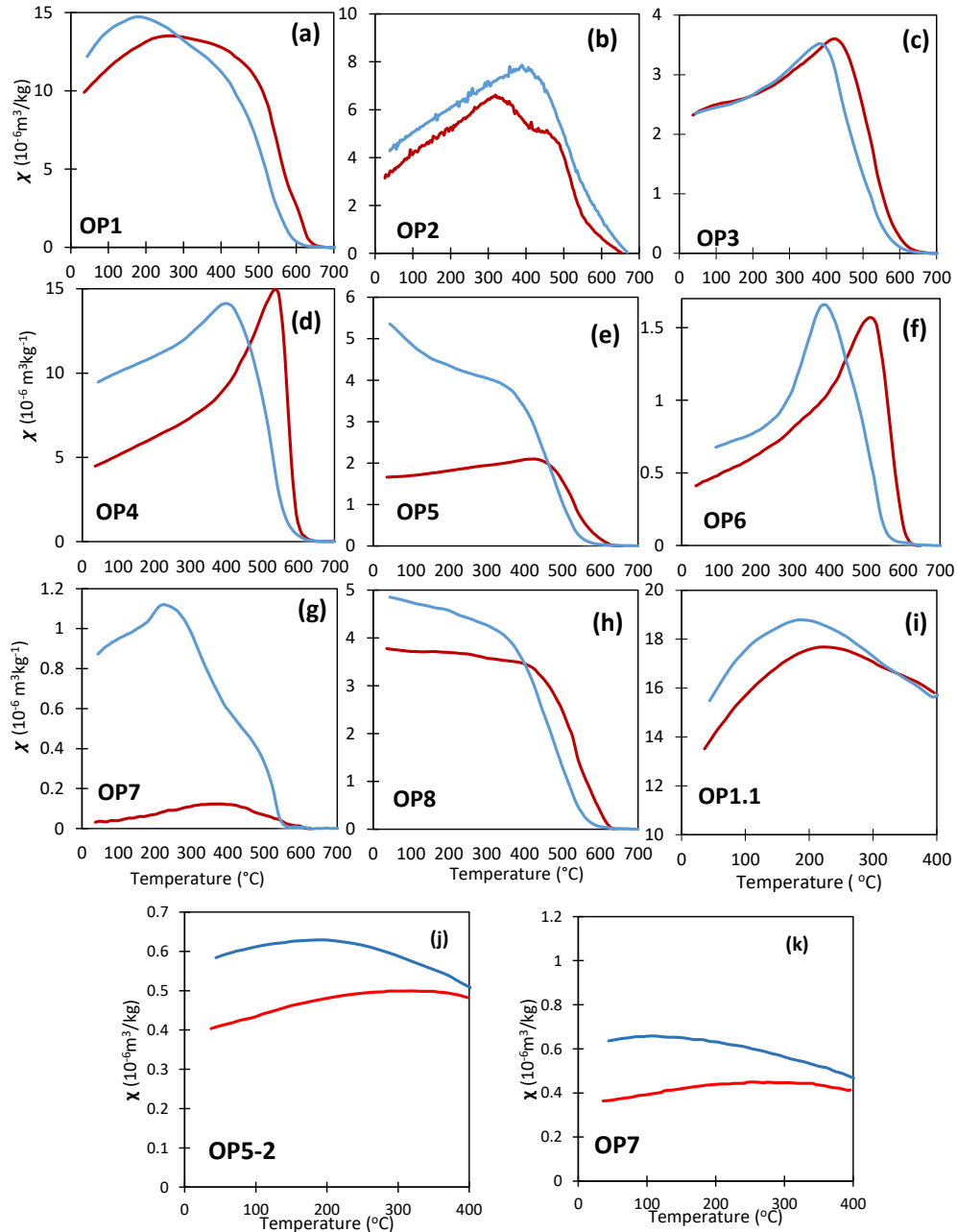


Figure 3.6. Thermomagnetic plots of Opihi River samples. (a)-(h) Plots of susceptibility versus temperature for hangi stones OP1, OP2, OP3, OP4, OP5, OP6, OP7, and OP8. Red lines indicate heating curves, blue are cooling curves. (i)-(k) Repeated experiment on samples from stones OP1, OP5 and OP7, up to 400°C. OP2 was measured using a Kappa-Bridge, rather than Bartington apparatus: this accounts for the increased noise in the data.

53

Table 3.4. Curie temperatures of Opihi River hangi stones. Calculations for $\chi$-T plots use the inverse susceptibility method (Petrovský & Kapička, 2006).

| Sample ID | $T_c$ Heating (°) | $T_c$ Cooling (°) | $T_c$ Cooling corrected (°) | Difference (°) |
|-----------|-------------------|-------------------|------------------------------|----------------|
| OP1 | 603 | 553 | 568 | 35 |
| OP2-2 | 596 | 628 | -- | 32 |
| OP3 | 566 | 528 | 543 | 23 |
| OP4 | 599 | 574 | 589 | 10 |
| OP5 | 577 | 539 | 554 | 23 |
| OP6 | 596 | 541 | 556 | 40 |
| OP7 | 537 | 560 | 575 | -38 |
| OP8 | 591 | 570 | 585 | 6 |

## 3.4.2. Hysteresis and IRM curves

To understand the magnetic mineralogy of the hangi stones, hysteresis and isothermal remanent magnetization (IRM) acquisition curves are plotted (Figure 3.7). Samples from hangi stones OP1, OP2, OP3, OP5 and OP8 were subjected to hysteresis and IRM experiments to determine remanent magnetization, coercivity, and saturation magnetization. The saturation magnetization ($M_s$) and coercivity ($B_c$) of stones OP1, OP2, OP3, OP5 and OP8 range between 10.7 - 438.2 mAm$^2$/kg and 4.8 - 31.9 mT. The graphs show the variability in the magnetic remanence carriers of all calcareous and lithified sandstones from Opihi River. Hysteresis measurements show the stones' paramagnetic character (Figure 3.7). A paramagnetic correction was applied to the hysteresis curves of samples OP2, OP3, and OP5. The red curves are the corrected hysteresis curves, while the blue loops include the paramagnetic character.

The hysteresis diagram of OP3 (Figure 3.7 (c)) shows higher paramagnetic content than sample OP3-3 (Figure 3.7 (g)). Such significantly different behaviour in samples drawn from the same stone indicates the inhomogeneity of the stone. OP2 and OP3-3 also have a narrow hysteresis loop. The isothermal remanent magnetization of OP2 and OP3 (Figure 3.7 (e) & (j)) saturated at a field less than 200mT. Thermomagnetic and rock magnetic properties of these samples are generally consistent with Ti-poor titanomagnetite and cation-deficient titanomagnetite (O'Reilly et al., 1976). The sample OP5-1 has a much wider hysteresis loop than any other samples from the Opihi River hangi site. Hysteresis and IRM data of OP2, OP3-3, OP3 and OP5-1 indicate the presence

of PSD titanomagnetite (Dunlop, 2002). Hysteresis loops of samples OP1 and OP8 do not have a closed section so no paramagnetic correction could be applied to them. The magnetization of these samples does not saturate in the field applied. The hysteresis loops are wasp-waisted, and the samples have a mixture of high and low coercivity minerals (Tauxe et al., 2010). OP1 and OP8-2 lie in the MD region, thus data points are not visible in Figure 3.8. These two stones have higher Curie temperatures in comparison to other stones from the site and do not saturate below the field of 1T. Thus, hysteresis parameters and thermomagnetic properties suggest that OP1 and OP8 contain oxidized titanomagnetite (Dunlop & Özdemir, 1997).
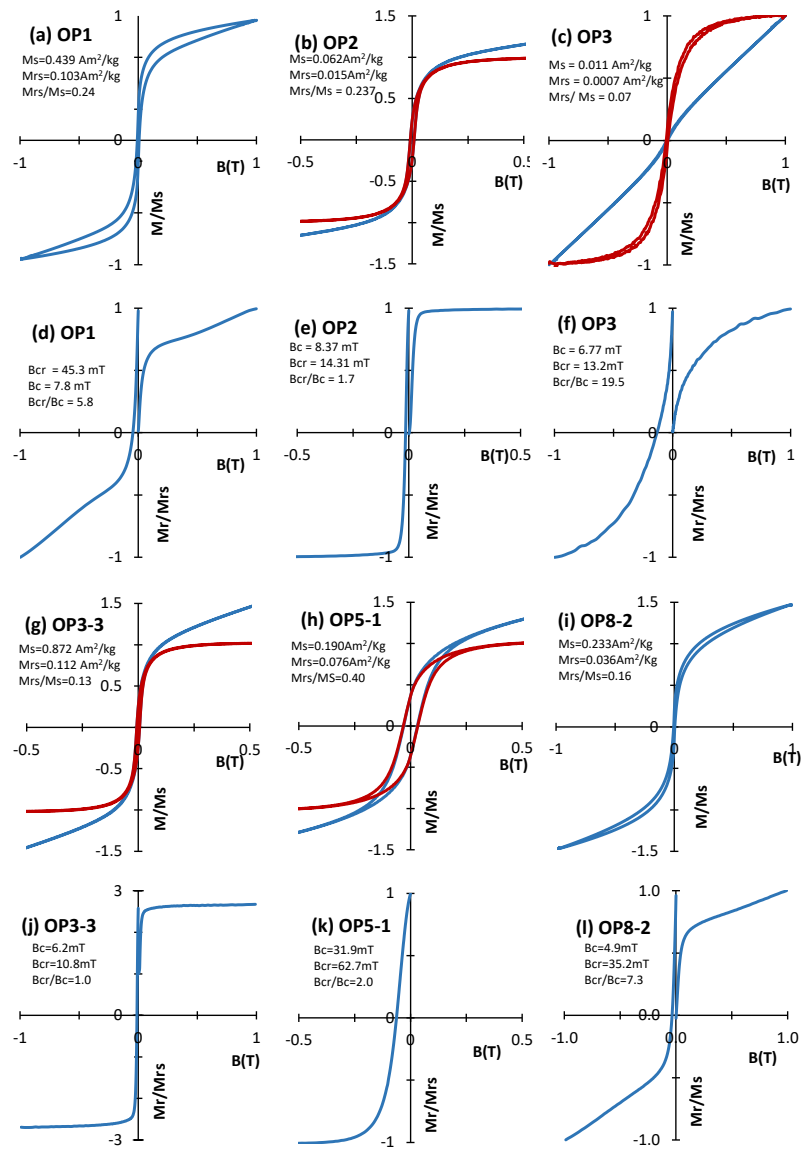


Figure 3.7. Hysteresis plots of samples OP1, OP2, OP3, OP5 and OP8 (a), (b), (c), (g), (h) & (i). The blue curves indicate paramagnetic character and red curves paramagnetic correction. The corresponding IRM and back-field curves of the samples are below them (d), (e), (f), (j), (k) & (l).

Table 3.5. Hysteresis and IRM data of hangi stones from Opihi River.

| Sample ID | $M_{rs}$(mAm$^2$/kg) | $M_s$(mAm$^2$/kg) | $M_{rs}/M_s$ | $B_{cr}$(mT) | $B_c$(mT) | $B_{cr}/B_c$ |
|-----------|---------------------|-------------------|--------------|--------------|-----------|--------------|
| OP1 | 103.2 | 438.2 | 0.24 | 45.3 | 7.8 | 5.8 |
| OP2 | 14.7 | 62.2 | 0.24 | 14.3 | 8.4 | 1.7 |
| OP3 | 0.75 | 10.7 | 0.07 | 13.2 | 6.8 | 1.94 |
| OP3-3 | 11.2 | 87.2 | 0.12 | 10.8 | 6.2 | 1.74 |
| OP5-1 | 76.2 | 190.0 | 0.40 | 62.7 | 31.9 | 1.97 |
| OP8-2 | 81.4 | 233.0 | 0.16 | 35.2 | 4.8 | 7.33 |

A Day Plot ($M_{rs}/M_s$ versus $B_{cr}/B_c$) has been plotted and superimposed on theoretical SD+MD and SD+SP mixing curves for magnetite and titanomagnetite (Dunlop, 2002) (Figure 3.8). The OP5-1 data-point lies in the upper portion of the plot, within the traditional PSD region, and close to the SD boundary. OP3 lies in the lower part of the PSD region and OP2 lies in the middle of OP3 and OP5. OP1 and OP8 are outside the plotted region, due to their high coercivities.
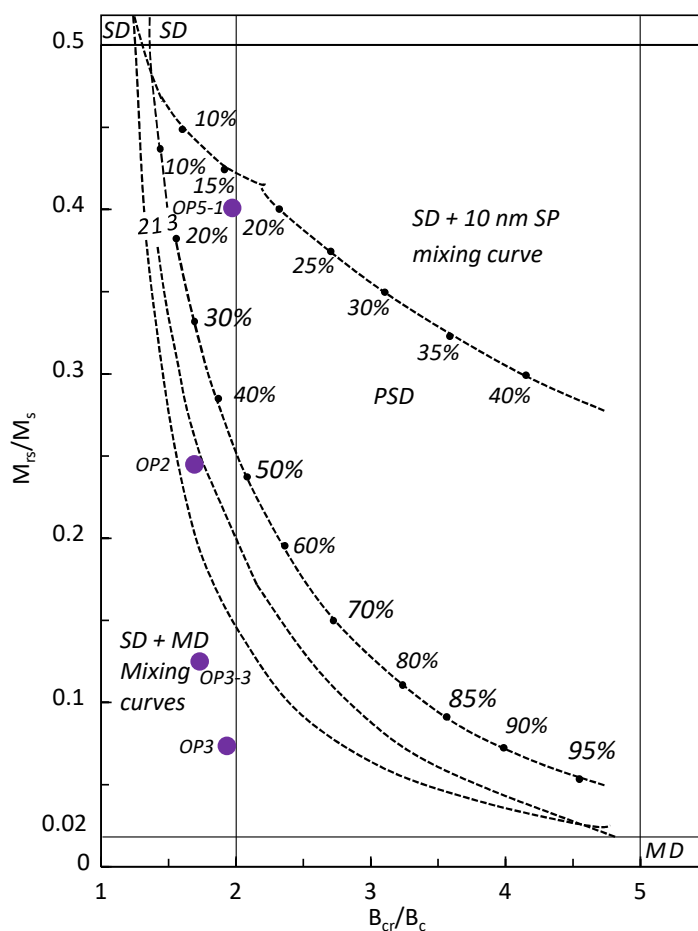


Figure 3.8. Day plot and $M_{rs}/M_s$ vs $B_{cr}/B_c$ (Day et al., 1977) data of Opihi River hangi stones (purple dots) superimposed on the mixing curves of Dunlop (2002) for a single domain, multidomain and superparamagnetic magnetite and titanomagnetite grains.

### 3.4.3 Summary

Thermomagnetic and hysteresis experiments on samples from the Opihi River hangi stones suggest the predominance of Ti-poor titanomagnetite as the main magnetic mineral. In most cases, this is either PSD or a mixture of SD, PSD, and minor MD. Two stones (OP1, OP8), showed evidence of a high coercivity magnetic mineral, probably haematite.

## 3.5 Archaeointensities

Since, the Opihi River hangi stones were not oriented in the field, demagnetization experiments designed specifically to determine absolute palaeodirections were not carried out.

The stones have NRMs in the range 0.02 - 32.2 A/m. The magnetization of 32.2 A/m is strong for calcareous sandstones, possibly as the stones may have undergone mineralogical changes during heating. The blocking temperature range of the samples is mainly between 300 and 500°C.

Archaeointensity experiments were carried out on two batches of specimens.

The first batch consisted of 14 specimens from three stones, OP1, OP2, and OP3. Zijderveld plots indicate that these stones carried a single component of magnetization (Figure 3.9 (a), (b), & (c)). No tail/pTRM checks were done on these specimens as it was the first archaeointensity experiment of this project and all equipment in the laboratory was being tested. The archaeointensities of the specimens are calculated using ThellierTool4.0 (Leonhardt et al., 2004). Experiments were continued until the specimens had lost 90% of their remanent magnetization. Most of the specimens have provided consistent archaeointensity values; intensities calculated from each specimen are shown in Table 3.6. There are some specimens from the same stones which have provided either stronger or weaker archaeointensity values. The difference in archaeointensities can be due to the inhomogeneity of rocks or if the temperature in different parts of the stone did not equilibrate. Inconsistent data were rejected by considering the threshold values of statistical parameters and comparing the

archaeointensities from the second batch of the experiment. Table 3.6 shows that all specimens of the first batch meet the (modified) TTA* or TTB* criteria (Paterson et al., 2014). Rock magnetic data can also explain the reason for the inconsistency in the intensity data of specimens from one stone. For example, two different specimens of stone OP3 have variable hysteresis parameters (Figure 3.7 (c), (f), (g), & (j)), demonstrating the range of domains in one stone. This means that individual specimens from such stones can provide unlike results. The average archaeointensity of ten specimens of the first batch is 65.1 ± 4.3 µT.

Further archaeointensity experiments were carried out on a second batch of 13 specimens from five stones, OP4, OP5, OP6, OP7 and OP8. Five of these specimens (from stones OP4, OP5, and OP8) provided consistent intensity values, comparable with the intensity values obtained from stones OP1, OP2, and OP3. Zijderveld plots show that OP4, OP5, OP7 and OP8 also have a stable single component of magnetization (Figure 3.9 (d), (e), (g), and (h)). Tail/pTRM tests were performed after every second step of the palaeointensity experiment. In specimens OP1-1A, OP2-1B, OP5-1A, OP6-1A and OP7-1B, archaeointensity was calculated by selecting a temperature range up to 450°C or 500°C. Since specimens passed tail/pTRM tests up to these temperature steps but at higher temperatures, the data are more scattered on the Arai plots, and specimens fail tail/pTRM tests. The scattering is due to thermal alterations in the magnetic mineral at high temperature. A difference between the results of A and B specimens from one core of stone OP2 is due to the large maximum angular deviation in A specimens, therefore only the results of B specimens were included in mean calculations. Three specimens of stone OP3 have provided data consistent with each other and other stones of the site. Three further specimens provided inconsistent intensity data. Since OP3's inhomogenous mineralogy has already been observed in rock magnetic properties, hence, the data of OP3 specimen's incompatible with other stones from the site is discarded. Furthermore, the specimens of stone OP6 provided anomalously high archaeointensities (Figure 3.9 (f)). It has two components of magnetization, and the low blocking temperature component has less than five data points in a cluster. The multi-vectorial palaeointensity determination method was not used since there should be at least five data points in the Arai plot to calculate intensity (Yu & Dunlop, 2002).

Additionally, the Arai plots of OP6 specimens produce concave curves; this is usually seen in samples showing multidomain behavior (Paterson et al., 2014). The archaeointensities from OP7 specimens are weaker (Figure 3.9 (g)) than in specimens drawn from other stones (OP1, OP2, OP3, OP4, OP5, and OP8). The average archaeointensity of the six specimens from the second batch provided successful results is 65.0 ± 3.6 μT, while the average archaeointensity of all 16 successful specimens from both the first and second batch is 63.3 ± 4.6 μT.

F=66.3± 5.5 µT

**(c) OP3-1A**

Unit= 25.7e-03 A/m

M$_{max}$= 0.177 A/m

F=59.9 ±3.4 µT

**(d) OP4-1A**

Unit= 2.75 A/m

Mmax= 15.5 A/m

F=63.2 ±2.6 µT

**(e) OP5-1A**

Unit= 0.452 A/m

M$_{max}$= 2.50 A/m

60
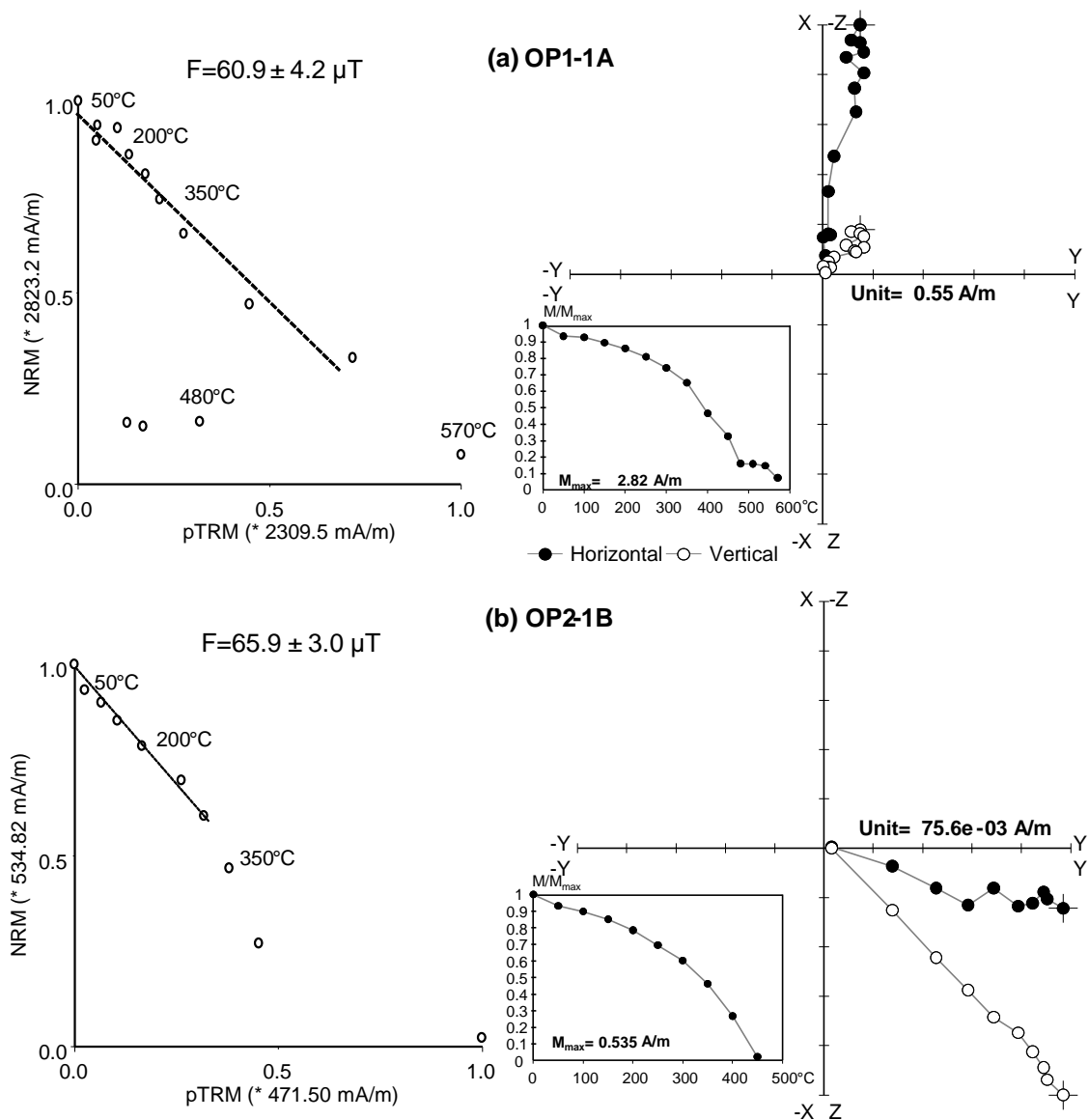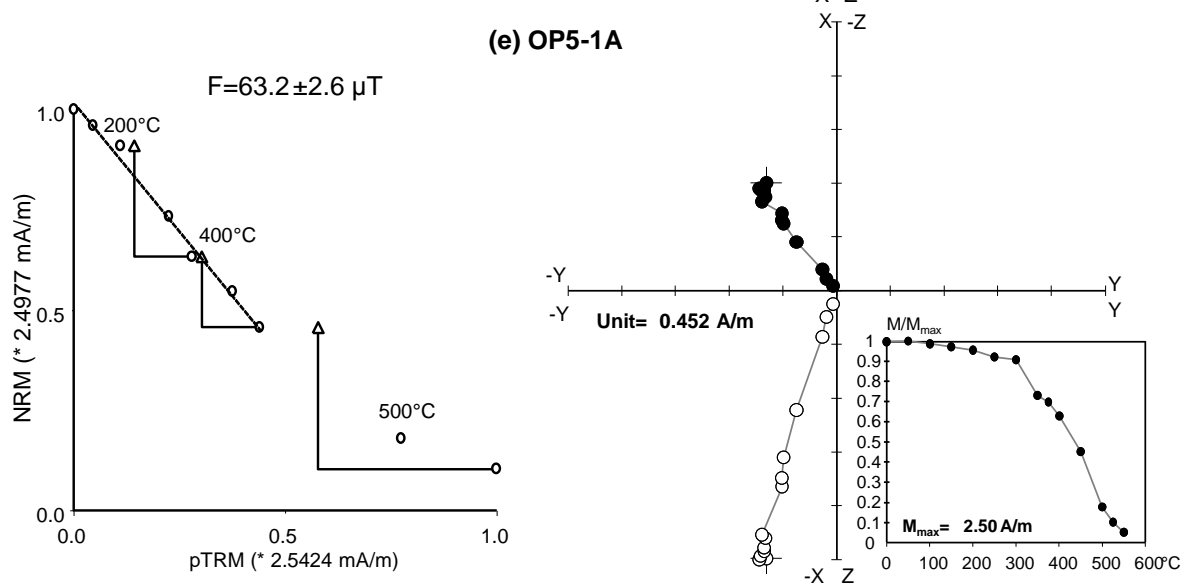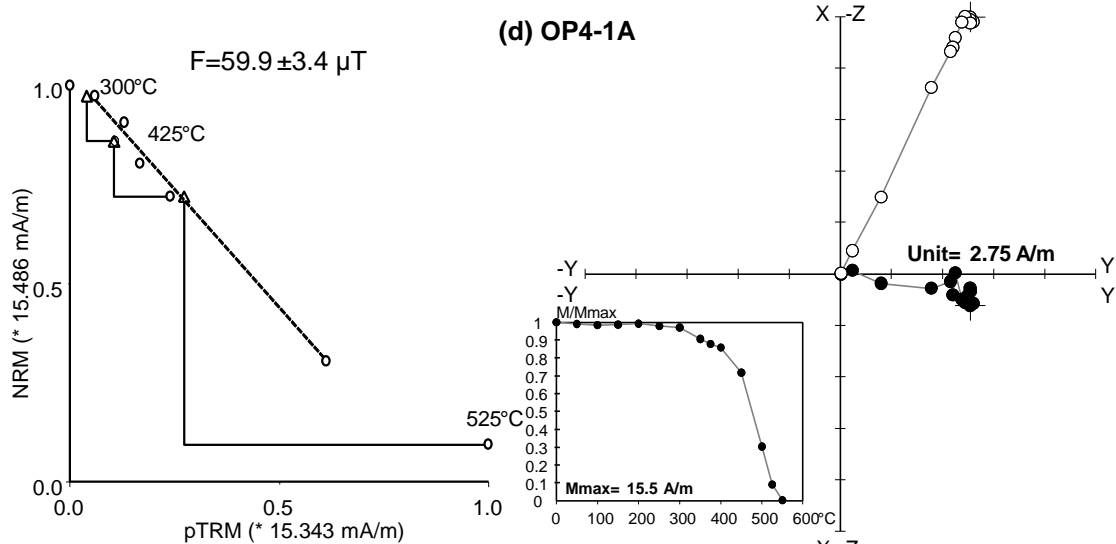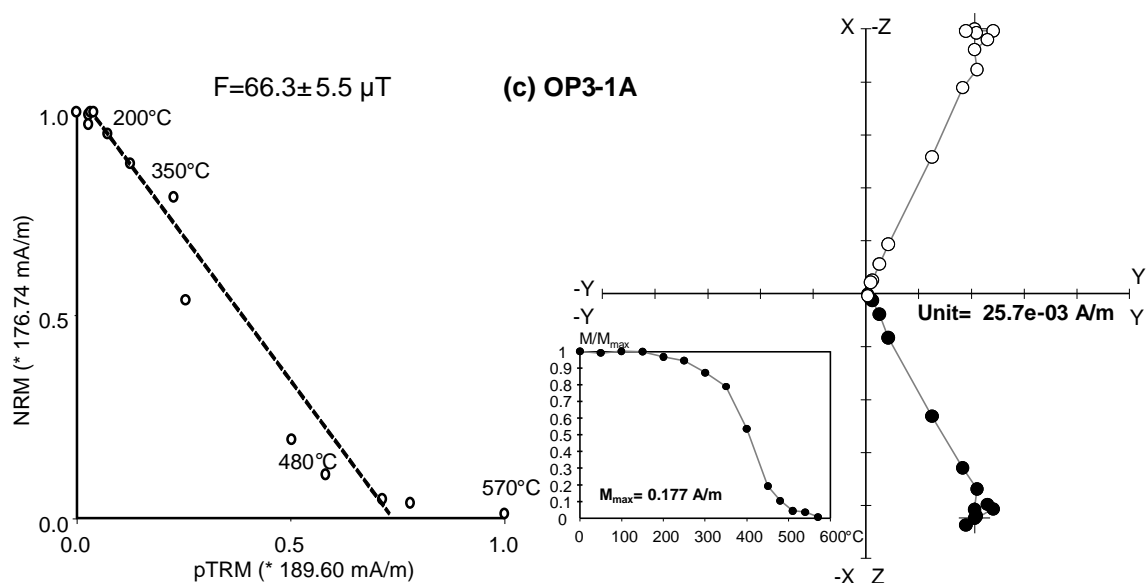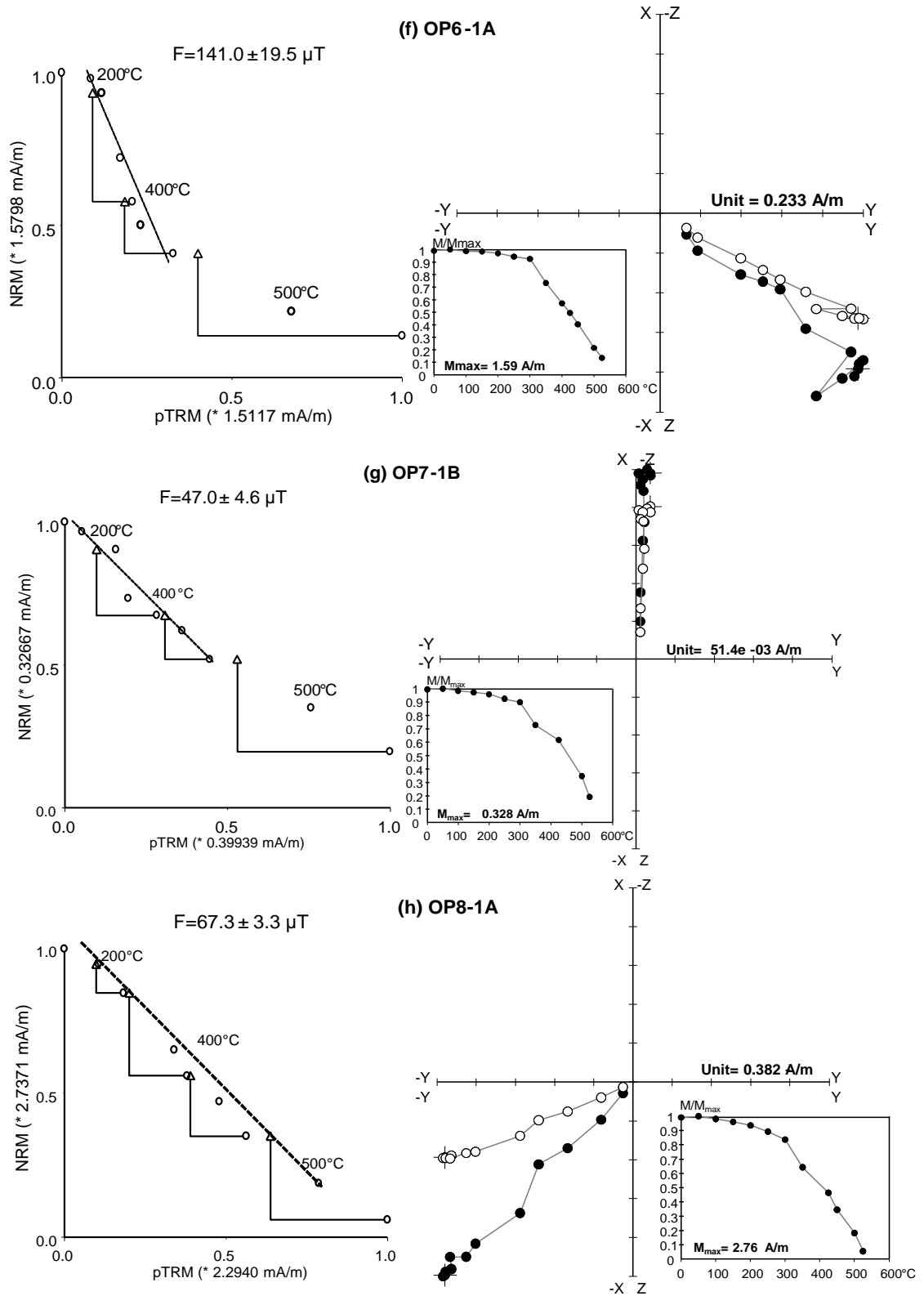
Figure 3.9. Arai diagrams obtained from specimens of stones OP1, OP2, OP3, OP4, OP5, OP6, OP7 and OP8 via Thellier Tool (a) - (h). Zijderveld diagrams, plotted using Remasoft30 software (Chadima & Hrouda, 2006), show demagnetization behaviour at each step in specimen coordinates (X, Y, Z) as the stones were non-oriented.

Table 3.6. Archaeointensity results measured for Opihi River hangi site. 'F' are the intensity results of individual specimens in µT. N is the number of data points used in a linear segment of the Arai plot. β, f, q, $\delta_{CK}$, $\delta_{pal}$, DRAT, MAD, $\delta_{TR}$, and $\delta_{t*}$ are statistical parameters defined in Chapter 2. Acceptable results are represented in black font.

| Sample ID | Temp (°C) | N | F ±σ (µT) | β | f | q | MAD | $\delta_{CK}$ | $\delta_{pal}$ | $\delta_{TR}$ | $\delta_{t*}$ | Class |
|---|---|---|---|---|---|---|---|---|---|---|---|---|
| **Threshold values for criteria** | | ≥5 | | ≤0.1 | ≥0.35 | ≥5 | ≤6 | ≤7 | ≤10 | ≤10 | ≤9 | TTA |
| | | ≥5 | | ≤0.15 | ≥0.35 | ≥0 | ≤15 | ≤9 | ≤18 | ≤20 | ≤99 | TTB |
| | | --- | | --- | --- | --- | --- | --- | --- | --- | --- | TTC |
| OP1-1A | 0-450 | 10 | 60.9±4.2 | 0.07 | 0.7 | 8.1 | 2.3 | | | | | A |
| OP1-1B | 200-450 | 6 | 63.8±5.3 | 0.08 | 0.59 | 5.2 | 1.1 | | | | | A |
| OP1-2A | 0-540 | 13 | 57.8±3.3 | 0.06 | 0.96 | 14.1 | 2.1 | | | | | A |
| OP1-2B | 200-450 | 6 | 61.1±7.1 | 0.12 | 0.60 | 3.6 | 2.1 | | | | | B |
| OP1-3A | 0-540 | 13 | 67.9±6.4 | 0.09 | 0.98 | 8.7 | 4.0 | | | | | A |
| OP2-1A | 50-400 | 8 | 51.6±2.5 | 0.05 | 0.74 | 12.2 | 11.4 | | | | | A |
| OP2-1B | 0-350 | 9 | 65.9±3.0 | 0.05 | 0.38 | 6.7 | 2.2 | | | | | A |
| OP2-2A | 100-400 | 6 | 49.6±4.2 | 0.09 | 0.69 | 5.9 | 5.0 | | | | | A |
| OP2-2B | 100-400 | 7 | 67.8±6.2 | 0.09 | 0.77 | 6.2 | 1.9 | | | | | A |
| OP3-1A | 200-540 | 9 | 66.3±5.5 | 0.08 | 0.95 | 9.2 | 1.2 | | | | | A |
| OP3-2A | 200-510 | 8 | 66.9±5.6 | 0.08 | 0.95 | 8.6 | 1.4 | | | | | A |
| OP3-2B | 200-480 | 6 | 82.8±3.0 | 0.04 | 0.65 | 13.4 | 1.6 | | | | | A |
| OP3-3A | 300-570 | 8 | 72.8±4.7 | 0.07 | 0.80 | 9.7 | 2.0 | | | | | A |
| OP3-4A | 100-570 | 12 | 78.4±7.5 | 0.10 | 0.93 | 7.5 | 3.6 | | | | | A |
| **Average** | **OP1, OP2, OP3** | **10** | **65.1±4.3** | | | | | | | | | |
| OP4-1A | 300-500 | 6 | 59.9±3.4 | 0.06 | 0.65 | 6.1 | 3.0 | 3.6 | 4.6 | 4.8 | 4.1 | A |
| OP4-2A | 200-500 | 7 | 65.3±4.3 | 0.07 | 0.48 | 3.6 | 2.0 | 6.9 | 2.6 | 3.0 | 10.0 | B |
| OP5-1A | 0-450 | 7 | 63.2±2.6 | 0.04 | 0.55 | 10.8 | 2.9 | 4.1 | 14.4 | 1.4 | 1.9 | B |
| OP5-2A | 0-450 | 7 | 69.1±2.7 | 0.04 | 0.51 | 10.7 | 1.6 | 3.2 | 3.1 | 1.7 | 3.7 | A |
| OP6-1A | 200-450 | 6 | 141.0±19.5 | 0.13 | 0.51 | 2.8 | 3.3 | 6.3 | 33.7 | 4.1 | 5.9 | C |
| OP6-2A | 200-450 | 5 | 168.4±21.8 | 0.13 | 0.44 | 2.6 | 1.7 | 3.5 | 2.8 | 2.3 | 12.5 | B |
| OP6-2B | 200-450 | 6 | 169.7±36.4 | 0.2 | 0.56 | 2.1 | 1.3 | 9.5 | 22.8 | 4.8 | 10.8 | C |
| OP6-3A | 300-500 | 6 | 138.4±24.9 | 0.2 | 0.59 | 2.4 | 2.2 | 2.9 | 5.7 | 1.7 | 14.1 | B |
| OP6-3B | 200-450 | 6 | 101.2±11.8 | 0.1 | 0.38 | 2.6 | 1.8 | 7.4 | 5.7 | 8.5 | 5.7 | B |
| OP7-1B | 0-450 | 7 | 46.9±4.6 | 0.1 | 0.49 | 4.1 | 1.6 | 6.9 | 9.6 | 2.6 | 3.3 | B |
| OP7-2A | 0-450 | 7 | 51.0±5.3 | 0.1 | 0.53 | 4.2 | 1.6 | 7.5 | 18 | 8.7 | 3.6 | C |
| OP8-1A | 0-500 | 8 | 67.3±3.3 | 0.05 | 0.83 | 14.1 | 2.3 | 8.3 | 11.4 | 2.3 | 2.6 | B |
| OP8-1B | 0-500 | 8 | 57.0±3.1 | 0.05 | 0.81 | 12.6 | 2.7 | 3.5 | 12.5 | 4.2 | 5.4 | B |
| **Average** | **OP4, OP5, OP6** | **6** | **63.3±4.6** | | | | | | | | | |
| **Site Mean** | | **16** | **64.6±4.3** | | | | | | | | | |

## 3.6. Discussion

To calculate archaeointensity, data points are chosen within a temperature range which varies slightly from stone to stone. For example, in the case of specimen OP1-1A (Figure 3.9 (a)), above the temperature step 450°C, pTRM gained shows a non-linear trend. The threshold values of statistical parameters must also be considered in the selection of data points. Specimens from stones OP4-OP8 thermally altered above 500°C, so the data points above this temperature are not used in intensity calculations (Figure 3.9 (d)-(h)). All specimens from stone OP6 gave anomalously high-intensity data with high uncertainties, and OP7 specimens provided lower values than the majority of specimens from other stones. This suggests that OP6 and OP7 have different thermal histories from the other stones, and so do not carry a record of the same thermal event and field. The data of these stones was therefore not included in the average archaeointensity calculation for the site. Four further specimens, from stones OP2 and OP3, gave data that were inconsistent with other data and not included in site's mean intensity.

The average archaeointensity, calculated from the remaining 16 specimens from six stones is 64.6 ± 4.3 µT. In Figure 3.10 the OP archaeointensity is plotted along with the field intensity at Opihi River (latitude/longitude ~ 44.2°S/ 171°E) calculated from the geomagnetic field model *gufm*1 of Jackson et al., (2000). *Gufm1* is based on absolute intensity measurements from the year 1838 to 1990 (the red line in Figure 3.10). Before 1838, there were no absolute intensity measurements, so *gufm*1 is based on the assumption that the Gauss coefficient $g_0^1$ decayed linearly over the preceding 200 years (the blue line in Figure 3.10). The black point with error bars shows Opihi River's archaeointensity calculated from the hangi stones. The point is plotted using the calibrated ^{14}C age of the site. With 95% confidence, the calibrated date range is between 1460 and 1625 AD. As given by *gufm1*, in the year 1590 the magnetic field intensity at Opihi River was 66.11µT and in the year 1990 the value had decreased to 59.0 µT. The field intensity has therefore decreased by 10% in last 400 years. The intensity was almost stable from 1750 to 1950 and then, after 1950, started to decrease linearly. From Figure 3.10 it can be seen that Opihi River archaeointensity is in good agreement with *gufm*1.

However, the age of the site could not be refined further, due to the uncertainty in the archaeointensity and a lack of palaeodirectional information.
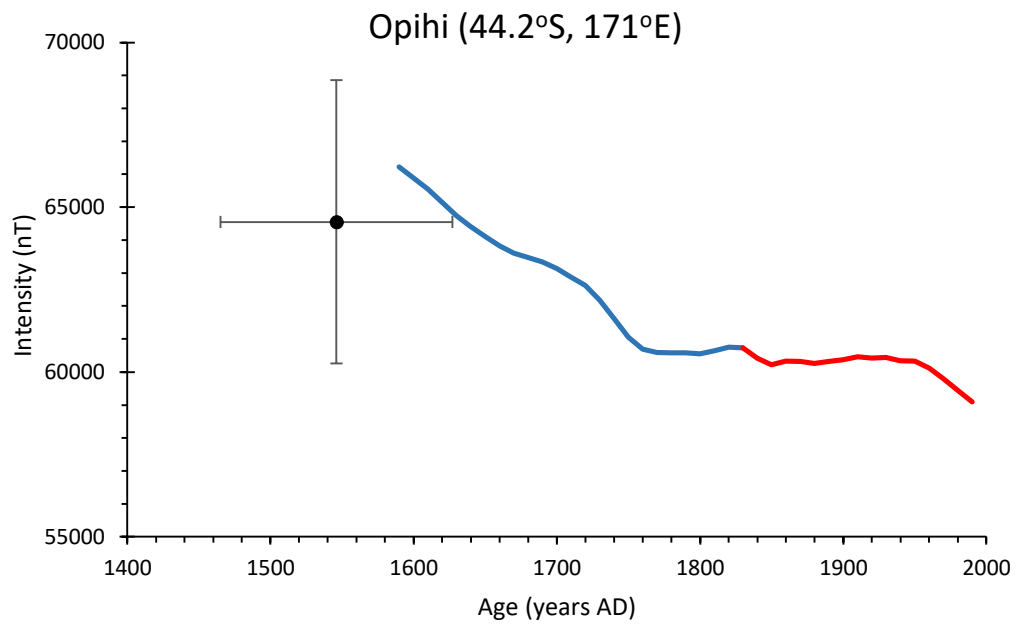


Figure 3.10. Archaeointensity and geomagnetic field intensity for the past 400 years at the Opihi River site, calculated from the *gufm1* model of Jackson et al., (2000).

# 4. Great Mercury Island Hangi Sites

## 4.1. Archaeological Setting

Great Mercury Island (GMI) lies off the Coromandel Peninsula, approximately 30 km NE of Whitianga. The geology of Great Mercury Island is dominated by volcanic features of the Miocene-Pleistocene age. The northern part of the island consists of andesites, basalts and rhyolitic pyroclastics, and is joined by a central thinner sandy bar to the southern part composed of pyroclastics and rhyolites (Hayward, 1976 ) (Zutelija, 1976).

The southern part of the island is currently covered with a dense radiata pine forest. Pa sites on the island were previously excavated in 1954 and 1984 by Jack Golson and Professor Geoff Irvin at Matakawau and Huruhi Harbour (www.auckland museum.com). The island is rich in pa sites, garden features and other evidences of Maori occupation. During 1972-73, Steve Edson comprehensively surveyed the island and identified 91 archaeological sites.
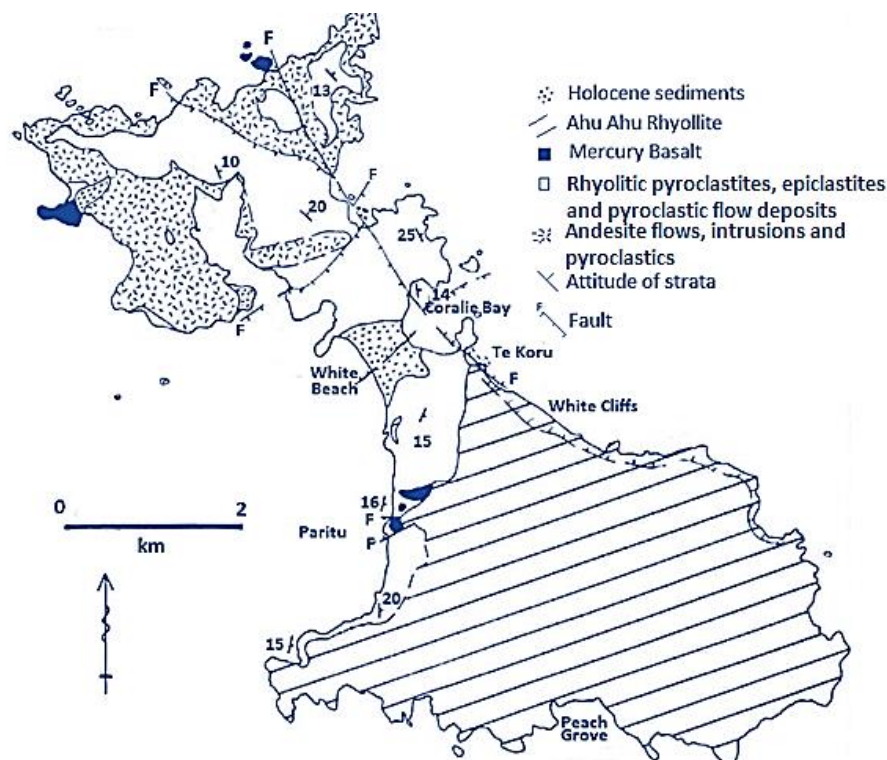


Figure 4.1. Geological map of Great Mercury Island (Hayward, 1976).
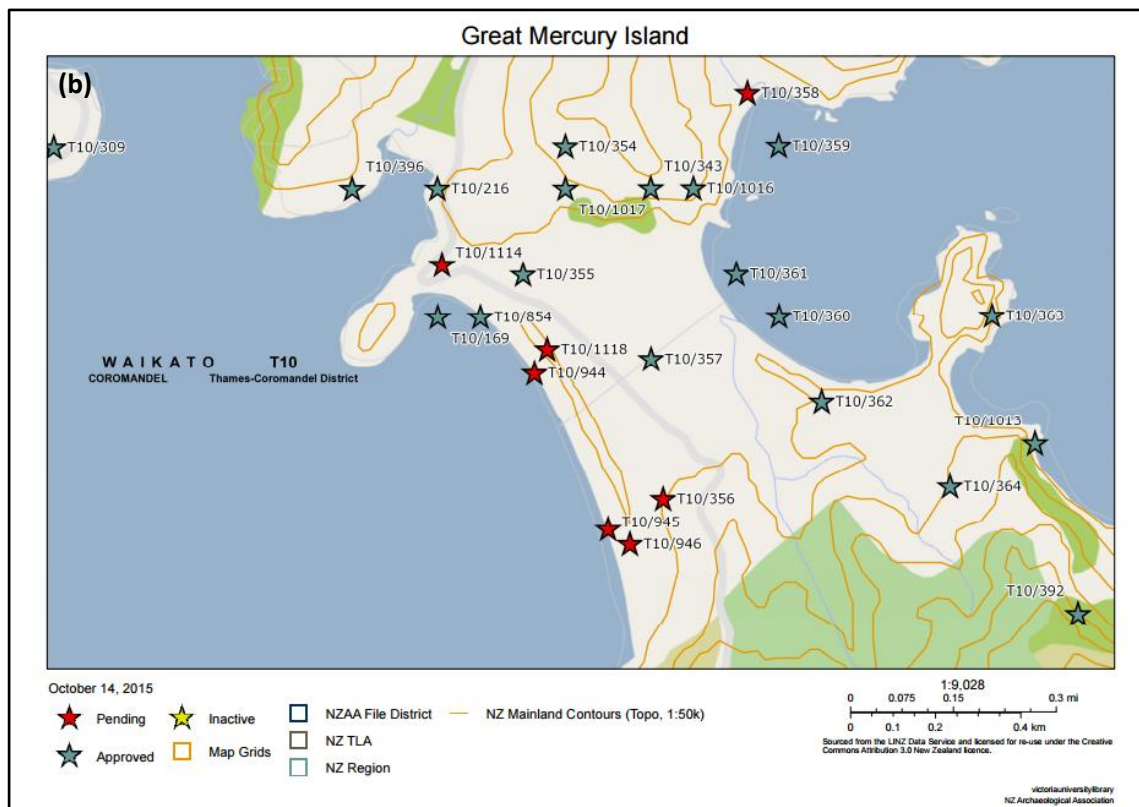
Figure 4.2. (a) Topographic and (b) Archsite map of Great Mercury Island (downloaded from www.topomap.co.nz). T10/944 and T10/1114 are sites from which samples of hangi stones were taken in February 2013(www.archsite.org.nz).

In July 2008, a severe storm cut back the coastal dune system of the white beach in the central part of the island (about a kilometre long) by about 10 metres. The island was then visited by archaeologists who recorded a series of nine features in the eroded beach area (Furey, 2009). These features were related to three separate sites, recorded as Archsite numbers T10/944, T10/945 and T10/946 (Furey, 2009).

In site T10/944, a darkened soil layer, midden deposits, and ovens were found in the exposed dune section (between 1.1m and 1.4m from the top of the dune) along the beach. Charcoal, blackened sand and midden shells were sampled by archaeologists for dating. Samples of the exposed archaeological features were retained for further analysis. Artefacts such as a stone chisel, chert flakes, obsidian flakes, basalt flakes and some petrified wood were also found. One of the hangi pits was subsequently sampled for this study and labelled GM1.

Sites T10/945 and T10/946 are both about 400m south of T10/944 (Figure 4.2(b)). T10/945 hold a blackened sand layer about 20m long, nearly 1.4m below the top of the dune surface. Exposed features at this site were a hangi and basalt flakes. A charcoal lens with a number of fire-cracked stones was found above the hangi and separated from it by a white sand layer (Furey, 2009). In site T10/946, about 2m below the top of the dune, a dark stained area was exposed containing a hangi, basalt and chert flakes. This site was not sampled by archaeologists as it could not be clearly defined (Furey, 2009). Neither sites T10/945 and T10/946 were sampled for archaeomagnetism.

T10/944 was later excavated in 2012 by archaeology students from the University of Auckland as part of a research project on Maori occupation. The project also excavated site T10/1114, uphill from Stingray Pa (Matakawau Point) (Figure 4.2 (a)), and found two further hangi. In February 2013, during further Auckland University fieldwork, we visited Great Mercury Island to carry out sampling of these three hangi pits. One hangi, labelled GM1 (Auckland University ID: EA4N99E98), was sampled from T10/944, and two hangi, GM2 (Auckland University ID: EA35) and GM3 (Auckland University ID: EA34), from T10/1114 (Table 4.1).

### 4.1.1. Hangi site GM1

Hangi site GM1 (Figure 4.3) was located in the sand dunes SE of Stingray Pa and adjacent to the farm accommodation buildings in the central part of the island. This hangi pit was originally located during an electrical resistivity survey (Feb, 2012) of site T10/944. The hangi was roughly circular and ~50 cm in diameter. It contained a lot of fire-cracked stones, blackened sand and charcoal. The latitude/longitude of the site is 36º 36′ 26″ S / 175º 47′ 11″ E.



Figure 4.3. Excavated hangi site GM1. The red circle indicates the position of fire-cracked stones; the arrow indicates north.

### 4.1.2. Hangi sites GM2 and GM3

The hangi sites GM2 and GM3 in site T10/1114 (latitude/longitude 36° 36′ 19″ S / 175° 46′ 59″ E) were located approximately 500m north of GM1, on the grassy spur above Stingray Pa. Both hangi pits were filled with fire-cracked stones and charcoal (Figure 4.4 (a) & (b)). The stones were tightly packed with sand, suggesting they were *in situ*. Most of the stones found in the three hangi pits are andesites, and a brief description of each hangi is given in Table 4.1.

Figure 4.4. Photos of hangi sites GM2 and GM3. (a) Lower layer of hangi stones in hangi GM2. (b) Upper layer and edge of hangi site GM3.

Table 4.1. Features of Arch site T10/944 and T10/1114. GPS coordinates converted to NZTM (http://apps.linz.govt.nz/coordinate-conversion/index.aspx).

| VUW site label and Archsite reference | Auckland University label | Age control (Conventional Radiocarbon Ages) | Features and comments | NZTM coordinates |
|---|---|---|---|---|
| GM1 (T10/944) | EA4N99E98 | 296±16BP NZA 53731 See table 4.3 | A hangi, 50cm diameter, containing fire-blackened soil and fire-cracked stones along some charcoal. | N5945283.5 E1849244.2 |
| GM2 (T10/1114) | EA35 | 257±16BP NZA 53737 See table 4.3 | A hangi, 60cm diameter, containing fire-blackened soil and fire-cracked stones along some charcoal. | N5945507.9 E1848952.2 |
| GM3 (T10/1114) | EA34 | 242±16BP NZA 53736 See table 4.3 | A hangi, 60cm diameter, containing fire-blackened soil and fire-cracked stones along some charcoal. | N5945507.9 E1848952.2 |

## 4.2. Sampling and specimen preparation

The uppermost layer of stones in GM1 had already been removed before we visited the site. Different layers of stones in the hangi were subsequently excavated after our arrival. Five oriented stones (GM1-1, GM1-2, GM1-3, GM1-4 and GM1-6) and one non-oriented stone (GM1-5) were sampled from the surface of the exposed layer. Five more oriented stones (GM1-7, GM1-8, GM1-9, GM1-10 and GM1-11) were collected from the underlying layer (Figure 4.5). After the removal of these two layers, more stones were exposed, and three non-oriented stones were sampled from this last excavated layer.



Figure 4.5. Sampling layer 2 of hangi site GM1, showing stones GM1-7 to GM1-11.

Altogether ten oriented stones and four non-oriented stones were sampled from hangi GM1. Charcoal fragments were also collected for $^{14}$C dating.

Hangi GM2 had also been partly excavated, exposing stones. This hangi was found during a magnetic field survey, due to the strong magnetization of the stones compared with the surrounding soil and stones. Three oriented stones (GM2-1, GM2-2 and GM2-3) and charcoal fragments were collected from the uppermost exposed layer, and further excavation of the lower layer provided seven more oriented stones (GM2-4, GM2-5, GM2-6, GM2-7, GM2-8, GM2-9 and GM2-10, Figure 4.6 (a)). Altogether ten oriented stones were sampled from GM2.
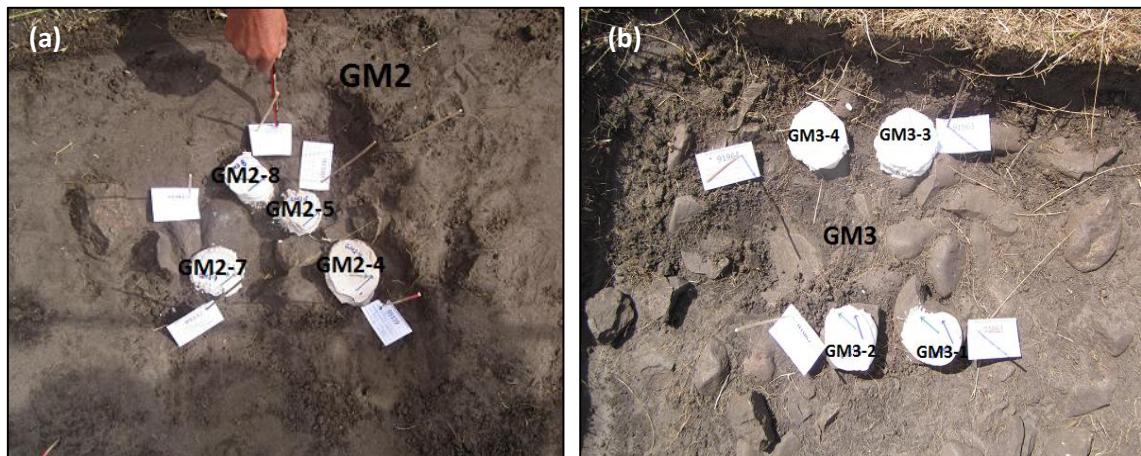


Figure 4.6. Hangi sites GM2 and GM3. (a) Sampling of stones from layer 2 of hangi site GM2. (b) Uppermost layer of hangi site GM3.

GM3 was about 2m east of GM2. We sampled four oriented stones (GM3-1, GM3-2, GM3-3 and GM3-4) from the uppermost layer (Figure 4.6 (b)). The remainder of GM3 was left intact for possible future sampling. A charcoal sample was also collected.

All samples were accurately positioned using an automated laser positioning system (total station) and entered into Auckland University's archaeological database with Auckland ID numbers (Table 4.2). Before drilling cores from the hangi stones, the stones were set into rectangular boxes with concrete. Details of the cores drilled from each stone, and the specimens cut from each core, are given in Table 4.2.

Table 4.2. Details of cores and specimens from each stone studied.

| Stone Name | Auckland University ID | Number of cores | Number of Specimens |
|---|---|---|---|
| GM1-2 | 96387 | 3 | 4 |
| GM1-3 | 96388 | 2 | 3 |
| GM1-4 | 96389 | 2 | 4 |
| GM1-7 | 96392 | 3 | 3 |
| GM1-8 | 96393 | 3 | 7 |
| GM1-9 | 96394 | 4 | 8 |
| GM1-10 | 96395 | 1 | 2 |
| GM1-11 | 96396 | 2 | 4 |
| Total = 8 | | 20 | 35 |
| GM2-1 | 97599 | 5 | 12 |
| GM2-2 | 97600 | 7 | 14 |
| GM2-3 | 97601 | 3 | 6 |
| GM2-4 | 99339 | 4 | 8 |
| GM2-5 | 99340 | 1 | 2 |
| GM2-6 | 99341 | 2 | 4 |
| GM2-8 | 99364 | 1 | 1 |
| GM2-9 | 99389 | 1 | 2 |
| Total = 8 | | 24 | 49 |
| GM3-1 | 91961 | 3 | 7 |
| GM3-2 | 91962 | 2 | 2 |
| GM3-3 | 91963 | 3 | 3 |
| GM3-4 | 91964 | 4 | 8 |
| Total = 4 | | 12 | 20 |

## 4.3. Age control

The charcoal samples collected from sites GM1, GM2 and GM3 were sent to Auckland University palaeobotanist Rod Wallace for species identification. The charcoal from GM1 was identified as pohutukawa twigs. Stratigraphic interpretation suggests that this hangi is almost certainly a single event (McFadgen, 2007). All the charcoal identified came from pohutakawa twigs, supporting this interpretation. Charcoal from GM2 was identified as a mixture of pittosporum, pohutukawa, tutu, hebe, coprosma, mapou and shrub species. The GM3 charcoal samples were also a mixture – coprosma, pohutukawa, mahoe and silicified wood.  All identified species are short-lived and so suitable for radiocarbon dating (McFadgen, 1982). One charcoal sample (pohutukawa twig) from GM1, two charcoal samples from GM2 (coprosma and pohutukawa) and one from GM3 (coprosma) were sent for $^{14}$C dating at GNS Science, Lower Hutt. Results are given in Table 4.3 and Figure 4.7. The GM1 sample returned a conventional radiocarbon age

(CRA) of 296±16 BP. Matching this to the southern hemisphere calibration curve (Hogg et al., 2013b) yields the most likely calendar date between 1625 and 1666 AD, with only a very small likelihood of the date lying between 1516 and 1542 AD (Table 4.3, Figure 4.7 (a)). The younger CRAs of the three other samples from GM2 and GM3 correlate with the calibration curve in multiple places, producing several possible calendar ages. The CRAs of the GM3 sample ($242 \pm 16$ BP) and the pohutukawa sample from GM2 ($257 \pm 16$ BP) correspond to possible calendar dates of about 1650 AD, similar to the GM1 date, but could also point to a date around 1750 AD (Figure 4.7 (b) and (d)). The even younger CRA of $181 \pm 16$ BP of the coprosma sample from GM2 is compatible with a broad range of calendar dates covering much of the past several centuries (Figure 4 (c)). These ambiguities and range may potentially be reduced by palaeomagnetic studies, including archaeomagnetic dating.

Table 4.3. Radiocarbon age estimation of GMI hangi sites.

| Site Name | Material | Lab No. | $^{14}$C age | Calibrated age range (95% confidence) |
|---|---|---|---|---|
| GM1 | Pohutukawa twig | NZA 53731 | 296±16 BP | 1625 AD -1666 AD (86.3% of area)<br>1516 AD -1542 AD (8.6% of area) |
| GM2 | Pohutukawa | NZA 53737 | 257±16 BP | 1643 AD -1673 AD (57.7% of area)<br>1743 AD -1772 AD (16.0% of area)<br>1779 AD -1797 AD (21.4% of area) |
| GM2 | Coprosma | NZA 53726 | 181±16 BP | 1672 AD -1712 AD (29.1% of area)<br>1719 AD -1746 AD (16.6% of area)<br>1755 AD -1765 AD (1.7% of area)<br>1770 AD -1780 AD (2.0% of area)<br>1797 AD -1813 AD (11.7% of area)<br>1836 AD -1891 AD (20.4% of area)<br>1923 AD -1950 AD (13.6% of area) |
| GM3 | Coprosma | NZA 53736 | 242±16 BP | 1740 AD -1798 AD (63.0% of area)<br>1650 AD -1675 AD (31.6% of area) |

(a)

GM1

NZA 53731
Pohutukawa twig

Calibrated age probability distribution
with 95% confidence interval shaded.

(b)

GM2

Calibrated age probability distribution with
95 % confidence interval shaded

NZA 53737
Pohutukawa
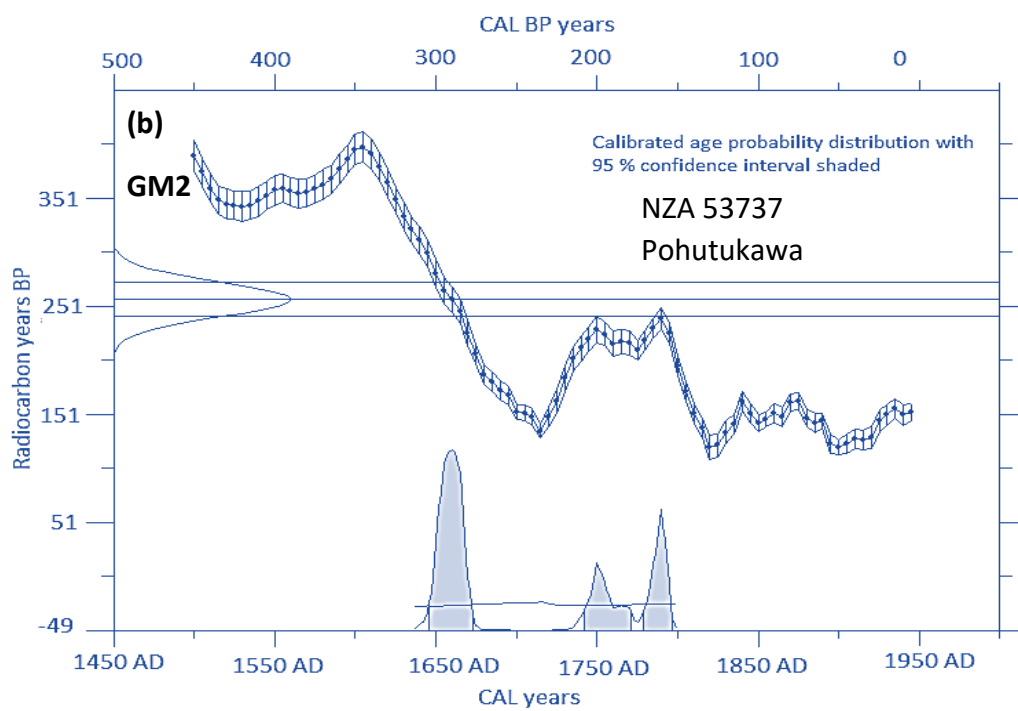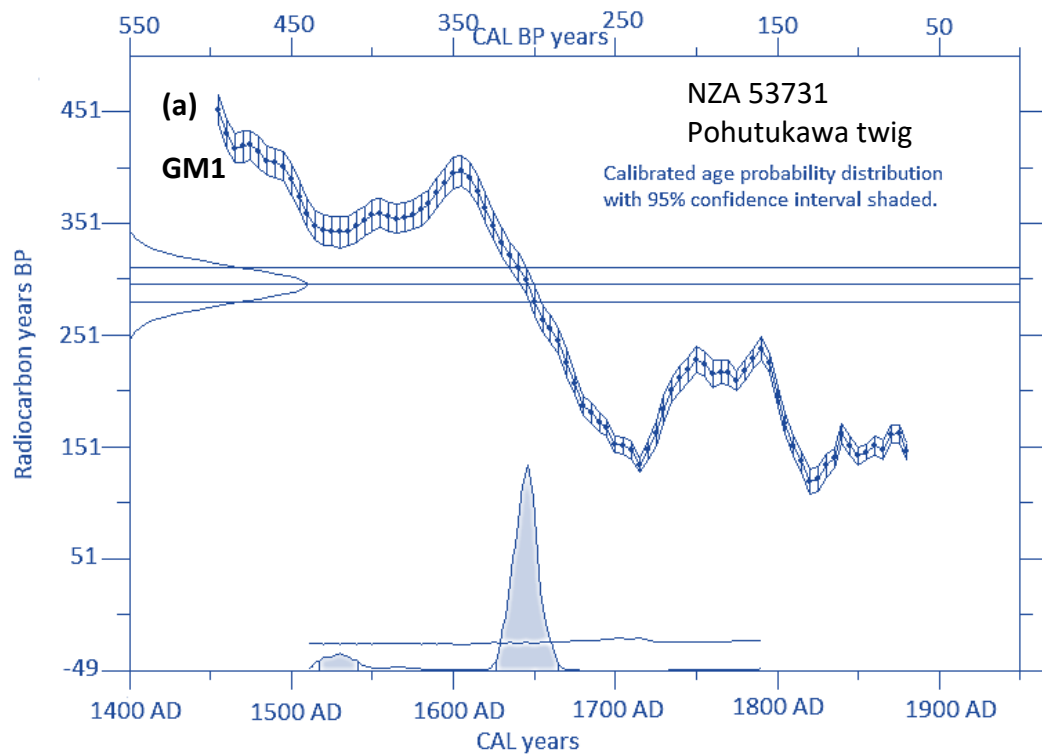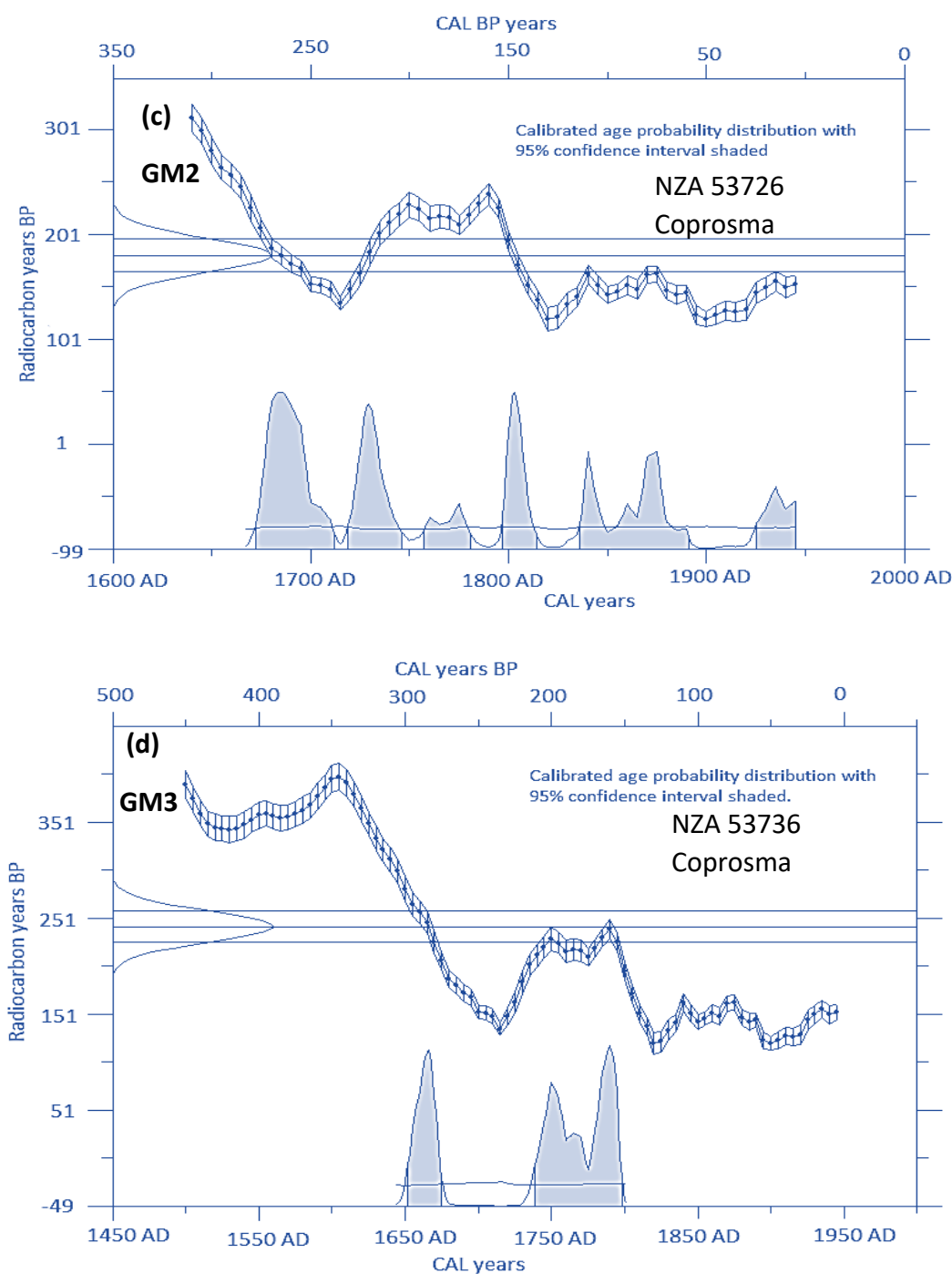
Figure 4.7. Calibration of radiocarbon age ages for sites (a) GM1, (b) & (c) GM2, and (d) GM3. Radiocarbon dating was carried out using accelerator mass spectrometry at GNS, Lower Hutt; calibration using the southern hemisphere calibration curve SHcal13 (Hogg et al., 2013); and figures and statistics using WINSCALX 5.1 (Sparks, R.J., and Manning, M.R. pers. comm.)

75

## 4.4. Rock Magnetism

Measurements of the rock magnetic properties of Great Mercury Island hangi stones are described below.

### 4.4.1. Curie Temperature

To determine the Curie temperature and the change in susceptibility after being heated to high temperature, susceptibility versus temperature experiments were carried out (Figure 4.8).

The susceptibility of the stones lies in the range 0.01-14 X $10^{-6}$ $m^3kg^{-1}$. The $\chi$-T curves for six different samples from sites GM1, GM2 and GM3 are shown in Figure 4.8. The samples were heated from room temperature to 700°C and cooled down to room temperature to check the thermal stability of magnetic minerals. The susceptibility increased with increases in temperature up to ~500°C or above, reaching a Hopkinson peak in most cases as the blocking temperatures of the magnetic grains are reached (Hopkinson, 1890). The difference between heating and cooling curves is due to the thermal alteration of minerals during the heating process so curves do not retrace their paths while cooling, and the susceptibility of some samples is increased after cooling curves (Figure 4.8 (a), (c) & (d)). GM1-9-2 and GM2-1-3 (Figure 4.8 (b) & (c)) show the presence of two phases of magnetic mineral. The first is a Ti-rich titanomagnetite, giving a drop-in susceptibility around 250-300°C, after which the susceptibility increased to a temperature around 500°C and, from this point, decayed to the principal Curie point around 590°C. The heating and cooling curves of GM1-9-2 are almost reversible.  On the other hand, GM2-1-3 is thermally altered and showed a single magnetic phase during cooling measurements. The experiment was repeated three times, to lower maximum temperatures of 300°, 400°C, and 500°C, to check the temperature at which thermal alteration begins (Hrouda et al., 2003). The change in susceptibility of the sample remained the same in all these cases. Similar behaviour may be observed in the $M_s$-T curves of GM1-10 and GM2-4 (Figure 4.8 (h) & (i)). It is not simple to find the exact Curie point of a low magnetic phase which cannot be seen in cooling curves. The saturation magnetization versus temperature curves for stones GM3-1, GM1-10 and GM2-4 give

principal Curie temperatures of 597°C, 623°C and 545°C. Thermal alteration in the case of the GM3 samples is more than that of GM1 and GM2 samples.

The principal Curie temperatures of the samples lie between 523-630°C, suggesting that these fine-grained andesites contain both (titano) magnetite (with Ti < 10%) and cation deficient (oxidized) titanomagnetite (Dunlop & Özdemir, 1997). The calculated Curie temperatures of each sample are given in Table 4.4.
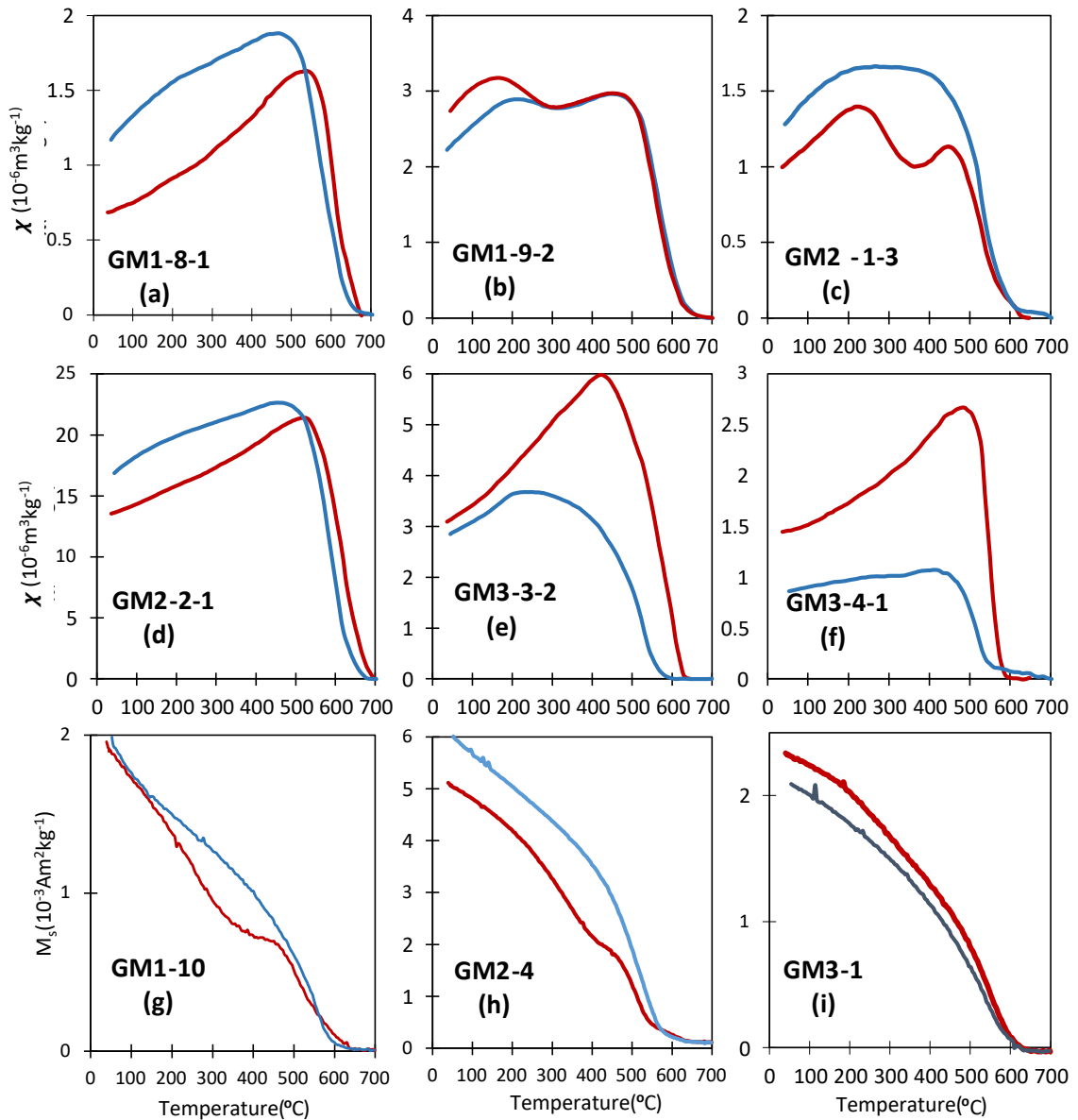


Figure 4.8. Susceptibility vs temperature plots for samples from hangi stones from sites GM1, GM2 and GM3 (a)-(f). (g)-(i) saturation magnetization vs temperature curves for samples GM1-10, GM1-3 and GM2-4. Red lines indicate the heating curves and blue lines the cooling curves.

Table 4.4. Curie temperatures of GMI hangi stones. Calculations for $\chi$-T plots use the inverse susceptibility method (Petrovský & Kapička, 2006). Curie temperatures from $M_s$-T plots are determined by the double derivative method, using Rockmag Analyser 1.0 (Leonhardt et al., 2006).

| Sample ID | $T_c$ Heating (°C) | $T_c$ Cooling (°C) | $T_c$ Cooling corrected (°C) | Difference (°C) | Description (Figure 4.8) |
|---|---|---|---|---|---|
| GM1-2-1 | 599 | 582 | 597 | 2 | $\chi$-T plot (not shown) |
| GM1-3-1 | 533 | 583 | 598 | -65 | $\chi$-T plot (not shown) |
| GM1-4-2 | 605 | 595 | 610 | -5 | $\chi$-T plot (not shown) |
| GM1-8-1 | 608 | 598 | 613 | -5 | $\chi$-T plot (a) |
| GM1-9-2 | $T_{c1} \approx 230$ $T_{c2} = 591$ | 578 | 593 | 2 | $\chi$-T plot (b) |
| GM1-10 | 588 | 564 | 579 | 9 | $\chi$-T plot (not shown) |
| GM1-10 | 623 | 590 | -- | --- | $M_s$-T plot (h) |
| GM1-11-2 | 599 | 609 | 624 | -25 | $\chi$-T plot (not shown) |
| GM2-1-3 | $T_{c1} \approx 300$ $T_{c2} = 583$ | 535 | 550 | 27 | $\chi$-T plot (not shown) |
| GM2-2-1 | 586 | 570 | 585 | 1 | $\chi$-T plot (d) |
| GM2-4 | 545 | 555 | -- | -- | $M_s$-T plot (h) |
| GM2-5-1 | 583 | 548 | 563 | 20 | $\chi$-T plot (not shown) |
| GM3-1-1 | 597 | 558 | 573 | 24 | $\chi$-T plot (not shown) |
| GM3-1 | 597 | 590 | -- | -- | $M_s$-T plot (i) |
| GM3-3-2 | 581 | 535 | 550 | 31 | $\chi$-T plot (e) |
| GM3-4-1 | 571 | 522 | 537 | 34 | $\chi$-T plot (f) |

## 4.4.2. Hysteresis and IRM Curves

To further investigate the magnetic mineralogy of the hangi stones, hysteresis and isothermal remanent magnetization (IRM) acquisition curves are plotted. Samples from hangi stones GM1-2, GM1-3, GM1-8, GM1-10, GM2-4 and GM3-1 were subjected to hysteresis and IRM experiments to determine remanent magnetization, coercivity and saturation magnetization (Heslop & Roberts, 2012). Hysteresis measurements show a dominant ferro/ferrimagnetic mineral (Figure 4.9 & Table 4.5), with some paramagnetic character. A paramagnetic correction has been applied to the hysteresis data of all samples. The red curves are the corrected hysteresis loops. Samples GM1-8, GM1-10 and GM1-11 have much broader loops than other samples from sites GM1, GM2 and GM3 (Figure 4.9). GMI andesites are completely saturated at a magnetic field below 0.3T. The saturation remanent magnetization ($M_{rs}$) and coercivity ($B_c$) of samples from

all three sites GM1, GM2 and GM3 range between 38.8 and 92.3 mAm$^2$/kg and 21.8 and 54 mT respectively.
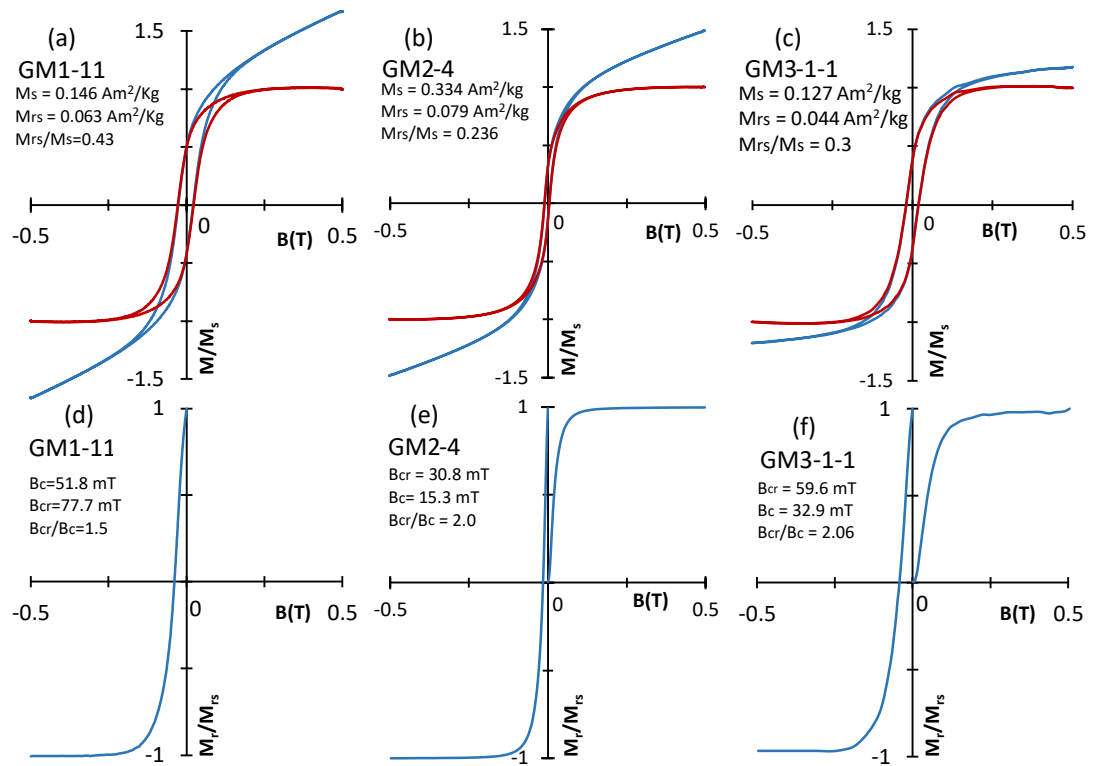


Figure 4.9. Hysteresis loops and back IRM curves for samples from stones GM1-11, GM2-4 and GM3-1. The blue and red curves are before and after removal of the paramagnetic component (see text for details).

Table 4.5. Hysteresis and IRM parameters of hangi stones from three different sites GM1, GM2 and GM3 at Great Mercury Island.

| Sample ID | $M_{rs}$(mAm$^2$/kg) | $M_s$(mAm$^2$/kg) | $M_{rs}/M_s$ | $B_{cr}$(mT) | $B_c$(mT) | $B_{cr}/B_c$ |
|---|---|---|---|---|---|---|
| GM1-2 | 81.4 | 223.7 | 0.36 | 51.4 | 25.1 | 2.05 |
| GM1-3 | 42.5 | 137.7 | 0.31 | 43.5 | 21.8 | 2 |
| GM1-8 | 38.8 | 86.6 | 0.47 | 88.2 | 46.9 | 1.74 |
| GM1-10 | 92.3 | 197.7 | 0.47 | 81.1 | 54.0 | 1.5 |
| GM1-11 | 62.9 | 146.0 | 0.43 | 77.7 | 51.8 | 1.5 |
| GM2-4 | 78.8 | 333.5 | 0.23 | 30.8 | 15.3 | 2.01 |
| GM3-1-1 | 43.5 | 127.0 | 0.35 | 59.6 | 32.9 | 2.06 |
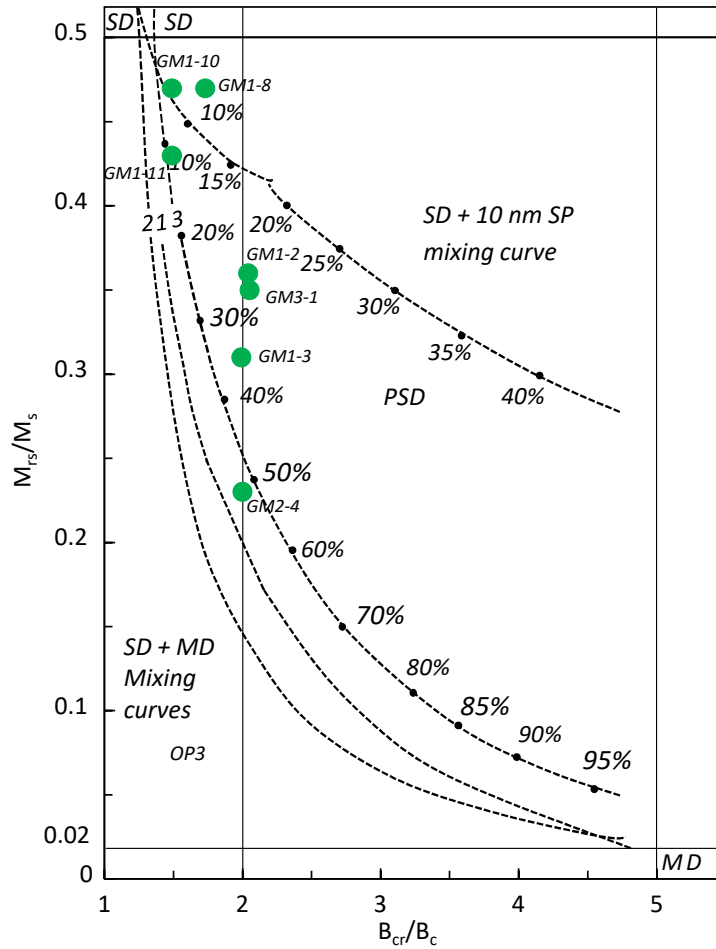
Figure 4.10. $M_{rs}/M_s$ vs $B_{cr}/B_c$ data (Day et al., 1977) of GMI hangi stones (green dots) superimposed on the mixing curves of Dunlop (2002) for a single domain, multidomain and superparamagnetic grains.

A Day plot for ratios $M_{rs}/M_s$ versus $B_{cr}/B_c$ has been plotted and superimposed on the theoretical mixing curves of Dunlop, (2002a & b) (Figure 4.10). The percentages along the curves are volume fractions of the soft magnetic component (MD or SP). All GM samples lie in the upper portion of the plot within the traditional PSD region. GM1-8, GM1-10 and GM1-11 are closer to the SD boundary. From rock magnetic data, it can be seen that most GMI samples have high remanent magnetization and coercivity values, and so may provide useful and reliable archaeomagnetic data.

## 4.4.3. Summary

Curie temperatures of all samples from GMI hangi sites are in the range from 523 to 630°C, suggesting the dominance of Ti-poor titanomagnetite and/or titanomaghemite

as a magnetic mineral. Some stones show two magnetic phases (e.g. GM1-9-2, GM1-10, GM2-1-3 and GM2-4). Hysteresis properties also show the ferro/ferrimagnetic remanence carrying grains lie in the SD to PSD range.

## 4.5. Progressive Demagnetization Results

Demagnetization experiments were carried out on 29 specimens from the three hangi sites GM1, GM2 and GM3. Results are explained below site-by-site.

### 4.5.1. GM1

Stepwise thermal demagnetization experiments were performed on 14 specimens from site GM1 (at least one specimen from each of the oriented stones GM1-2, GM1-3, GM1-4, GM1-7, GM1-8, GM1-9, GM1-10 and GM1-11). Typical results are shown in Figure 4.11(a)-(h). These stones have NRMs in the range 0.2-8 A/m – also typical of andesites containing (titano) magnetite a low percentage of titanium. The decay curves of stones GM1-2, GM1-3, GM1-4, GM1-8 and GM1-10 are similar, indicating grains which start to unblock at low-temperature steps. In the secimens of stone GM1-11, only few grains unblocked below temperature 400°C. The Zijderveld plots show the presence of more than one component of magnetization in specimens from stones GM1-2, GM1-3, GM1-4 and GM1-9, indicating these stones were disturbed in the hangi during the cooling process. The decay plots are also consistent with two components with distinct unblocking temperature spectra. The stones GM1-7, GM1-8, GM1-10 and GM1-11, have a stable single component of magnetization. The separation of components can be clearly seen in the Zijderveld plots (Figure 4.11 (a) & (f)) of stones GM1-2 and GM1-9, which both show a bend at the temperature step of 400°C. In GM1-3, a curve exists, indicating the presence of two components, and the magnetization vectors of GM1-4 at high temperature do not head towards the origin. For statistical purposes, the demagnetization data is combined with directional data obtained from archaeointensity experiments and AFD results from three specimens (Table 4.6). Altogether 12 specimens showed consistent directions. In the case of the specimens having more than one component of magnetization, the lowest blocking temperature component has been included in the calculation of the site's mean direction. The overall mean GM1 direction

calculated from stones GM1-4, GM1-7, GM1-8 and GM1-9 is: Dec = 1.5°, Inc = -55.9°, $\alpha_{95}$ =3.3° and N = 12 (Chadima & Hrouda, 2006). Figure 4.11 (i) shows the increase in susceptibility, by a factor of two, of specimens during thermal demagnetization. Significant changes can be observed in GM1-9 specimens above 400°C. The direction of the characteristic remanent magnetization, or, where there is more than one component, the low blocking temperature component of remanence for specimens from GM1 stones, is shown in Figure 4.12 (a). Figure 4.12 (b) shows the high blocking temperature component for cases where it is distinctly different from the low blocking temperature component. In general, there is a good agreement between components calculated from the specimens from each stone. The clear differences between the high and low blocking temperature components of stones GM1-2 and GM1-9 show that these stones were disturbed while at about 400°C, possibly during raking of the hangi. The graph in Fig 4.14 (b) for specimens from stone GM1-11 also show a high temperature component that has been reoriented, this component could also be acquired during rake out.

The directions plotted in Figure 4.12 (a) reflect magnetization acquired during the later stage of cooling. Directional data agreement within the stone is excellent, and the clustering of directions between stones suggests that little disturbance of the stones has occurred during or since the acquisition of these components of remanence.

For the calculation of a preliminary site mean direction, GM1-3 was disregarded as an outlier – it seems to have rotated slightly compared with the other six stones. Averaging the ChRM or low blocking temperature components of the 18 specimens from these six stones gives a mean archaeodirection of Dec = 3.4°, Inc = -59.1°, $\alpha_{95}$ = 4.6°. The directions of stones GM1-2 and GM1-10, and two of the specimens from GM1-7 lie significantly outside the main cluster. If they are disregarded, an archaeodirection of Dec = 1.5°, Inc = -55.9°, $\alpha_{95}$ = 3.3°, N = 12 specimens from four stones results. This is adopted as the best estimate of the archaeodirection for hangi GM1.

(a)    GM1-2-1A

(b) GM1-3-1A

(c) GM1-4-1A

(d) GM1-7-4A

● Horizontal  ● Vertical

Unit= 0.634 A/m    Mmax= 3.7 A/m

Unit=0.0 42 A/m    Mmax= 0.236 A/m

Unit= 0.114 A/m    Mmax= 0.745 A/m

Unit= 0. 436 A/m    Mmax= 2.45 A/m
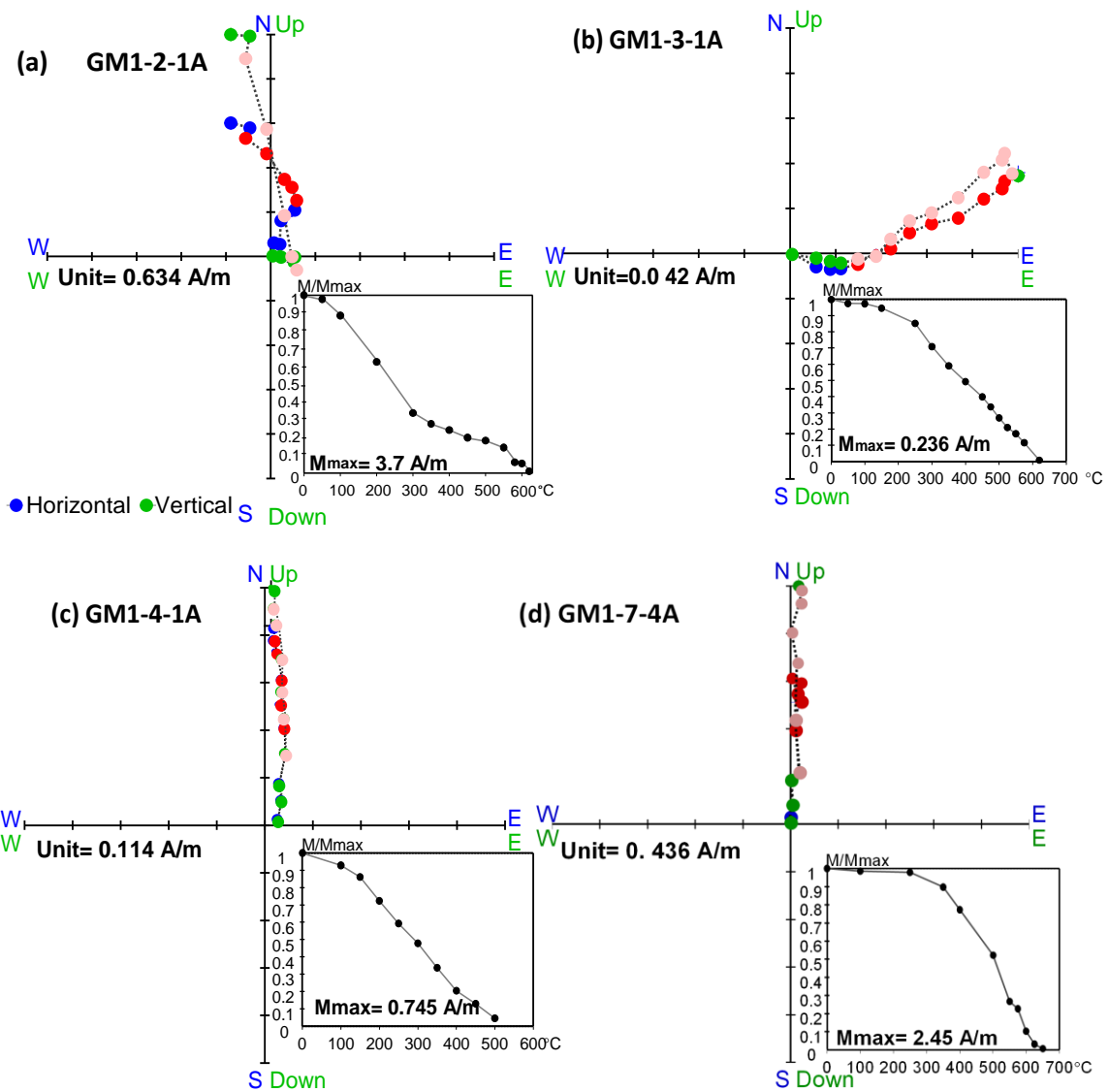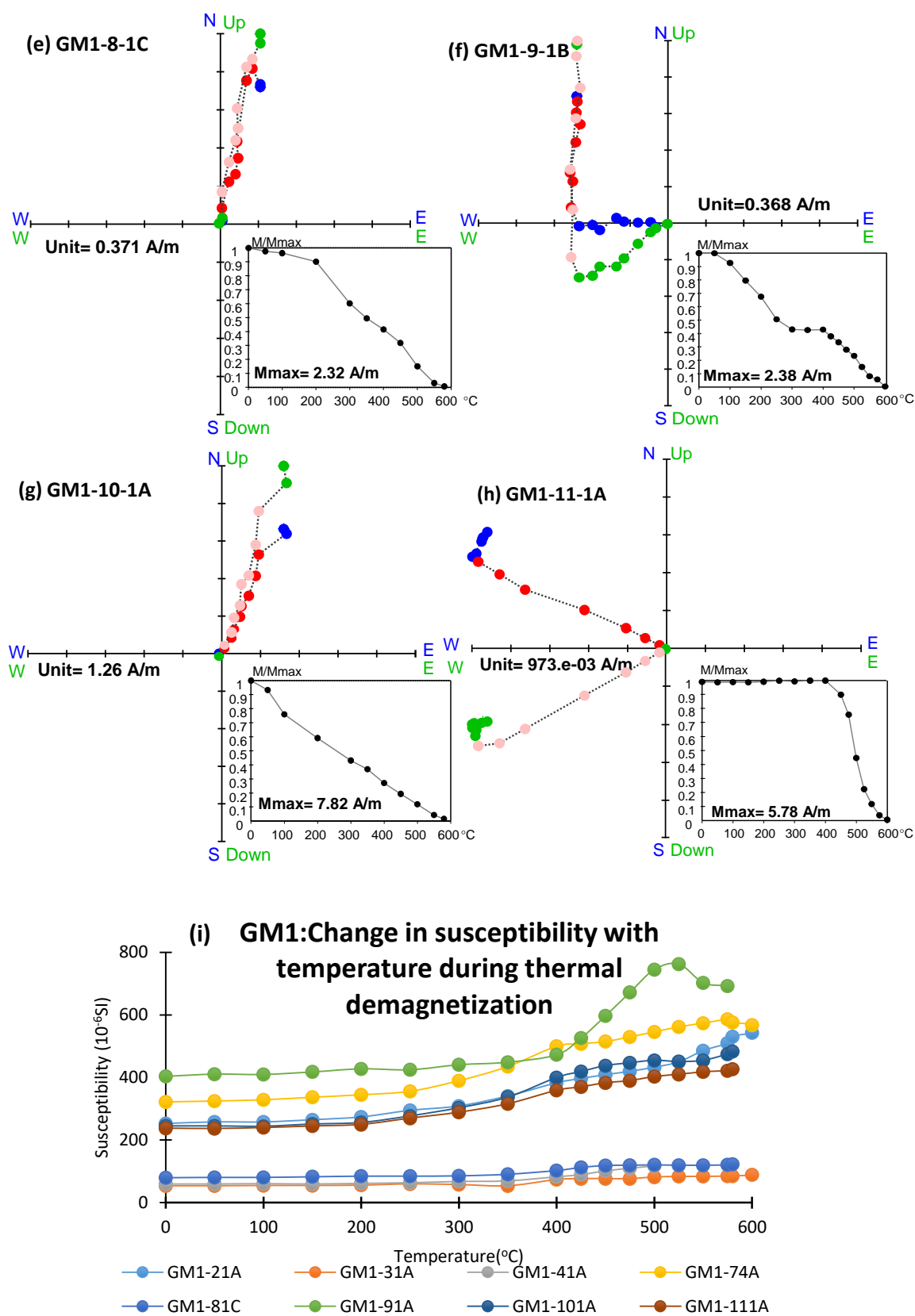
Figure 4.11. Thermal demagnetization results of specimens from eight hangi stones from site GM1 (a)-(h). Each figure includes Zijderveld plot and inset decay plot of specimen. Red and pink coloured dots indicate the data points included for PCA. (i) Shows change in susceptibility at each temperature step.

Table 4.6. Directional data of hangi site GM1, calculated from thermal (THD) and alternating field demagnetization (AFD). C1 is the high blocking temperature component, and C2 the low blocking temperature component of magnetization. N is number of specimens and n is number of data points used for calculations. Calculations made with Remasoft30 software. RT indicates room temperature. Only black coloured data is included for the calculation of mean directional data.

| Sample ID | Temp range (°C) | N or n | Dec (°) | Inc (°) | MAD/$\alpha_{95}$ (°) |
|---|---|---|---|---|---|
| GM1-2-1A(C1) | 400-600 THD | 5 | 29.5 | 6.4 | 9.9 |
| GM1-2-1A(C2) | RT-350 THD | 5 | 323.3 | -71.2 | 3.3 |
| GM1-3-1A | 100-450 THD | 7 | 60.7 | -32.3 | 2.3 |
| GM1-3-1B | 250-575 THD(P) | 11 | 55.4 | -34.7 | 4.4 |
| GM1-3-2A | 150-450 THD | 7 | 61 | -29.9 | 1.9 |
| **Mean GM1-3** | | **3** | **59.1** | **-32.3** | **5.4** |
| GM1-4-1A | 100-350 THD | 6 | 355.6 | -51.2 | 0.8 |
| GM1-4-2A | 15-100mT AFD | 9 | 353.4 | -48.9 | 1.5 |
| **Mean GM1-4** | | **2** | **354.5** | **-50.1** | **5.9** |
| GM1-7-1A | 35-100mT AFD | 7 | 347.5 | -75.5 | 1 |
| GM1-7-2A | 25-100mT AFD | 8 | 354.5 | -75.7 | 1.2 |
| GM1-7-4A | 350-625 THD | 7 | 2.4 | -50.9 | 2.6 |
| **Mean GM1-7** | | **1** | **2.4** | **-50.9** | **2.6** |
| GM1-8-1A | 200-500 THD(P) | 8 | 9.8 | -54.2 | 1.6 |
| GM1-8-1B | 200-525 THD(P) | 9 | 5.6 | -51.5 | 1.8 |
| GM1-8-1C | 100-500 THD | 9 | 1.6 | -49.6 | 4.5 |
| **Mean GM1-8** | | **3** | **5.5** | **-51.8** | **5.2** |
| GM1-9-1A(C1) | 450-575 THD(P) | 6 | 263.4 | 35.1 | 3.4 |
| GM1-9-1A(C2) | RT-400 THD(P) | 8 | 354.9 | -58.6 | 2.1 |
| GM1-9-1B(C1) | 400-575 THD(P) | 8 | 268.8 | 35.1 | 4.4 |
| GM1-9-1B(C2) | RT-250 THD(P) | 6 | 6.2 | -60.1 | 1.8 |
| GM1-9-2B(C1) | 400-550 THD(P) | 5 | 278.8 | 29.6 | 4.9 |
| GM1-9-2B(C2) | 50-400 THD(P) | 6 | 7.9 | -62.8 | 1.9 |
| GM1-9-3B(C1) | 400-575 THD(P) | 5 | 276.3 | 37.7 | 5 |
| GM1-9-3B(C2) | 50-350 THD(P) | 7 | 358.4 | -63.7 | 3.9 |
| GM1-9-4A(C2) | 2.5-65mT AFD | 8 | 359.8 | -56 | 1.5 |
| GM1-9-4B(C1) | 400-575 THD(P) | 8 | 268.5 | 37 | 8.2 |
| GM1-9-4B(C2) | 50-350 THD(P) | 7 | 5.2 | -61.5 | 1.6 |
| Mean GM1-9C1 | | **5** | **271.6** | **34.7** | **5.5** |
| **Mean GM1-9C2** | | **6** | **1.9** | **-60.5** | **3.1** |
| GM1-10-1A | 100-550 THD | 8 | 22.1 | -52.6 | 1.8 |
| GM1-10-1B | 100-500 THD(P) | 9 | 26.3 | -53.1 | 2.3 |
| **Mean GM1-10** | | **2** | **24.2** | **-52.9** | **5.6** |
| GM1-11-1A | 400-575 THD(P) | 7 | 294.7 | 27.2 | 1.5 |
| GM1-11-1B | 400-580 THD | 5 | 298.7 | 29.3 | 1 |
| GM1-11-2A | 400-580 THD | 5 | 301.1 | 31.4 | 1.8 |
| GM1-11-2B | 400-575 THD(P) | 7 | 293.8 | 30.3 | 1.2 |
| **Mean GM1-11** | | **4** | **297** | **29.6** | **3.9** |
| **Site Mean** | | **12** | **1.5** | **-55.9** | **3.3** |
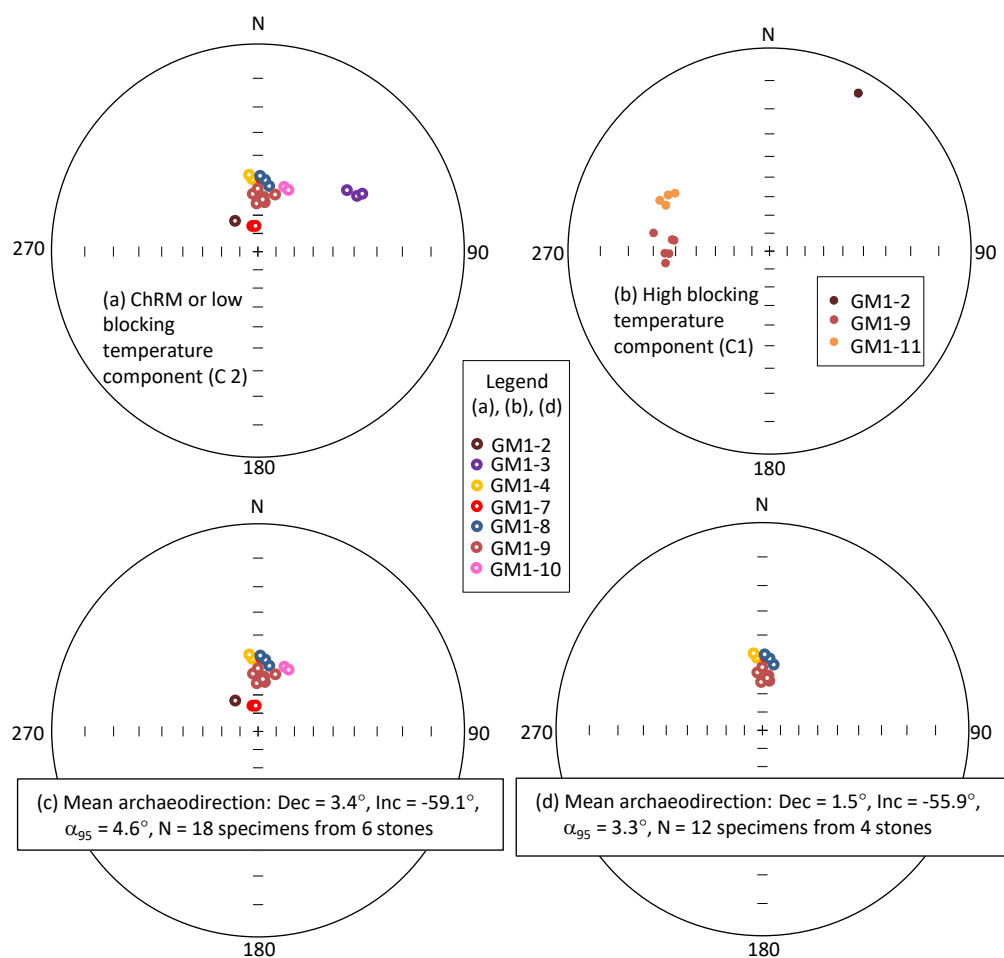
Figure 4.12. Stereographic projection of directional data of each specimen listed in Table 4.6. (a) Low blocking temperature component (C2), (b) high blocking temperature component (C1), (c) mean archaeodirection of 18 specimens from six stones, and (d) mean archaeodirection of 12 specimens from four stones.

## 4.5.2. GM2

Nine specimens were measured to obtain directional data from five hangi stones from site GM2. GM2 stones are magnetically stronger than those from GM1, having NRMs in the range 1-30A/m. A VRM component is removed during the initial demagnetization steps. Zijderveld and decay plots of GM2-1-4B show that the specimen has two components of magnetization with $T_{BS}$ below and above 350°C (Figure 4.13 (a)). The grains of stones GM2-3, GM2-4 and GM2-5 unblock above 200°C (Figure 4.13 (c), (d) & (e)). The remanence of stones GM2-3 and GM2-5 also consists of two components. GM2-2 and GM2-4 have a single stable component of magnetization. GM2-2-1A (Figure 4.13 (b)) demagnetized completely above 620°C, whereas all other specimens lost all magnetization in the temperature range of 575 to 600°C, showing the presence of titano-magnetite and titanomaghemite. The directional data of the five stones is not consistent. Therefore, the average directional data of the site is not calculated. Mean directions are calculated for each stone having a stable component of magnetization from thermal demagnetization and palaeointensity experiments, and are summarized in Table 4.7. Some plots were curved and it was impossible to isolate individual components of magnetization. The stereographic projection of the directional data from each specimen of site GM2 is shown in Figure 4.14.
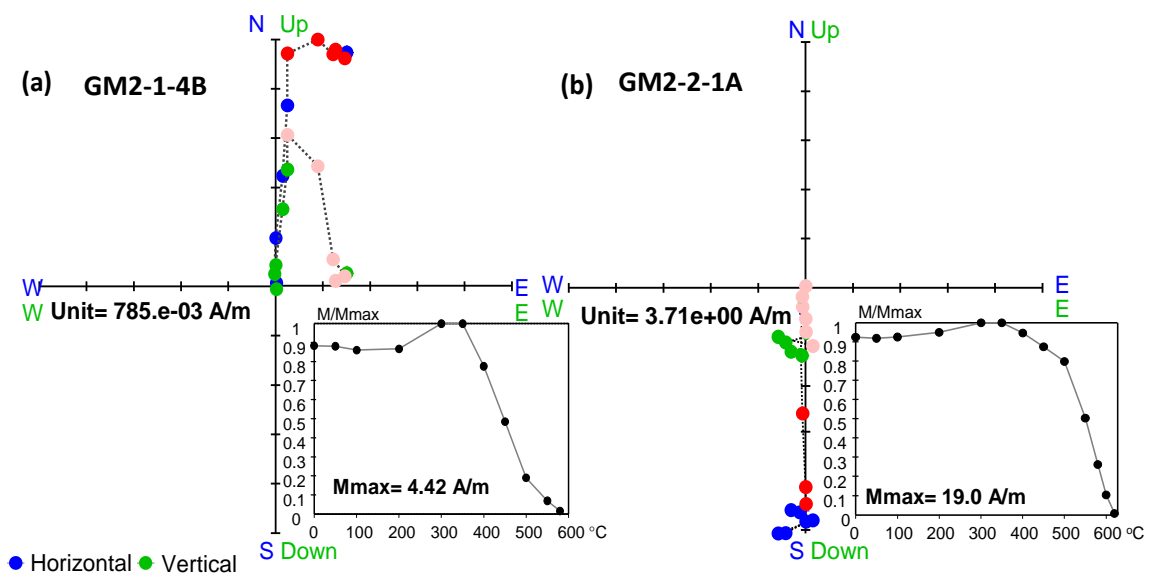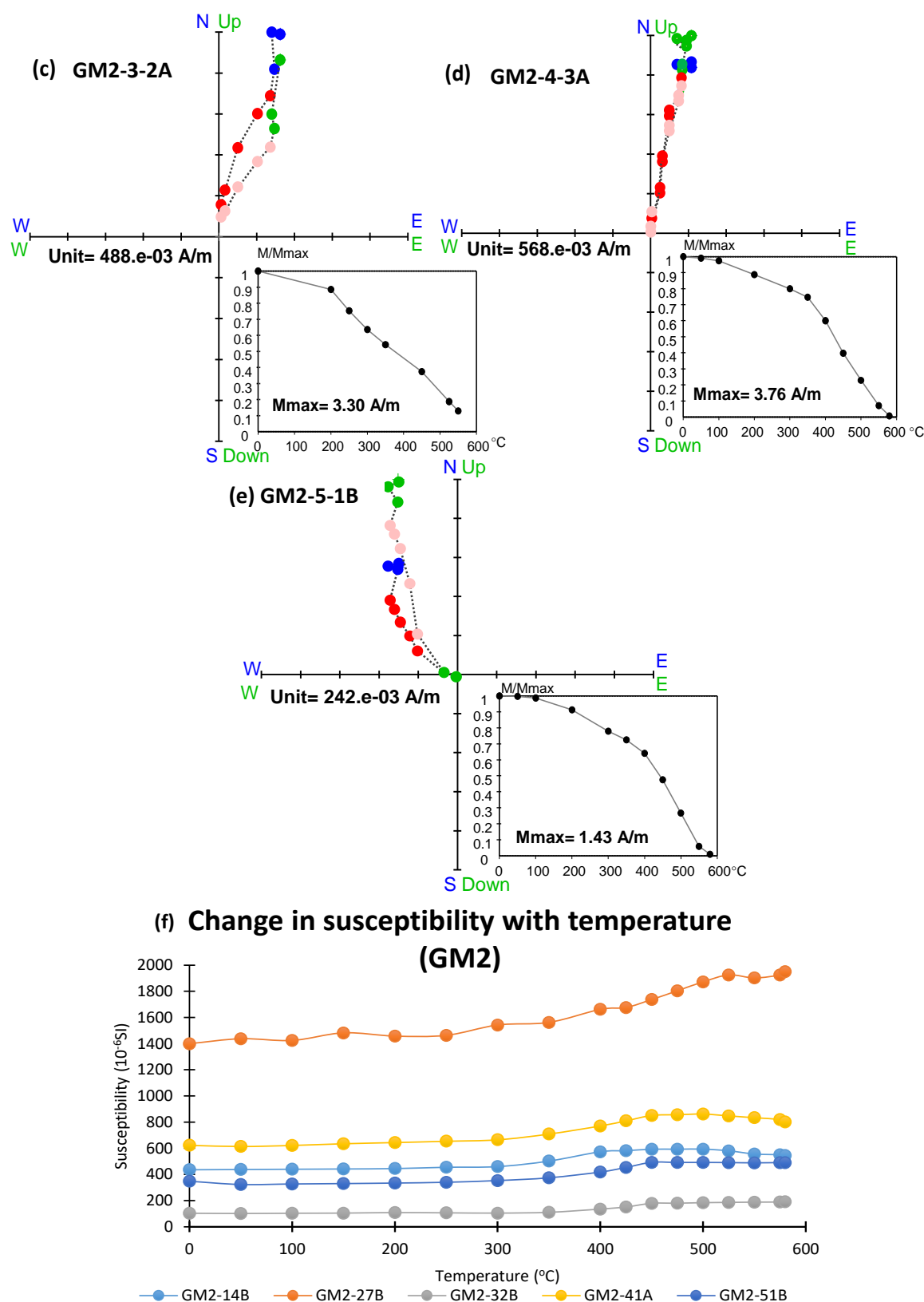
Figure 4.13. Thermal demagnetization results of typical specimens from stones GM2-1, GM2-2, GM2-3, GM2-4 and GM2-5. For each specimen, the Zijderveld plot and the intensity decay plot are shown. Red and pink coloured dots indicate the data points included for PCA. (f) Change in susceptibility of specimens with increase in temperature during stepwise progressive thermal demagnetization.

Table 4.7. Directional data of specimens from hangi site GM2, calculated from thermal demagnetization (THD) data. C1 is the high blocking temperature component, and C2 the low blocking temperature component of magnetization. N is number of specimens and n is data points used for calculations. Calculations made using Remasoft30 software. RT indicates room temperature.

| Sample ID | Temp range (°C) | N or n | Dec (°) | Inc (°) | MAD/$\alpha_{95}$ (°) |
|---|---|---|---|---|---|
| GM2-1-4B(C1) | 350-580 THD | 6 | 3.1 | -34.2 | 1.7 |
| GM2-1-4B(C2) | RT-350 THD | 6 | 89.2 | 67.7 | 4.9 |
| GM2-2-1A | 300-600 THD | 8 | 182.6 | 11.2 | 3.1 |
| GM2-2-2B | 400-550 THD (P) | 6 | 183.5 | 18.4 | 2 |
| GM2-2-3B | 400-600 THD | 6 | 184.2 | 17.3 | 1.6 |
| GM2-2-4B | 400-550 THD(P) | 6 | 184.1 | 16.3 | 2.3 |
| GM2-2-6A | 450-600 THD(P) | 6 | 187.6 | 17.1 | 2.4 |
| GM2-2-7A | 475-600 THD(P) | 6 | 190.3 | 17.5 | 1.9 |
| GM2-2-7B | 475-600 THD(P) | 6 | 187.8 | 15.7 | 3.7 |
| **Mean GM2-2** | | **7** | **185.7** | **16.2** | **2.7** |
| GM2-3-1A | 200-550 THD (P) | 8 | 12.2 | -28.1 | 2 |
| GM2-3-1B | 350-550 THD(P) | 5 | 10.8 | -30 | 2 |
| GM2-3-2A | 300-550 THD(P) | 5 | 18.4 | -30 | 3.7 |
| GM2-3-2B | 350-580 THD | 6 | 17.2 | -34.8 | 2.3 |
| **Mean GM2-3** | | **4** | **14.6** | **-30.8** | **4.9** |
| GM2-4-1A | 200-580 THD | 8 | 6.1 | -43.6 | 3.1 |
| GM2-4-1B | 300-550 THD(P) | 8 | 19.6 | -43.5 | 2.7 |
| GM2-4-2A | 350-550 THD(P) | 7 | 12.7 | -50.2 | 1.6 |
| GM2-4-3A | 100-580 THD | 9 | 11.7 | -44.4 | 2.4 |
| GM2-4-3B | 100-575 THD(P) | 12 | 18.1 | -47.3 | 2 |
| **Mean GM2-4** | | **5** | **13.6** | **-45.9** | **4.5** |
| GM2-5-1A | 300-475 THD(P) | 5 | 314.6 | -62 | 5.1 |
| GM2-5-1B | 300-500 THD | 5 | 311.2 | -65 | 3.1 |
| **Mean GM2-5** | | **2** | **313** | **-63.5** | **7.3** |
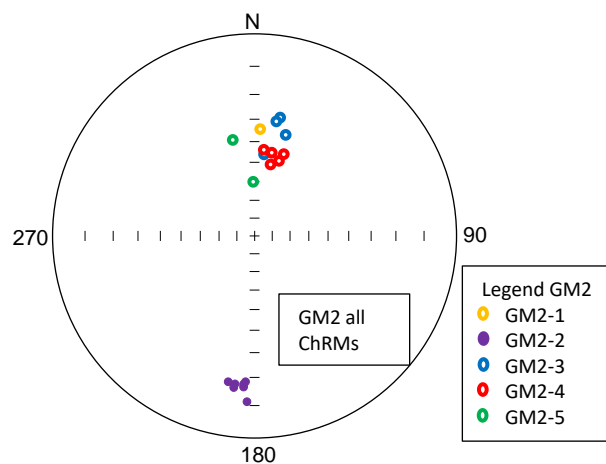


Figure 4.14. Stereographic projection of directional data of each specimen listed in Table 4.7.

### 4.5.3. GM3

Six specimens from three stones, GM3-1, GM3-3 and GM3-4, were thermally demagnetized. GM3 stones have NRMs in the range 1.0-8.0 A/m. The specimens lost their magnetization completely between 580 and 600°C (Figure 4.15). This is consistent with the results of the Curie temperature experiments, which show the presence of Ti-poor titano-magnetite or titanomaghemite.

Stone GM3-1 has a single direction of magnetization (Figure 4.15 (a)). However, it unblocks in two intervals, below and above 300°C, showing the presence of two magnetic minerals, a Ti-rich and a Ti-poor titanomagnetite.

Two components of magnetization in GM3-3-1A are isolated below and above 500°C (Figure 4.15 (b)). Neither component lies in a direction likely to reflect the palaeomagnetic field.

In GM3-4-4A, the magnetization vectors up to 450°C are not isolated clearly, and remaining vectors head towards origin (Figure 4.15 (c)). Other specimens from stone GM3-4 show the presence of a single component of magnetization. The susceptibility of GM3-3 starts increasing after heating to 300°C, whereas the susceptibility of GM3-1 and GM3-4 remains almost stable. The stereographic projection of directional data from each specimen is shown in Figure 4.16 (a). The averaged directional data calculated for the site from stones GM3-1, GM3-3 and GM3-4 is: Dec = 6.1°, Inc = -57.3°, $\alpha_{95}$ = 2.4° and N = 8 (Table 4.8 and Figure 4.16b).
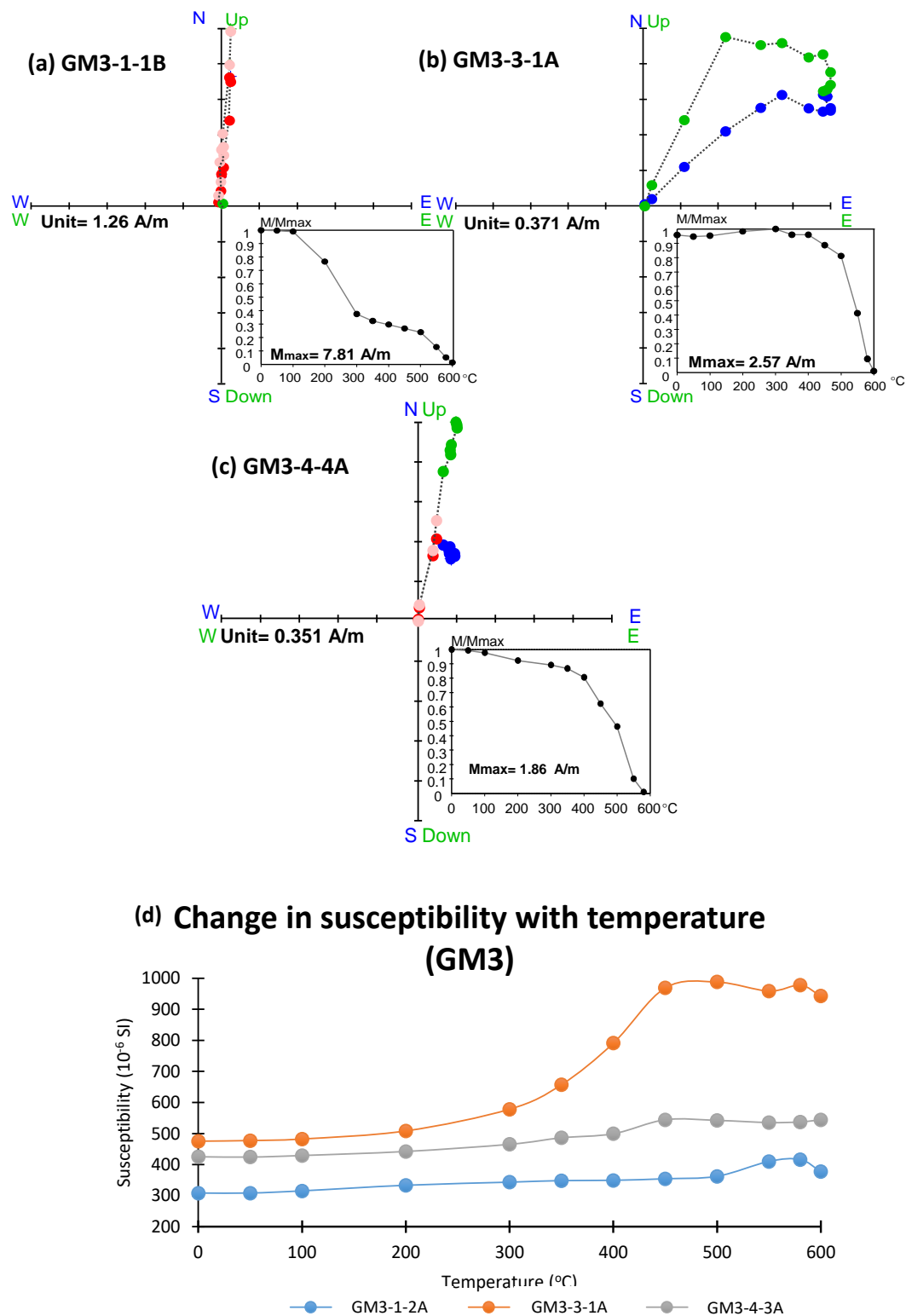
Figure 4.15. GM3 Thermal demagnetization results of typical specimens from stones GM3-1, GM3-3, and GM3-4 (a)-(c). For each specimen, the Zijderveld plot and the intensity decay plot are shown. Red and pink coloured dots indicate the data points included for PCA. (f) Change in susceptibility of specimens with increase in temperature during stepwise progressive thermal demagnetization.

Table 4.8. Directional data of hangi site GM3, calculated from thermal demagnetization (THD). C1 is the high blocking temperature component, and C2 is the low blocking temperature component of magnetization. N is number of specimens and n is number of data points used for calculations. Calculations made using Remasoft30 software. RT indicates room temperature.

| Sample ID | Temp range (°C) | N or n | Dec (°) | Inc (°) | MAD/$\alpha_{95}$ (°) |
|---|---|---|---|---|---|
| GM3-1-1A | 100-550 THD(P) | 11 | 5.3 | -55.6 | 1.3 |
| GM3-1-1B | 50-580 THD | 10 | 3.6 | -55.9 | 2.9 |
| GM3-1-1C | 100-550 THD(P) | 11 | 3.4 | -55 | 1.6 |
| GM3-1-2A | 50-350 THD | 5 | 6.2 | -60.8 | 0.9 |
| GM3-1-2B | 100-400 THD(P) | 6 | 5.2 | -61.3 | 1.9 |
| GM3-1-2C | 100-400 THD(P) | 6 | 6.2 | -60.8 | 2.5 |
| **Mean GM3-1** | | **6** | **4.9** | **-58.2** | **2.6** |
| GM3-3-1A(C1) | 450-600 THD | 5 | 47.6 | -53.2 | 5.3 |
| GM3-3-1A(C2) | 100-400 THD | 5 | 110 | 31.7 | 9.8 |
| GM3-4-1A | 100-550 THD | 8 | 12.1 | -54.2 | 3.5 |
| GM3-4-1B | 250-550 THD(P) | 9 | 6.7 | -54.4 | 3.4 |
| GM3-4-2A | 350-550 THD | 5 | 10.2 | -35.3 | 2.7 |
| GM3-4-3A | 450-575 THD(P) | 6 | 9 | -42.7 | 2.6 |
| GM3-4-3B | 350-575 THD(P) | 9 | 7.7 | -43.9 | 0.9 |
| GM3-4-4B | 425-550 THD(P) | 6 | 5.1 | -42.7 | 2.2 |
| **Mean GM3-4** | | **2** | **9.4** | **-54.3** | **6.9** |
| **Mean GM3** | | **8** | **6.1** | **-57.3** | **2.4** |
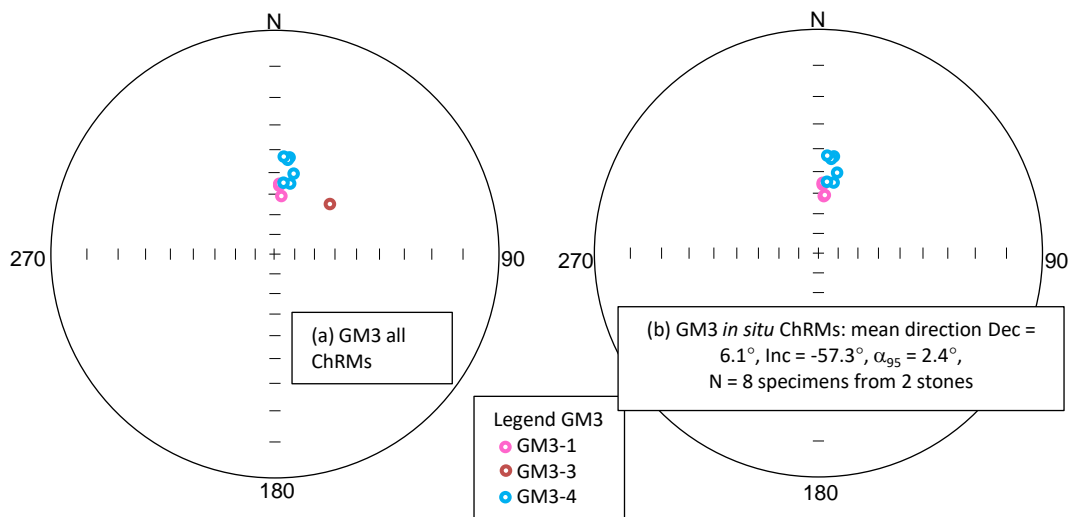


Figure 4.16. Stereographic projection of directional data of each specimen listed in Table 4.8. (a) ChRMs of all GM3 specimens, (b) mean archaeodirection of 8 specimens from two stones.

## 4.6. Archaeointensities

### 4.6.1. GM1

To determine the archaeointensity of site GM1, 19 specimens were chosen from six stones, GM1-2, GM1-3, GM1-8, GM1-9, GM1-10 and GM1-11. The intensity data and Zijderveld plots of one specimen from each stone are shown in Figure 4.15. It has already been observed from demagnetization results (Figure 4.11) that some hangi stones (GM1-2, GM1-3 and GM1-9) carry more than one component of magnetization. Intensity data of those samples is analyzed using Yu and Dunlop's (2002) palaeointensity determination method. Archaeointensities of GM1-8, GM1-10 and GM1-11 are calculated using ThellierTool4.0 (Leonhardt et al., 2004). The experiments were continued until the specimens had lost 90% of their total remanent magnetization.

The Arai plot of GM1-2-1B (Figure 4.18 (a)) has scattered data points and it was not possible to fit a straight line through them. GM1-3-1A gives a higher intensity value than other specimens (Figure 4.15 (b)). Curie temperature and thermal demagnetization results show that thermal alteration takes place in the mineralogy of this sample upon heating at high temperature, so this is not included in the calculation of the site-mean intensity. The specimens from stones GM1-8, GM1-10 and GM1-11 (Figure 4.15 (c), (e), & (f)) provided high quality data and consistent intensity values (Table 4.9). Rock magnetic data has shown that these stones have high remanence, coercivity, and nearly SD grains, so the intensity calculated is reliable. The average archaeointensity of the site is 59.3 ± 2.2 µT. Most of the GM1-9 specimens give lower intensity values in comparison to other specimens. For these specimens, only a small, low temperature range could be used to calculate intensity, due to the presence of two components of magnetization.
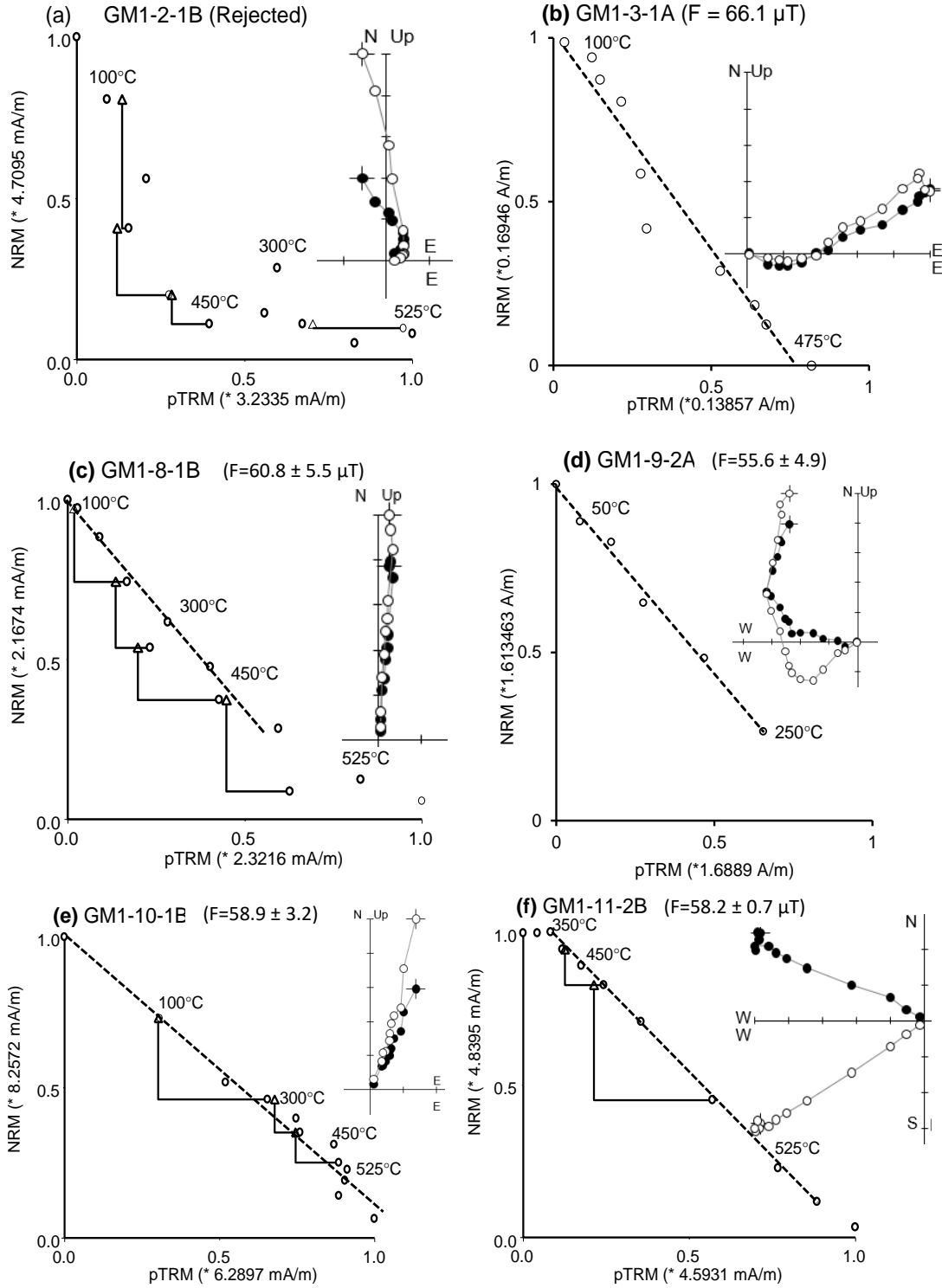
Figure 4.17. GM1 Arai diagrams obtained for specimens from stones GM1-2, GM1-3, GM1-8, GM1-9, GM1-10 and GM1-11, from manual calculations for specimens with two components of magnetization (GM1-3-1A, GM1-9-2A) following Yu and Dunlop (2002). Diagrams for specimens with a single component of magnetization (GM1-8-1B, GM1-10-1B, and GM1-11-1B) are calculated with ThellierTool4.0. Zijderveld diagrams are plotted using Remasoft30 software, and show demagnetization behaviour at each step.

Table 4.9. Archaeointensity results for hangi site GM1. 'F' are intensity results of individual specimens in µT. N is the number of data points included in linear segment of Arai plot. β, f, q, $\delta_{CK}$, $\delta_{pal}$, α, MAD, $\delta_{TR}$ and $\delta_{t*}$ are statistical parameters defined in Chapter 2. Acceptable results are represented in black font. Yellow and red font denote class B and class C criteria.

| Sample ID | Temp range (°C) | F ± σ (µT) | N | β | f | q | MAD | α | $\delta_{CK}$ | $\delta_{pal}$ | $\delta_{TR}$ | $\delta_{t*}$ | Class |
|---|---|---|---|---|---|---|---|---|---|---|---|---|---|
| Quality Criteria | | | ≥5 ≥5 --- | ≤0.1 ≤0.15 --- | ≥0.35 ≥0.35 --- | ≥5 ≥0 --- | ≤6 ≤15 --- | ≤15 ≤15 --- | ≤7 ≤9 --- | ≤10 ≤18 --- | ≤10 ≤20 --- | ≤99 ≤99 --- | TTA TTB TTC |
| GM1-3-1A | RT-475 | 66.1±12 | 10 | 0.09 | 1 | 10.2 | | | 12 | 0.2 | 3.9 | 11 | C |
| | | | | | | | | | | | | | |
| GM1-8-1A | RT-500 | 59.1±4.5 | 9 | 0.08 | 0.75 | 8.4 | 1.6 | 1 | 3.9 | 4.3 | 12.4 | 12.6 | B |
| GM1-8-1B | RT-475 | 60.8±5.5 | 9 | 0.09 | 0.75 | 7 | 1.9 | 2 | 4.7 | 11 | 13.4 | 0 | B |
| GM1-8-2A | RT-350 | 61.9±2.7 | 6 | 0.04 | 0.57 | 10.1 | 3.9 | 7.8 | 2.3 | 6.2 | 12.9 | 0.4 | B |
| GM1-8-3A | 100-525 | 58.2±2.1 | 10 | 0.04 | 0.87 | 21 | 3.1 | 3.7 | 5.8 | 7.1 | 15.5 | 8.24 | B |
| GM1-8-3B | RT-450 | 62.6±3.2 | 8 | 0.05 | 0.64 | 10.7 | 4.5 | 10 | 5.4 | 13 | 13.5 | 0 | B |
| Mean GM1-8 | | 60.5±2.1 | | | | | | | | | | | |
| GM1-9-1A | RT-250 | 54.2±5.1 | 6 | 0.05 | 0.73 | 11.9 | | | 1.8 | 0.0 | 4.9 | | A |
| GM1-9-1B | RT-250 | 52.8±3.5 | 6 | 0.03 | 1 | 21.1 | | | 5.2 | 0.1 | 6.8 | | A |
| GM1-9-2A | RT-250 | 55.6±4.9 | 6 | 0.04 | 0.73 | 14.6 | | | 2.2 | 0.0 | 5.7 | | A |
| GM1-9-2B | RT-350 | 52.8±4.6 | 8 | 0.04 | 1 | 19.2 | | | 11 | 0.1 | 10.1 | | C |
| GM1-9-3B | RT-250 | 53.3±3.0 | 6 | 0.03 | 1 | 25.6 | | | 3.4 | 0.0 | 1.0 | | A |
| GM1-9-4B | 50-400 | 50.3±1.7 | 8 | 0.02 | 1 | 48 | | | 0.7 | 0.2 | 20.7 | | c |
| Mean GM1-9 | | 53.2±2.0 | 6 | | | | | | | | | | |
| GM1-10-1B | RT-550 | 58.9±3.2 | 12 | 0.05 | 0.9 | 13.9 | 2.7 | 2.7 | 1.9 | 0.4 | 5.7 | 2.9 | A |
| GM1-11-1A | 425-525 | 58.1±0.3 | 5 | 0.01 | 0.62 | 76 | 2.1 | 1.8 | 2.6 | 0.2 | 0.1 | 2.2 | A |
| GM1-11-2B | 325-550 | 58.2±0.7 | 8 | 0.01 | 0.81 | 53 | 1.3 | 1.6 | 3.1 | 3.9 | 0.5 | 3.2 | A |
| Mean GM1-11 | | 58.2±0.1 | 2 | | | | | | | | | | |
| Site Mean | | 59.3±2.2 | 9 | | | | | | | | | | |

## 4.6.2. GM2

Arai and Zijderveld plots of specimens GM2-1-1C, GM2-2-7B, GM2-3-2A, GM2-4-3B and GM2-5-1A are shown in Figure 4.16 (a)–(e). Archaeointensity experiments were carried out on 24 specimens. Stones GM2-1, GM2-3 and GM2-5 have two components of magnetization (Figure 4.16 (a), (c) & (e)) – specimens from these did not meet selection criteria due to high MAD (Table 4.10) and failure of pTRM checks. The specimens of these stones are analyzed using Yu and Dunlop's (2002) method. GM2-1-1C is shown in Figure 4.16 (a). GM2-1 looks like a stone that has been disturbed and turned several times during the cooling process. However, because the field strength in which it was cooled has remained stable, it is still possible to extract a palaeointensity from a suitable

sequence of steps, despite there being no useful directional information.  The intensity values which are lying in quality criteria TTB/TTC, and consistent with the high-quality specimen results, are also accepted and included in the calculation of the site's mean intensity. GM2-2-7B and GM2-5-1A (Figure 4.16 (b) & (e)) pass pTRM and tail checks at low-temperature steps, but give high intensity values with thermal alterations occurring at high temperatures, so the results of these specimens are rejected. The results of these specimens are dependent on temperature ranges – if the temperature range is reduced, they provide lower intensity values. GM2-2 is quite different from the other stones of the site. It is stronger, and it does not fully demagnetize until well above 580°C. The Arai plots are not of good quality as the mineralogy has been altered and there may be some CRM on top of the TRM, which would invalidate the assumptions of the Thellier palaeointensity method. GM2-2-7B is the only one of eight specimens for which there is any chance of getting a result. The average archaeointensity of 11 specimens is 54.1 ± 2.2 µT. The Intensity data for each specimen is summarized in Table 4.9 (see page 97).



**(a)** GM2-1-1C (F= 54.2 µT)

**(b)** GM2-2-7B   (F=62.3 ± 8.2 µT)

**(c)** GM2-3-2A    (F=51.9 ± 5.5 µT)

**(d)** GM2-4-3B    (F=54.6 ± 4.9 µT)
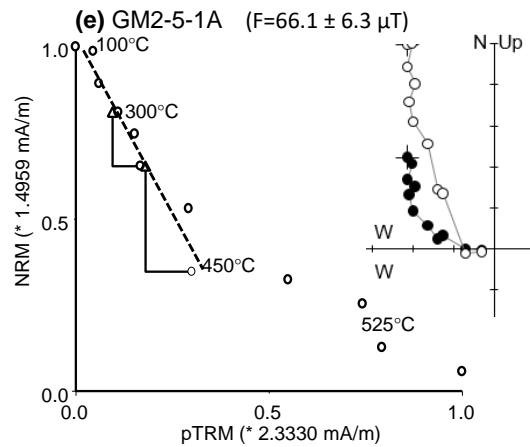
Figure 4.18. GM2 Arai diagrams obtained from specimens of stones GM2-1, GM2-2, GM2-3, GM2-4 and GM2-5, from manual calculations for specimens with two components of magnetization following Yu and Dunlop (2002) and using Thellier Tool. Zijderveld diagrams, plotted using Remasoft30 software, show demagnetization behaviour at each step.

Table 4.10. Archaeointensity results measured for hangi site GM2. F are intensity results of individual specimens in µT. N is the number of data points included in linear segment of Arai plot. β, f, q, $\delta_{CK}$, $\delta_{pal}$, α, MAD, $\delta_{TR}$ and $\delta_{t*}$ are statistical parameters defined in Chapter 2. Acceptable results are represented in black font. Yellow and red font denote class B and class C criteria.

| Sample ID | Temp range °C | F ± σ (µT) | N | B | F | q | MAD | α | $\delta_{CK}$ | $\delta_{pal}$ | $\delta_{TR}$ | $\delta_{t*}$ | Class |
|---|---|---|---|---|---|---|---|---|---|---|---|---|---|
| Quality Criteria | | | ≥5 ≥5 --- | ≤0.1 ≤0.15 --- | ≥0.35 ≥0.35 --- | ≥5 ≥0 --- | ≤6 ≤15 --- | ≤15 ≤15 --- | ≤7 ≤9 --- | ≤10 ≤18 --- | ≤10 ≤20 --- | ≤99 ≤99 --- | TTA TTB TTC |
| GM2-1-1A | 300-575 | 36.9±2.7 | 10 | 0.07 | 0.73 | 8.5 | 16.1 | 11.5 | 2.3 | 0.27 | 2.7 | 1.7 | B |
| GM2-1-1C | RT-475 | 54.2±3.0 | 12 | 0.03 | 1 | 29.2 | | | 4 | 0.12 | 7.5 | 5.5 | A |
| GM2-1-2A | 300-450 | 43.1±2.9 | 5 | 0.07 | 0.35 | 3.8 | 19.1 | 33.6 | 3.9 | 6.9 | 2.2 | 7.7 | B |
| GM2-1-2C | 150-450 | 55.0±2.0 | 8 | 0.04 | 0.76 | 17.4 | 7.8 | 12.7 | 5 | 2.8 | 14.5 | 4.2 | B |
| GM2-1-3A | 250-525 | 52.2±5.1 | 9 | 0.1 | 0.54 | 4.6 | 8.4 | 8.8 | 4.4 | 13.4 | 3.1 | 10 | B |
| GM2-1-4A | 300-525 | 50.6±2.0 | 8 | 0.04 | 0.52 | 11.2 | 9.6 | 2.6 | 4 | 8.8 | 2.5 | 1 | B |
| Mean GM2-1 | | 53.0±2.3 | 4 | | | | | | | | | | |
| GM2-2-7B | 400-550 | 62.3±8.2 | 7 | 0.13 | 0.59 | 3.3 | 10.2 | 5 | 9.7 | 4.1 | 4.2 | 5.3 | C |
| GM2-3-1A | 200-525 | 56.7±7.6 | 7 | 0.13 | 0.58 | 3.4 | 2 | 1.3 | 8.5 | 21.7 | 2.4 | 4.5 | C |
| GM2-3-1B | 200-525 | 52.0±5.4 | 8 | 0.1 | 0.61 | 4.9 | 4.9 | 6.3 | 7.5 | 10.9 | 5.7 | 3.7 | B |
| GM2-3-2A | RT-500 | 51.8±5.4 | 10 | 0.11 | 0.66 | 5.4 | 5.4 | 7.9 | 6.9 | 0.11 | 5.1 | 4.5 | A |
| Mean GM2-3 | | 53.5±3.9 | 3 | | | | | | | | | | |
| GM2-4-1B | 150-400 | 57.1±11.6 | 6 | 0.1 | 0.83 | 3.2 | | | 31.9 | 0.48 | 7.05 | | C |
| GM2-4-2A | RT-425 | 55.5±3.6 | 8 | 0.07 | 0.43 | 5.4 | 2.3 | 3.8 | 1.7 | 9.9 | 6.7 | 5 | A |
| GM2-4-3B | RT-425 | 54.6±4.8 | 8 | 0.09 | 0.46 | 4.1 | 3.6 | 10.1 | 3.2 | 4 | 6.4 | 5.2 | A |
| GM2-4-4A | 50-350 | 67.8±10.1 | 7 | 0.07 | 1 | 9.8 | | | 33.9 | 0.44 | 18.6 | | C |
| GM2-4-4B | 400-525 | 55.8±8.3 | 6 | 0.14 | 0.36 | 1.9 | 2.4 | 3.1 | 11.6 | 39.6 | 3.3 | 5.4 | C |
| Mean GM2-4 | | 55.8±1.3 | 4 | | | | | | | | | | |
| GM2-5-1A | RT-450 | 66.1±6.3 | 8 | 0.1 | 0.61 | 5.3 | 5.7 | 14.4 | 3 | 1.4 | 3.1 | 0.9 | A |
| Site Mean | | 54.1±2.2 | 11 | | | | | | | | | | |

## 4.6.3. GM3

Ten specimens from three stones, GM3-1, GM3-3 and GM3-4, were used to determine the archaeointensity for site GM3 (Figure 4.17 (a), (b), & (c)). The specimens of stone GM3-1 give high-quality intensity data (Figure 4.17 (a)). pTRM and tail checks are passed even at high-temperature steps. Although the Zijderveld plot of GM3-3-3A indicates the disturbance of this stone at 500°C, the intensity calculated below this temperature is comparable with intensity data for stone GM3-1. GM3-4 intensity data are calculated from room temperature up to 450°C. Seven specimens out of ten have provided consistent results, averaged to 59.1 ± 2.1 µT and summarized in Table 4.11. Rock magnetic properties suggest the presence of Fe-rich titanomagnetite and an assemblage of PSD grains in stone GM3-1, thus the accepted intensity values are reliable.
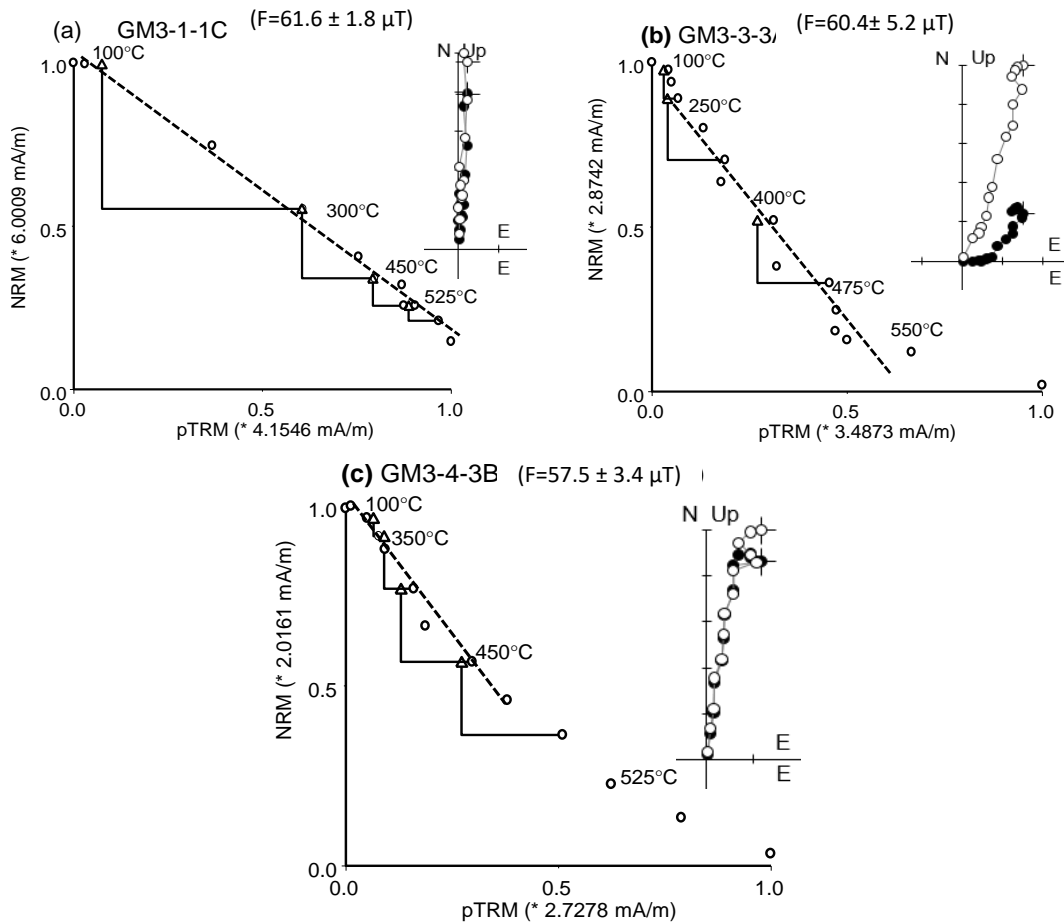


Figure 4.19. GM3 Arai diagrams obtained from specimens of stones GM3-1, GM3-3 and GM3-4 using Thellier Tool. Zijderveld diagrams, plotted using Remasoft30 software, show demagnetization behaviour at each step.

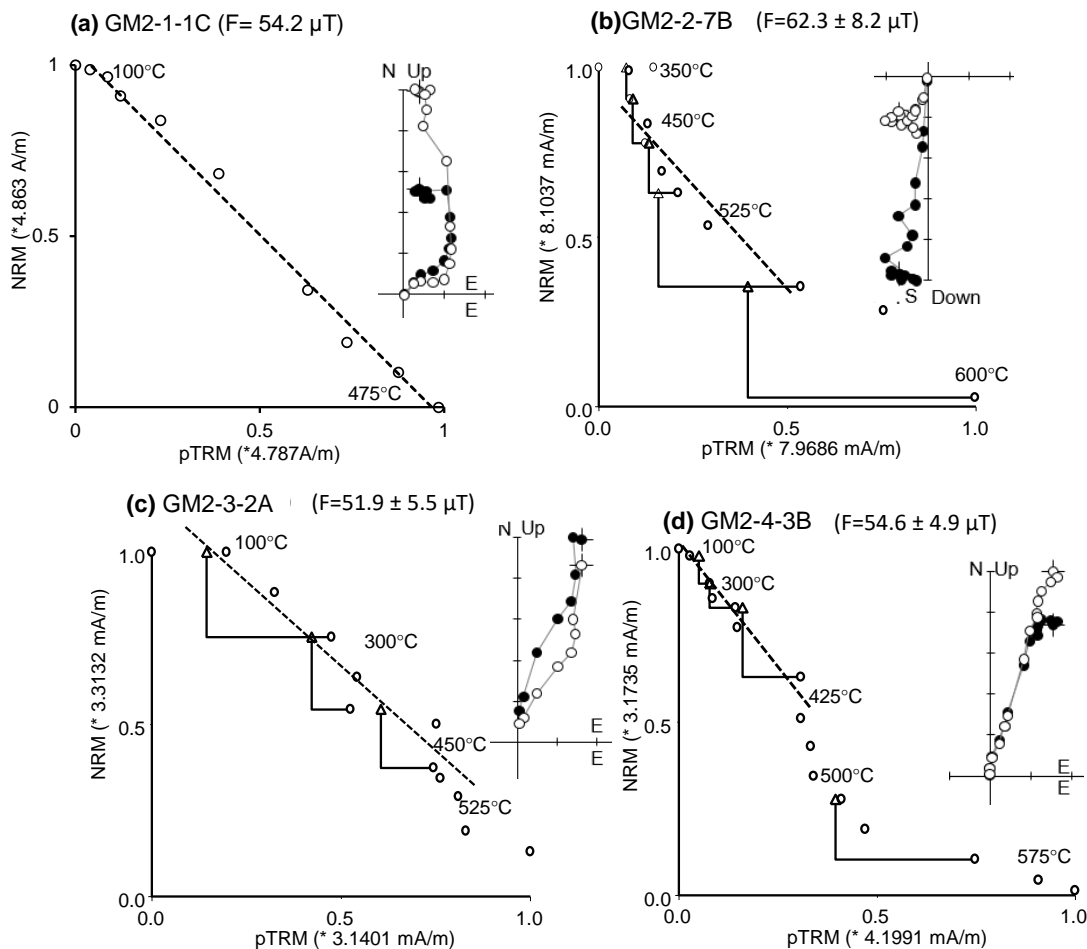Table 4.11. Archaeointensity results measured for hangi site GM3. F are intensity results of individual specimens in μT. N is the number of data points included in linear segment of Arai plot. β, f, q, $\delta_{CK}$, $\delta_{pal}$, α, MAD, $\delta_{TR}$ and $\delta_{t*}$ are statistical parameters defined in Chapter 2. Acceptable results are represented in black font. Yellow and red font denote class B and class C criteria.

| Sample ID | Temp range °C | F ± σ (μT) | N | B | F | q | MAD | α | $\delta_{CK}$ | $\delta_{pal}$ | $\delta_{TR}$ | $\delta_{t*}$ | Class |
|---|---|---|---|---|---|---|---|---|---|---|---|---|---|
| Quality Criteria | | | ≥5 ≥5 --- | ≤0.1 ≤0.15 --- | ≥0.35 ≥0.35 --- | ≥5 ≥0 --- | ≤6 ≤15 --- | ≤15 ≤15 --- | ≤7 ≤9 --- | ≤10 ≤18 --- | ≤10 ≤20 --- | ≤99 ≤99 --- | TTA TTB TTC |
| GM3-1-1A | 100-550 | 56.4±1.9 | 11 | 0.03 | 0.82 | 19.1 | 2.1 | 1.2 | 3.3 | 7.1 | 3.6 | 0 | A |
| GM3-1-1C | RT-525 | 61.6±1.8 | 11 | 0.03 | 0.82 | 23.3 | 2.6 | 2.4 | 3.9 | 5.7 | 4.6 | 3.9 | A |
| GM3-1-2A | RT-400 | 57.8±9 | 7 | 0.08 | 0.86 | 11.8 | | | 9.5 | 0.11 | 0.7 | | C |
| GM3-1-2C | RT-400 | 52.0±7.1 | 7 | 0.07 | 1 | 13.7 | | | 9.8 | 0.11 | 2.3 | | C |
| Mean GM3-1 | | 58.6±3.8 | 3 | | | | | | | | | | |
| GM3-3-2A | RT-450 | 53.7±7.0 | 11 | 0.07 | 1 | 13 | | | 15.5 | 0.17 | 17 | | C |
| GM3-3-3A | RT-475 | 67.9±4 | 11 | 0.05 | 0.76 | 11.1 | 3.6 | 7.6 | 7 | 13 | 12.2 | 9.5 | B |
| | | | | | | | | | | | | | |
| GM3-4-1B | RT-500 | 61.7±4.7 | 11 | 0.08 | 0.59 | 6.6 | 3.7 | 8.2 | 5.6 | 10.3 | 6.1 | 6 | B |
| GM3-4-3A | RT-475 | 60.2±3.8 | 9 | 0.06 | 0.51 | 6.7 | 3.4 | 7.8 | 4.3 | 0.7 | 8.3 | 3.3 | A |
| GM3-4-3B | 100-475 | 57.5±3.3 | 8 | 0.06 | 0.54 | 7.7 | 2.1 | 2.5 | 4.2 | 5.6 | 3.8 | 4.8 | A |
| GM3-4-4B | 100-500 | 58.5±5.8 | 10 | 0.01 | 0.53 | 5.4 | 4.7 | 9.3 | 2.9 | 1.36 | 8.2 | 6.2 | A |
| Mean GM3 | | 59.5±2.3 | 4 | | | | | | | | | | |
| Site Mean | | 59.1±2.1 | 7 | | | | | | | | | | |

# 4.7. Discussion

Site mean directions, interpreted as representing the magnetic field in which the stones cooled, was retrieved from hangi GM1 and GM3. The demagnetization results show that the GM2 stones were disturbed during cooling, probably due to raking of the hangi. In general, there are stones from three sites which had acquired more than one component of magnetization, and the lowest blocking temperature component was thus used for calculation of the site's mean data. The directional data, given in Tables 4.6-4.8, show that all specimens and stone averages meet the selection criteria: MAD ≤ 5° and $\alpha_{95}$ ≤ 10° (Figure 4.18). It is clear from the stereoplot that there are several stones GM1-2, GM1-3, GM1-7, GM1-9, GM2-1, GM2-5 and GM3-3 are outliers from the main cluster of the data points as the $\alpha_{95}$ of these stones are not in approximation of main cluster in the middle of the plot. The circles representing $\alpha_{95}$ of each specimen are either very close or intersect the $\alpha_{95}$ of other specimens of the same stone. Intensity data for

the three sites are listed in Tables 4.9-4.11. The averaged intensity data has a small standard deviation of ± 2μT.
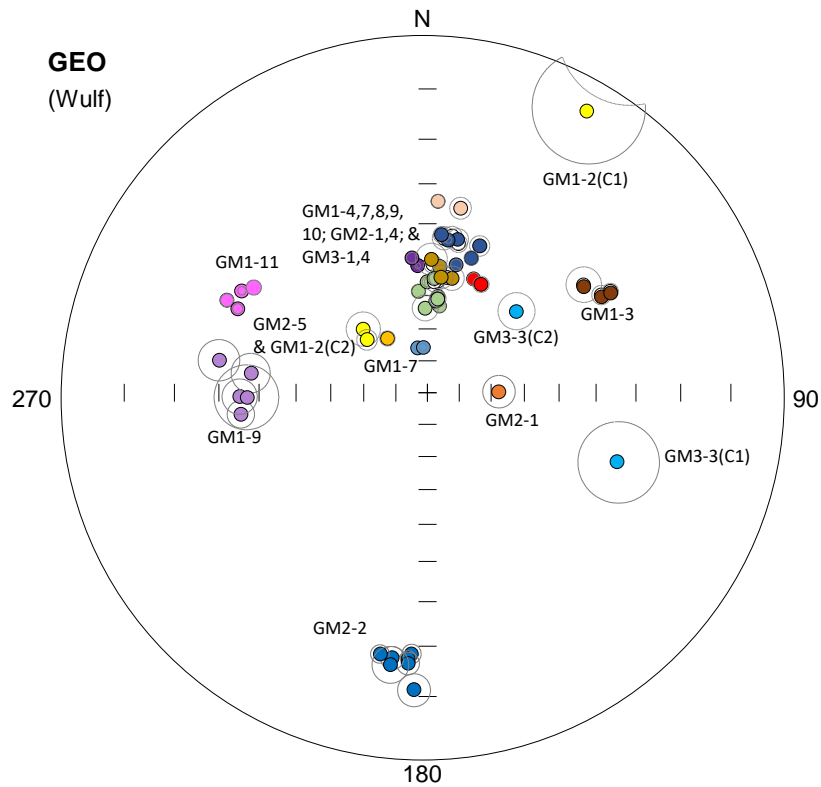


Figure 4.20. Stereographic plot of directions of hangi stones from sites GM1, GM2 and GM3. The data points of specimens from the same stone are shown in the same colour. Circles around the dots represent the maximum angular deviation for each specimen.

The directional data can be used for preliminary archaeomagnetic dating. The declination and inclination are compared with NZPSV1K (Turner et al., 2015) using the dating tool of Pavon-Carrasco et al., (2011). Average declination and inclination of the sites GM1 and GM3 give probability density functions of age range. Archaeomagnetic dating of the sites is determined from the combination of both probability density functions and suggest an age range of 1380-1587 AD for hangi GM1, and 1516-1647 AD for hangi GM3 (Figure 4.20 (a) & (b)). In comparison with the ^{14}C dates (Section 4.3) small portions in the probability density curves suggest GM1 and GM3 may have age ranges from 1516 to 1542AD and 1650 to 1675AD respectively. Archaeomagnetic dating results suggest that the sites are older if we compare the dates with radiocarbon dates. Figure 4.21 compares the mean archaeointensities of the sites GM1, GM2 and GM3 with field intensities calculated from the global geomagnetic field model *gufm*1 (Jackson et

al., 2000), at the location of Great Mercury Island (latitude/longitude ~ -36.6°S/ 175°E). For sites GM1 and GM3, the best age range is estimated using $^{14}$C and archaeomagnetic dating. GM2 has only a $^{14}$C age range as the directional data of stones sampled from this site is not consistent and cannot be used for archaeomagnetic dating.
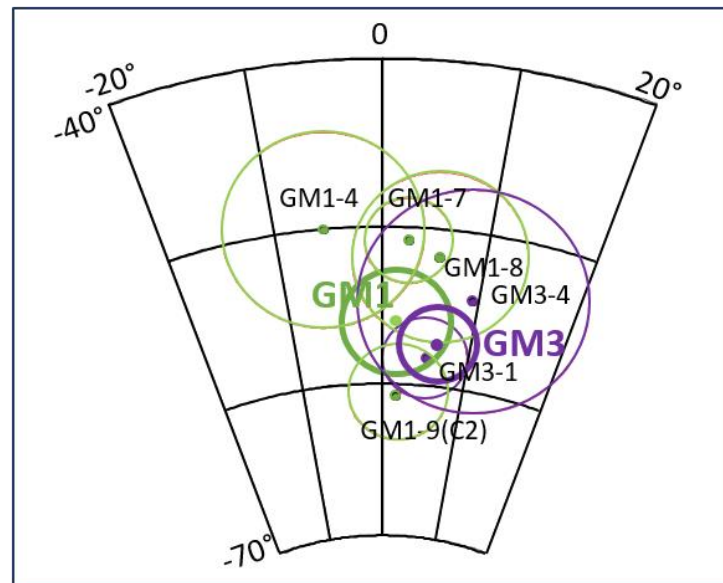


Figure 4.21. Equal angle projection of directional data of stones from sites GM1 and GM3. Purple and green dots indicate directional data used to calculate the mean direction of the stones from sites GM1 and GM3 respectively. Circles around the dots indicate the $\alpha_{95}$'s of the mean direction of each stone. Dots within bold circles indicate the mean directions of the sites GM1 and GM3.

(a)

Declination = 1.5°
Inclination = -55.9°
$\alpha_{95}$ = 3.3°
F = 59.3±2.2 µT
[14]C dating results: 1516-1542 AD (8.6% of area), 1625-1666 AD (86.3% of area)

Dating : GM1
Combining Probability Density Functions
Threshold = 0.0018998 (Confidence = 95%)
Between t = 1030AD and 1990AD
[1380AD   1587AD]

(b)

Declination = 6.1°
Inclination = -57.3°
$\alpha_{95}$ = 2.4°
F = 59.1±2.1 µT
[14]C dating results: 1650-1675 AD (31.6% of area), 1740-1798 AD (63% of area)

Dating : GM3
Combining Probability Density Functions
Threshold = 0.0016139 (Confidence = 95%)
Between t = 1030AD and 1990AD
[1516AD   1647AD]

Figure 4.22. Archaeomagnetic dating of sites GM1 and GM3. For archaeomagnetic dating and the comparison of directional data with reference curves, the directional data of GM1 and GM3 are relocated to the location for which the reference curve is used.

102

## 4.8. Conclusion

The Great Mercury Island directional data matches with NZPSV1k (Turner et al., 2015) and suggests an age range for the sites between 1500 and 1650AD, with hangi GM1 being older than GM3. Archaeointensity determinations on the GM hangi stones yielded a success rate of about 50% and did not show much variability in intensity values. Stones GM1-8, GM1-10, GM1-11, GM2-4 and GM3-1 provided high quality and reliable results. Archaeointensities of GM1 and GM3 are comparable, but the directional data have a noticeable difference. GM2 has slightly lower archaeointensity and an archaeodirection could not be obtained due to the evident disturbance of the stones during cooling. Archaeomagnetic data from all three sites, GM1, GM2 and GM3, has helped us classify the archaeological features according to their period of occupation. Archaeomagnetic dating helps in narrowing the age range of the hangi sites GM1 and GM3.
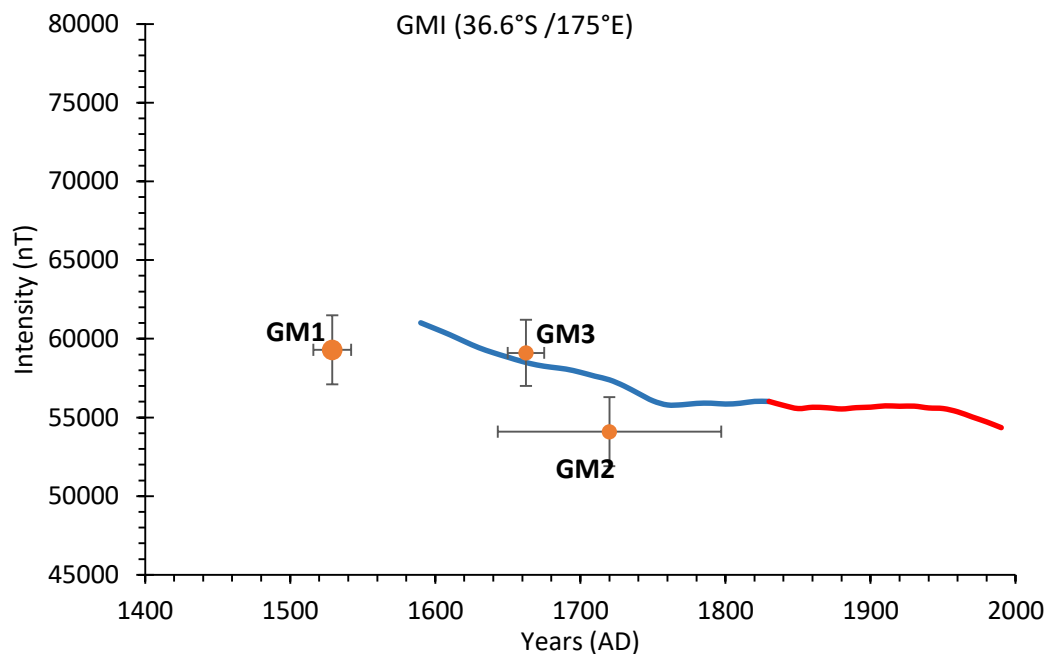


Figure 4.23. Geomagnetic field intensity at Great Mercury Island for the last 400 years, at latitude/ longitude ~36.6°S /175°E (Jackson et al., 2000). Orange dots show data from sites GM1, GM2 and GM3 with error bars showing standard deviations.

# 5. Weld Pass Hangi Sites

## 5.1. Archaeological Setting

The location of the Weld Pass archaeological sites is alongside State Highway 1 (S.H.1) between Blenheim and Seddon, approximately 1km south of Dashwood Pass. The geology of this area consists of mostly sandstones, mudstones, siltstones, quartzite, conglomerate and limestone (Figure 5.1).
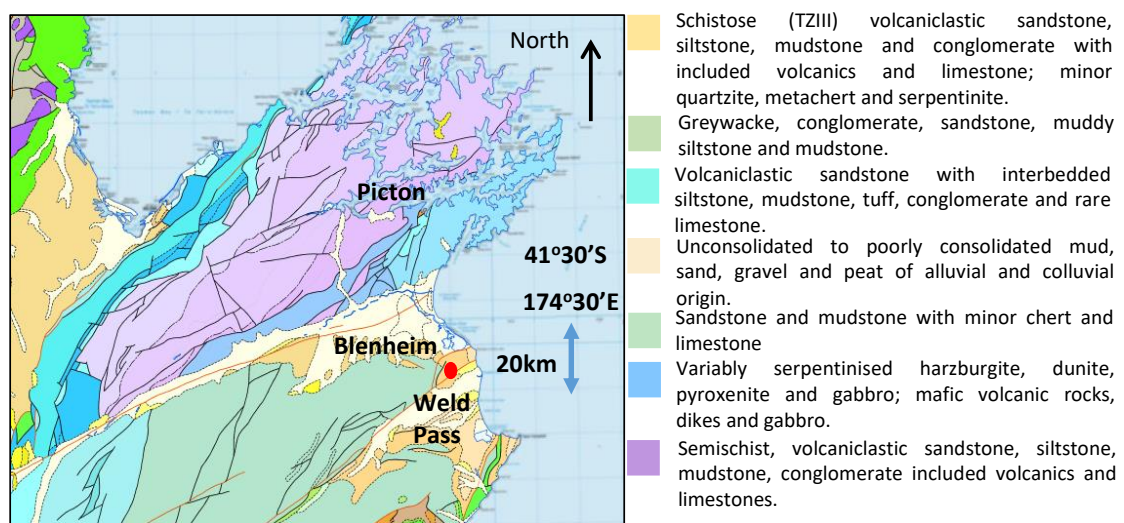


Figure 5.1. Geological map of Marlborough region. From GNS website (http://data.gns.cri.nz/geology/).

The Weld Pass hangi sites sampled for archaeomagnetic experiments (Archsite numbers P28/145,146) were discovered during roadside earthworks for modification of S.H.1 in January 2014, and described in an archaeological report by Foster (2014). The hangi sites were located between the existing line of S.H.1 and the railway track at latitude/ longitude 41°36'39''S/ 174°03'18'' (Figure 5.2 (b)).

### 5.1.1. Previous Records

Other archaeological sites in the area (P28/37, P28/49, and P28/50) were reported by Nevil Matthews in 1970 (Figure 5.2) and later recorded by Barry Brailsford in 1976 (Foster, 2014). These sites were located near the Weld/ Utawai overbridge, about 1.5km north from the area excavated in 2014 (see map Figure 5.2 (b)). Sites P28/37 and P28/50

are pit features with respective diameters of 4m and 2m, and depths of 1.5m and 1m – these could not be relocated in 2006 and 2011. Site P28/49 contained five pit features with an average diameter of 2m and an average depth of 1m (Figure 5.2 (b)). Four of these were relocated in 2011 and thought to be ovens, but were not sampled. Others might have been destroyed by the work on either the road or the railway.
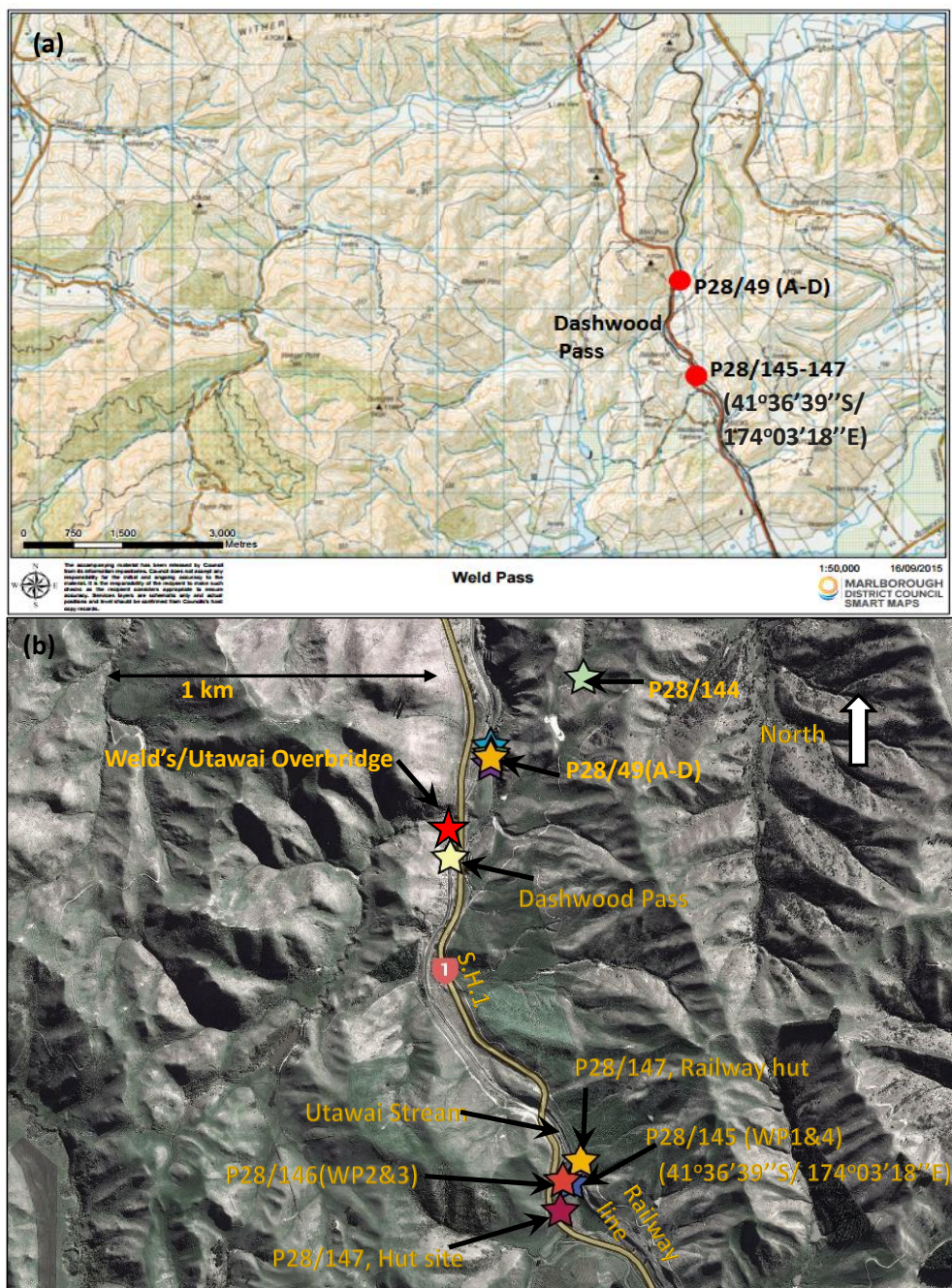


Figure 5.2. (a) Topographic map of Marlborough region (http://maps.marlborough. govt.nz/viewer). (b) Aerial photo of archaeological sites P28/49, P28/144, P28/145, P28/146) and P28/147 at Weld Pass. Photo downloaded from Google Earth, date of image 2010.

P28/144 is a cluster of three circular depressions in farmland, about 400m northeast of site P28/49 (shown in Figure 5.2 (a)), and which was already in records and relocated in 2014. The area about 500m south of Dashwood Pass was inspected in January 2014. These depressions, interpreted as *umu* (hangi), were large, being some 3m in diameter and 0.5-1m deep. This site was not sampled for our project as the sites were already destroyed. The significant archaeological features relevant to our study are described below and were recorded by archaeologist Deb Foster (Foster, 2014).

## 5.1.2. Site P28/145

A large-scale sketch map shows the road, railway track, stream, and the real positions of P28/145, 146, and the two parts of 147 (Figure 5.3). P28/145 is between S.H.1 and the railway line, about 1.5 km south of P28/49. It was found during stripping of topsoil. Several fire-scoops on both sides of Utawai Stream were excavated by archaeologist Deb Foster in the sites P28/145 and P28/146. Feature 1 (F1) a hangi located on the eastern side of Utawai Stream, contained a thick layer of fire-cracked stones with some charcoal. This hangi was sampled and labelled WP1. The fire-blackened sand was easily distinguished from the normal sand of the area (Figure 5.4 (a), Table 5.1). The diameter of the oven was about 3m and its depth 1m.
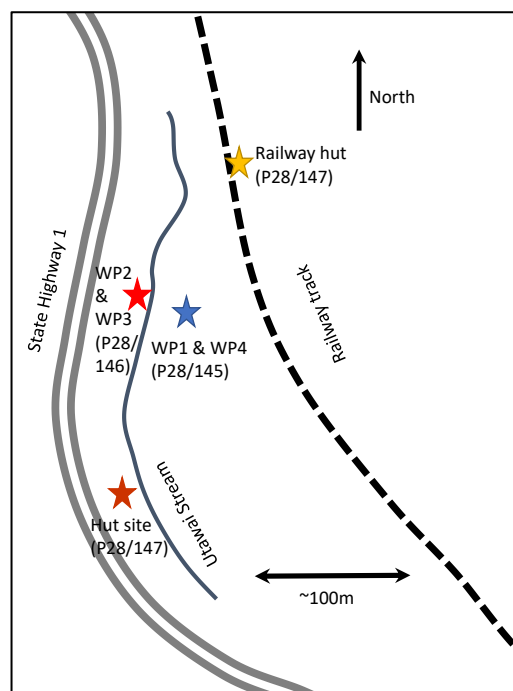


Figure 5.3. Sketch map showing the state highway, railway track, stream, and the relative positions of P28/145, P28/146 and the two parts of P28/147.
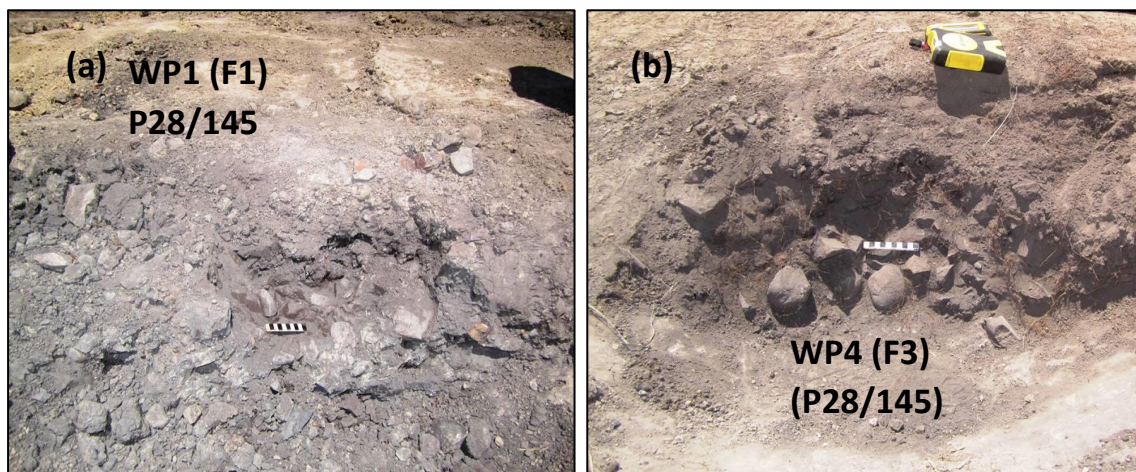
Figure 5.4. Arch site P28/145, (a) hangi WP1 (F1) before sampling. (b) Hangi site WP4 (F3), 3.2m northwest of WP1.

A second hangi F3, located 3.2m northwest of WP1, was labelled WP4, and was also sampled. This hangi, 1.25m diameter and 0.35m deep, was filled with reddened stones and lined with charcoal (Figure 5.4 (b)).

Other features discovered during earthworks were recorded by Deb Foster (Figure 5.5) (Foster, 2014). They included raked out stones, labelled F5 and F6, found around the pit, and indicating multiple uses of the hangi. About 7m northeast, a small chert flake and one dark grey argillite flake were found.
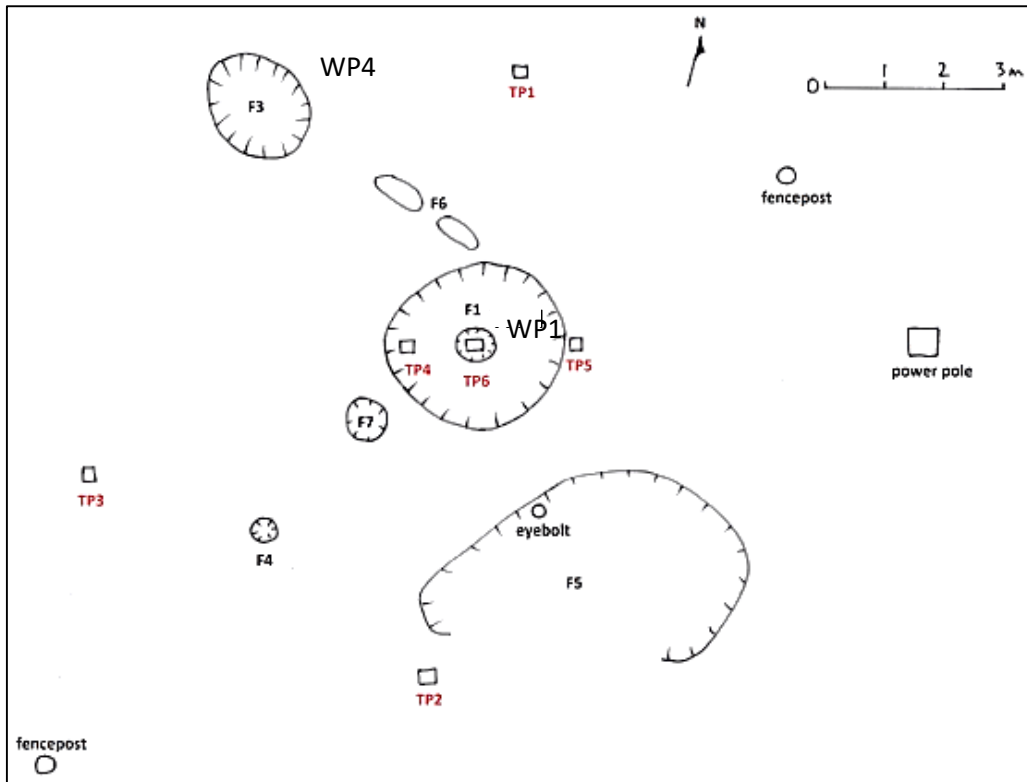
Figure 5.5. Plan of P28/145 ovens fire-scoops and rake-out. Original test pit sites (TP) are marked in red. Picture adapted from Foster, 2014. Features are labelled as F1, F3, F4, F5, F6 and F7. The sampled hangi is WP1 and WP4, features F1 and F3 respectively.

## 5.1.3. Site P28/146

ArchSite P28/146 is a hangi pit (F8) along with a fire-scoop (F9) about 30m northwest of P28/145 (on the west side of Utawai Stream) found during removal of topsoil. F8 was sampled and labelled as WP2 and F9 as WP3. The circular shaped hangi pit, WP2, had a diameter of 1.7m and a depth of 0.4m. The hangi was filled with fire-cracked stones, fire-blackened sand and a thin layer of charcoal below the stones (Figure 5.6). WP3, the fire-scoop located 9m north of WP2, had a diameter of 1m and a depth of 0.1m. The soil and rocks in the fire-scoop were blackened and mixed with some charcoal. There were only a few stones in the scoop compared to the hangi sites, while archaeologists suggested that the blackened sand and cracked rocks could be the waste of blasts done previously during preparation to mount power poles, railway ballast or a campfire used by railway workers (Foster, 2014 and Bruce McFadgen pers. comm.). The stones from this fire-scoop were not sampled.

Figure 5.6. Hangi site WP2 (F8) in Arch site area P28/146 on the western side of Utawai Stream.

## 5.1.4. Site P28/147

ArchSite P28/147 comprises two separate areas. The first was a rectangular area, measuring 9 x 7m, about 100m southwest of P28/145 (Figure 5.3), excavated during stripping of topsoil. The site contained a lot of nails, a melted glass bottle, a kerosene lamp and ceramics, suggesting it might be the footprint of a burnt-out hut, possibly used by a road worker. More artefacts (glass bottle fragments, a pair of rail wagon wheels, metal, fence wire and window glass) were found in a second area on the east side of the railway track at a distance of about 90m from WP1, suggesting the presence of another railway hut, although no signs of hut building could be located (Foster, 2014). The railway line across Weld Pass was built in 1890, and the artefacts are consistent with that period.

None of the sites at Weld Pass show what was cooked in the hangi, and there was no evidence which might relate the hangi sites to the huts. Wairau Bar, an important archaeological site that was a settlement in the early part of the prehistoric period, is only about 12km north of Weld Pass. It is possible the Weld Pass sites were used by people moving from the bar southwards, but there is no evidence of this. Charcoal

fragments were collected from each site sampled during our fieldwork for radiocarbon dating. The stones found in all hangi sites were lithified sandstones and may have been gathered from the Utawai Stream gullies. This source of stones could have attracted people to live around the stream (Foster, 2014).

Table 5.1. Features of Arch sites P28/145 and P28/146 sampled (Information based on Foster's 2014 report and field trip observations). GPS coordinates converted to NZTM (http://apps.linz.govt.nz/coordinate-conversion/index.aspx). No useful apriori age-control.

| Hangi site and Archsite no. | Foster's feature label | Age control | Features and comments | NZTM coordinates |
|---|---|---|---|---|
| WP1 (P28/145) | Feature 1 or F1 | NZA58797 See table 5.3 | A hangi, 3.2m diameter X 1m depth, containing fire-blackened soil and fire-cracked stones along some charcoal. | N5392891 E1687911 |
| WP4 (P28/145) | Feature 3 or F3 | --- | A hangi, 1.7m diameter X 0.4m depth filled with fire-blackened soil and fire-cracked stones. Charcoal lined at the bottom. | N5392891 E1687909 |
| WP2 (P28/146) | Feature 8 or F8 | --- | A hangi, 1.25m diameter X 0.35m depth filled with fire-cracked stones and charcoal. | N5392899 E1687880 |
| WP3 (P28/146) | Feature 9 or F9 | --- | Fire-scoop, 1m diameter X 0.10m deep. Not sampled. | N5392908 E1687880 |

## 5.2. Sampling

The three hangi sites, WP1, WP2 and WP3, at Weld Pass had all been excavated in 2014 before sampling. WP1, the largest site, was in an excavated rectangular-shaped area. The hangi lay along the southern wall of the excavated area. The stones from the very top of the hangi were not sampled as they had been laid on the sand and so were not *in situ*. The fire-blackened sand and stones beneath the very top stones, down to a depth of about 20cm, were sampled very carefully so that the other stones lower in the hangi were not disturbed. The stones were mostly cracked due to intense heating in the hangi and small in size (5-8 cm). Two stones, WP1-1 and WP1-2, were sampled first. After the removal of these stones, two more stones from the top 20cm, WP1-3 and WP1-4, were sampled, as shown in Figure 5.7 (b). The stones were tightly packed with sand and thought to be *in situ.* Four oriented stones with orientation marks of magnetic north and

sun bearing were sampled from hangi site WP1. None were found below the top 30cm of the site.

WP2, on the western side of Utawai Stream, had also been excavated before our arrival on the site. WP2 was about half the size of WP1. The fire-cracked stones and fire-blackened sand can be seen in Figure 5.8 (a). The stones in the hangi were abundant, but most were very small and not suitable for orienting. As with WP1, stones were sampled from the layer about 20cm below the ground surface. Four hangi stones (WP2-1, WP2-2, WP2-3 and WP2-4), each about 4-5 cm in size, were selected from the same layer for sampling and were removed without disturbing other stones in the hangi (Figure 5.8 (a)). The remaining stones in the hangi were more cracked and very small in size.
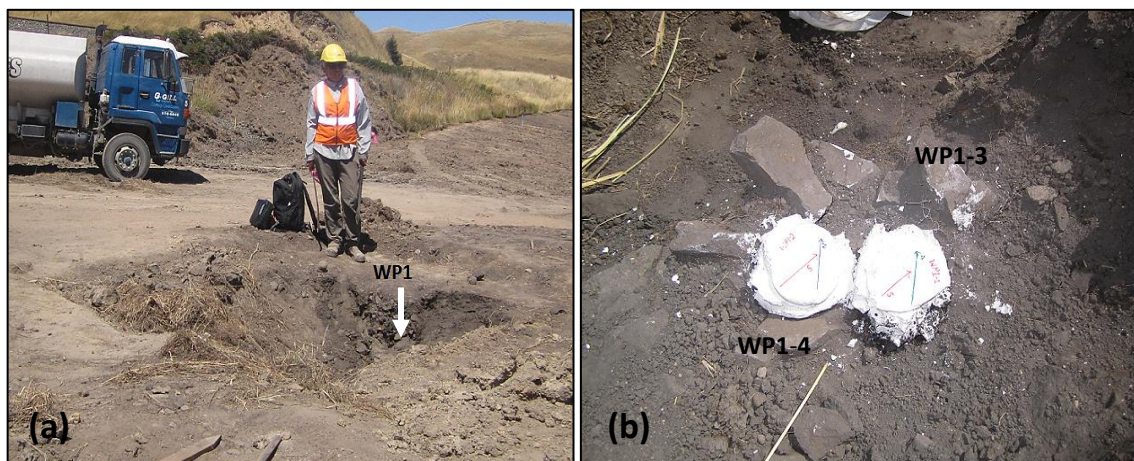


Figure 5.7. (a) Excavated hangi site WP1 in a rectangular pit. (b) The hangi stones WP1-1 and WP1-2 with poP caps and orientation marks. WP1-3 and WP1-4 are marked in black font and were sampled later.

WP3 was not sampled. The hangi site WP4, beside WP1, was sampled last. This hangi was smaller than WP1 (see dimensions in Table 5.1). Stones were sampled from the middle layer of the hangi. The reddened stones were tightly packed in the fire-blackened sand (so thought to be *in situ*) but less in quantity than the other two hangi sites. Four oriented stones (WP4-1, WP4-2, WP4-3 and WP4-4) were sampled without disturbing other stones (Figure 5.8 (b)).
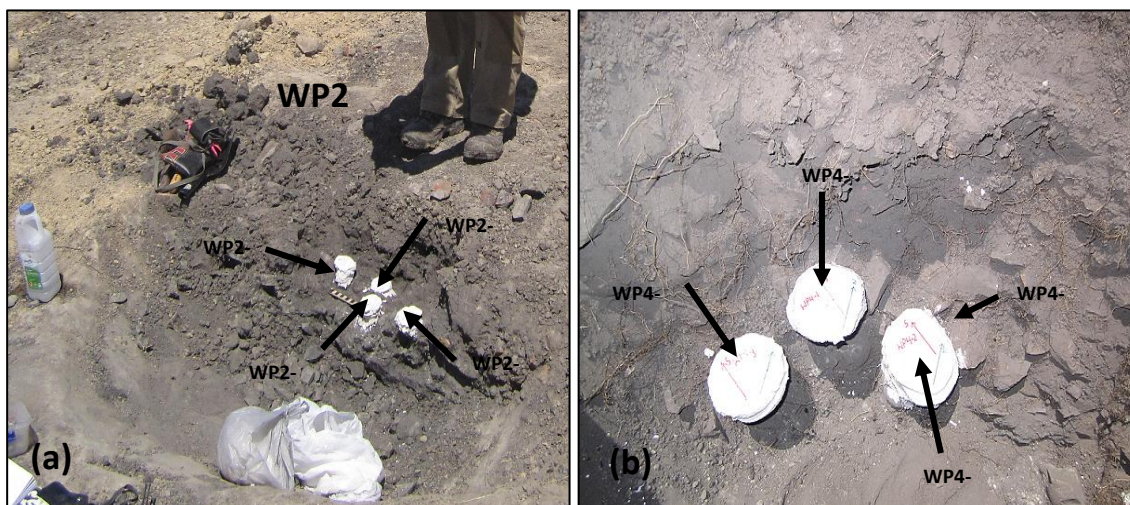
Figure 5.8. (a) Hangi site WP2, and four stones (WP2-1, WP2-2, WP2-3 and WP2-4) with POP caps and orientation labels. (b) Hangi site WP4, and three stones (WP4-1, WP4-2 and WP4-3) with poP caps and orientation labels. WP4-4 was sampled after the stones had been removed.

Altogether 12 oriented stones were sampled from three of the hangi sites at Weld Pass under the supervision of Dr Bruce McFadgen. The latitudes/ longitudes of each site were recorded using GPS. Some stones were drilled and cut into cylindrical specimens – other stones smaller in size were cut into cubes. Details of the samples and specimens obtained from each stone are given in Table 5.2.

Table 5.2. Detail of cores and specimens from each stone.

| Name of stone | Number of cores | Number of specimens |
|---|---|---|
| WP1-1 | 5 | 10 |
| WP1-2 | 8 | 8 |
| WP1-3 | 4 | 6 |
| WP1-4 | 3 | 4 |
| Total = 4 | 20 | 28 |
| WP2-1 | 2 | 3 |
| WP2-2 | 4 | 9 |
| WP2-3 | 2 | 3 |
| WP2-4 | 2 | 4 |
| Total = 4 | 10 | 19 |
| WP4-1 | 2 | 3 |
| WP4-2 | 4 | 8 |
| WP4-3 | 1 | 2 |
| WP4-4 | 2 | 2 |
| Total = 4 | 9 | 15 |

## 5.3. Age Control

The charcoal samples collected from sites WP1, WP2 and WP3 were sent to Auckland University palaeobotanist Dr Rod Wallace for identification of species. Matai (*Prumnopitys taxifolia or black-pine*) species were identified among the charcoal fragments from WP1 and WP4. The charcoal from WP2 was identified as a mixture of southern rata, beech, kahikatea and totara. The WP4 charcoal samples also contain southern rata species. All these species are long-lived (with a life span of 400-1000 years (http://terranature.org/bigTrees.htm) and were not recommended for ^{14}C dating. One WP1 charcoal sample was however sent for ^{14}C dating at GNS, Lower Hutt, which returned a conventional radiocarbon age (CRA) of 769 ± 21 AD ^{14}C years BP. The corresponding calibrated ^{14}C date is between 1262 and 1301AD (86.9% of area) (Figure 5.9). This is significantly earlier than the estimates of when Maori arrived in New Zealand and so unlikely to represent the date of use of the hangi. As matai may live up to 1000 years, the wood may have had a significant age at the time of burning in the hangi, and the date therefore have a significant, unwanted "in-built" age component (McFadgen, 1982).
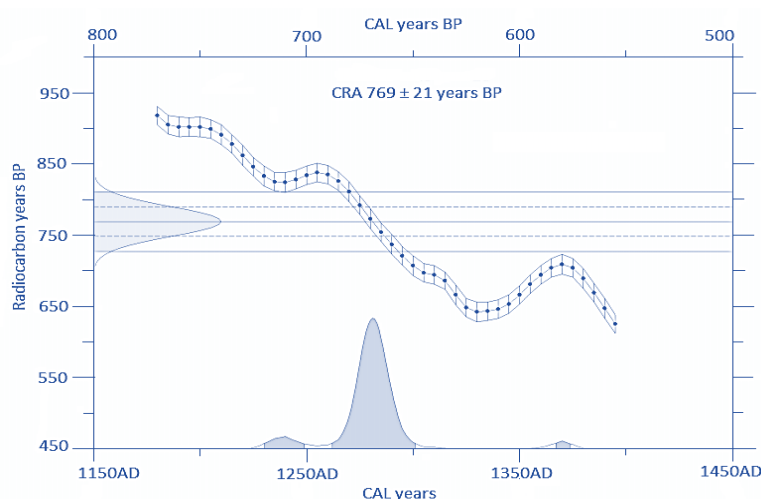


Figure 5.9. Radiocarbon dates representation using SHCAL13 calibration curve for site WP1 (Hogg et al., 2013). Dates have been determined using Accelerator Mass Spectrometry at GNS, Lower Hutt. Figure created from program WINSCALX 5.1 (Sparks, R.J., and Manning, M.R. pers. com. WinscalX, version 5.1. GNS Science, 2011).

Table 5.3. Radiocarbon age estimation and calibration (see figure5.8)

| Site Name | Material | Lab No. | $^{14}$C age | Calibrated age range (95% confidence) |
|-----------|----------|---------|--------------|----------------------------------------|
| WP1 | Matai | NZA58797 | 769±21 BP | 1262 AD to 1301 AD (86.9% of area) |

# 5.4. Rock Magnetism

Measurements of the rock magnetic properties of samples of the Weld Pass hangi stones are described below.

## 5.4.1. Thermomagnetic properties

To determine the Curie temperature and any magneto-mineralogical alteration in heating, susceptibility versus temperature experiments were conducted on Weld Pass hangi stones (Figure 5.9 (a)–(l)). The room temperature susceptibility of the stones from the three sites lies in the range 0.4-12.0 X $10^{-6}$m$^3$/kg. WP1 stones have the highest initial susceptibility among the three sites, from 3.0-12.0 X $10^{-6}$m$^3$/kg. The pinkish stones WP1-1, WP1-2 and WP1-3 (Figure 5.10 (a)–(c)) have almost reversible χ-T curves, whereas the greyish WP1-4 samples show enhanced susceptibility in the cooling curve (Figure 5.10 (d)). Susceptibility increases with temperatures up to 450-500°C and then decreases to a single Curie point below 600°C. All WP1 samples have sharp Hopkinson peaks (Hopkinson, 1890) in the heating curves which, except for sample WP1-4, remains in the cooling curves, indicating a thermally stable magnetic mineralogy. The principal Curie temperature of WP1 stones lies between 570°C and 600°C on heating and between 510°C and 580°C on cooling. WP2 stones have the lowest initial susceptibility range: 0.04-1.0 X $10^{-6}$m$^3$/kg. Heating and cooling curves show thermal alteration in minerals is more significant than for WP1 stones (Figure 5.10 (e)–(h)). Susceptibility increases significantly in the cooling curves of all samples except WP2-2-2. There is also no sharp Hopkinson peak, meaning these stones may have a broader spectrum of magnetic grain-sizes. In addition to this, the stones probably did not undergo repeated heating and cooling processes in the hangi. Heating and cooling Curie temperature ranges for WP2 stones are 515°C to 570°C and 510°C to

530°C respectively. WP4 stones have an initial susceptibility range of 2.0-5.0 X $10^{-6}$ $m^3$/kg, which is higher than WP2 stones and lower than WP1 stones (Figure 5.10 (i)–(l)). The heating and cooling curves of WP4-3 and WP4-4 are almost reversible. WP4-1 and WP4-2 also show magnetic enhancement in the cooling curves.

The principal Curie temperature of WP4 stones is in the range 550°C-600°C on heating and 515°C-590°C on αcooling. Susceptibility versus temperature plots suggest that WP1 and WP4 stones have been sufficiently heated in the hangi to have undergone alteration prior to their final cooling, and thus have enhanced their susceptibility from their original state. WP2 stones are closer to their original state and have not been heated sufficiently in the hangi to have reached the end point of thermal alteration. Hence laboratory heating enhanced the susceptibility of WP2 samples (Hrouda et al., 2003).

WP2-2 and WP4-2 show two magnetic phases in the heating curve (Figure 5.9 (f) & (j)), whereas slight inflections can be noticed in WP1-4 (at ~ 430°C, Figure 5.10 (d)), WP4-1 (at ~ 400°C, Figure 5.10 (i)) and WP4-4 (at ~ 300°C, Figure 5.10 (l)). In WP4-1 and WP4-4 these magnetic phases turned into a single magnetic phase in the cooling curves giving a strong Hopkinson peak at about 400°C in the cooling curve. Two magnetic phases are apparent in the cooling curves of WP1-4 and WP2-4 (Figure 5.10 (d) & (h)). A later experiment to only 400°C (not shown here) done on a sample from stone WP1-4 shows that heating and cooling curves are reversible, suggesting that the samples can provide reliable results up to 400°C as minerals will not alter thermally, and that the stones were not heated sufficiently in the hangi to reach the endpoint of thermal alteration. WP2-4 has a very weak susceptibility of the order of $10^{-8}$ $m^3$/kg (Figure 5.9h), so the susceptibility versus temperature plot (Figure 5.10 (h)) provided little information on the magnetic mineralogy of the sample due to the low resolution of the measurement. Curie temperatures of samples, calculated using the inverse susceptibility method (Petrovský & Kapička, 2006), are listed in Table 5.4. These experiments have provided a Curie temperature range of 515° to 610°C.
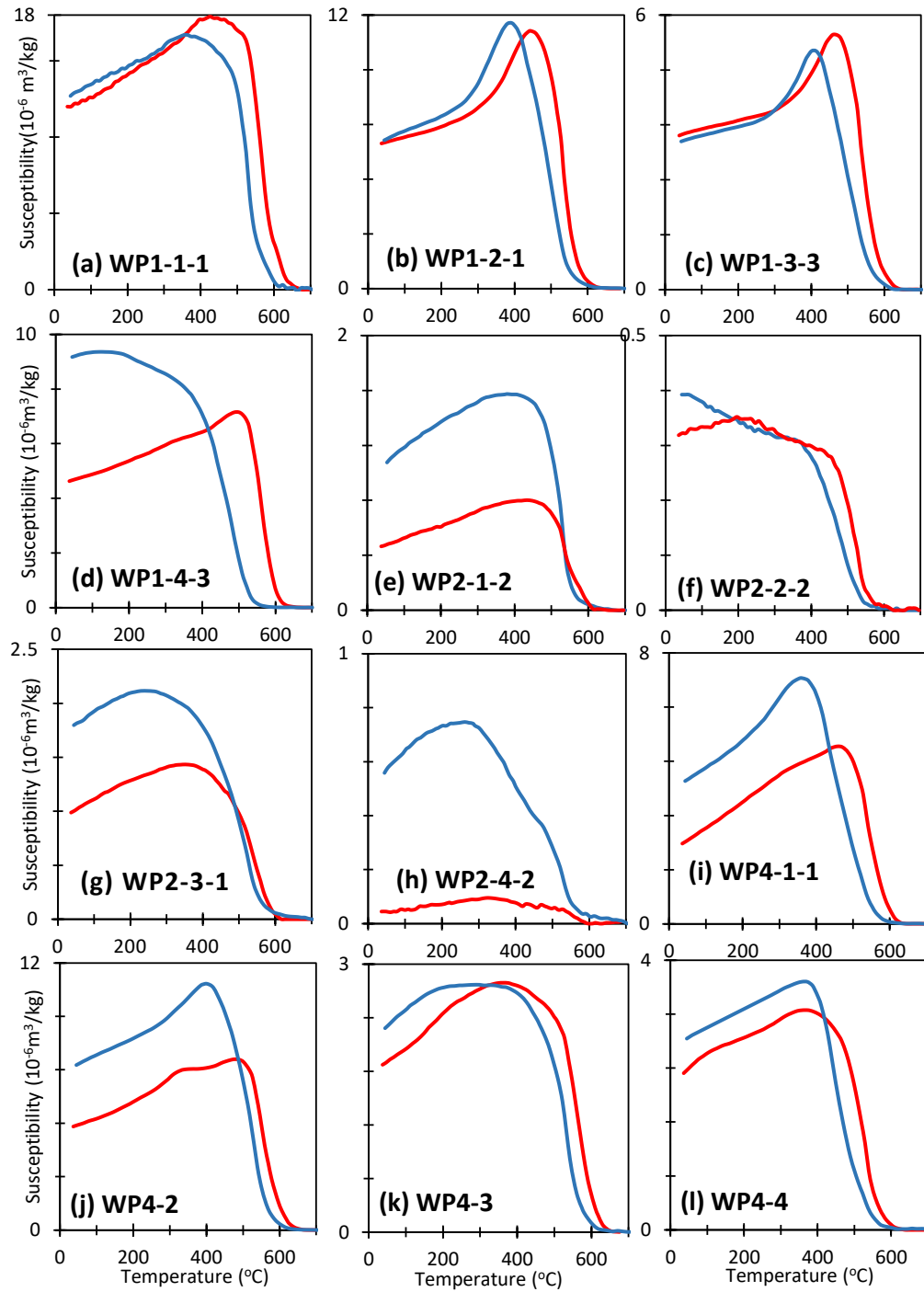
Figure 5.10. Plots of susceptibility vs temperature for hangi stones from sites WP1, WP2 and WP4. Red coloured lines indicate the heating curves and blue lines the cooling curves.

Saturation magnetization versus temperature plots of samples WP1-1-6, WP1-2-7, WP1-3, WP1-4-3, WP2-2-2, WP4-1 and WP4-2 are shown in Figure 5.10. Curie temperatures calculated from these plots using the double derivative method (Tauxe et al., 2010) are listed in Table 5.5 and range between 564 and 601°C. On comparing

117

Figures 5.10 and 5.11, it can be noticed that a sample of stone WP1-1 (Figure 5.10 (a) & 5.11 (a)) shows two magnetic phases in the $M_s$ vs T plot which turned into a single magnetic phase in the cooling curve. However, WP2-2 and WP4-2 have a single magnetic phase in $M_s$ vs T plots.

The Curie temperatures calculated from $M_s$-T experiments tend to be slightly higher than those from $\chi$-T experiments, probably due to at least one (and perhaps all) of the following reasons: the experiment is different, the instrument is different, and the method of calculating $T_c$ is different. The principal Curie temperatures of all the WP samples lie between 515° and 610°C, which suggests these stones carry small percentages of (titano) magnetite (with Ti < 10%) and/or cation-deficient (oxidized) titanomagnetite (Dunlop & Özdemir, 1997).
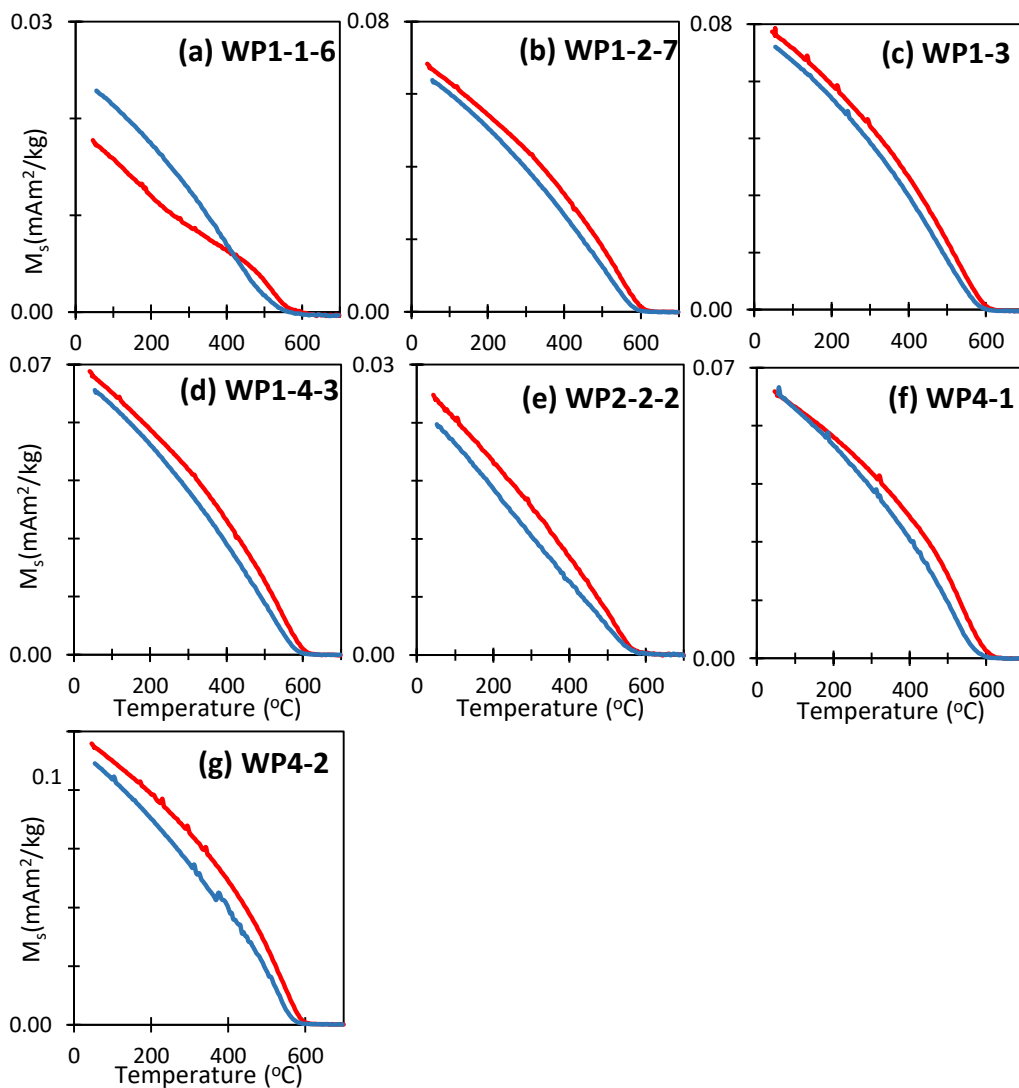


Figure 5.11. $M_s$ vs T plots of Weld Pass hangi stones, analyzed using RockMag Analyzer. Red coloured lines indicate the heating curves and blue lines the cooling curves.

Table 5.4. Curie temperatures of Weld Pass hangi stones. $\chi$-T plots are calculated using the inverse susceptibility method.

| Sample ID | $T_c$ (Heating °C) | $T_c$ (Cooling °C) | $T_c$ (Cooling °C) corrected | Difference (°C) |
|-----------|--------------------|--------------------|------------------------------|-----------------|
| WP1-1-1 | 597 | 549 | 564 | 33 |
| WP1-2-1 | 585 | 557 | 572 | 13 |
| WP1-3-3 | 592 | 567 | 582 | 10 |
| WP1-4-3 | 577 | 495 | 510 | 67 |
| WP2-1-2 | 569 | 516 | 531 | 38 |
| WP2-2-2 | 515 | 492 | 507 | 8 |
| WP2-3-1 | 547 | 500 | 515 | 32 |
| WP4-1-1 | 595 | 529 | 544 | 51 |
| WP4-2 | 610 | 577 | 592 | 18 |
| WP4-3 | 596 | 562 | 577 | 19 |
| WP4-4 | 550 | 500 | 515 | 35 |

Table 5.5. Curie temperature of Weld Pass hangi stones calculated from $M_s$ vs T plots using the double derivative method.

| Sample ID | $T_c$ Heating (°C) | $T_c$ Cooling (°C) | Difference (°C) |
|-----------|--------------------|--------------------|-----------------|
| WP1-1-6 | 582 | 566 | 16 |
| WP1-2-7 | 582 | 568 | 14 |
| WP1-3 | 592 | 578 | 14 |
| WP1-4-3 | 601 | 578 | 23 |
| WP2-2-2 | 564 | 555 | 9 |
| WP4-1 | 602 | 567 | 35 |
| WP4-2 | 584 | 557 | 27 |

## 5.4.2. Hysteresis and IRM curves

To understand the magnetic mineralogy of the hangi stones, hysteresis and isothermal remanent magnetization (IRM) acquisition curves are plotted for samples from stones WP1-1, WP1-2, WP1-3, WP1-4, WP2-2, WP4-1 and WP4-2 (Figure 5.12). Values of saturation magnetization ($M_s$), saturation remanence ($M_{rs}$), coercivity ($B_c$) and coercivity of remanence ($B_{cr}$) were also calculated (Table 6.6) (Heslop & Roberts, 2012). The VFTB at the University of Liverpool was used for these experiments. Data has been analyzed using RockMag Analyzer 1.1 (Leonhardt, 2006). Hysteresis curves show the presence of a ferrimagnetic mineral with some paramagnetic component (Figure 5.12 (a), (b), (c), (d), (g), (h), (i), (j) & (m), blue curves). The red curves show the data after the removal of the paramagnetic trend. Hysteresis loops of samples from stones WP1-2, WP4-1 and WP4-3 are broader than those of all other samples. These

samples have higher values of saturation magnetization, saturation remanence and coercivities. The samples saturated at a field less than 300mT (Figure 5.12); the saturation remanence of WP stones is between 0.03-0.25 mAm$^2$/kg; and $B_{cr}$ values are between 25.7 and 71.1mT. The rock magnetic properties of WP samples show that these sandstones carry PSD grain-sized, low titanium titanomagnetite and cation-deficient titanomagnetite. Hysteresis parameters and ratios are shown in Table 5.6.
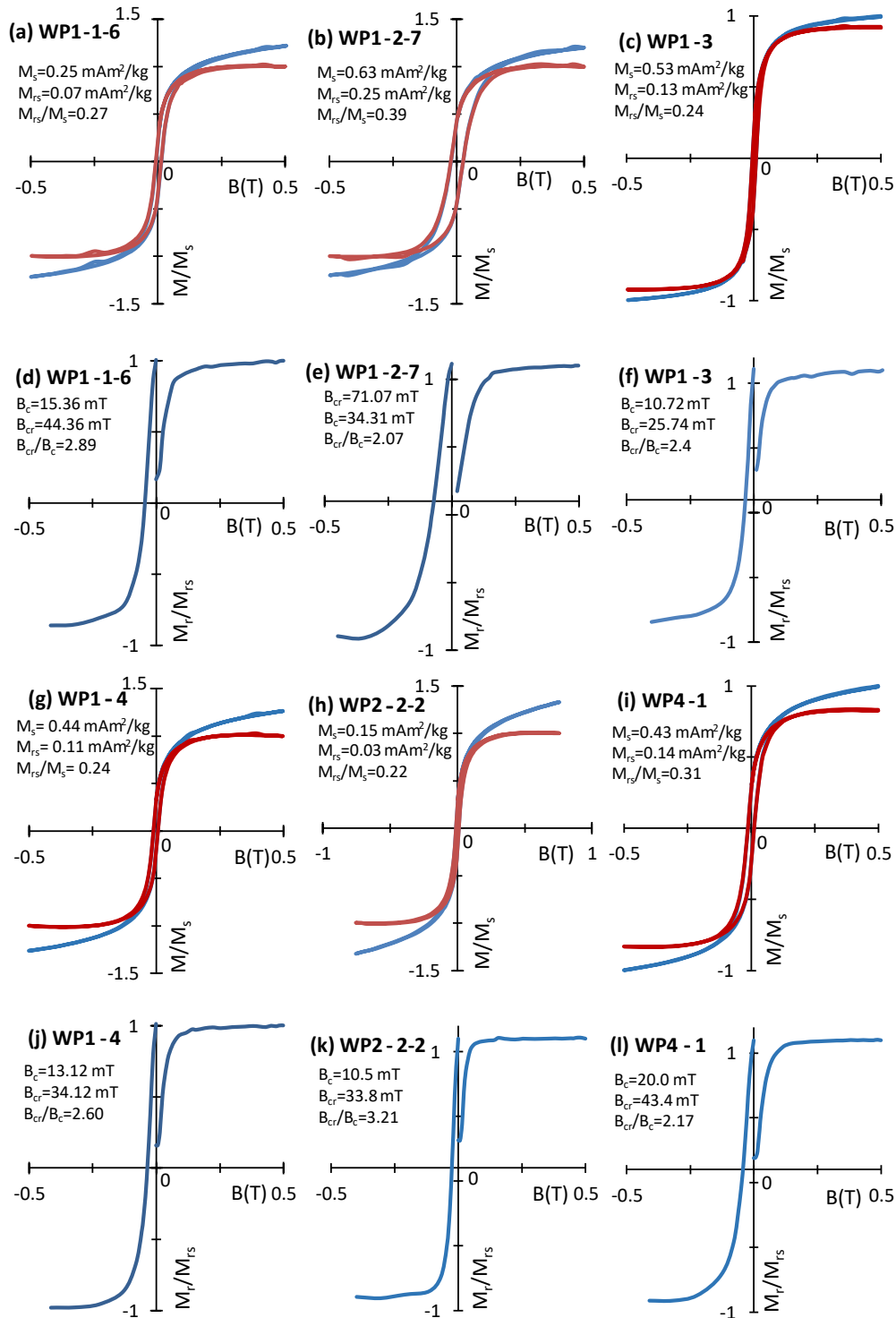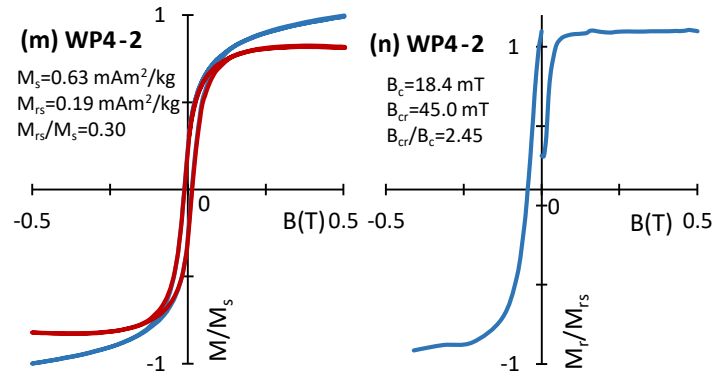
Figure 5.12. Hysteresis and IRM plots of samples WP1-1, WP1-2, WP1-3, WP1-4, WP2-2, WP4-1 and WP4-2 (a)-(n). The blue curves include the paramagnetic character and paramagnetic correction is applied to red curves.

Table 5.6. Hysteresis and IRM data of hangi stones from sites WP1, WP2 and WP4.

| Sample ID | $M_{rs}$(mAm²/kg) | $M_s$ (mAm²/kg) | $B_c$ (mT) | $B_{cr}$(mT) | $M_{rs}/M_s$ | $B_{cr}/B_c$ |
|-----------|-------------------|-----------------|------------|--------------|--------------|--------------|
| WP1-1-6 | 0.068 | 0.247 | 15.4 | 44.4 | 0.27 | 2.89 |
| WP1-2-7 | 0.249 | 0.629 | 34.3 | 71.1 | 0.40 | 2.07 |
| WP1-3 | 0.129 | 0.532 | 10.7 | 25.7 | 0.24 | 2.4 |
| WP1-4-3 | 0.107 | 0.443 | 13.1 | 34.1 | 0.24 | 2.6 |
| WP2-2-2 | 0.033 | 0.151 | 10.5 | 33.8 | 0.22 | 3.22 |
| WP4-1 | 0.135 | 0.433 | 20.0 | 43.4 | 0.31 | 2.17 |
| WP4-2 | 0.191 | 0.634 | 18.4 | 45.0 | 0.30 | 2.45 |

In Figure 5.13 the data are shown on a Day plot (Day et al., 1977) together with SD/SP and SD/MD mixing curves (Dunlop, 2002). The data points lie above the third SD/MD mixing curve and in the middle of the traditional PSD region. WP1-2-7 is near to the SD boundary and WP2-2-2 is below all other samples. Figure 5.12 shows that the remanence carriers of all WP stones have PSD characteristics.
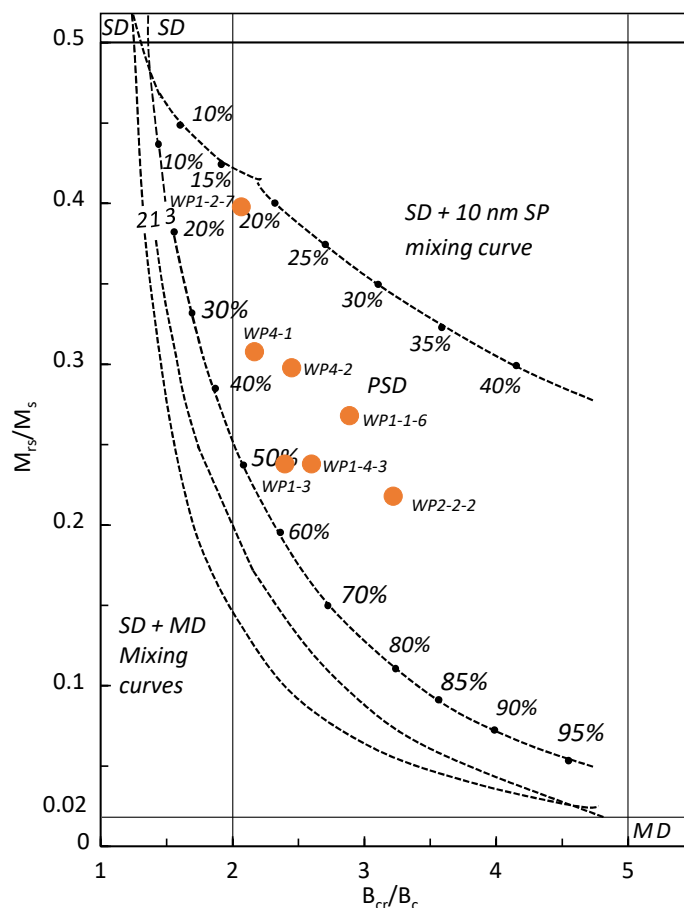
Figure 5.13. Day Plot showing $M_{rs}/M_s$ vs $B_{cr}/B_c$ (Day et al., 1977) data of Weld Pass hangi stones (orange dots) superimposed on the mixing curves of Dunlop (2002) for a single domain/ multidomain and single domain/superparamagnetic grain mixtures.

### 5.4.3. Summary

Thermomagnetic and hysteresis data are consistent with the remanence carriers in the Weld Pass hangi stones being principally Ti-poor titanomagnetite, with occasional cation-deficient titanomagnetite, in the PSD grainsize range.

## 5.5. Thermal Demagnetization

Progressive thermal demagnetization experiments were initially carried out on 12 specimens from the three hangi sites of Weld Pass (four stones from each site and one specimen from each stone). Since the stones were relatively small and specimens were few, the remaining specimens were put aside for archaeointensity experiments. The

directional data subsequently obtained during the archaeointensity experiments are included in the discussion below.

## 5.5.1. WP1

Typical demagnetization data of specimens from site WP1 are shown in Figure 5.14 (a)–(d). Weld Pass stones have NRMs between 1.0 and 18.6 A/m, which is high for sandstones and is probably due to enhancement in the hangi. From thermomagnetic properties, rock magnetic properties and field observations, it is thought likely that hangi WP1 was used many times and the stones were heated over and over and finally left *in situ*, tightly packed. The Zijderveld plot of each sample shows that a weak VRM is removed by 50°C-100°C and all stones carry a stable component of magnetization that demagnetizes towards the origin. The demagnetization curves of specimens show that WP1-1-4A and WP1-2-1A have grains which start to unblock above 200°C, in WP1-3-1A grains unblock above 300°C and in WP1-4-1A above 100°C. The specimens completely demagnetized at a temperature between 550 and 600°C. Figure 5.14 (e) shows the change in susceptibility of specimens during thermal demagnetization. A slight rise in susceptibility can be observed in WP1-4-1A above 350°C, consistent with results of the susceptibility versus temperature experiments (Figure 5.10).

From the Zijderveld plot (Figure 5.14), and data shown in Table 5.7 it can be deduced that the stones carry a stable component of magnetization. The mean declinations of four stones WP1-1, WP1-2, WP1-3 and WP1-4 are similar. However, mean inclination of stone WP1-1 is steeper and WP1-4 is shallower than for stones WP1-2 and WP1-3. WP1-1, WP1-2 and WP1-3 yield an average direction of Dec = 14.8°, Inc = -60.5°, $\alpha_{95}$ = 3.9° for 15 specimens (including the results of both THD and palaeointensity experiments).

Figure 5.14. (a)- (d) Thermal demagnetization results of specimens from four hangi stones from site WP1. Each figure includes Zijderveld plot and inset decay plot of specimen. Red and pink coloured dots indicate the data points included for PCA. (e) Shows change in susceptibility at each temperature step.

Table 5.7. Directional data of hangi site WP1, calculated from thermal (THD). N is number of specimens and n is number of data points used for calculations. Calculations are done with Remasoft30 software (Chadima & Hrouda, 2006). RT indicates room temperature. Only black coloured data is included for calculation of mean directional data for the site.

| Sample ID | Temperature Range (°C) | N/n | Dec (°) | Inc (°) | MAD/$\alpha_{95}$ (°) |
|---|---|---|---|---|---|
| WP1-1-1A | 100-550 (P) | 10 | 15.6 | -71.6 | 2.7 |
| WP1-1-2B | 250-550 (P) | 10 | 12.2 | -71.5 | 1.7 |
| WP1-1-4A | 300-500 (THD) | 6 | 2.1 | -71.4 | 1.9 |
| WP1-1-4B | 200-475 (P) | 6 | 13.6 | -72.2 | 1.7 |
| WP1-1-5B | 300-500 (P) | 6 | 14.9 | -67.8 | 1.8 |
| **WP1-1** | | **5** | **12.7** | **-70.9** | **2.1** |
| WP1-2-1A | 200-550 (THD) | 6 | 12.5 | -56.8 | 2.5 |
| WP1-2-2A | 350-500 (P) | 6 | 14.3 | -57.2 | 1.5 |
| WP1-2-5A | 300-500 (P) | 5 | 18.6 | -57 | 1.9 |
| WP1-2-6A | 300-500 (P) | 6 | 17.3 | -56.3 | 1.7 |
| WP1-2-8A | 300-500 (P) | 8 | 18.6 | -51.6 | 2 |
| **WP1-2** | | **5** | **16.3** | **-55.8** | **2.7** |
| WP1-3-1A | 425-550 (THD) | 5 | 17.3 | -51.7 | 1.8 |
| WP1-3-1B | 350-500 (P) | 5 | 18 | -51.1 | 2.4 |
| WP1-3-2B | 375-550 (P) | 7 | 12.5 | -54.6 | 2 |
| WP1-3-3A | 200-500 (P) | 7 | 13.3 | -58.2 | 1.2 |
| WP1-3-4A | 375-550 (P) | 7 | 10.9 | -58 | 2 |
| **WP1-3** | | **5** | **14.6** | **-54.8** | **3.6** |
| WP1-4-1A | 375-575 (THD) | 7 | 6.3 | -38.5 | 1 |
| WP1-4-2A | 425-550 (P) | 5 | 1 | -40.7 | 2.2 |
| WP1-4-3B | 300-550 (P) | 8 | 5.1 | -39.5 | 0.9 |
| **WP1-4** | | **3** | **4.2** | **-39.6** | **3.7** |
| **Mean of WP1-1, WP1-2 & WP1-3** | | **15** | **14.8** | **-60.5** | **3.9** |

## 5.5.2. WP2

Four specimens were initially measured to obtain directional data from four hangi stones from site WP2, WP2 stones having NRM in the range 0.1-4A/m. Zijderveld plots (Figure 5.15 (a)-(d)) of WP2 specimens show that after a VRM component has been removed in the initial demagnetization steps, each of the stones carries a single, stable component of magnetization. However, each is in a different direction. WP2 is the smallest of the three hangi stones sampled and is at ~30m from WP1 and WP4. From χ-T plots it seems that the stones were not heated thoroughly. In contrast to WP1 and WP4, WP2 appears to be a little-used site that was probably raked over after the stones

had cooled, randomizing their directions of magnetization. The mean direction of each stone is calculated and summarized in Table 5.8. The change in susceptibility of each specimen during thermal demagnetization from the temperature step 350°C can be seen in Figure 5.15 (f).
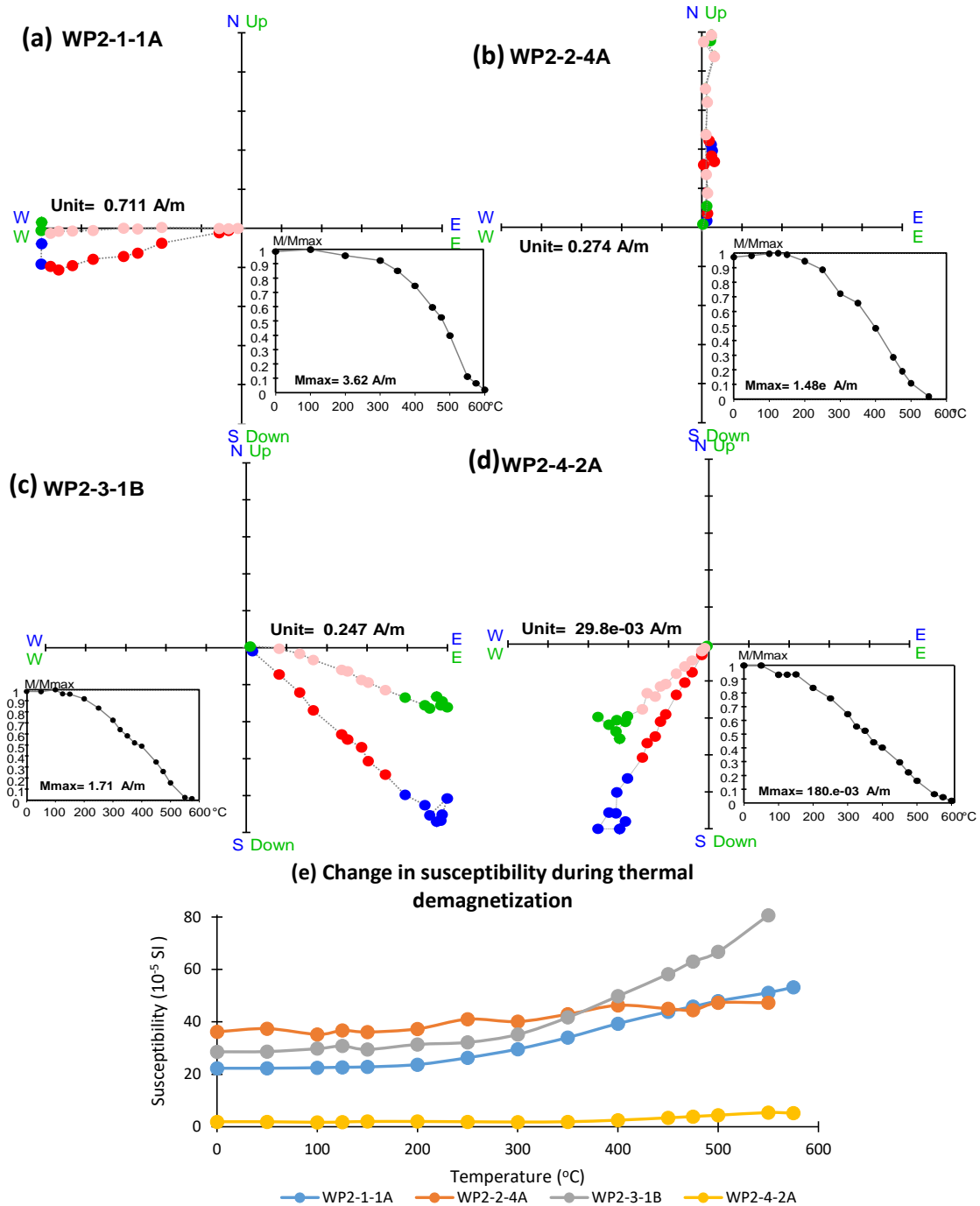


Figure 5.15 (a)-(d) Thermal demagnetization results of specimens from four hangi stones from site WP2. Each figure includes Zijderveld plot and inset decay plot of specimen. Red and pink coloured dots indicate the data points included for PCA. (e) Shows change in susceptibility at each temperature step.

126

Table 5.8. Directional data of hangi site WP2, calculated from thermal (THD). N is number of specimens and n is number of data points used for calculations. Calculations are done with Remasoft30 software (Chadima & Hrouda, 2006). RT indicates room temperature. Only black coloured data is included for calculation of mean directional data for the site.

| Sample ID | Temperature Range (°C) | N/n | Dec (°) | Inc (°) | MAD/$\alpha_{95}$ (°) |
|---|---|---|---|---|---|
| WP2-1-1A | 200-600 (THD) | 10 | 257.5 | 0.8 | 1 |
| WP2-1-1B | 100-525 (P) | 8 | 277.7 | 3.5 | 1.6 |
| WP2-1-2A | 200-525 (P) | 7 | 263.8 | 2.5 | 4 |
| **WP2-1 Mean** | | **3** | **267.7** | **2.3** | **16** |
| WP2-2-1B | 250-500 (P) | 9 | 15.7 | -71.8 | 2.6 |
| WP2-2-1C | 350-550 (P) | 8 | 15.4 | -65 | 4.2 |
| WP2-2-3B | 350-475 (P) | 6 | 4.3 | -66.5 | 2 |
| WP2-2-4A | 300-500 (THD) | 6 | 5.9 | -68 | 1.6 |
| WP2-2-4B | 150-475 (P) | 8 | 17.5 | -66.7 | 1.1 |
| **WP2-2 Mean** | | **5** | **11.6** | **-67.4** | **3.5** |
| WP2-3-1B | 300-500 (THD) | 8 | 134.5 | 11.4 | 2.4 |
| WP2-4-1A | 300-525 (P) | 8 | 211.5 | 23.4 | 3.4 |
| WP2-4-1B | 300-525 (P) | 8 | 208.9 | 20.7 | 2.4 |
| WP2-4-2A | 300-575 (P) | 11 | 209.1 | 25.8 | 1.6 |
| WP2-4-2B | 300-525 (PI) | 7 | 212.9 | 23.6 | 1.8 |
| **WP2-4 Mean** | | **4** | **210.6** | **23.4** | **3.1** |

## 5.5.3. WP4

Four specimens from four hangi stones of the site WP4 were initially used for thermal demagnetization. WP4 stones have NRM in the range 0.5-11A/m. The specimens lost their magnetization completely at a temperature of about 600°C (Figure 5.16). The Zijderveld plots of specimens from stones WP4-1, WP4-3 and WP4-4 show a slight curve (Figure 5.16 (a), (b), & (c)), suggesting the stones were disturbed during the cooling process. However, WP4-2 has acquired a single stable component of magnetization (Figure 5.16 (b)). The blocking temperature spectra of all specimens can be seen in the thermal demagnetization curves of Figure 5.16 (a)-(d). Low blocking temperature components of specimens WP4-1-2B, WP4-3-1B and WP4-4-2A have been calculated and are given in Table 5.9, as the low blocking temperature component gives the record of the field recorded after the last cooling/disturbance of the stones. It can be observed that there are some other specimens from stones WP4-1, WP4-3 and WP4-4 whose low blocking temperature components are not calculated because they could not be isolated

well enough. WT4-3-1A was a very small specimen, poorly oriented, and gave data dissimilar to another specimen from the same stone, WP4-3-1B (Table 5.9). The susceptibility of WP4-1 and WP4-2 start increasing after heating at 300°C, whereas the susceptibility of WP4-3 and WP4-4 remain almost stable. The averaged directional data calculated for each stone is calculated and given in Table 5.9.

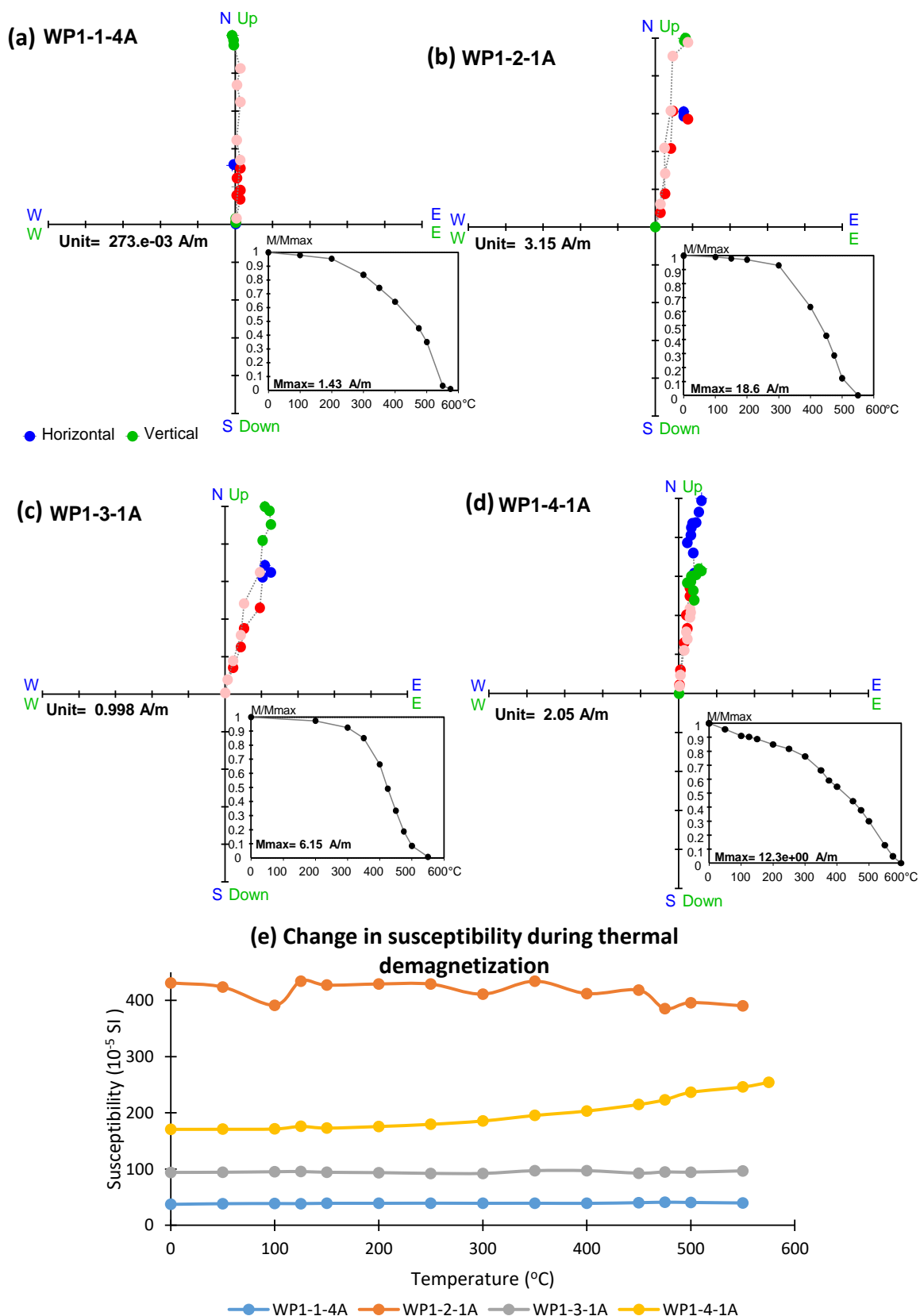**(e) Change in susceptibility during thermal demagnetization**
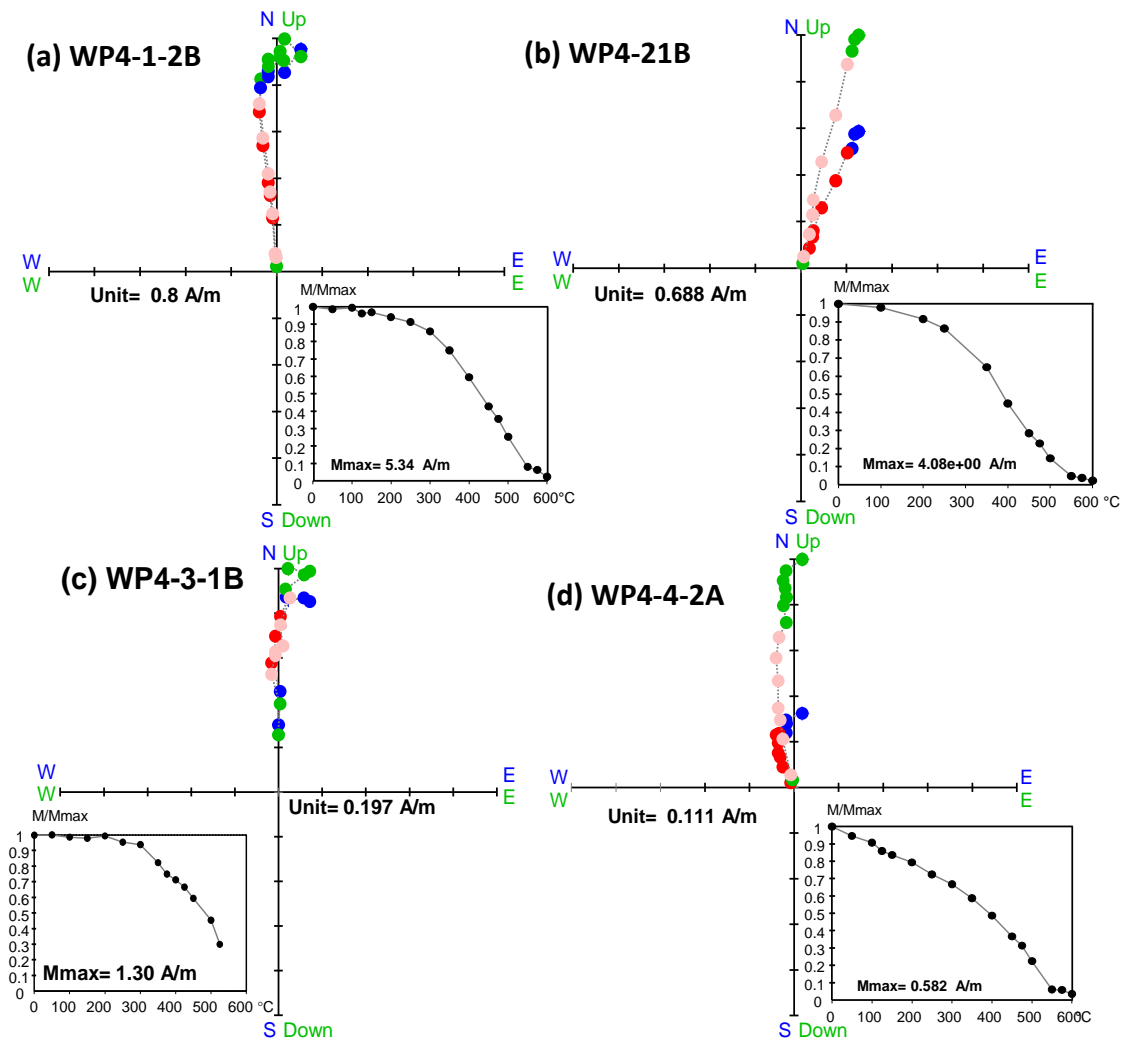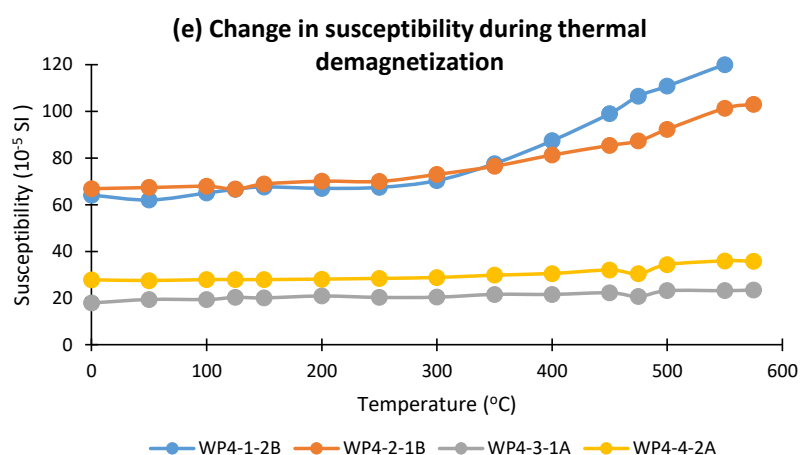
Figure 5.16. (a)-(d) Thermal demagnetization results of specimens from four hangi stones from site WP4. Each figure includes Zijderveld plot and inset decay plot of specimen. (e) Shows change in susceptibility at each temperature step.

Table 5.9. Directional data of hangi site WP4, calculated from thermal (THD). N is number of specimens and n is number of data points used for calculations. Calculations are done with Remasoft30 software (Chadima & Hrouda, 2006). RT indicates room temperature. Only black coloured data is included for calculation of mean directional data for the site.

| Sample ID | Temperature Range (°C) | N/n | Dec (°) | Inc (°) | MAD/$\alpha_{95}$ (°) |
|---|---|---|---|---|---|
| WP4-1-1A | 300-525 (P) | 8 | 357.3 | -45.9 | 1.3 |
| WP4-1-2A | 300-525 (P) | 7 | 3.7 | -46 | 1.9 |
| WP4-1-2B (C1) | 350-575 (THD) | 7 | 354 | -46.5 | 0.6 |
| WP4-1-2B (C2) | 125-350 (THD) | 6 | 19.2 | -42.2 | 6.2 |
| **WP4-1 Mean** | | **3** | **358.3** | **-46.2** | **5.2** |
| WP4-2-1B | 200-550 (THD) | 8 | 22.3 | -58.6 | 0.9 |
| WP4-2-2A | 350-550 (P) | 7 | 18.5 | -62.1 | 1.3 |
| WP4-2-3B | 150-550 (P) | 11 | 18.6 | -58.3 | 2.3 |
| WP4-2-4A | 350-500 (P) | 6 | 17 | -60.1 | 1.5 |
| WP4-2-4B | 300-500 (P) | 7 | 16.8 | -61.4 | 1.4 |
| **WP2-2 Mean** | | **5** | **18.7** | **-60.1** | **1.9** |
| WP4-3-1A | 350-575 (P) | 7 | 152.1 | -45.9 | 1.9 |
| WP4-3-1B (C1) | 450-525 (THD) | 3 | 355.6 | -43.9 | 2.8 |
| WP4-3-1B (C2) | 300-450 (P) | 6 | 14.5 | -45.6 | 4.5 |
| | | | | | |
| WP4-4-1A (C1) | 350-525 (THD) | 7 | 349.2 | -72.6 | 2.5 |
| WP4-4-2B (C1) | 450-600 (P) | 6 | 337.7 | -64.4 | 1.2 |
| WP4-4-2B (C2) | 300-450 (P) | 4 | 358.7 | -72.8 | 2.6 |
| **WP4-4 Mean** | | **2** | **343.9** | **-69.9** | **14.1** |

## 5.6. Archaeointensities

Archaeointensity experiments were made on 33 specimens from 12 stones from the three sites WP1, WP2 and WP4. The results are described below and shown in figures 5.17, 5.18 and 5.19.

### 5.6.1. WP1

Thirteen out of 14 specimens provided high-quality successful archaeointensity results. Specimens did not show alteration and passed tail/pTRM checks throughout the experiment, even at high temperature steps. Archaeointensities are calculated using Thellier Tool. Arai plots with Zijderveld plots of one specimen from each stone are shown in Figure 5.17 (a)-(d). A straight line is fitted to the data points over the blocking temperature range where scattering is least. The experiments were continued until specimens lost 70-90% of their magnetization. The data are summarized in Table 5.10. It can be seen from the table that most specimens meet selection criteria with class TTA. Only WP1-3-2B gives an anomalously high archaeointensity value, which may be due to the breakage of the specimen during the experiment such that, when glued back together, it did not have its all parts. Its results were therefore rejected. All other specimens have provided consistent intensity values. The average archaeointensity of hangi site WP1, calculated from the results of 13 specimens is 61.4 ± 2.6 µT. Rock magnetic properties suggested the presence of Fe-rich titanomagnetite and assemblage of PSD grains in WP1 stones, thus the intensity values are reliable.
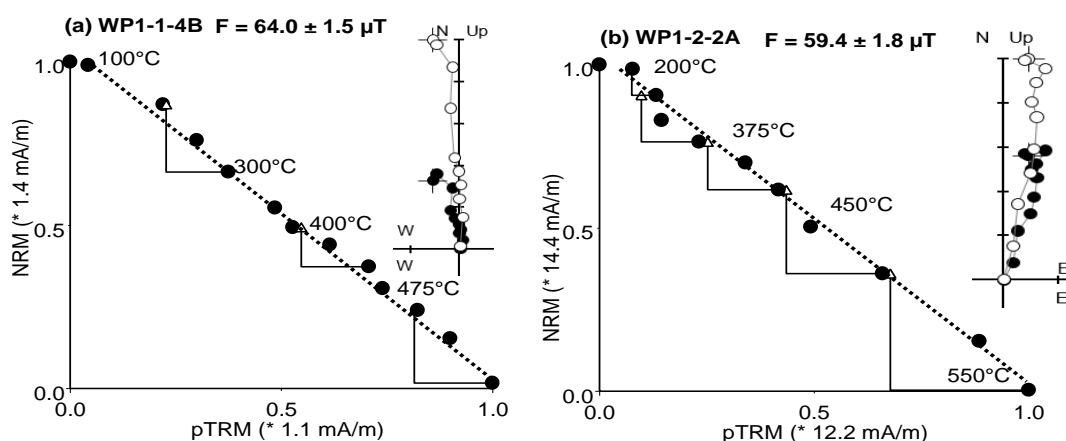
Figure 5.17. Arai diagrams of specimens of stones WP1-1, WP1-2, WP1-3 and WP1-4 using Thellier Tool (Leonhardt et al., 2004). Zijderveld diagrams plotted using Remasoft30 software, show demagnetization behaviour at each step (Chadima & Hrouda, 2006)

Table 5.10. Archaeointensity results measured for hangi site WP1. F are intensity results of individual specimens in µT. N is the number of data points included in linear segment of Arai plot. β, f, q, $\delta_{CK}$, $\delta_{pal}$, α, MAD, $\delta_{TR}$ and $\delta_{t*}$ are statistical parameters defined in Chapter 2. Acceptable results are represented in black font; yellow font indicates parameters of class TTB and red font TTC.

| Sample ID | Temp range (°C) | F±σ (µT) | N | β | f | q | $\delta_{CK}$ | $\delta_{pal}$ | α | MAD | $\delta_{TR}$ | $\delta_{t*}$ | Class |
|---|---|---|---|---|---|---|---|---|---|---|---|---|---|
| Quality Criteria | | | ≥5 ≥5 --- | ≤0.1 ≤0.15 --- | ≥0.35 ≥0.35 --- | ≥5 ≥0 --- | ≤7 ≤9 --- | ≤10 ≤18 --- | ≤15 ≤15 --- | ≤15 ≤15 --- | ≤10 ≤20 --- | ≤9 ≤99 --- | TTA TTB TTC |
| WP1-1-1A | 100-550 | 57.4±2.3 | 10 | 0.04 | 0.92 | 19.4 | 2.6 | 4.9 | 1.9 | 2.7 | 1.4 | 0 | A |
| WP1-1-2B | 100-550 | 58.5±2.1 | 11 | 0.04 | 0.94 | 22.9 | 3.1 | 9.1 | 2.5 | 2.7 | 0.8 | 0 | A |
| WP1-1-4B | 100-550 | 64.0±1.5 | 12 | 0.02 | 0.92 | 35.1 | 1.9 | 0.9 | 1.5 | 2.3 | 1.2 | 4.7 | A |
| WP1-1-5B | 350-550 | 60.4±1.2 | 8 | 0.02 | 0.78 | 32.5 | 3.4 | 16.5 | 1.8 | 2.3 | 2 | 4.7 | B |
| WP1-2-2A | 200-550 | 59.4±1.8 | 10 | 0.03 | 0.93 | 27.3 | 3.5 | 3.3 | 0.7 | 1.3 | 1.3 | 8.8 | A |
| WP1-2-5A | 200-550 | 61.4±2.0 | 10 | 0.03 | 0.95 | 23.8 | 2.8 | 3.9 | 0.7 | 3.1 | 1.5 | 2.1 | A |
| WP1-2-6A | 300-550 | 62.6±1.9 | 9 | 0.03 | 0.89 | 22.9 | 4.9 | 2.3 | 2 | 2.3 | 1.4 | 3.7 | A |
| WP1-2-8A | 350-550 | 62.6±4.8 | 8 | 0.08 | 0.81 | 7.8 | 6.1 | 7.5 | 1.2 | 2.2 | 1.3 | 0.9 | A |
| WP1-3-1B | 200-550 | 67±2.2 | 11 | 0.03 | 0.96 | 25.8 | 6.7 | 5.4 | 0.83 | 1.7 | 1.4 | 0 | A |
| WP1-3-2B | 200-450 | 127.5±8.3 | 7 | 0.07 | 0.71 | 8.6 | 9 | 21.3 | 0.8 | 2.1 | 3.3 | 0 | C |
| WP1-3-3A | 375-550 | 59.6±1.5 | 6 | 0.03 | 0.76 | 20.8 | 3.8 | 4.1 | 1 | 2.1 | 2 | 0 | A |
| WP1-3-4A | 400-550 | 63.8±3.7 | 6 | 0.06 | 0.64 | 8.6 | 3.4 | 20.9 | 0.9 | 1.6 | 2.3 | 3.9 | C |
| WP1-4-2A | 100-500 | 61.2±4.8 | 10 | 0.08 | 0.62 | 6.8 | 2.5 | 4.3 | 2.4 | 3 | 2.3 | 0.5 | A |
| WP1-4-3B | 100-500 | 59.8±5.4 | 10 | 0.09 | 0.67 | 6.6 | 4.5 | 0.7 | 1.1 | 1.5 | 2 | 0.8 | A |
| WP1 MEAN | | 61.4±2.6 | 13 | | | | | | | | | | |

## 5.6.2. WP2

Eleven specimens from the four hangi stones WP2-1, WP2-2, WP2-3 and WP4-4 were used to determine the archaeointensity at site WP2 (Figure 5.18 (a)-(d)). The specimens of stone WP2-2 and WP2-3 provided high-quality intensity data, meeting selection criteria with TTA (Table 5.11). Zijderveld plots have already indicated the disturbance of the stones after cooling in the hangi. Specimens from stone WP2-1 returned an archaeointensity of about 33μT. The specimens of this stone did not pass pTRM tests as the difference between pTRM gained and repeated pTRM gained for the same temperature is large. On the other hand, the grains of specimens from stone WP2-4 did unblock at a low temperature step and thermally altered at high temperature steps, so could not provide archaeointensity results consistent with data from the other stones. From the thermomagnetic properties of WP2-1 and WP2-4 it can also be observed that heating and cooling curves are not reversible, therefore it is possible that thermal alteration took place in the mineral during heating in the experiment (Figure 5.10 (e) & (h)). While specimen WP2-3-1A does not meet selection criteria TTA or TTB either, the intensity result of this specimen is included in the calculation of the average intensity of the site as it was consistent with the specimens providing high quality results. Six out of 11 specimens have provided consistent results, averaged to 57.7 ± 1.7 μT and summarized in Table 5.11.

(c) WP2-3-2A    F = 54.3 ± 6.4 µT
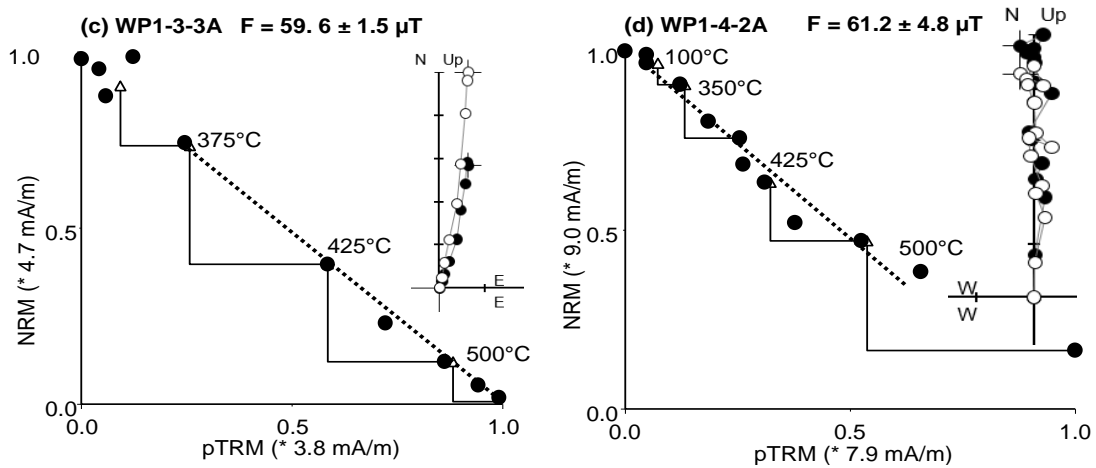
(d) WP2-4-2B    F = 0. 0 ± 0.0 µT

Figure 5.18. Arai diagrams of specimens from stones WP2-1, WP2-2, WP2-3 and WP2-4 using Thellier Tool (Leonhardt et al., 2004). Zijderveld diagrams, plotted using Remasoft30 software, show demagnetization behaviour at each step (Chadima & Hrouda, 2006).

Table 5.11. Archaeointensity results measured for hangi site WP2. Table includes intensity values and statistical parameters of each specimen.

| Sample ID | Temp range (°C) | F±σ (µT) | N | β | f | q | δ$_{CK}$ | δ$_{pal}$ | α | MAD | δ$_{TR}$ | δ$_{t^*}$ | Class |
|---|---|---|---|---|---|---|---|---|---|---|---|---|---|
| Quality Criteria | | | ≥5 ≥5 --- | ≤0.1 ≤0.15 --- | ≥0.35 ≥0.35 --- | ≥5 ≥0 --- | ≤7 ≤9 --- | ≤10 ≤18 --- | ≤15 ≤15 --- | ≤15 ≤15 --- | ≤10 ≤20 --- | ≤9 ≤99 --- | TTA TTB TTC |
| WP2-1-1B | RT-500 | 33.7±1.2 | 13 | 0.03 | 0.75 | 16.8 | 14 | 7.6 | 3 | 2.3 | 4.6 | 2.6 | C |
| WP2-1-2A | RT-500 | 30.1±2.3 | 13 | 0.08 | 0.75 | 7.7 | 7.5 | 7.7 | 0.8 | 2.9 | 4.8 | 4.8 | B |
| WP2-2-1B | 150-500 | 58.9±4.1 | 10 | 0.07 | 0.88 | 11.1 | 2.3 | 4.9 | 2.7 | 2.3 | 2.3 | 0 | A |
| WP2-2-1C | 50-450 | 58.4±3.7 | 9 | 0.06 | 0.72 | 9.4 | 3.5 | 5.4 | 3.7 | 3.2 | 2.6 | 9 | A |
| WP2-2-3B | 200-550 | 58.0±4.3 | 11 | 0.07 | 0.92 | 11 | 5.4 | 7.5 | 0.2 | 2.3 | 3 | 0 | A |
| WP2-2-4B | 200-425 | 59.3±4.0 | 7 | 0.07 | 0.52 | 6.3 | 2.3 | 6.2 | 2.8 | 2.9 | 3.1 | 0 | A |
| WP2-3-1A | 50-425 | 58.0±6.3 | 10 | 0.1 | 0.57 | 4.2 | 23 | 9.5 | 8.1 | 3.7 | 13.5 | 0.6 | C |
| WP2-3-2A | 100-450 | 54.3±6.4 | 8 | 0.1 | 0.54 | 3.7 | 7 | 2.8 | 3.5 | 3.7 | 7.4 | 1.5 | A |
| WP2 Mean | | 57.7±1.7 | 6 | | | | | | | | | | |

## 5.6.3. WP4

Arai and Zijderveld plots for specimens from stones WP4-1, WP4-2, WP4-3 and WP4-4 are shown in Figure 5.19 (a)-(d). Archaeointensity experiments were carried out on eight specimens and seven specimens provided consistent intensity values. Specimen WP4-1-1A passed all tail/pTRM checks and met selection criteria with class TTA (Table 5.12). All other results are of either TTB or TTC class, due to the failure of pTRM

checks. These results are accepted and included in the calculation of the site's mean intensity as the intensity values are consistent with those of the quality. WP4-2-2A (Table 5.12) thermal alteration is not large, but gives high intensity value, so the result of this specimen is excluded from the calculation of average intensity. The reason for low quality may be the slight disturbance of stones during the cooling process. The multivectorial intensity calculation method did not help in this case as it provided similar intensity values shown in Figure 5.19 (Yu & Dunlop, 2002). In Figure 5.19 (b), WP4-2-4B has large uncertainty which reflects the scatter in data points on the graph. The specimen meets quality criteria TTA. The average archaeointensity of seven specimens is 57.5 ± 3.6 µT. Intensity data for each specimen is summarized in Table 5.12.
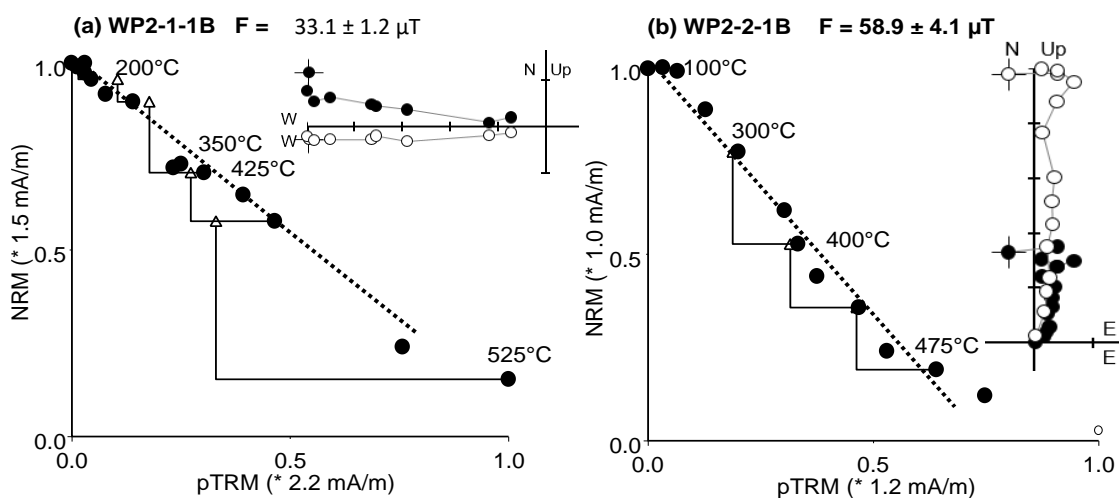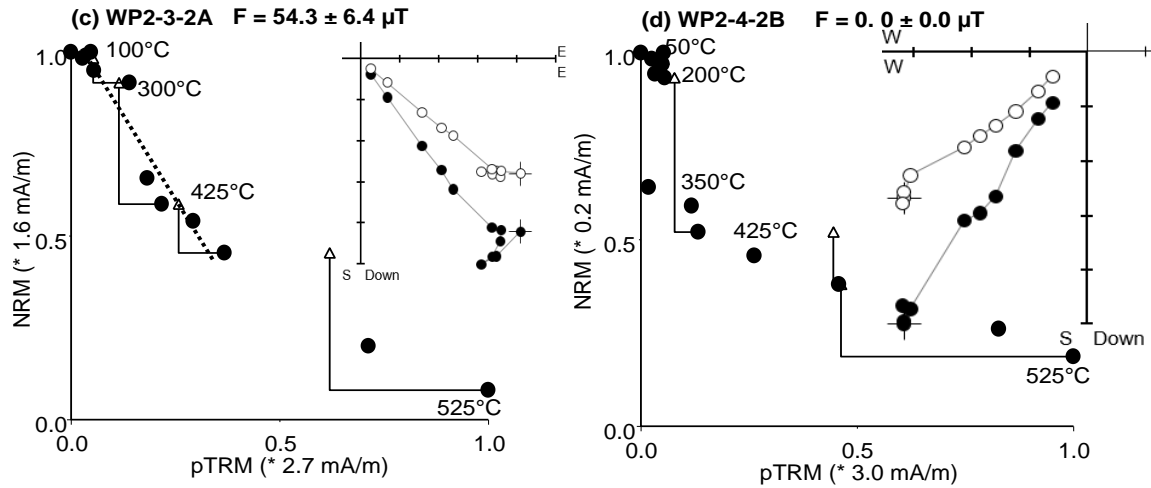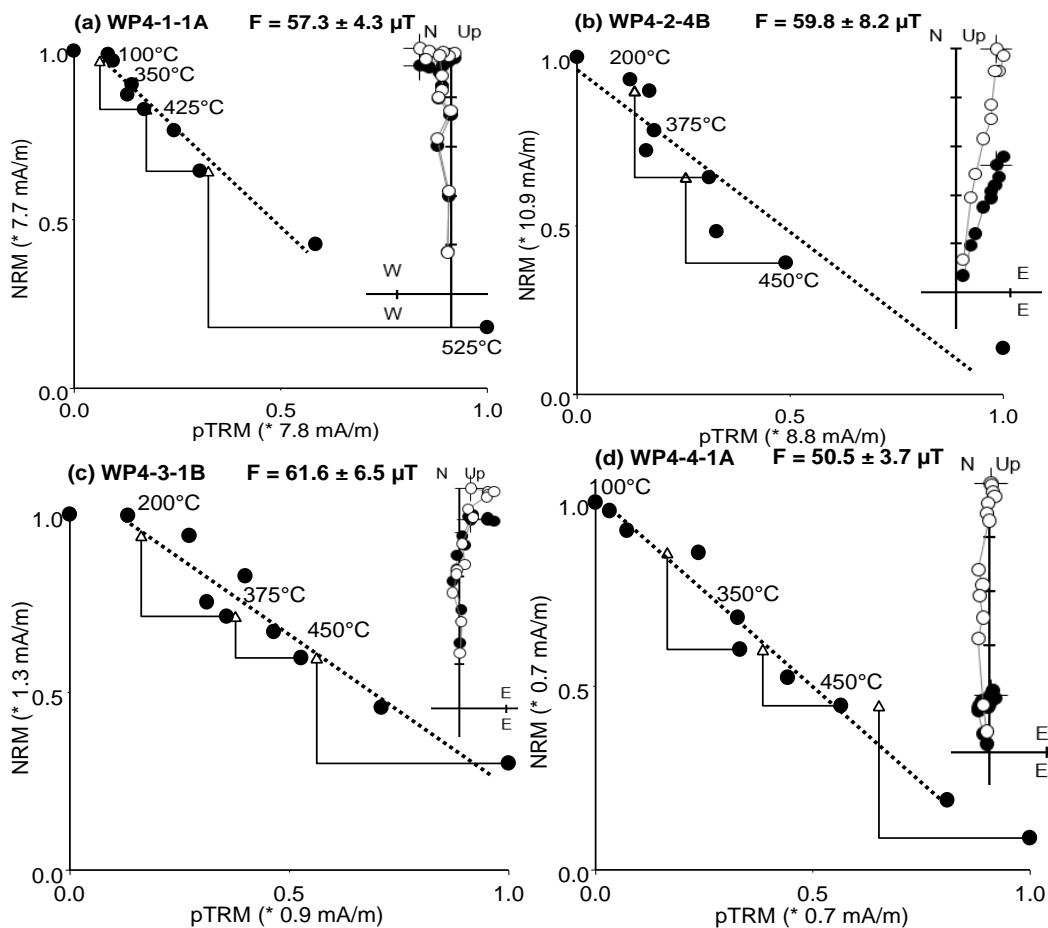


Figure 5.19. (a)-(d) Arai diagrams of specimens from stones WP4-1, WP4-2, WP4-3 and WP4-4 using Thellier Tool (Leonhardt et al., 2004). Zijderveld diagrams, plotted using Remasoft30 software, show demagnetization behaviour at each step (Chadima & Hrouda, 2006).

Table 5.12. Archaeointensity results measured for hangi site WP4. Table includes intensity values and statistical parameters of each specimen.

| Sample ID | Temp range (°C) | F±σ (μT) | N | B | f | q | $\delta_{CK}$ | $\delta_{pal}$ | α | MAD | $\delta_{TR}$ | $\delta_{t*}$ | Class |
|---|---|---|---|---|---|---|---|---|---|---|---|---|---|
| Quality Criteria | | | ≥5 ≥5 --- | ≤0.1 ≤0.15 --- | ≥0.35 ≥0.35 --- | ≥5 ≥0 --- | ≤7 ≤9 --- | ≤10 ≤18 --- | ≤15 ≤15 --- | ≤15 ≤15 --- | ≤10 ≤20 --- | ≤9 ≤99 --- | TTA TTB TTC |
| WP4-1-1A | 100-500 | 57.3±4.3 | 9 | 0.08 | 0.54 | 5.2 | 3.7 | 1.6 | 0.4 | 1.4 | 5.1 | 7.1 | A |
| WP4-1-2A | 100-450 | 54..7±19.3 | 10 | 0.4 | 0.67 | 1.5 | 5.5 | 16 | 1.7 | 2.1 | 11.2 | 3.6 | C |
| WP4-2-2A | 100-500 | 91.6±10.9 | 11 | 0.11 | 0.7 | 5 | 7 | 19.4 | 1.6 | 2.1 | 5.4 | 0.3 | C |
| WP4-2-3B | 375-500 | 55.2±8.3 | 6 | 0.15 | 0.5 | 2.6 | 14 | 20.5 | 1.2 | 2 | 10.5 | 0 | C |
| WP4-2-4A | RT-500 | 61.3±6.3 | 9 | 0.11 | 0.78 | 6.1 | 5.1 | 94.2 | 0.7 | 1.8 | 7.3 | 0 | C |
| WP4-2-4B | RT-500 | 59.8±8.2 | 9 | 0.14 | 0.92 | 5.2 | 5.6 | 9.8 | 0.8 | 2 | 8.6 | 0 | A |
| WP4-3-1B | 200-525 | 61.6±6.5 | 9 | 0.11 | 0.66 | 5.1 | 8.6 | 4.6 | 6.5 | 3.9 | 2.8 | 2.8 | B |
| WP4-4-1A | 100-450 | 52.4±5.9 | 7 | 0.11 | 0.54 | 3.9 | 7.9 | 8 | 7.9 | 3.4 | 4 | 2.3 | B |
| WP4 Mean | | 57.5±3.6 | 7 | | | | | | | | | | |

# 5.7. Discussion

Thermal demagnetization experiments on the Weld Pass hangi sites WP1, WP2 and WP4 resulted in the directional data of all specimens as shown in Figure 5.20. Data points of the same colour indicate data of specimens from one stone. It can be clearly seen that the directions of stones WP2-1, WP2-3, WP2-4, and one specimen from WP4-3, are scattered at large angles from the main cluster, indicating that the stones have been completely disturbed from their original orientations. Accordingly, the directional data of these stones has been rejected for calculations of the mean direction of the site. WP1-4, WP4-1, and WP4-4 are also shifted slightly away from the main cluster, so nor are they included in the calculation of mean directional data of the sites WP1, WP2 and WP4. It can be observed that the $\alpha_{95}$ of WP4-4 intersects with the main cluster due to its large value greater than 10°, which lies outside the selection criteria. WP4 was a smaller hangi in comparison to WP1 and perhaps not used as much – or perhaps the stones did not undergo multiple heating. Although the stones were packed in sand, some do seem to have been moved slightly as indicated by demagnetization results. The average directional data from stones WP1-1, WP1-2, WP1-3, WP1-4, WP2-2, WP4-1, WP4-2 and WP4-4 with $\alpha_{95}$ are plotted on a Wulffnet (Figure 5.21). The declinations of these five stones are between 10°-20°, whereas the

inclination has a larger scatter in the range -52° to -72°. Therefore, rather than calculating the mean directional data of individual hangi sites, the mean directional data of 25 specimens from the three hangi, WP1, WP2 and WP4, is collectively calculated: Dec = 15.1°, Inc = - 61.8°, $\alpha_{95}$ = 2.6°. This data has been used for the archaeomagnetic dating of Weld Pass hangi sites (Pavon-Carrasco et al., 2011). The average declination and inclination of the site are compared with the respective palaeosecular variation reference curves for New Zealand (NZPSV1K) (Turner et al., 2015). The experimental data of Weld Pass is relocated to the location for which the reference curve is used. Probability density functions resulting from the comparison give a combined result for the archaeomagnetic dating of the site. The estimated age ranges of the site are 1711-1765AD (Figure 5.22 (a)) with confidence of 65%, and 1662-1859AD (Figure 5.22 (b)) with confidence of 95%. From archaeomagnetic dating figures (Figure 5.22 (a) & (b)), it can be seen that the uncertainty in the inclination curve where hangi data intersects is greater than that in comparison to the declination curve. So it is more likely that the age range of Weld Pass sites is on the younger side of the age range given by the archaeomagnetic dating tool.
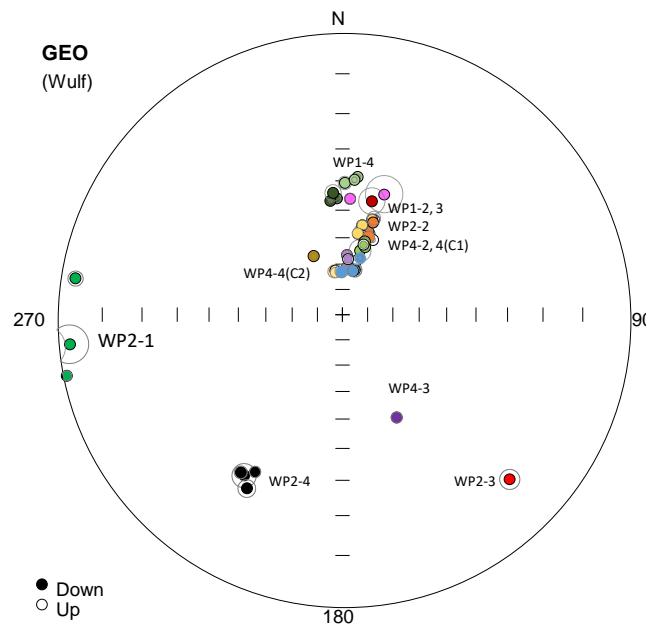


Figure 5.20. Stereographic projection of directional data of each specimen from the stones of sites WP1, WP2 and WP4.
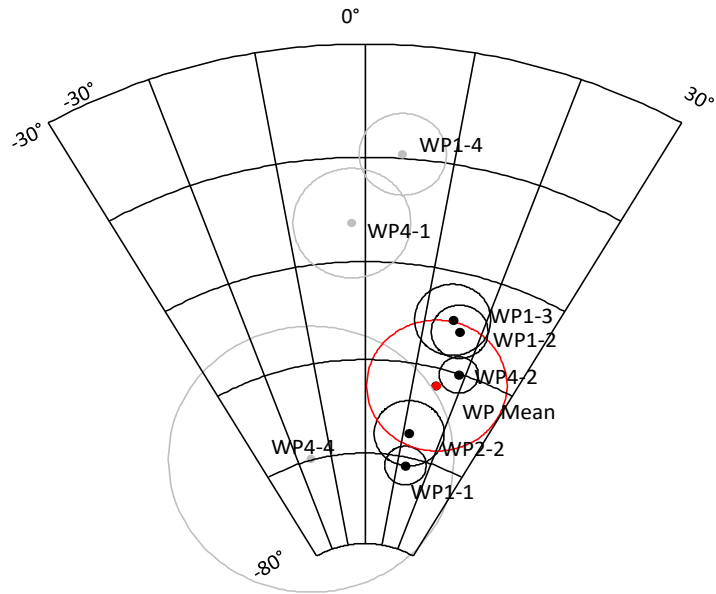
Figure 5.21. Equal angle stereographic plot of directions of hangi stones from Weld Pass. Black and grey dots are average directional data of specimens from stones WP1-1, WP1-2, WP1-3, WP2-2, WP4-2, WP1-4, WP4-1 and WP4-4. Circles around the dots are $\alpha_{95}$'s of mean direction. The red encircled dot is the mean directional data of stones WP1-1, WP1-2, WP1-3, WP2-2, and WP4-2, with $\alpha_{95}$ calculated for each stone.



(a) WP Directional data:
Latitude: -41.61° S
Longitude: 174.055° E
Dec = 15.1°, Inc = -61.8°, $\alpha_{95}$ = 2.6°

Dating: WP

Combining Probability Density Functions

Threshold = 0.0011049 (Confidence = 95%)
Between t = 1030AD and 1990AD
**[1662AD   1859AD]**
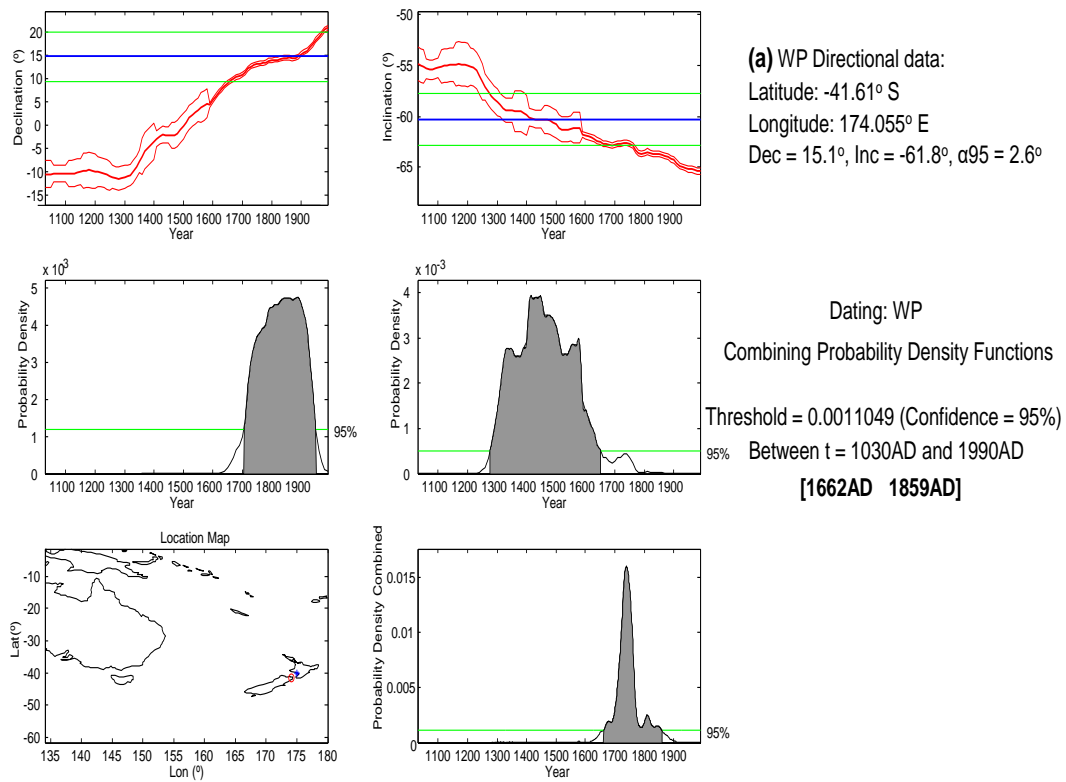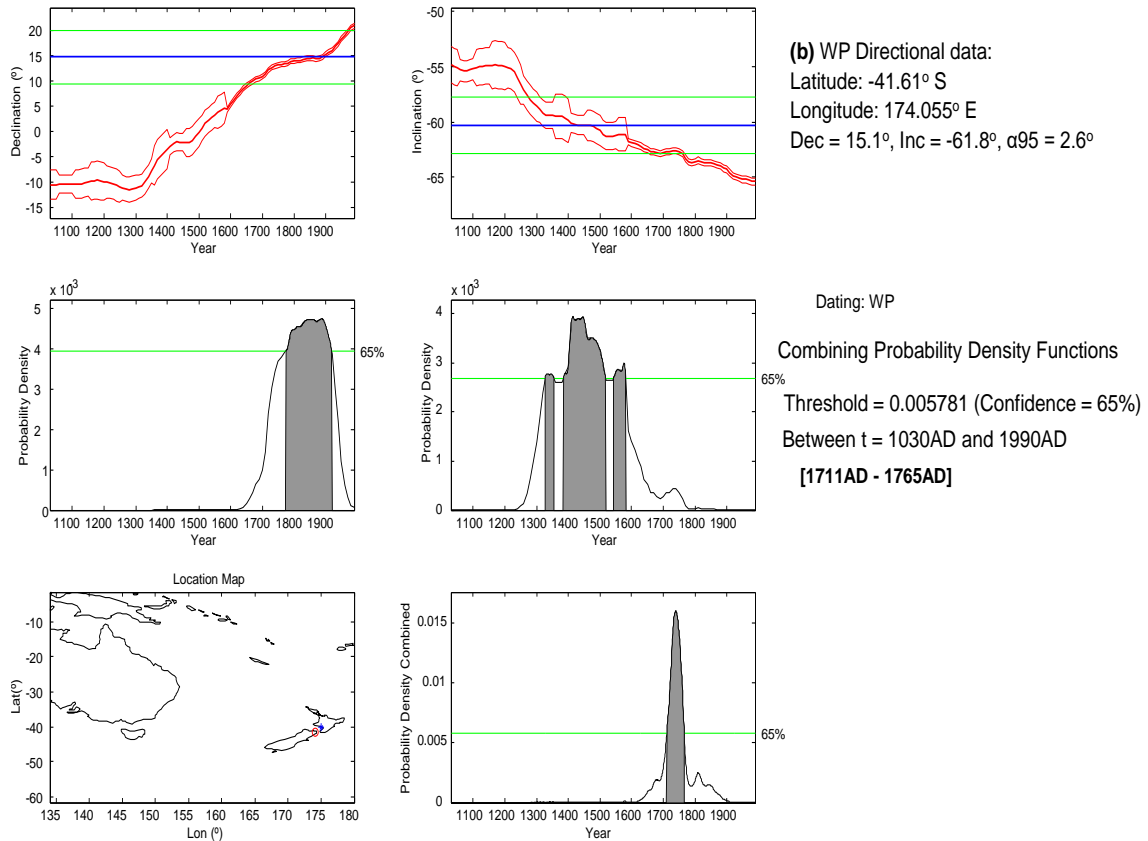
Figure 5.22. Archaeomagnetic dating of Weld Pass hangi sites with 95% confidence (a), and 65% confidence (b).

Archaeointensity determinations yielded a success rate of 80%. In Figure 5.23, the mean archaeointensity of the site, 59.9 ± 3.3 µT, is compared with field intensities calculated from the geomagnetic field model *gufm*1 at the location of Weld Pass (Jackson et al., 2000), Blenheim (latitude/longitude ~ 41.6°S/ 174.0°E). *gufm*1 is a global field model. For 1838 and later *gufm*1 is based on absolute field measurements (red line in Figure 5.23), but prior to this it is based on the assumption of a linear decay of the geocentric axial dipole moment with time (blue line in Figure 5.23). The graph represents the Weld Pass archaeointensity and archaeomagnetic date described above. It can be seen that the mean intensity value is in excellent agreement with the reference curve.

138
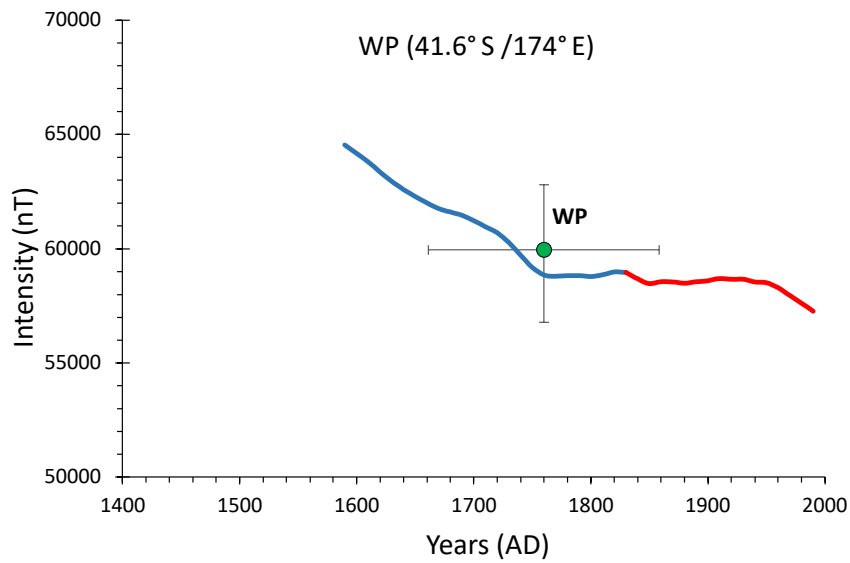
Figure 5.23. Archaeointensity and archaeomagnetic date for WP plotted with the variation in geomagnetic field intensity at Weld Pass (latitude/ longitude 41.6°S /174°E ) over the past 400 years, calculated using the *gufm1* model of Jackson et al. (2000).

## 5.8. Conclusion

Rock magnetic data indicates that most of the lithified sandstones contain titano-magnetite. The carrier of magnetization in the stones are PSD grains. The archaeomagnetic direction of the Weld Pass hangi sites, Dec =15.1°, Inc = -61.8°, $\alpha_{95}$ =2.6°, N =26 (from five stones of three sites WP1, WP2, and WP4), is used to obtain an archaeomagnetic date for the site of 1662-1859AD with 95% confidence, or 1711-1765AD with 65% confidence. The average archaeointensity calculated from the data of all three sites is F = 59.9 ± 3.3 µT.

# 6. Riverlands Hangi Site

## 6.1. Archaeological Setting

Riverlands archaeological site, P28/149, 5km south of Blenheim, was uncovered during the development of an area behind Riverlands Industrial Estate. The geology of this area consists of mostly unconsolidated to poorly consolidated mud, sand, gravel, and peat of mostly alluvial and colluvial origin (Figure 6.1). Next to the Riverlands Industrial site is a canal named on maps as Co-op drain (Figure 6.2). The canal, originally known as Ohine-anau-mate, and which connects a former swamp to coastal lagoons, attracted archaeologists to investigate the construction area. Traditional accounts say that the canal is part of a 19km-long system of canals, dug by Rangitane people from the mid- to late-1700s (Skinner, 1912), to attract fish and birds for hunting and to link natural waterways. The canal, which has not been modified, can be seen on maps from before and after 1900 (Foster, 2015). The canal was previously recorded as archsite P28/47.
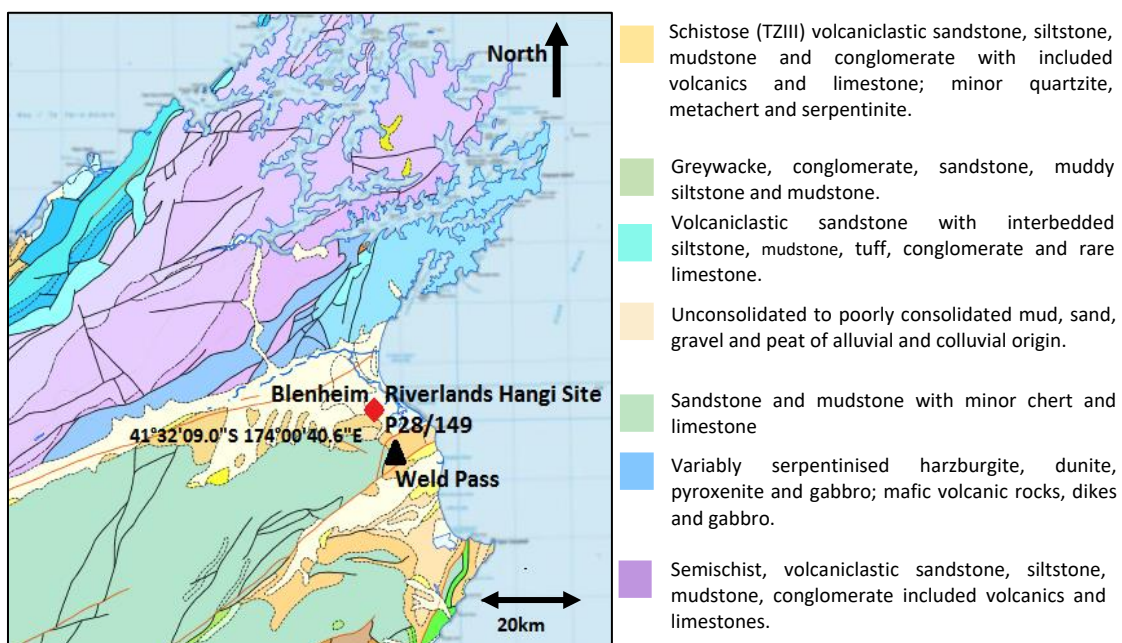


Figure 6.1. Geological map of Marlborough region. From GNS website (http://data.gns.cri.nz/geology/)
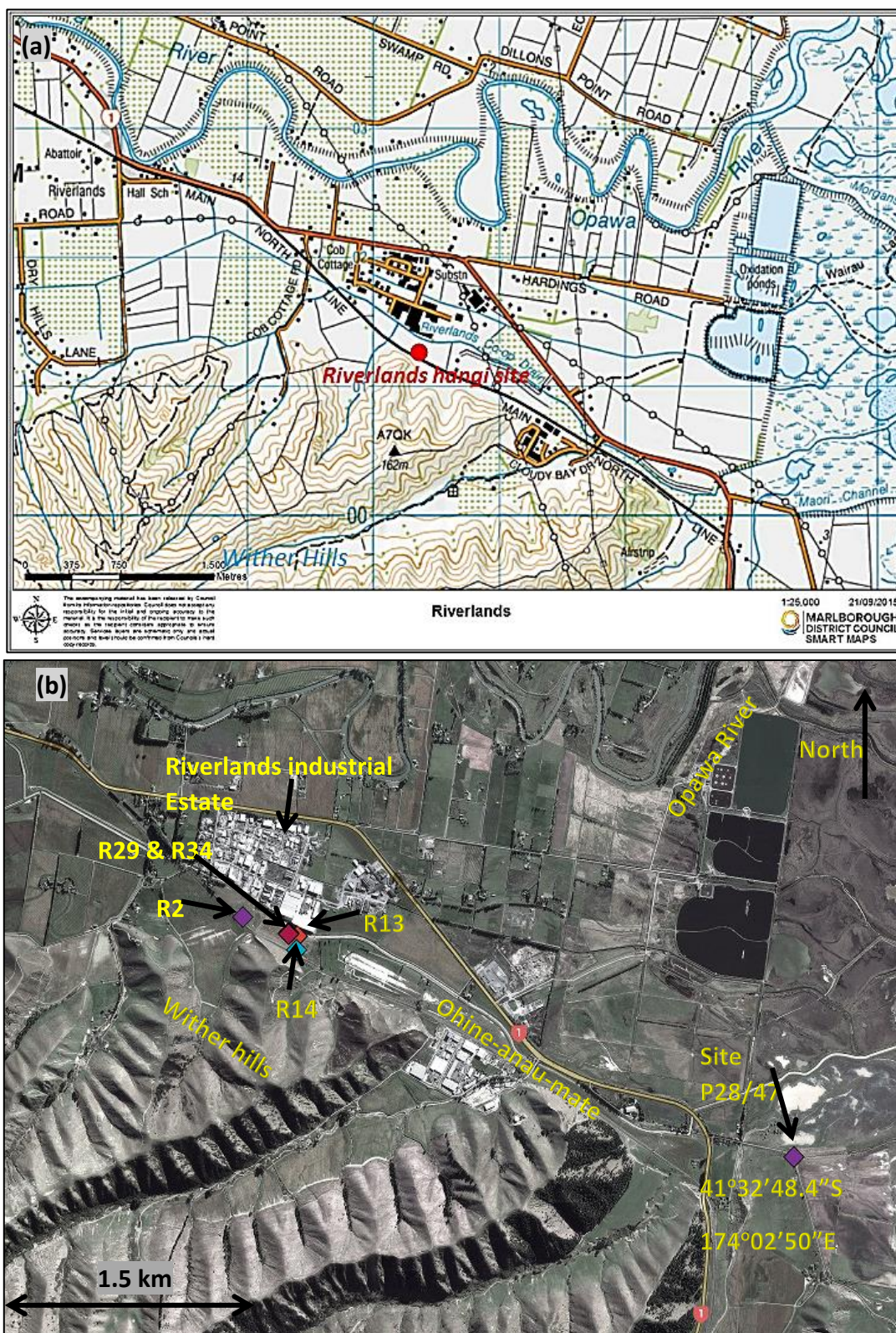
Figure 6.2. (a) Topographic map of Riverlands area (http://maps.marlborough.govt.nz/portal/). (b) Aerial photo of Riverlands area, showing locations of archaeological features R2, R13, R14, R29 and R34 (see Figure 6.3 and text) (photo downloaded from Google Earth, date of image 2010).

Figure 6.3. (a) Riverlands rear site development plan: areas A and B, with green and red boundaries, are the areas which were inspected by archaeologists (map used from site report by Foster, 2015. The blue dashed line encloses the archaeological features in lot 5, lot 6 and the pond areas. (b) Cultural features in lot 5, lot 6 and storm water retention ponds (map produced by Reg Nichol).

The archaeological features were found in 7.2ha between the canal and the railway line, just west of Wither Hills. The area was used historically for grazing and recently as a storage place. The earthworks were done for the sub-divisional development of the area into 17 lots. The important features noticed by archaeologist Deb Foster were in the areas marked A (a dune formation) and B (a long strip along the canal (Figure 6.3)). On the basis of information from previously recorded sites, it was suggested that dune areas were preferred by people for temporary settlement, so there was the possibility of finding more archaeological features in the area. The hangi site RL1 was found in lot 6 and sampled during fieldwork. The hangi site is labelled in Figures 6.2 and 6.3 as archaeological feature R14.

## 6.1.1. Features found in subdivision

Stripping of topsoil did not reveal any cultural features in lot 1. In the dune formation area, A (Figure 6.3 (a)) of lot 2, two features, R1 and R2, were noticed by archaeologist Reg Nichol. R1 was a small hangi containing reddened stones and charcoal. R2 had randomly scattered reddened stones but no charcoal or other evidence of cooking and was interpreted as a cache of cooking stones. Neither of these was sampled for this project. No archaeological features were found in lot 3 (Foster, 2015).

Patches of dark brown sand, interpreted as the residue of burnt trees and bushes, were found in lot 5. Cultural features observed by Foster in this lot were recorded as feature R17, a fire-scoop with a cockle shell but no fire-cracked stones, and R29, a fire-scoop, which had neither stones nor cockle shells. R34 was also a hangi filled with fire-cracked stones and cockle shells.

Foster (2015) identified 12 cultural features in lot 6 (Figure 6.3 (b)). R3, R4, R6 and R12 were fire-scoops; R5, R13 and R14 were hangi pits; and R7, R9, R10 and R11 showed evidence of fire. There were chalky-type and marly-type chert pieces in feature R8 (Figure 6.3 (b)). One of the chert pieces was identified as a flake. The detailed description of all these features is given in the archaeological report of the site by Foster (2015). Features R3, R4 and R10 were also identified as cultural and were in the

area to be used as storm water retention ponds. We sampled feature R14 at NZTM coordinates E16684358 N5401265 (±3m). This site has ArchSite number P28/149. All other sites excavated before the sampling day had been destroyed, so could not be sampled.

## 6.1.2. Site of interest

A hangi feature noticed by Foster in lot 6, 100m away from Ohine-anau-mate, and isolated from other archaeological features on the site, was recorded as R14 (Figures 6.3 & 6.4). This site was sampled during a field trip in March 2014. The hangi was located on a slightly elevated area, which was thought to be the edge of a swamp (Foster, 2015). The topsoil of the hangi had been scraped off, and the stones seemed to be slightly disturbed. The hangi had a diameter of 1.3m but had not been excavated completely, so the depth of the hangi was not known. The hangi contained fire-cracked stones, blackened greasy sand, and charcoal in between the stones (Figure 6.4). The greasy sand suggested that the hangi may have been used for cooking meat: seals or pigs, or possibly moa. A 300mm long, partly-crushed moa bone was found within 20m of the hangi site, in an area where earthworks were done for construction of a road parallel to the railway line (Foster, 2015).



Figure 6.4. Riverlands hangi site R14, hangi stones sampled from this in March 2014.

## 6.2. Sampling

Although some hangi sites and fires-scoops were found in the Riverlands archaeological area P28/149, only one hangi (R14) could be sampled. Some had already been destroyed before the fieldwork, while others were not excavated until later. The topsoil of the hangi had already been removed by the contractor with a scraper (Figure 6.4). Blackened sand and some reddened stones were visible at the top of the hangi at the time of sampling, but there is a possibility that the uppermost stones of the hangi could have been disturbed by the scraping. The soil and some cracked stones were removed from the top, using a plastic trowel. Three stones, RL1, RL2 and RL3, were oriented and sampled from the top, exposed layer of the hangi. There were more stones available in the hangi beneath these three stones. Four more stones, RL4, RL5, RL6 and RL7, were oriented and sampled from this next layer of the hangi. Due to rainy weather, the sun compass could not be used, and only the direction of the magnetic north was marked on the stones.

Back in the laboratory five stones, RL1, RL2, RL3, RL5 and RL7 were set in concrete and drilled to produce cylindrical cores. The stones RL4 and RL6 were not drilled because RL4 was cracked, and RL6 was thin. Details of the cores and specimens from each stone are given in Table 6.1.

Table 6.1. Details of cores and specimens from each stone

| Name of stone | Number of cores | Number of specimens |
|---------------|-----------------|---------------------|
| RL1 | 3 | 7 |
| RL2 | 3 | 6 |
| RL3 | 2 | 4 |
| RL5 | 3 | 6 |
| RL7 | 3 | 6 |
| Total | **14** | **29** |

## 6.3. Age Control

Three charcoal samples collected from the Riverlands hangi site were sent to Auckland University palaeobotanist, Dr. Rod Wallace, for identification of species. All were identified as matai which lives up to 1000 years, and so not recommended for $^{14}$C dating of the last use of the hangi. However, since there was no other age control for this site, one charcoal sample was sent for $^{14}$C dating to GNS, Lower Hutt. The calibrated $^{14}$C date lies between 1161 and 1264AD (Figure 6.5 & Table 6.2), which predates the accepted settlement date of New Zealand of around 1300AD. The $^{14}$C date therefore probably includes a significant inbuilt age – the age of the wood at the time of burning in the hangi. A realistic estimate of the age of this archaeological site, therefore, depends on archaeomagnetic dating.
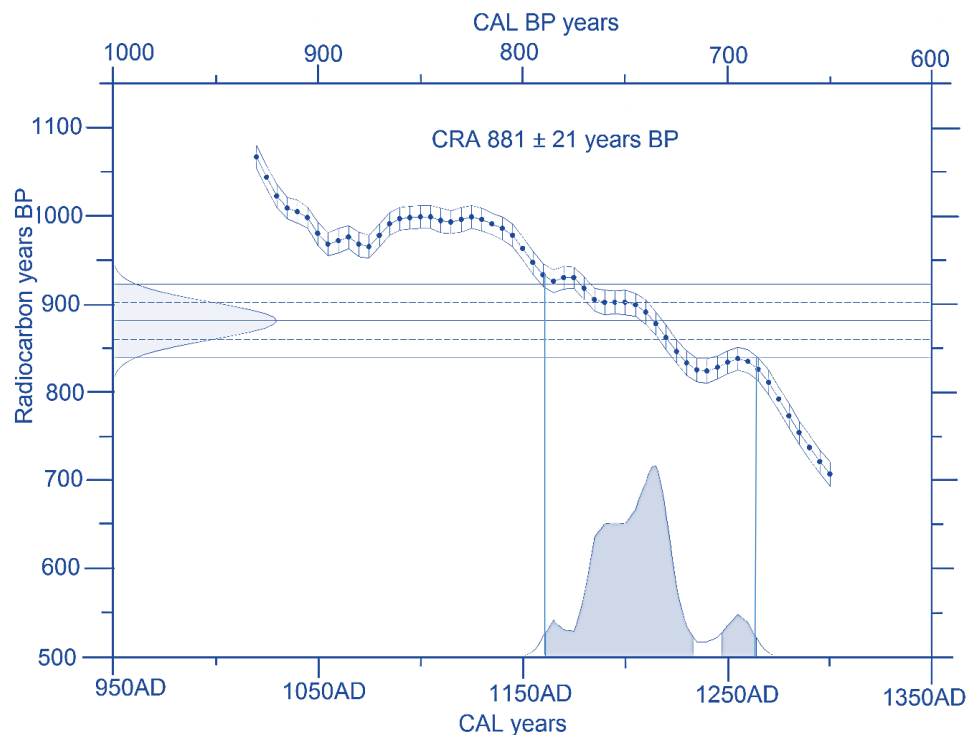


Figure 6.5. Radiocarbon date representation using SHCAL13 calibration curve for hangi site at Riverlands (Hogg et al., 2013. Dates have been determined using Accelerator Mass Spectrometry at GNS, Lower Hutt. Figures are created from program WINSCALX 5.1 (Sparks, R.J., and Manning, M.R. pers. com. WinscalX, version 5.1. GNS Science, 2011).

Table 6.2. Radiocarbon age estimation.

| Site Name | Material | Lab No. | $^{14}$C age (CRA) | Calibrated age range (95% confidence) |
|-----------|----------|---------|--------------------|---------------------------------------|
| RL | Matai | NZA58798 | 881±21BP | 1161 AD to 1264 AD (88.1% of area) |

# 6.4. Rock Magnetism

Measurements of the rock magnetic properties of the Riverlands hangi stones are described below.

## 6.4.1. Thermomagnetic Properties

To determine the Curie temperature and magneto-mineralogical alteration on heating, susceptibility versus temperature experiments were conducted on samples of the Riverlands hangi stones (Figure 6.6 (a)-(g)). The room temperature susceptibility of the stones lies in the range 0.01-1 × $10^{-6}$ m$^3$/kg. The susceptibility increases with temperature up to 300°C for stones RL1 and RL7 (Figure 6.6a & f) and then decreases to the Curie point. RL1 shows three magnetic phases in the heating curve, which turned into two in the cooling curve, showing a slight rise at 600°C and a strong Hopkinson peak at about 300°C. The results of RL7 are similar, but with only two phases apparent in the heating curve. In all other samples, there is no sharp Hopkinson peak, meaning that these stones may have a broader spectrum of grain sizes. Both RL1 and RL7 show significant magnetic enhancement, but subsequent experiments to only 400°C (Fig. 6.6 (b) & (g)) indicate that the onset of thermal alteration occurs above this temperature. RL2 has a very weak susceptibility of the order of $10^{-8}$ m$^3$/kg, so the susceptibility versus temperature plot (not shown) provided little information on the magnetic mineralogy of the sample due to the low signal to noise ratio of the measurement. RL3 also shows two phases of magnetization in the heating and cooling curves, with $T_{c1}$ around 550°C and $T_{c2}$ around 596°C (Figure 6.6 (c)). In the cooling curve, these points are shifted to 500°C and 622°C. Figure 6.6 (e) shows that RL5 also has weak susceptibility and resulted in an irregular heating curve.

The cooling curves of all samples show evidence of magnetic enhancement at high temperature: it is possible that these stones were not heated sufficiently in the hangi to reach the endpoint of thermal alteration. Heating-cooling curves to a maximum of 400°C are almost reversible, however, suggesting that the samples can provide reliable results up to 400°C as minerals will not alter thermally. The principal Curie temperatures of all the samples lie between 551 and 596°C, indicating that these stones carry small percentages of (titano) magnetite (with Ti < 10%) and/or cation-deficient (oxidized) titanomagnetite (Dunlop & Özdemir, 1997). The inverse susceptibility method was used for the calculation of Curie temperatures (Petrovský & Kapička, 2006), which are given in Table 6.3.
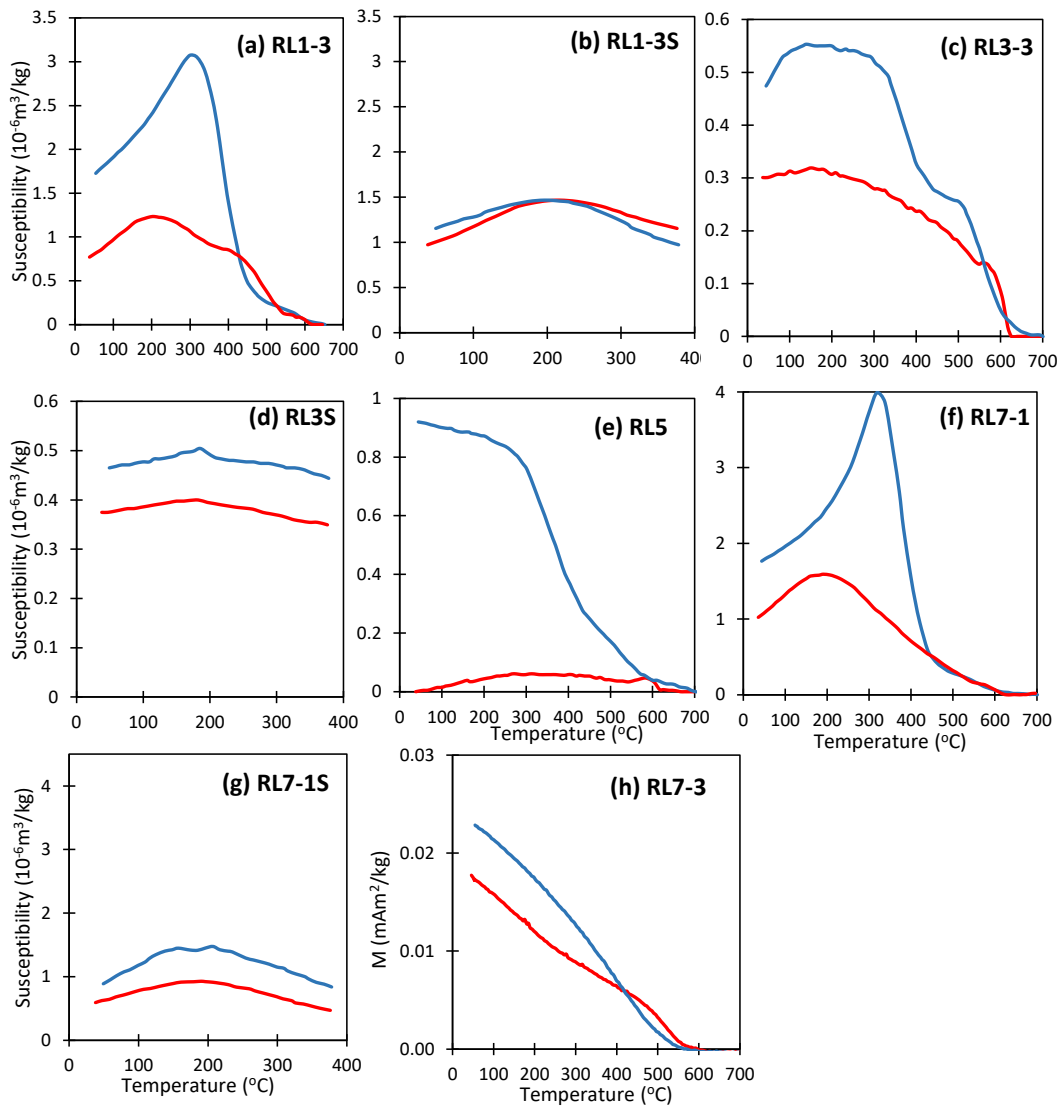


Figure 6.6. (a)-(f) Plots of susceptibility vs temperature for hangi stones RL1, RL3, RL5 & RL7. Red coloured lines indicate the heating curves and blue the cooling curves. (b), (d) & (g) Repeated experiment for samples from stones RL1, RL35 and RL7 up to 400°C. (h) $M_s$ vs T plot of a sample RL7-3, graph plotted using RockMag Analyzer 1.1 (Leonhardt et al., 2006).

149

A M$_s$ versus T curve for sample RL7-3 has also been plotted (Figure 6.6 (h)) using the VFTB at the University of Liverpool. As in the susceptibility versus temperature curve of Figure 6.6 (f), the heating curve indicates two phases: a weak inflection at about 350°C, and a principal Curie temperature at 551°C, calculated using the Moskowitz method (Moskowitz, 1981) in RockMag Analyzer (Leonhardt, 2006).

Table 6.3. Curie temperatures of Riverlands hangi stones. Calculations for $\chi$-T plots use the inverse susceptibility method (Petrovský & Kapička, 2006), and M$_s$ vs T plot is analyzed using software RockMag Analyzer (Leonhardt, 2006).

| Sample ID | Experiment | T$_c$ Heating (°C) | T$_c$ Cooling (°C) | T$_c$ Cooling Corrected (°C) | Difference (°C) |
|-----------|-----------|-----------|-----------|-----------|-----------|
| RL1-3 | $\chi$ vs T | 585 | 594 | 609 | 24 |
| RL3 | $\chi$ vs T | 596 | 622 | 637 | 41 |
| RL7 | $\chi$ vs T | 597 | 607 | 622 | 23 |
| RL7-3 | M$_s$ vs T | 551 | 540 | -- | 62 |

## 6.4.2. Hysteresis and IRM curves

To understand magnetic behaviour of Opihi River hangi stones hysteresis and IRM acquisition experiments were carried out Saturaion magnetization, saturation remanence (M$_{rs}$), coercivity (B$_c$) and coercivity of remanence (B$_{cr}$) were calculated and are given in Table 6.4. The VSM at the Australian National University and the VFTB at the University of Liverpool were used for these experiments. Data have been analyzed in an Excel spreadsheet (for RL1 & RL5) and with RockMag Analyzer 1.1 (for RL7) (Leonhardt, 2006). Hysteresis curves show the presence of a ferrimagnetic mineral with a considerable additional paramagnetic component (Figure 6.7 (a), (c) & (e), blue curves). The red curves show the data after removal of the paramagnetic trend. All the hysteresis loops are relatively narrow. The samples saturated at a field less than 250mT (Figure 6.7). B$_{cr}$ values are between 24.5 - 44.6 mT. RL7 has the lowest remanence saturation and coercivity (Table 6.4) of the three samples. The rock magnetic properties of RL1, RL5 and RL7 suggest that these weakly magnetized sandstones carry PSD grain-sized, low titanium titanomagnetite and cation-deficient titanomagnetite. Hysteresis parameters and ratios are shown in Table 6.4.
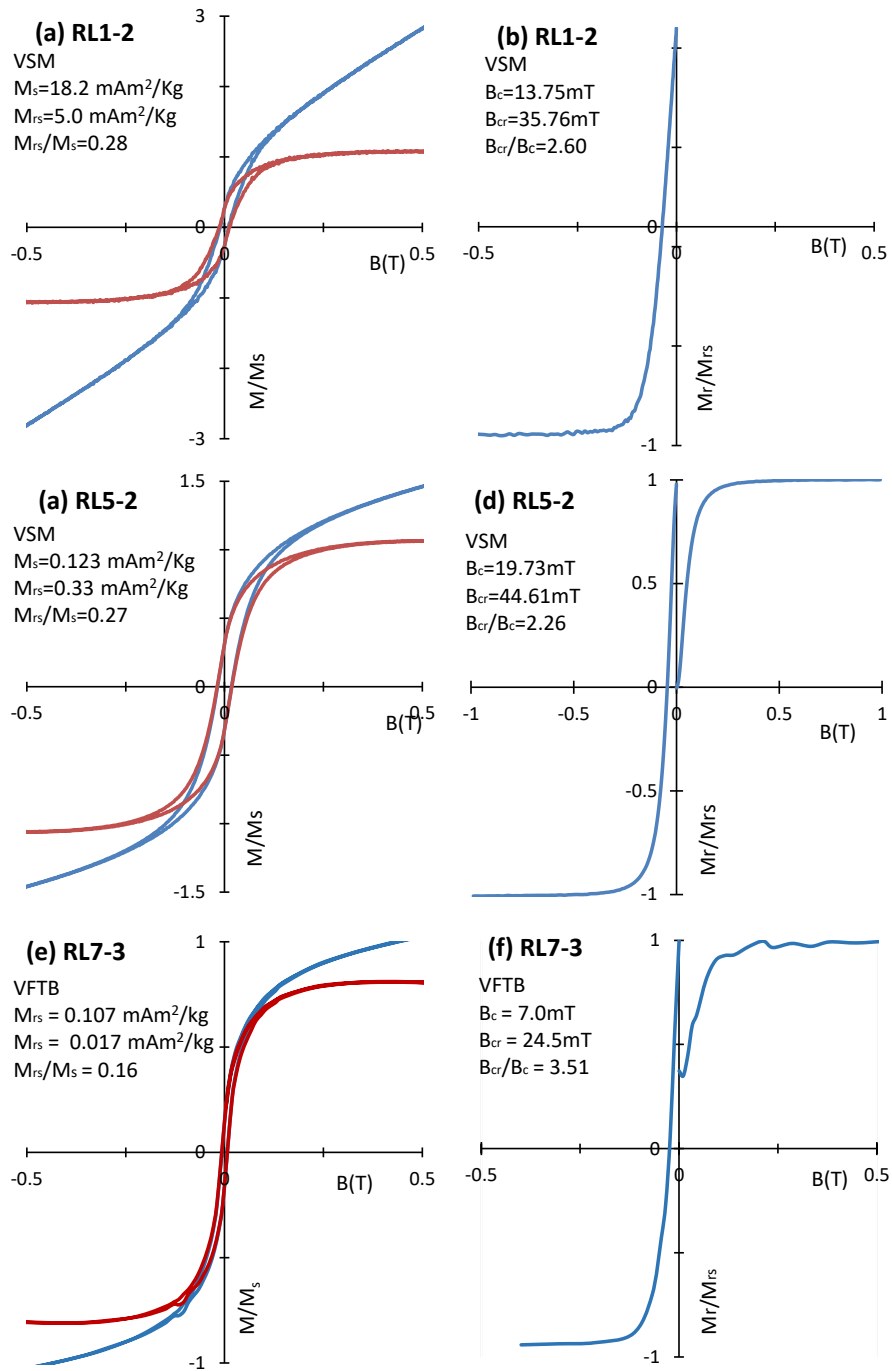
Figure 6.7. Hysteresis plots of samples RL1, RL5 and RL7 (a), (c), & (e)). The blue curves include the paramagnetic character and the red curves are after application of paramagnetic correction. The corresponding IRM and back-field curves of the samples are shown alongside (b), (d), & (f)).

Table 6.4. Hysteresis and IRM data of hangi stones from Riverlands.

| Sample ID | $M_{rs}$(mAm²/kg) | $M_s$(mAm²/kg) | $B_{cr}$(mT) | $B_c$(mT) | $M_{rs}/M_s$ | $B_{cr}/B_c$ |
|---|---|---|---|---|---|---|
| RL1-2 | 5.01 | 18.2 | 35.8 | 13.8 | 0.28 | 2.6 |
| RL5-2 | 0.033 | 0.123 | 44.6 | 19.7 | 0.27 | 2.3 |
| RL7-3 | 0.017 | 0.107 | 24.5 | 7.0 | 0.16 | 3.5 |

Figure 6.8 shows data in a Day plot (Day et al., 1977), together with Dunlop's mixing curves (Dunlop, 2002). The Riverlands stones have relatively low values of $M_{rs}/M_s$ and relatively high values of $B_{cr}/B_c$. The data points are beyond the third mixing curve and between the SD and MD regions. RL7-3 is closer to the MD area. The data are consistent with PSD or a mixture of SD and MD grains.
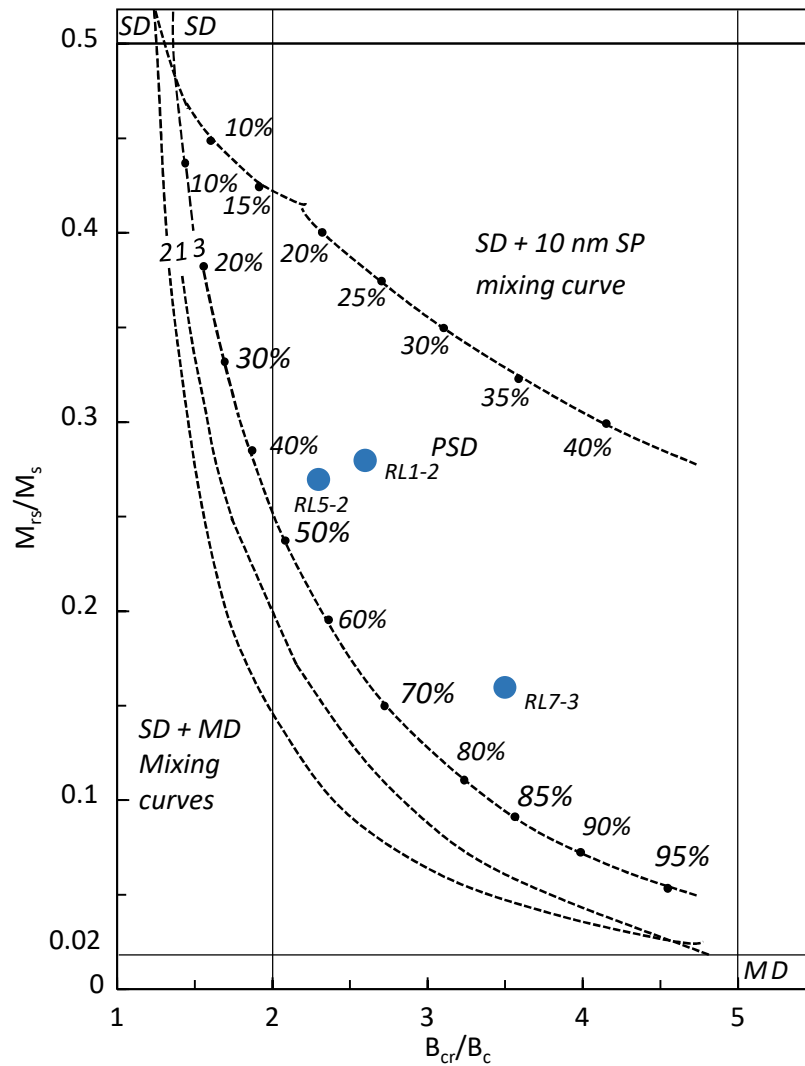


Figure 6.8. $M_{rs}/M_s$ vs $B_{cr}/B_c$ (Day et al., 1977) data of Riverlands hangi stones (blue dots) superimposed on the mixing curves of Dunlop (2002) for a single domain, multidomain and superparamagnetic grains.

### 6.4.3. Summary

Thermomagnetic and hysteresis data are consistent with the remanence carriers in the Riverlands hangi stones being Ti-poor titanomagnetite and titanomaghemite in the PSD grain size range or a mixture of SD and MD grains.

## 6.5. Thermal Demagnetization

Progressive thermal demagnetization experiments were carried out on six specimens from the five Riverlands hangi stones. Since the stones were relatively small, the remaining specimens were put aside for archaeointensity experiments.

Typical demagnetization data are shown in Figure 6.9 (a)-(e). The Riverlands stones have NRMs between 0.005 and 0.794 A/m, characteristic of silty sandstones. The Zijderveld plot of each sample shows that a weak VRM is removed by 50°C-100°C. All stones acquired a stable component of magnetization heading towards the origin. The demagnetization curves of specimens show that these samples have grains which start to unblock at 100°C. The common blocking temperature range is between 100 and 450°C. Small temperature steps of 25°C were used for specimens of stones RL2, RL3 and RL7. Figure 6.10 (f) shows the change in susceptibility of specimens during thermal demagnetization. Significant changes can be observed in RL3 above 200°C.

From the Zijderveld plot of specimen RL2-3B (Figure 6.9 (b)), and from Figure 6.10, it can be seen that the direction of its ChRM is quite different from the other four stones, and is unlikely to reflect a palaeomagnetic field direction. This means stone RL2 was disturbed after cooling, possibly during recent construction work on the site. Therefore, the directional data of stone RL2 is not included in the calculations of mean directional data of the site. The demagnetization curve of RL7-3A (Figure 6.9 (e)) is similar in shape to its thermomagnetic curve (Figure 6.6 (h)), completely demagnetized at temperature 550°C. RL1, RL3, RL5 and RL7 all have consistent declinations, but the inclinations are paired in two groups (Figure 6.10). RL1 and RL3 yield an average direction of Dec = 18.1°, Inc = -50.2°, $\alpha_{95}$ = 2.3° for 9 specimens. The average direction of stones RL5 and RL7 is: Dec = 19.6°, Inc = -68.3°, $\alpha_{95}$ = 1.6° for 10 specimens. This inclination difference may be

due to stones RL1, RL2 and RL3 being from the topmost layer of the hangi, where they may have been disturbed during levelling of the site, as mentioned in section 6.2.

The ChRM directions listed in Table 6.5 and plotted in Figure 6.10 also includes directional data obtained during archaeointensity experiments. The mean direction calculated from the 10 specimens of stones RL5 and RL7 is our best estimate of the ambient field at the time the hangi was last used.

**(e)** RL7-3A

Unit= 138.e-03 A/m

Mmax= 0.729 A/m

**(f)** Change in susceptibility during thermal demagnetization

—●— RL1-1A  —●— RL2-3B  —●— RL3-1A  —●— RL5-1C  —●— RL7-3A
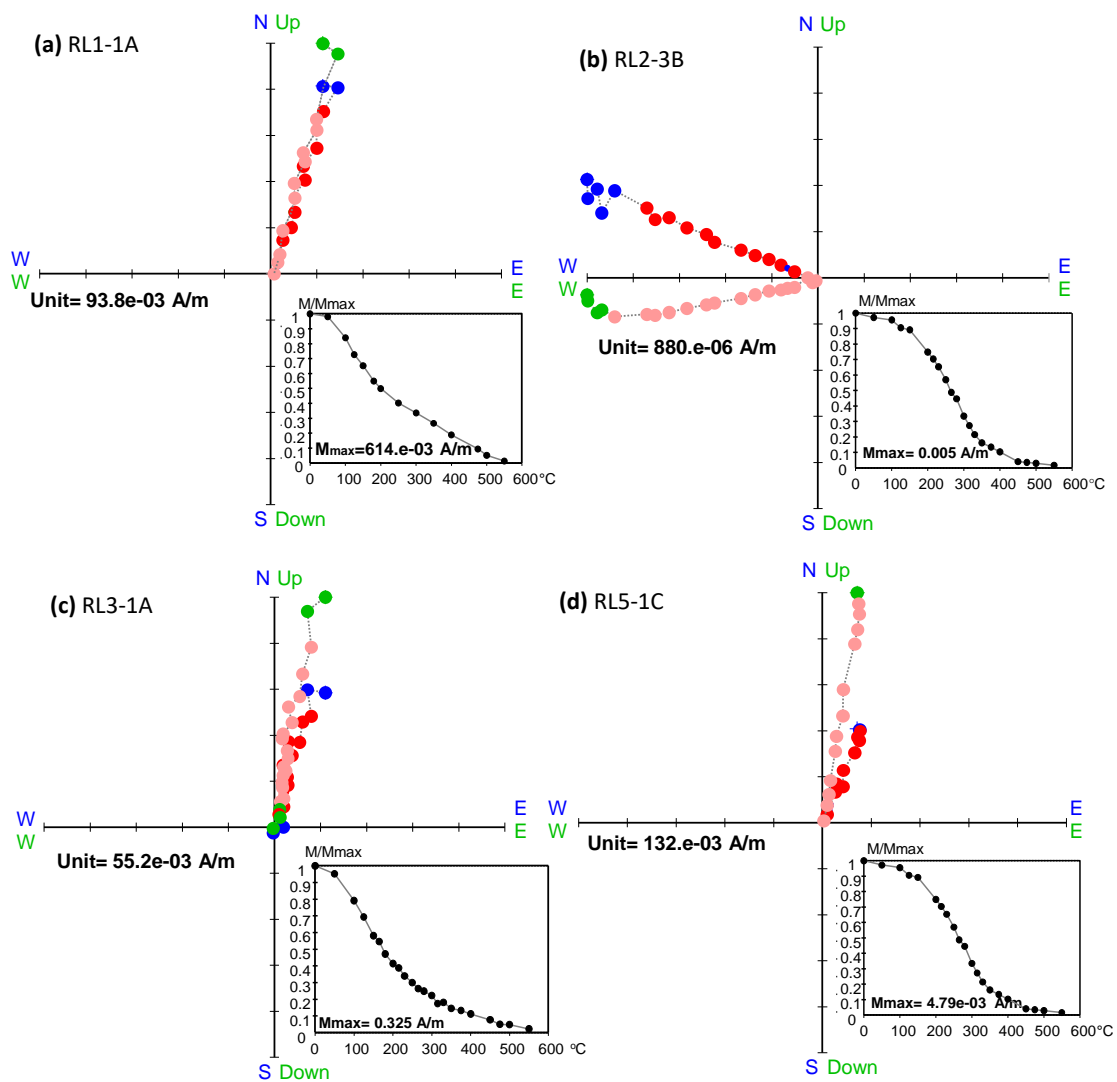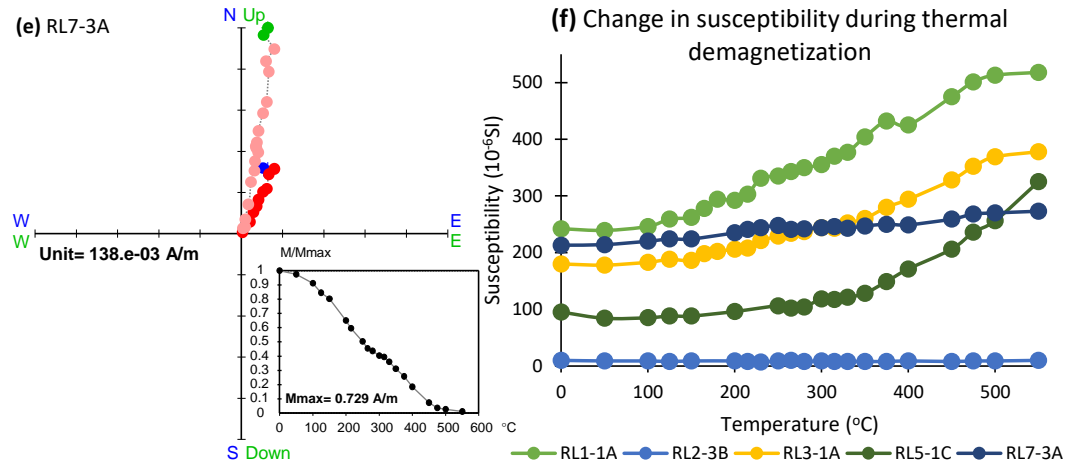
Figure 6.9. (a)- (e) Thermal demagnetization results of specimens from five hangi stones from Riverlands. Each figure includes Zijderveld plot and inset decay plot of specimen. Red and pink coloured dots indicate the data points included for PCA. (f) Shows change in susceptibility at each temperature step.



ChRMs of stones RL1, RL2, RL3, RL5, and RL7. Mean RL2: D = 292.8°, I = 10.2°, $\alpha_{95}$ = 2.4°, N = 5. Mean RL1, RL3, RL5, & RL7: D = 18.7°, I = -59.7°, $\alpha_{95}$ = 4.1°, N = 19. Mean RL1 & RL3: D = 18.1°, I = -50.2°, $\alpha_{95}$ = 2.3°, N = 9. Mean RL5 & RL7: D = 19.6°, I = -68.3°, $\alpha_{95}$ = 1.6°, N = 10.

Legend
○ RL1
● RL2
○ RL3
○ RL5
○ RL7
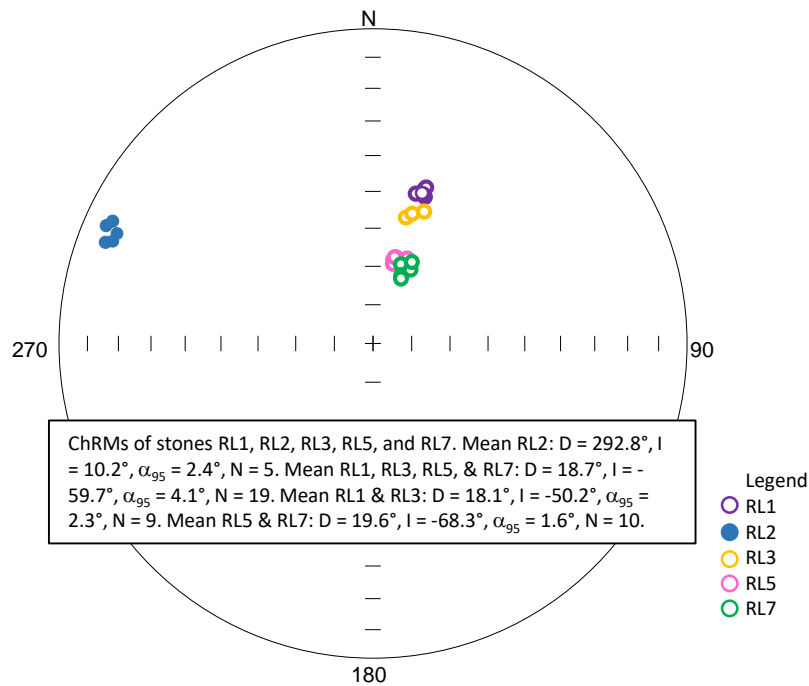
Figure 6.10. Stereographic projection of directional data for each specimen listed in Table 6.5. Here D and I refer to declination and inclination.

Table 6.5. Directional data of hangi site RL, calculated from thermal (THD). N is a number of specimens and n is a number of data points used for calculations. Calculations are made Remasoft30 software ((Chadima & Hrouda, 2006)). RT indicates room temperature. Only black coloured data is included for the calculation of mean directional data for the site.

| Sample ID | Temp range (°C) | N or n | Dec (°) | Inc (°) | MAD/$\alpha_{95}$ (°) |
|---|---|---|---|---|---|
| RL1-1A | 100-550 (THD) | 11 | 18.5 | -47.2 | 1.9 |
| RL1-1C | 100-550 (THD) | 17 | 18.8 | -46.5 | 2.3 |
| RL1-2A | 50-300 (P) | 12 | 16 | -49 | 2.4 |
| RL1-2B | 100-350 (P) | 11 | 19.6 | -49.1 | 1.8 |
| RL1-3A | RT-225 (P) | 9 | 18.8 | -48.6 | 1.9 |
| RL1-3B | RT-350 (P) | 14 | 18.2 | -48.3 | 2.8 |
| RL1 AVERAGE | | 6 | 18.3 | -48.1 | 1.1 |
| RL2-1A | RT-350 (P) | 12 | 294.1 | 9 | 5 |
| RL2-1B | RT-350 (P) | 12 | 295.1 | 9.3 | 3.1 |
| RL2-2B | 50-350 (P) | 11 | 290.7 | 9.8 | 3.1 |
| RL2-3A | 150-350 (P) | 7 | 293.2 | 12.3 | 2.7 |
| RL2-3B | 150-550 (THD) | 16 | 291.4 | 11.9 | 2.3 |
| RL2 AVERAGE | | 5 | 292.8 | 10.2 | 2.4 |
| RL3-1A | 100-550 (THD) | 18 | 14.7 | -56 | 2.6 |
| RL3-1B | RT-350 (P) | 14 | 16.9 | -54.5 | 2 |
| RL3-2A | RT-350 (P) | 14 | 21.2 | -52.9 | 2.2 |
| RL3 AVERAGE | | 3 | 17.7 | -54.4 | 3.8 |
| RL5-1B | 100-450 (P) | 15 | 13.4 | -67.8 | 2 |
| RL5-1C | 100-550 (THD) | 12 | 22.0 | -66.2 | 1.4 |
| RL5-2A | RT-425 (P) | 16 | 15.0 | -68.2 | 1.8 |
| RL5-2B | RT-500 (P) | 19 | 14.9 | -66.8 | 1.7 |
| RL5-3A | RT-500 (P) | 18 | 14.0 | -66.9 | 2 |
| RL5 AVERAGE | | 5 | 15.9 | -67.2 | 1.5 |
| RL7-1B | RT-350 (P) | 14 | 19.5 | -68.2 | 1.6 |
| RL7-2A | 50-350 (P) | 13 | 22.7 | -70.9 | 1 |
| RL7-2B | RT-350 (P) | 14 | 23.3 | -71.7 | 1.4 |
| RL7-3A | 100-550 (THD) | 10 | 27.1 | -68.5 | 1 |
| RL7-3B | RT-350 (P) | 14 | 25.7 | -66.6 | 1.1 |
| RL7 AVERAGE | | 5 | 23.7 | -69.2 | 2.2 |
| Mean RL1, RL3, RL5, &RL7 | | 19 | 18.7 | -59.7 | 4.1 |
| Mean RL1 & RL3 | | 9 | 18.1 | -50.2 | 2.3 |
| Mean RL5 & RL7 | | 10 | 19.6 | -68.3 | 1.6 |

## 6.6. Archaeointensities

Thellier-type archaeointensity experiments were performed on 18 specimens from five stones: RL1, RL2, RL3, RL5 and RL7. The Arai and Zijderveld plots of one specimen from each stone are shown in Figure 6.11 (a), (b), (c), (d) & (e). Tail/pTRM checks were performed to check for any thermal alteration. The archaeointensities were calculated using ThellierTool4.0 (Leonhardt et al., 2004). The experiments were continued until each specimen had lost at least 70% of its remanent magnetization. Most of the specimens provided consistent archaeointensity values (Table 6.6). Some specimens from the same stones gave stronger archaeointensity values, and have been rejected. It can be seen that some specimens (of stones RL2, RL3, RL5 and RL7) did not meet either the TTA or TTB selection criteria (Class TTC). However, their results are included in the calculation of average palaeointensity of the site (Table 6.6). The reason for the failure of tests is mineralogical changes in the specimens due to repeated heating steps. However, for each of these specimens, the gradient of the Arai plot gives an archaeointensity that is comparable to those of specimens which meet the selection criteria with class TTA/TTB (Table 6.6) (Paterson et al., 2014). The average archaeointensity of 15 specimens is 57.0 ± 3.6 µT.



(a) RL1-2A    F=57.9 ± 2.8 µT

**(b) RL2-2B    F=56.3 ± 3.3 µT**

**(c) RL3-2A    F= 59.8 ± 5.5 µT**

**(d) RL5-1B    F= 52.55 ± 3.7 µT**

**(e) RL7-3B**      **F= 60.0 ± 3.4 µT**
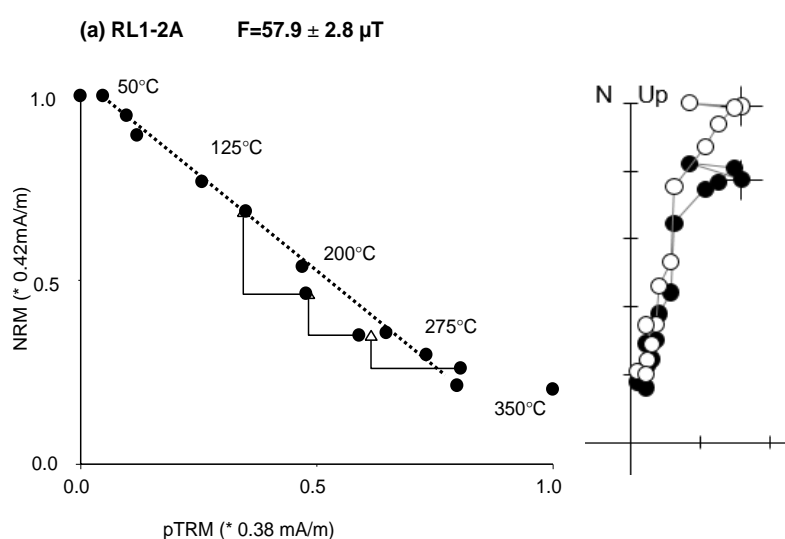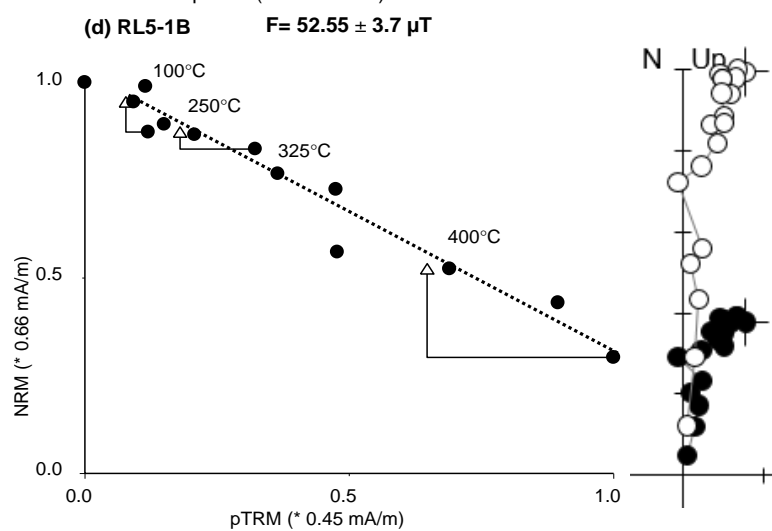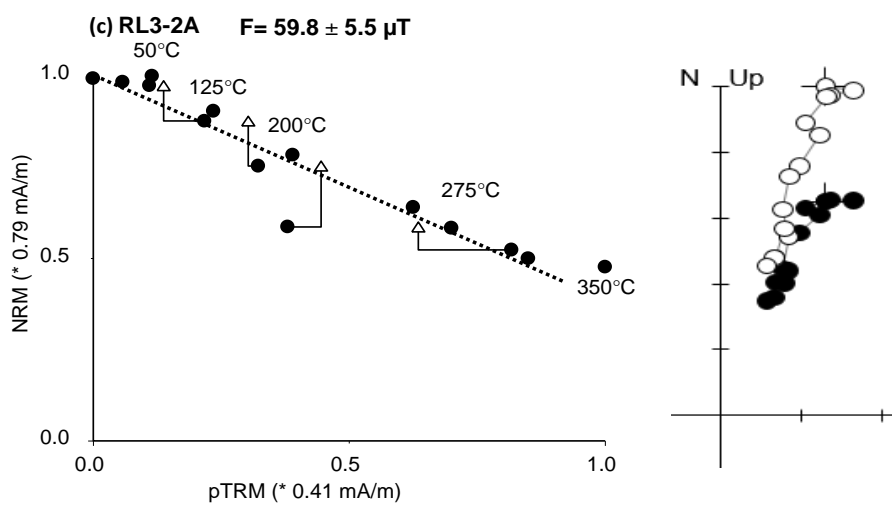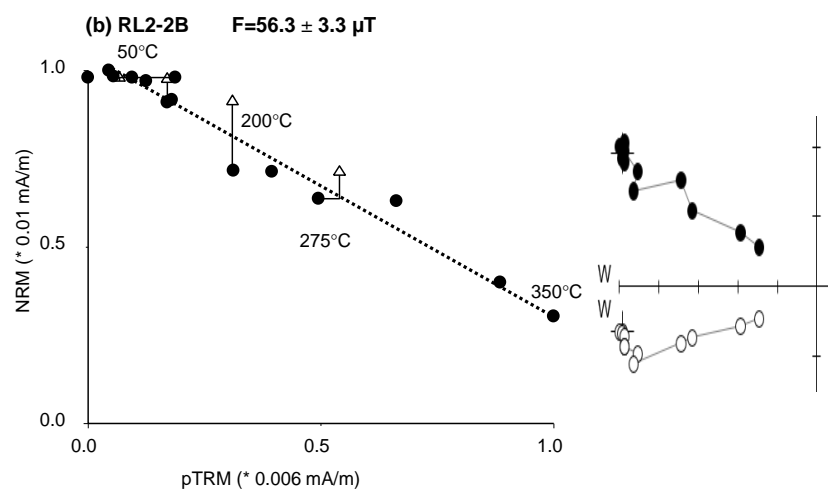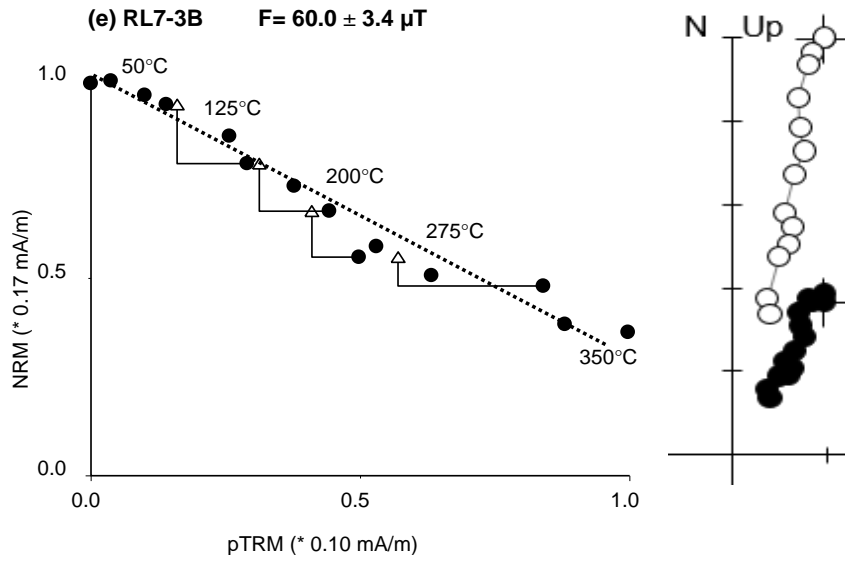
Figure 6.11. Arai diagrams of specimens from stones RL1, RL2, RL3, RL5 and RL7, plotted using Thellier Tool (Leonhardt et al., 2004). Zijderveld diagrams, plotted using Remasoft30 software, show demagnetization behaviour at each step (Chadima & Hrouda, 2006).

Table 6.6. Archaeointensity results obtained from Riverlands hangi stones. F are intensity results of individual specimens in µT. N is the number of data points included in each calculation. β, f, q, $\delta_{CK}$, $\delta_{pal}$, α, MAD, $\delta_{TR}$ and $\delta_{t*}$ are statistical parameters defined in Chapter 2. Parameters and results that meet TTA criteria are shown in black; those that fail TTA but meet TTB criteria are in yellow, and those that fail both TTA and TTB criteria are in the red.

| ID | Temp range (°C) | F±σ (µT) | N | β | f | q | $\delta_{CK}$ | $\delta_{pal}$ | α | MAD | $\delta_{TR}$ | $\delta_{t*}$ | Class |
|---|---|---|---|---|---|---|---|---|---|---|---|---|---|
| **Quality Criteria** | | | ≥5 ≥5 --- | ≤0.1 ≤0.15 --- | ≥0.35 ≥0.35 --- | ≥5 ≥0 --- | ≤7 ≤9 --- | ≤10 ≤18 --- | ≤15 ≤15 --- | ≤15 ≤15 --- | ≤10 ≤20 --- | ≤9 ≤99 --- | TTA TTB TTC |
| RL1-2A | 50-300 | 57.9±2.8 | 11 | 0.05 | 0.74 | 13.2 | 2.4 | 0.22 | 2.8 | 2.4 | 4.6 | 6 | A |
| RL1-2B | 100-350 | 60.8±5.4 | 11 | 0.09 | 0.67 | 6.3 | 3.1 | 9.7 | 2.5 | 1.8 | 5.3 | 4.6 | A |
| RL1-3A | RT-225 | 57.0±5.0 | 9 | 0.09 | 0.57 | 4.8 | 2.1 | 7 | 4.3 | 1.9 | 6.7 | 0.2 | A |
| RL1-3B | RT-350 | 60.9±5.7 | 12 | 0.09 | 0.75 | 6.9 | 14.4 | 33.4 | 4 | 2.8 | 6.9 | 0 | C |
| RL2-1A | RT-350 | 53.4±11.2 | 14 | 0.2 | 0.7 | 2.5 | 12.9 | 76.9 | 8.6 | 5 | 12 | 2.3 | C |
| RL2-1B | RT-350 | 52.5±2.5 | 14 | 0.05 | 0.76 | 10 | 17.3 | 48.1 | 11.1 | 6.5 | 17 | 0 | C |
| RL2-2B | 50-350 | 56.3±3.3 | 13 | 0.06 | 0.67 | 8.1 | 16.1 | 87.7 | 9 | 5.1 | 12 | 1 | C |
| RL2-3A | 150-350 | 51.5±4.3 | 9 | 0.08 | 0.53 | 4.4 | 12.7 | 73 | 7.4 | 4.2 | 7.6 | 1.3 | C |
| RL3-1B | RT-350 | 71.9±5.1 | 14 | 0.07 | 0.66 | 7.7 | 14.5 | 78.1 | 2.4 | 2 | 3.9 | 8.7 | C |
| RL3-2A | RT-350 | 59.8±5.5 | 14 | 0.09 | 0.56 | 4.9 | 15.5 | 144 | 5.1 | 2.2 | 4.3 | 2 | C |
| RL5-1B | 100-450 | 52.5±3.7 | 12 | 0.07 | 0.65 | 8.1 | 4.1 | 3.2 | 2.4 | 2.2 | 6.9 | 8.7 | A |
| RL5-2A | RT-425 | 53.0±11.7 | 11 | 0.2 | 0.67 | 2 | 40.8 | 77.3 | 1.6 | 2.8 | 8.6 | 4.9 | C |
| RL5-2B | RT-500 | 61.7±10.5 | 15 | 0.2 | 0.87 | 4.6 | 12.7 | 14.6 | 2.1 | 1.9 | 8.5 | 3.4 | C |
| RL5-3A | RT-500 | 58.0±8.1 | 15 | 0.14 | 0.89 | 5.8 | 16 | 21.3 | 1.3 | 2.1 | 10 | 12 | C |
| RL7-1B | RT-350 | 72.1±4.3 | 14 | 0.06 | 0.66 | 9.9 | 3.5 | 4.7 | 3.2 | 1.6 | 8.1 | 5 | A |
| RL7-2A | 50-350 | 88.7±8.0 | 13 | 0.09 | 0.63 | 6 | 6.1 | 28.3 | 1.3 | 1 | 6.6 | 6.2 | C |
| RL7-2B | RT-350 | 59.4±3.3 | 14 | 0.06 | 0.72 | 11.6 | 7.5 | 15.2 | 2.7 | 1.4 | 6.1 | 3.2 | B |
| RL7-3B | RT-350 | 60.0±3.4 | 14 | 0.06 | 0.68 | 10.8 | 5.2 | 8.7 | 1.8 | 1.1 | 6.9 | 6.7 | A |
| Average | | **57.0±3.6** | 15 | | | | | | | | | | |

159

## 6.7. Discussion

The initial magnetic susceptibilities and NRM of Riverlands samples have a difference of two orders of magnitude. A possible reason for the difference can be variability in the mineralogy and chemical composition of the stones (Yang et al., 2013). RL2 has the lowest susceptibility and weakest NRM among all experimented stones. Directional data representing the ambient magnetic field in which the stones last cooled was retrieved from stones RL5 and RL7. RL1, RL2 and RL3 appear to have been disturbed (Figure 6.12), so their results were discarded. The mean direction calculated from RL5 and RL7 can be used for preliminary archaeomagnetic dating. The declination and inclination are compared with NZPSV1K (Turner et al., 2015) using the dating tool of Pavon-Carrasco et al., (2011). Archaeomagnetic dating suggests an age range of 1938-1990AD (Figure 6.13). The sample used for ^{14}C dating had a significant inbuilt age so did not provide a realistic age estimate of the site. Archaeomagnetic dating suggests that the Riverlands hangi site is much younger in age. Therefore, the interpretation of the hangi as a moa-cooking hangi is probably not true, as the moa became extinct about 500 years ago, (http://www.teara.govt.nz/en/moa). The industrial area near the canal was a racecourse from 1886 until 1919AD, and it is possible that use of the hangi dates to this time (Figure 6.3 (a)). Also, there was intensive work on rivers in the area between 1877 and 1902AD (Skinner, 1912) and the hangi could alternatively have been used by people employed in this work.
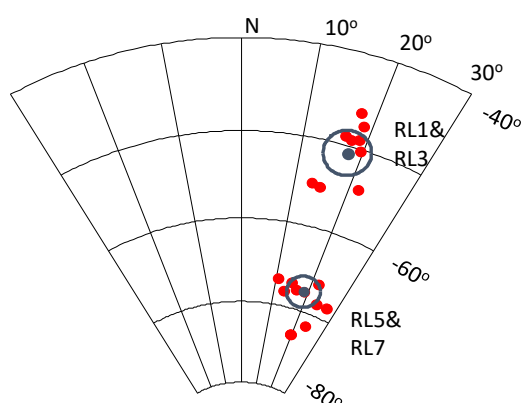


Figure 6.12. Equal angle stereographic plot of directions of hangi stones from Riverlands. All red dots are directional data of specimens from stones RL1, RL3, RL5 and RL7. Grey circles are $\alpha_{95}$ of mean direction (dark dots) of both clusters.

The average archaeointensity calculated above, 57.0 ± 3.6 μT, was calculated using 5 TTA 1 TTB and 9 TTC. It does not differ significantly from the value of 57.6 ± 2.9 μT obtained from only the TTA data. In Figure 6.14 the former value is superimposed on the curve of field intensities provided by geomagnetic field model *gufm*1 (Jackson et al., 2000) at the location of Riverlands, Blenheim (latitude/longitude ~ 41.6°S/ 174°E). *gufm*1 is a global field model, and for 1838 and later it is based on absolute field measurements (red line in Figure 6.14), and so the values are directly comparable with Riverlands archaeointensity values. For an age range 1938-1990 that is 1964 ± 26 AD as given by archaeomagnetic dating, according to *gufm*1, the field intensity lay between 58.8 and 57.3μT. It can be seen that archaeointensity obtained from TTA data sits nearer to the intensity curve, since both archaeointensity results are in very good agreement with *gufm*1. Therefore, 57.0 ± 3.6 μT is considered as reliable site's mean archaeointensity result.



**Dating : RL**
**Combining Probability Density Functions**
**Threshold = 0.0050685 (Confidence = 95%)**
**Between t = 1030AD and 1990AD**

**[1938AD   1990AD]**

Dec = 19.6°
Inc = -68.3°
$\alpha_{95}$ = 1.6°
F = 57.0 ± 3.6 μT
$^{14}$C dating results: 1161-1264 AD
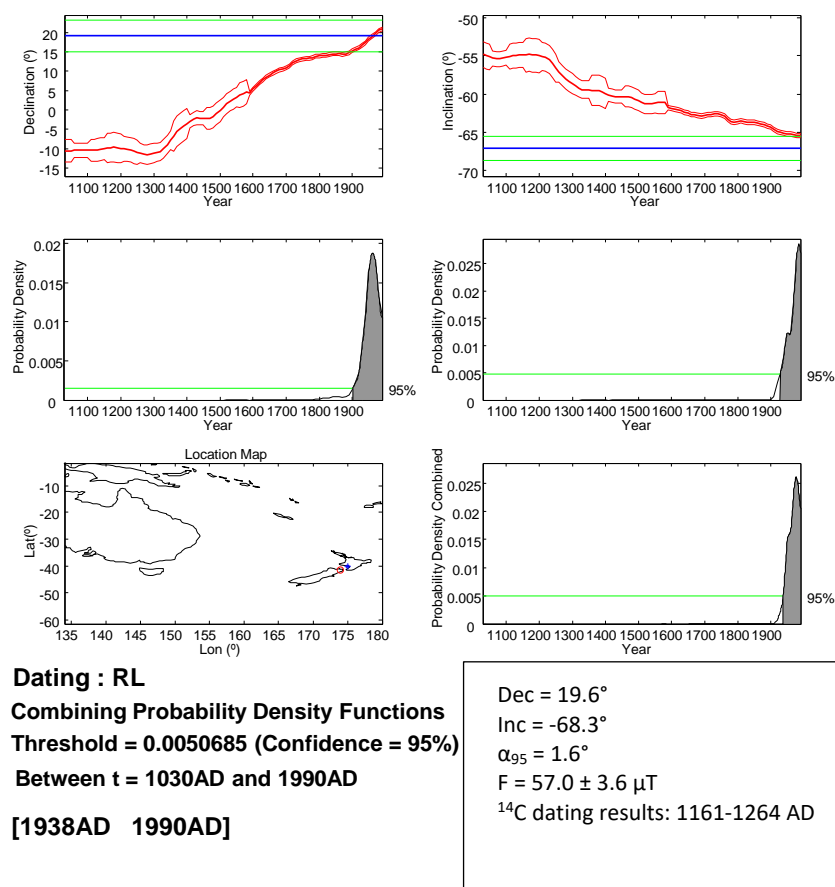
Figure 6.13. Archaeomagnetic dating of Riverlands hangi site. The RL archaeodirection has been relocated to 40°S, 175°E, using a VGP transformation, before matching with the NZPSV1k declination and inclination reference curves.

## 6.8. Conclusion

The demagnetization experiments show that the directional data is clustered in two different groups: the shallower is thought to result from disturbance of stones RL1 and RL3 in the field during construction work. On the basis of archaeological reports, field observations and intensity data, the archaeomagnetic direction obtained from RL5 and RL7, Dec =19.6°, Inc = -68.3°, $\alpha_{95}$ =1.6°, is accepted. This yielded an archaeomagnetic date of the site between 1938 and 1990. The mean archaeointensity of the site is F = 57.0 ± 3.6 µT.
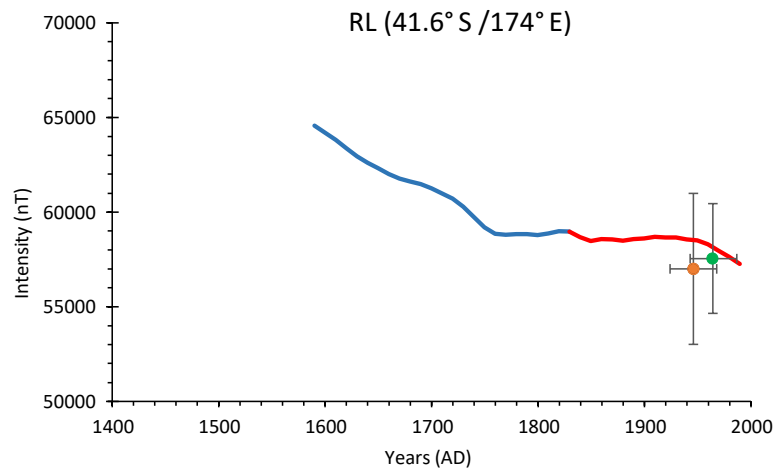


**Figure 6.14.** Geomagnetic field intensity at Riverlands site for last 400 years at latitude/ longitude 41.6°S /174°E (Jackson et al., 2000), and the RL archaeointensity. Green dot indicates the result of quality TTA and orange dot include data of quality TTA, TTB, and TTC.

# 7. Whitianga hangi sites

## 7.1. Archaeological setting

Whitianga lies on the east coast of Coromandel Peninsula. The geology of the Peninsula is dominated by volcanic features: remnants of the major andesitic volcanoes, active between 20 and 10 million years ago, remain largely in the northern part of the Peninsula, while the south is covered by rhyolites from large caldera-forming events that began about 9 million years ago (Figure7.1; Monin, 2012).
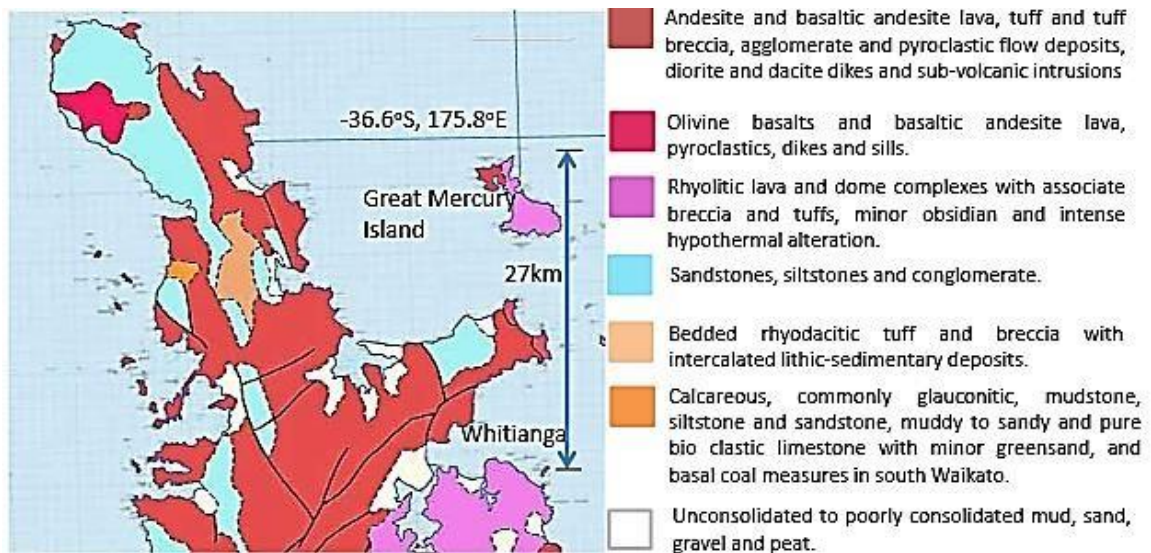


Figure 7.1. Geological map of Coromandel Peninsula. From GNS geology website (http://data.gns.cri.nz/geology/)

The archaeological site sampled at Whitianga (T11/914) was found in July 2008, during the development of a new subdivision, and has been excavated by archaeologists Andrew Hoffman and Greg Gedson. Fieldwork was carried out in July 2014. Hangi stones were sampled from Hoffman's features, F1, F4, F5 and F19, which were then relabelled with VUW IDs, WT1, WT3, WT2 and WT4 respectively (Table 7.1). A topographic map and an aerial photograph of the site are shown in Figure 7.2. The site is located at the north end of Cook Drive, on the southern bank of Taputapuatae Stream. Before subdivision, the area near the stream consisted of low sand dunes.
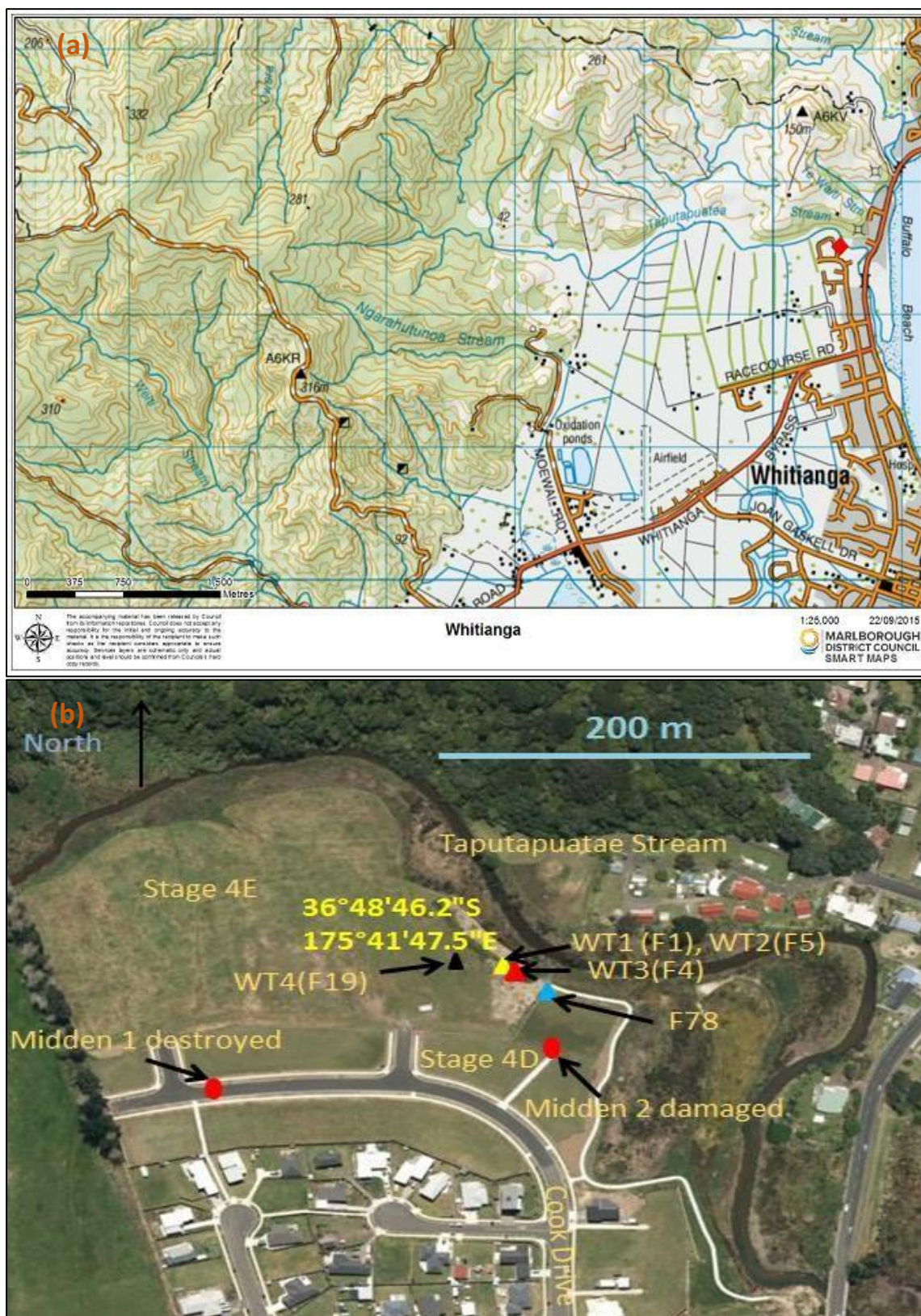
Figure 7.2. (a) Topographic map of Whitianga (downloaded from http://maps.marlborough.govt.nz/portal/). (b) Aerial photo of archaeological site T11/914 at Whitianga showing locations of hangi WT1 (F1), WT2 (F5), WT3 (F4), WT4 (F19) and middens discovered. The white boundary separates stages 4D and 4E. Photo downloaded from Google Earth, date of image 10/1/2010.

When the site was excavated in 2008, the earthworks in the whole area were divided into different stages. Two discrete middens were found during stripping of topsoil in the stage 4D area. One was completely destroyed during earthworks and the second was partially damaged. The first hangi (Feature 78-2008ex, not sampled) was found near the stream bank by Peter Johnston of Ngati Hei. Two more pits were excavated in the area between the hangi and the midden, but no further archaeological features were noticed at that time.

The area remained undisturbed until July 2014, when an investigation of the site was resumed by archaeologists Andrew Hoffmann and Greg Gedson. The dunes along the stream bank showed two main erosion events (flooding) that separate the site into three stratigraphic periods. The earliest period was estimated to be of long-term use close to the time of early Polynesian settlement, inferred from obsidian flakes and other artefacts found on the site. The younger periods were short term, falling in the 16th and 17th centuries.

A second hangi (WT1, F1) was found 11m to the west of the first hangi (F78) at latitude and longitude, 36°48′46″S and 175°41′47″E (Figure 7.2), during subdivision of area 4E. The site was sampled in 2014. The archaeologists had half-sectioned the hangi before we sampled it. It was otherwise undisturbed; the stones were closely packed with fire-blackened sand. Figure 7.3 (a) shows the hangi before sampling. During the excavation of the second half of WT1, another feature (WT2) was found above, separated by a thick layer (about 35cm) of windblown sand (Figure 7.3 (b)), so therefore younger than hangi WT1. In feature WT2, fire-cracked and reddened stones lay on the sand between WT1 and WT2, along with charcoal fragments (Figure 7.3 (b)). The appearance of WT2 was dissimilar to WT1 because the stones of WT2 were smaller in comparison to WT1 (possibly broken due to intense heating), less closely packed, and did not seem to be *in situ*.
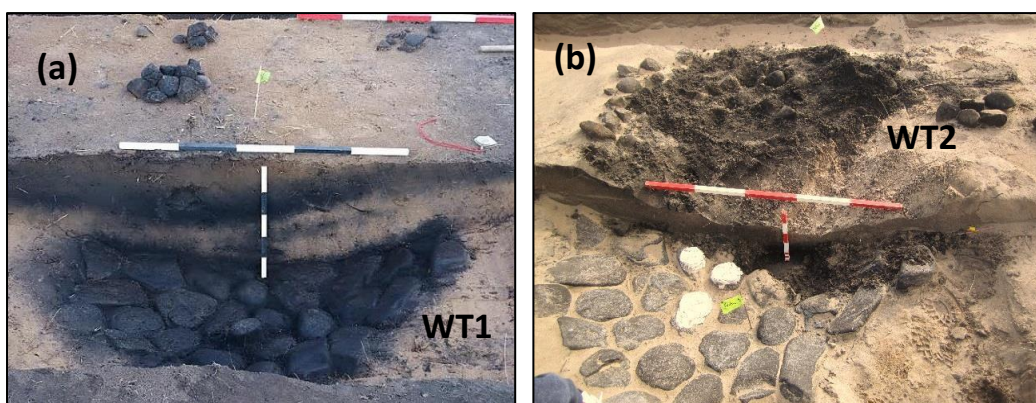
Figure 7.3. (a) WT1 (F1) hangi site before fieldwork, when WT2 (F5) was uncovered (picture: Greg Gedson). (b) WT1 and WT2 during fieldwork and sampling.

More fire-cracked and reddened stones were found approximately 1.5m southeast of WT1 and were labeled WT3. These stones appeared to be a cache of cooking stones: a store of stones removed from a hangi after cooking to be reused later. The stones were laid on the sand and no charcoal or cooking features were associated with them. WT1, WT2 and WT3 (Figure 7.4 (a)) were all located on the sediments built up above the second erosion unconformity, and thus belong to the third phase of occupation (Andrew Hoffmann, pers. comm.).
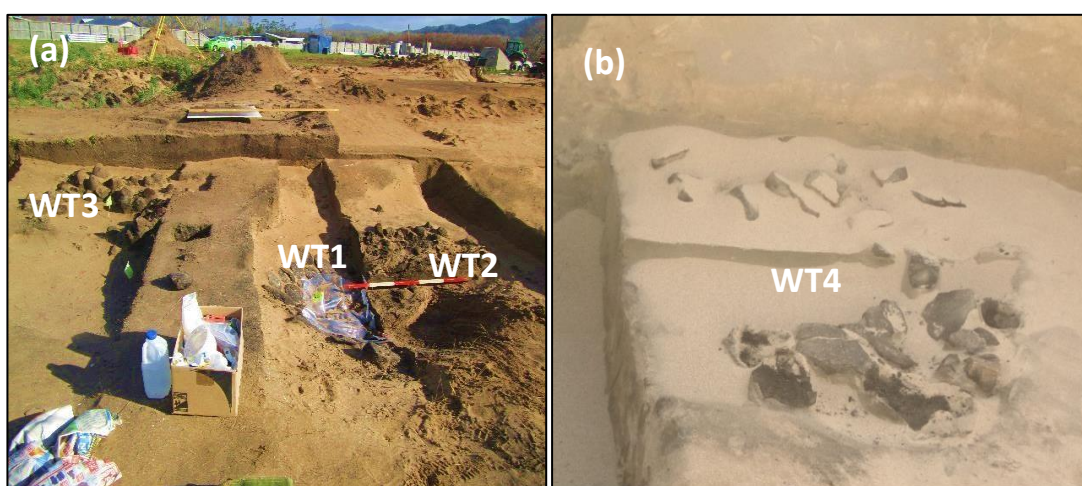


Figure 7.4. (a) Locations of features WT1, WT2 and WT3 with respect to each other. (b) Hangi site WT4 (F19).

A fourth feature containing more hangi stones, WT4 (F19), was approximately 12m northwest of WT1. Here fire-cracked stones were found lying on the sand along with

charcoal pieces (Figure 7.4 (b)). These stones are not thought to have been *in situ*. They were located on the sediments built up above the first erosion unconformity, but beneath the second, and so are associated with the middle period of occupation (Andrew Hoffmann, pers. comm.). WT4 is thus older than WT1, WT2 and WT3 (Figure 7.5).

Most of the hangi stones from all four features are andesites. Taputapuatae Stream itself does not contain andesite stones, although several other rivers flowing into Mercury Bay do carry andesite stones, and so could be the source of these hangi stones. The stratigraphic relationship between the four sites is shown in Figure 7.5 and site details are given in Table 7.1. More, unoriented hangi stones were later provided by archaeologist Andrew Hoffmann for further work, not reported here.
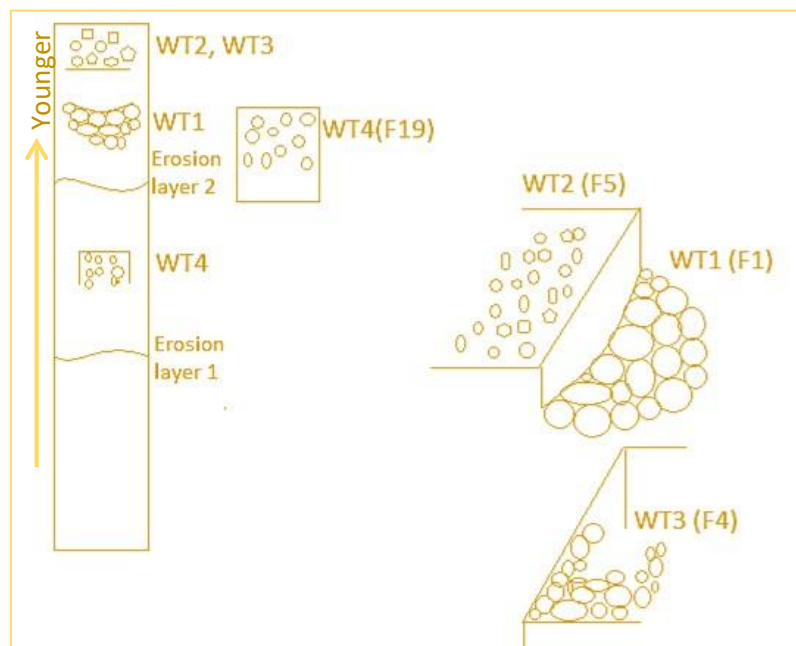


Figure 7.5. Schematic section showing stratigraphic relationship of sampled sites WT1, WT2, WT3 and WT4.

Table 7.1. Features sampled at Whitianga archaeological site T11/914. GPS coordinates were converted to NZTM using (http://apps.linz.govt.nz/coordinate-conversion/index.aspx).

| VUW site label | Hoffmann's reference number | Description | Age control (Conventional Radiocarbon Ages) | NZTM coordinates |
|---|---|---|---|---|
| WT1 | Feature 1 or F1 | Stones in the hangi closely packed, appear to be *in situ.* | Latest period of occupation, above second erosion event. | N5922503.7 E1840526.3 |
| WT2 | Feature 5 or F5 | Fire-cracked stones with charcoal overlie WT1, separated by a windblown sand layer. | 482±20 BP (Wk-41157); belongs to the latest period of occupation but after WT1. | --- |
| WT3 | Feature 4 or F4 | Fire-cracked stones located ~1.5m SE of WT1 & WT2, no charcoal was found, and the stones appear to be a cache of cooking stones. | The site belongs to the latest period of occupation. | --- |
| WT4 | Feature 19 or F19 | Fire-cracked stones located ~12m NW of WT1 & WT2, no charcoal was found. | 465±20 BP (Wk-41160); belongs to the middle period of occupation, between first and second erosion events. | --- |

## 7.2. Sampling Details

WT1 was the largest of the features sampled at the Whitianga site. The hangi stones extended over a circular area about 2m in diameter. The western half (the left-hand side of Figure 7.6) of the oven had been excavated prior to our arrival at the site, revealing closely-packed stones lining the base of a shallow saucer-shaped hollow. We oriented and removed five stones from this half of the oven (WT1-1, WT1-2, WT1-3, WT1-4 and WT1-10). Following the sampling and removal of the remainder of WT2, described below, we then excavated the eastern (the right-hand side of figure 7.6) half of WT1, taking care not to disturb the remaining stones in the western half.

Five more oriented stones were then collected from the west half of the hangi (WT1-5, WT1-6, WT1-7, WT1-8 and WT1-9) (Figure 7.6). There were no more stones beneath

the layer from which these 10 stones were taken. All stones were marked with magnetic north and a sun bearing for orientation purposes. Most of the stones in WT1 were not cracked, which suggested they had not been used many times for cooking. Samples of fire-blackened sand were collected in plastic bags by archaeologist Greg Gedson. No charcoal pieces were available in the hangi on the date of sampling, but Greg Gedson had previously collected some from WT1. Most of the stones were near round, hemispherical (possibly broken due to overheating) or oval. Some were irregularly shaped with round edges. The typical length of the stones was about 20cm.



Figure 7.6. Hangi site WT1, completely excavated. Stones WT1-5, WT1-6, WT1-7, WT1-8 and WT1-9 with Plaster of Paris caps on the top.

WT2 was about half the size of WT1 and contained fire-cracked and reddened stones, suggesting that stones may have been re-used multiple times. Some uncovered stones were seen at the time of sampling but were not *in situ* because the sand from above had already been removed and the stones were not closely-packed. Four non-oriented stones of appropriate size were collected from here (WT2-1, WT2-2, WT2-3 and WT2-4). Samples of blackened sand and charcoal were also gathered by the archaeologists for dating the hangi. WT3 did not contain any charcoal or blackened sand. Four non-oriented stones (WT3-1, WT3-2, WT3-3 and WT3-4) were taken from

this feature. As WT3 was not a cooking oven, the stones were assumed to be cold when placed here, so they were not oriented.

Four non-oriented fire-cracked stones were collected from site WT4 (WT4-1, WT4-2, WT4-3 and WT4-4). Although the stones did not appear to be *in situ*, charcoal fragments were found between them, and a sample was collected. The stones were also not closely-packed as in WT1.

Altogether 10 oriented and 12 non-oriented stones were taken from the four features. The WT1 stones were set in expanding foam before drilling, while the others were clamped on the drill table. A minimum of four cores was drilled from the WT1, WT3 and WT4 stones. The stones from WT2 were small, so only three cores were drilled from each. The cores were then cut into cylindrical specimens about 2cm in length. Details of cores drilled from each stone and specimens cut from each core are given in Table 7.2.

Table 7.2. Details of cores drilled and specimens from each stone.

| Name of stone | Number of cores | Number of specimens |
|---|---|---|
| WT1-2 | 4 | 8 |
| WT1-3 | 5 | 8 |
| WT1-6 | 5 | 14 |
| WT1-7 | 6 | 13 |
| WT1-8 | 6 | 10 |
| **Total** | **26** | **53** |
| WT2-1 | 3 | 4 |
| WT2-2 | 3 | 4 |
| WT2-3 | 3 | 6 |
| WT2-4 | 3 | 6 |
| **Total** | **12** | **20** |
| WT3-1 | 4 | 8 |
| WT3-2 | 5 | 9 |
| WT3-3 | 5 | 10 |
| WT3-4 | 4 | 4 |
| **Total** | **18** | **31** |
| WT4-1 | 4 | 5 |
| WT4-2 | 2 | 4 |
| WT4-4 | 5 | 5 |
| **Total** | **11** | **14** |

## 7.3. Age Control

The collection of charcoal samples from sites WT1, WT2 and WT4 was sent to Auckland University palaeobotanist Dr. Rod Wallace for identification of species. WT1 charcoal contained long-lived species such as matai, totara or beech and was not suitable for radiocarbon dating. Such species can have a significant inbuilt age (B. G. McFadgen, 1982) at the time of burning in a hangi. For example, the charcoal samples from the Weld Pass (WP1) and Riverlands hangi sites were identified as matai, which may live to about 1000 years, and returned ages of 769 ± 21 BP and 881 ± 21 BP, despite evidence that the hangi sites were much younger.

On the other hand, dracophyllum and mahoe identified in the charcoal from WT2 and WT4 respectively, are short-lived species, and so do not add a significant inbuilt component to the age of a sample. These charcoal samples were submitted for radiocarbon dating at the University of Waikato. The results are given in Table 7.3, and the probability distribution curves for calibration of the dates are shown in Figure 7.7.

Table 7.3. Radiocarbon age estimation and calibration (see Figure7.7)

| Site Name | Material | Lab No. | $^{14}$C age | Calibrated age range (95% confidence) |
|---|---|---|---|---|
| WT2 (F5) | Dracophyllum | Wk-41157 | 1468±20AD | 1427-1464AD (94.8%) |
| WT4(F19) | Mahoe twig | Wk-41157 | 1485±20AD | 1436-1488AD (95.2%) |

The radiocarbon dating does not give an exact date for occupation but provides a range of calendar years as shown in Table 7.3. The results are quoted at a confidence level of 95%. The calibrated ages for WT2 and WT4 are very similar, and their probability density functions overlap to a significant extent, making it impossible to say which is the earlier. Both have means of between 1445 and 1460AD, with the probability density function for WT4 extending to slightly younger dates. However, this cannot be the case as WT4 lies stratigraphically below the upper (second) erosion horizon, while WT2 is above it. The dates confirm that the whole site is relatively early Maori, in agreement with the archaeologist's deductions, made on the basis of

artefacts found during the 2008 excavation. Feature WT1 is prior than WT2, and unsampled features beneath the lower erosion horizon must be earlier still. The Whitianga site as a whole will provide valuable early data for the New Zealand archaeomagnetic PSV record.

.
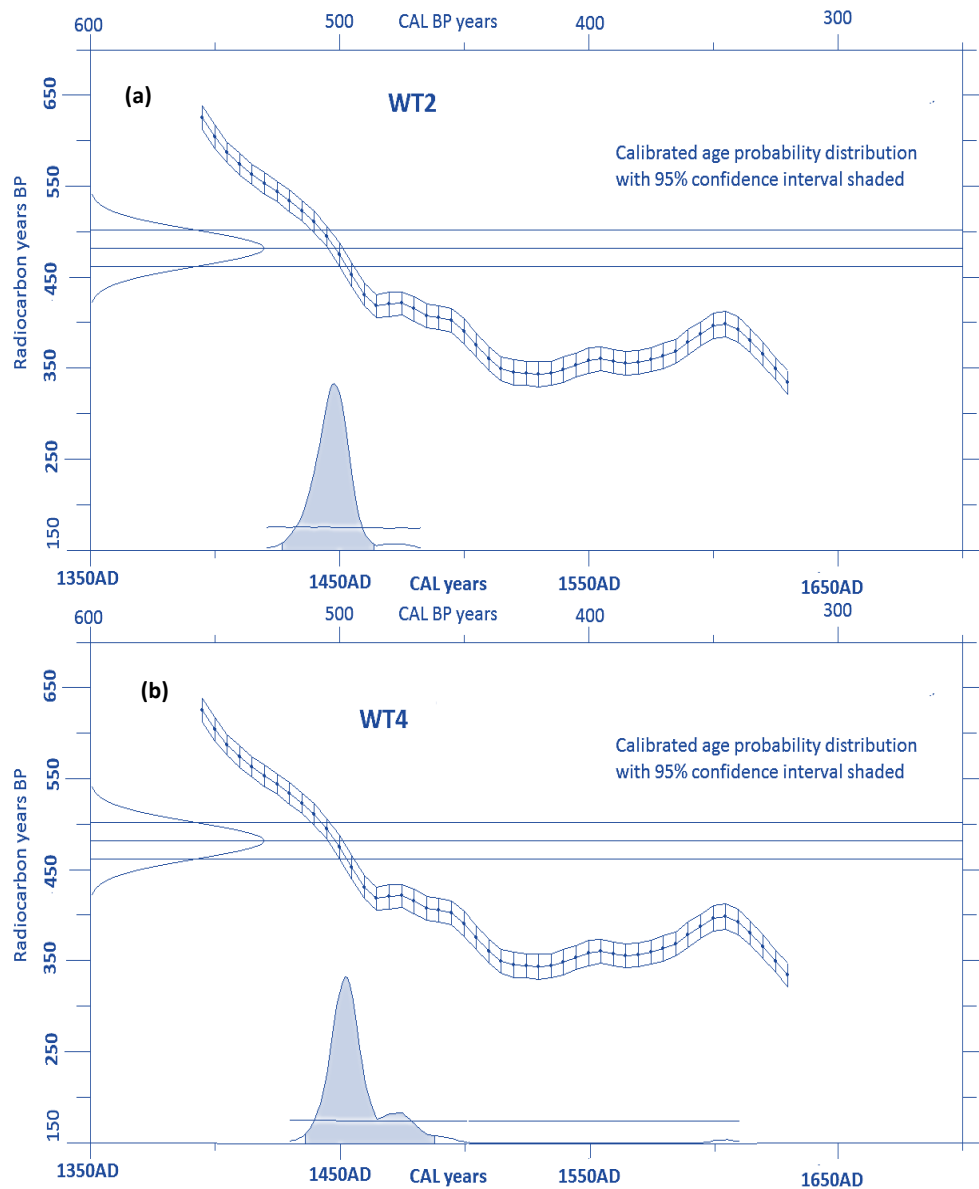


Figure 7.7. Calibration of radiocarbon dates (a) for site WT2, (b) for site WT4, using WinscalX (Sparks and Manning, pers. comm.) and SHCAL13 (Hogg et al., 2013). Dates have been determined using Accelerator Mass Spectrometry at The University of Waikato.

## 7.4. Rock magnetic properties

Measurements of the rock magnetic properties of the Whitianga hangi stones are described below.

### 7.4.1. Curie temperature

Susceptibility versus temperature experiments provided a range of types of behaviour. The room temperature susceptibilities range from 2.5 to 12 X $10^{-6}$ $m^3kg^{-1}$. This is typical of andesites carrying a few percent of (titano) magnetite. One sample from each stone was heated from room temperature to 700°C and then cooled back to room temperature while susceptibility was measured at 10° intervals. The heating and cooling curves are not all reversible (Figure 7.8). During heating, the susceptibility increases up to a temperature of 500°C, often showing a pronounced Hopkinson peak, and then decreases sharply at higher temperatures. In all WT1 samples, cooling curves lie below the heating curves. This is due to thermal alteration after being heated to high temperature. Repeated experiments to only 400°C did not show any alteration. The heating curve of WT1-7 indicates the presence of two magnetic phases, the first giving a drop in susceptibility around 400°C, after which the susceptibility increased to a temperature around 530°C and from this point decayed to the Curie point, close to 600°C. The cooling curve shows a single magnetic phase. The principal Curie temperature of the WT1 stones ranges between 580°C and 602°C and indicates the presence of Fe-rich titanomagnetite (with titanium composition less than 5%) and oxidized titanomagnetite (Tauxe et al., 2010).

The stones from WT2, WT3 and WT4 are different from the WT1 stones to some extent. Figure 7.8 shows that thermal alteration is much less than for the WT1 stones. Hopkinson peaks can be seen in all plots. There is an indication of two stable magnetic phases in WT2-3 ($T_{c1}$ = 280°C & $T_{c2}$=602.5°C) and WT4-4 ($T_{c1} \approx$ 250°C & $T_{c2}$=547.4°C), for which the heating and cooling curves are reversible. This indicates a degree of inhomogeneity between the stones' magnetic mineralogies.

The principal $T_c$ of WT3-4, WT4-1, and WT4-4 ranges from 538° to 547°C and indicates the presence of titanomagnetite, $Fe_{3-x}Ti_xO_4$, with x≈0.1. The principal $T_c$ of all other WT stones lies in the range 580-603°C. The thermomagnetic curves ($M_s$ vs. T, Figure 7.9) for stones WT3-4, WT4-1, and WT4-2 give principal $T_c$ of 534°C, 546°C and 566°C respectively, calculated using the second derivative method (Tauxe et al., 2010). Values of WT3-4 and WT4-1 are similar to those calculated from $\chi$-T plots, whereas that for WT4-2 is some 20° lower, probably due to inhomogeneity in the stone's mineralogy. The calculated Curie temperatures are summarized in Table 7.4. Table 7.4 lists the $T_c$'s both for heating and cooling curves, the values after correction for temperature-lag and the difference between the calculated and corrected values.
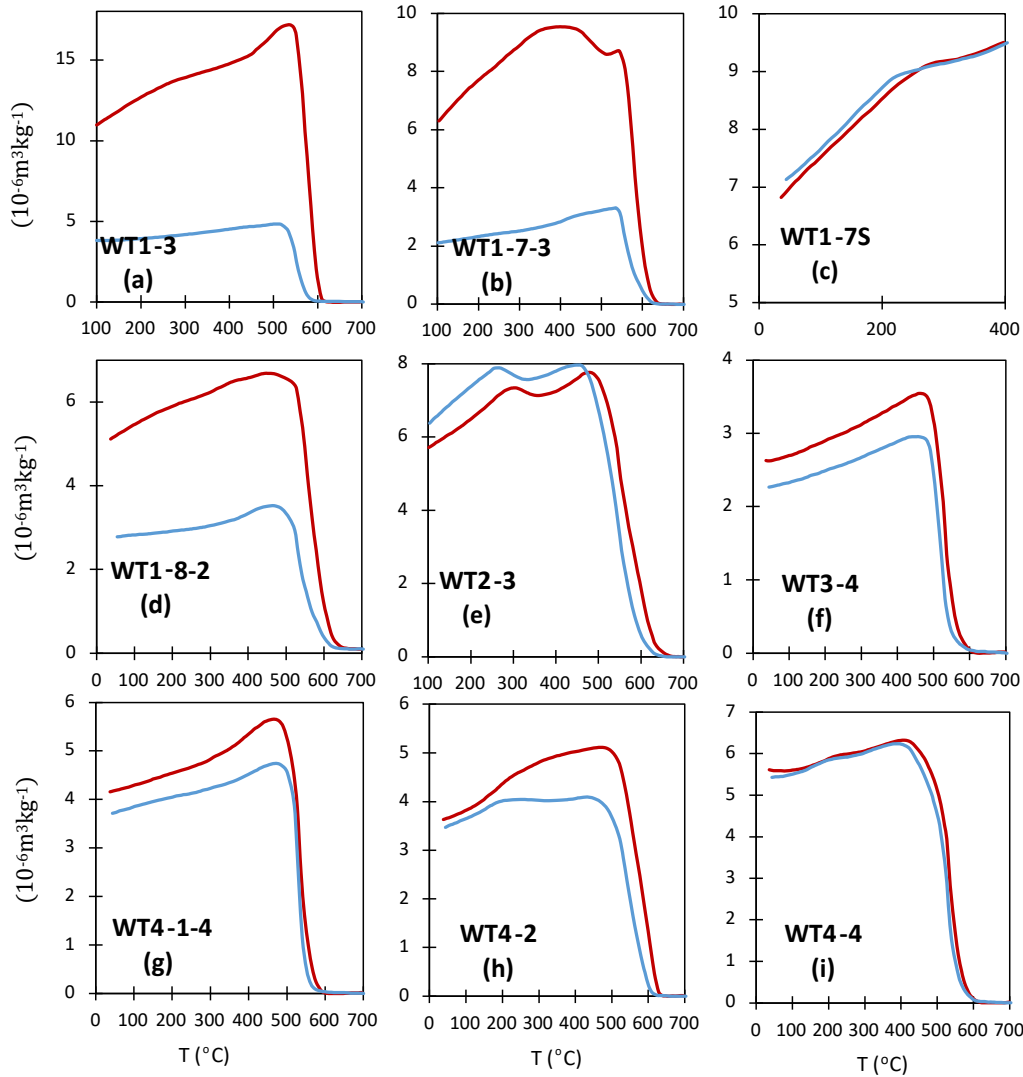


Figure 7.8. Susceptibility vs temperature curves for samples from hangi stones from sites WT1, WT2, WT3 and WT4. Red lines indicate the heating curves and blue the cooling curves.
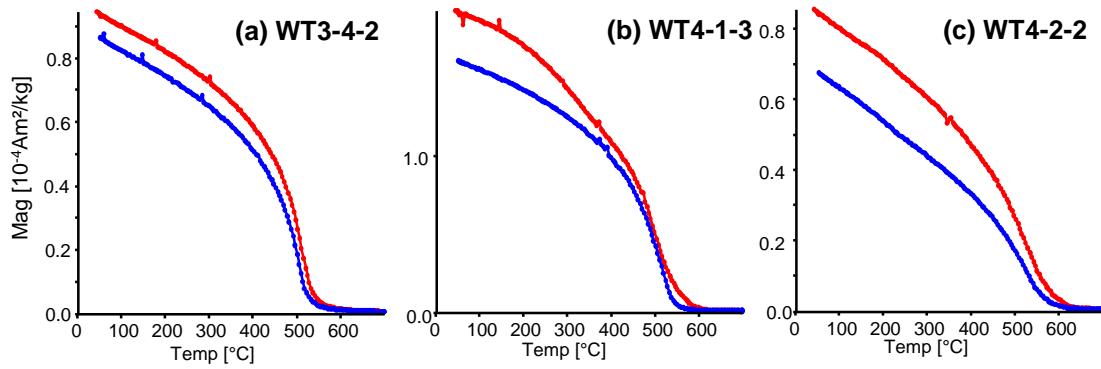
Figure 7.9. Thermomagnetic curves of samples WT3-42, WT4-13 and WT4-22.

Table 7.4. Curie temperatures of WT hangi stones. Calculations for $\chi$-T plots use the inverse susceptibility method (Petrovský & Kapička, 2006). Curie temperature from $M_s$-T plots are determined by the double derivative method, using Rockmag Analyser 1.0 (Leonhardt, 2006).

| Sample ID | Susceptibility versus temperature plots | | | Difference (°C) | $T_c$ from $M_s$-T plots (°C) |
|---|---|---|---|---|---|
| | $T_c$ heating (°C) | $T_c$ cooling (°C) | $T_c$ cooling corrected (°C) | | |
| WT1-3 | 581 | 544 | 559 | 22 | --- |
| WT1-6 | 590 | 560 | 575 | 15 | --- |
| WT1-7 | 598 | 583 | 598 | 0 | --- |
| WT1-8 | 603 | 583 | 598 | 5 | --- |
| WT2-3 | $T_{c1}$ = 603 | $T_{c1}$ = 569 | 584 | 19 | --- |
| | $T_{c2}$ ≈ 280 | $T_{c2}$ ≈ 250 | 265 | 15 | |
| WT3-4 | 539 | 507 | 522 | 17 | 534 |
| WT4-1 | 547 | 532 | 547 | 0 | 546 |
| WT4-2 | 599 | 573 | 588 | 11 | 566 |
| WT4-4 | $T_{c1}$ = 547 | $T_{c1}$ = 545 | --- | 2 | --- |
| | $T_{c2}$ ≈ 250 | $T_{c2}$ ≈ 250 | --- | 0 | |

## 7.4.2. Hysteresis and backfield curves

Hysteresis loops and backfield IRM curves for the Whitianga samples are shown in Figure 7.10. The results demonstrate the dominance of ferri/ferromagnetic behaviour over paramagnetic behaviour. The blue and red curves are before and after removal of the high-field slope which results from the paramagnetic component. The hysteresis and IRM parameters, $M_s$, $M_{rs}$, $B_c$, $B_{cr}$ and their ratios are listed in Table 7.5. All WT samples saturated in a field of <0.3T. The hysteresis loops of the WT1 samples are narrow, providing low coercivities (5.90-7.90 mT), saturation remanence ranging from 27 to 68 mAm$^2$kg$^{-1}$, relatively low values for the ratio $M_{rs}/M_s$ (0.09-0.13) and relatively

high $B_{cr}/B_c$ ratios (2.29-3.21). By contrast, the samples from sites WT2, WT3 and WT4 provided higher coercivities (14.9-31.3mT), higher saturation remanence values in range 105-430 mAm$^2$kg$^{-1}$, $M_{rs}/M_s$ between 0.32 and 0.40 and $B_{cr}/B_c$ between 1.5 and 2.0. The hysteresis loops of these stones are broader and can be easily distinguished from the WT1 loops.
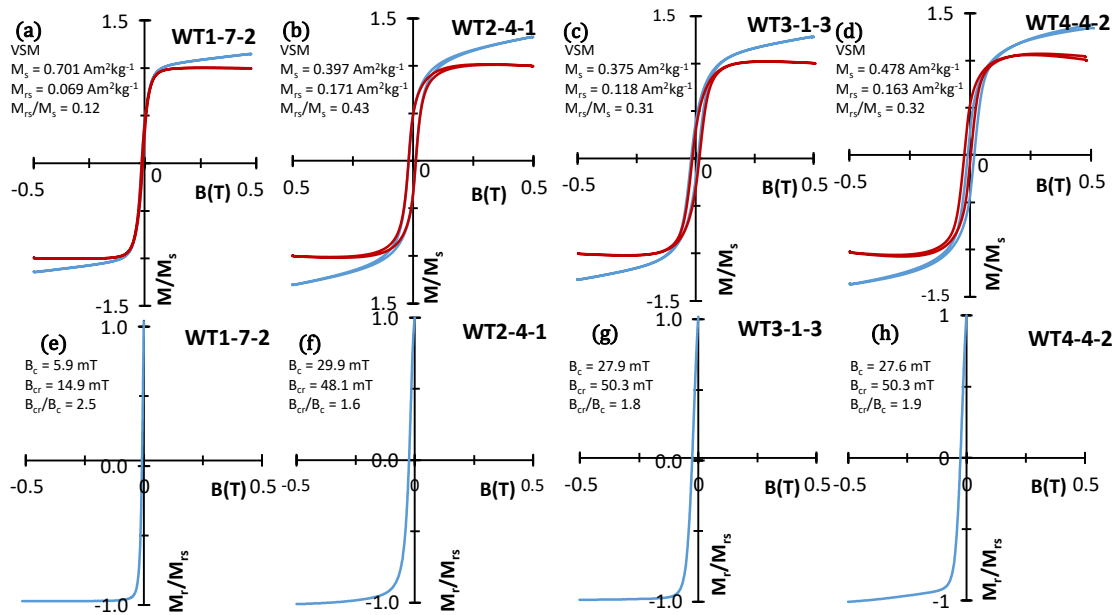


Figure 7.10. Hysteresis plots of samples WT1-7-2, WT2-4-1, WT3-1-3 and WT4-4-2. The blue curves include the paramagnetic character and paramagnetic correction is applied to red curves. The corresponding back-field curves of the samples are below them.

Table 7.5. Hysteresis and backfield IRM data of Whitianga hangi stones.

| Sample ID | $M_{rs}$ | $M_s$ (mAm$^2$/kg) | $B_c$ | B | $M_{rs}/$ | $B_{cr}/B_c$ |
|---|---|---|---|---|---|---|
| WT1-3-3 | 27.0 | 185.4 | 7.9 | 1 | 0.15 | 2.2 |
| WT1-6-5 | 42.1 | 338.8 | 6.0 | 2 | 0.12 | 3.71 |
| WT1-7-2 | 68.02 | 701.2 | 5.9 | 1 | 0.10 | 2.5 |
| WT2-3-3 | 193.9 | 557 | 21.8 | 4 | 0.34 | 1.97 |
| WT2-4-1 | 170.9 | 396.7 | 29.9 | 4 | 0.43 | 1.60 |
| WT3-1-3 | 117.5 | 375.4 | 27.9 | 5 | 0.31 | 1.8 |
| WT3-4-2 | 105 | 747 | 14.9 | 4 | 0.14 | 3.06 |
| WT4-1-3 | 428 | 127 | 31.3 | 5 | 0.34 | 1.86 |
| WT4-2-2 | 177 | 575 | 27.6 | 5 | 0.31 | 2.11 |
| WT4-4-2 | 151.8 | 478.4 | 26.8 | 5 | 0.32 | 1.87 |

The $M_{rs}/M_s$ ratios have been plotted against the $B_{cr}/B_c$ ratios in Figure 7.11, along with the theoretical SD+MD and SD + 10nm SP mixing curves of Dunlop (2002). All samples

fall on or close to the theoretical hyperbolic mixing (SD+MD) curves. WT1-3, WT1-6, WT1-7 and WT3-4 lie on the lower portion of the curves, whereas other samples sit on the upper part, while all samples are within PSD (or SD and MD mixture) region (Dunlop & Özdemir, 1997).

Differences in the mineralogy of the stones from the same site can be seen from Figure 7.11. It can be understood on the basis of rock magnetic data that the samples from the sites WT1, WT2, WT3, and WT4 have high coercivity phase and can provide us with reliable archaeomagnetic data.
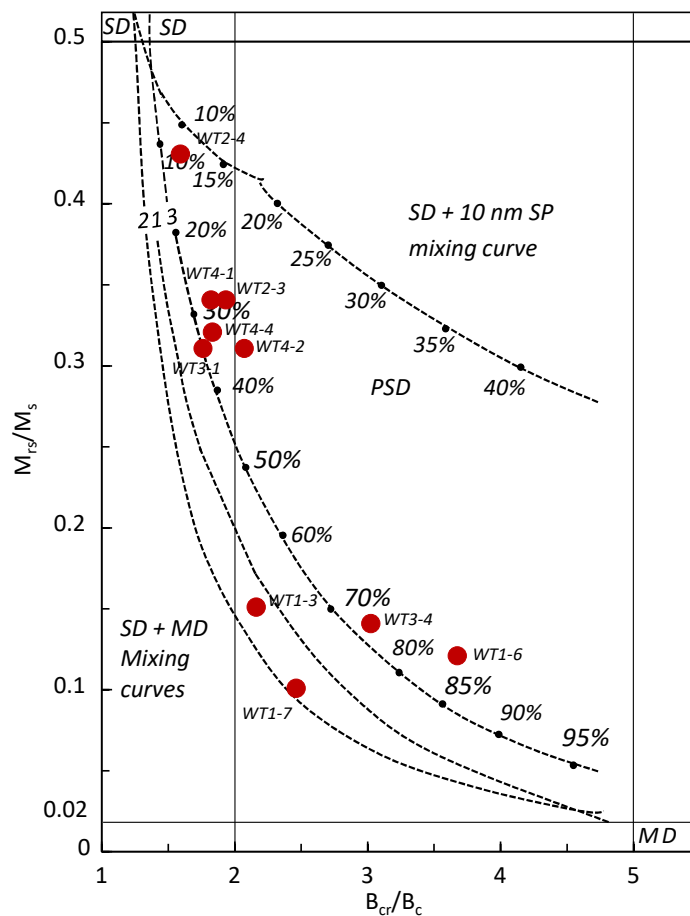


Figure 7.11. $M_{rs}/M_s$ vs $B_{cr}/B_c$ (Day et al., 1977) data of Whitianga hangi stones (red dots) superimposed on the mixing curves of Dunlop, 2002 for single domain, multidomain and superparamagnetic grains. The curves 1 and 2 are plotted using data by Day et al. (1997) and Parry (1965). Curve 3 has been drawn using data of Parry (1980, 1982). The numbers along the curves are volume fractions (for MD or SP) of the soft magnetic component. The equations used to calculate all parameters are also explained in detail by Dunlop (2002).

### 7.4.3. Summary

The principal Curie temperatures of all samples from Whitianga hangi sites are in the range 540-600°C suggesting the dominance of Ti-poor titanomagnetite as a magnetic mineral. WT1 stones show considerable thermal alterations after being heated above 400°C, and some stones have two magnetic phases (WT1-7, WT2-3 and WT4-4). Rock magnetic properties also show the presence of ferro/ferrimagnetic remanence carriers with grains ranging from PSD to MD.

## 7.5. Progressive Demagnetization Results

Absolute directional data could be retrieved only from hangi WT1, as this was the only site from which oriented stones were collected. WT1 specimens were demagnetized using both thermal and alternating field methods. Although the stones from sites WT2, WT3 and WT4 were not oriented, they were demagnetized thermally to check their blocking temperature spectra and components of magnetization carried by the stones. The results are explained below, site by site.

### 7.5.1. Hangi site WT1

Thermal demagnetization (THD) was carried out on five specimens (one from each of the stones WT1-2, WT1-3, WT1-6, WT1-7 and WT1-8). Alternating field demagnetization (AFD) was applied to 16 specimens from the same five stones. Altogether 15 specimens showed consistent results, summarized in Table 7.6. Other specimens provided unreliable directional data due to loss of orientation marks on the specimens during drilling and cutting. These data could not be included in the calculation of a site-mean direction. Typical results are shown in Figure 7.12 (a)-(j). These stones have a natural remanent magnetization (NRM) in the range 0.4-1.0 A/m also typical of andesites containing a few percent (titano) magnetite. Demagnetization curves (inset figures of Figure 7.12) are consistent with the $\chi$-T and Ms –T data described above. In WT1-2, WT1-3 and WT1-7 a low blocking temperature component

is removed between 100°C and 300°C (Figure 7.12a, c & g) and a higher blocking temperature component from 450°C to the principal Curie temperature. In WT1-6 very few grains unblocked below 300°C.

The Zijderveld plots show the presence of more than one component of magnetization in specimens from stones WT1-2, WT1-3, WT1-7 and WT1-8, indicating disturbance of these stones in the hangi during the cooling process. Only WT1-6-1 has a stable single component of magnetization. In WT1-7-1B a curve is apparent rather than a sharp edge, due to overlap of the blocking temperature spectra of the two components (Robert F. Butler, 1992b). In general, the separation of the components is clearer in AFD (specimens WT1-2-1B and WT1-8-2A) than in THD (specimens WT1-2-1A and WT1-8-3A). WT1-7-6B shows a slight curve and then a straight single component heading towards the origin. WT1-6 and WT1-8 could not be completely demagnetized by AFD to 99mT.

The component of remanence carried by the lowest blocking temperature or coercivity grains is interpreted to have been acquired after the disturbance of the stones. Agreement in direction between the stones indicate that the stones have remained *in situ* and that it reflects the ambient magnetic field at the time of cooling. For statistical purposes, the data listed in Table 7.6 have been combined with directional data obtained from palaeointensity experiments.

The direction of the characteristic remanent magnetization, or, where there is more than one component, high blocking temperature component (C1) and the low blocking temperature component (C2) of remanence for specimens from WT1 stones, is shown in Figure 7.13 (a) & (b). In general, the components calculated from specimens from each stone are in good agreement and shown with same colour coding.

The directions plotted in Figure 7.13 (b) reflect magnetization acquired during the later stage of cooling and the clustering of directions between stones suggests that little disturbance of the stones has occurred during or since the acquisition of these components of remanence.

For the calculation of a preliminary site mean direction, WT1-2 (C1) and WT1-8 were disregarded as outliers. Averaging the ChRM or low blocking temperature components

of the 15 specimens from these six stones gives a mean archaeodirection of Dec = 6.3°, Inc = -52.2°, $\alpha_{95}$ = 2.5° (Figure 7.14).
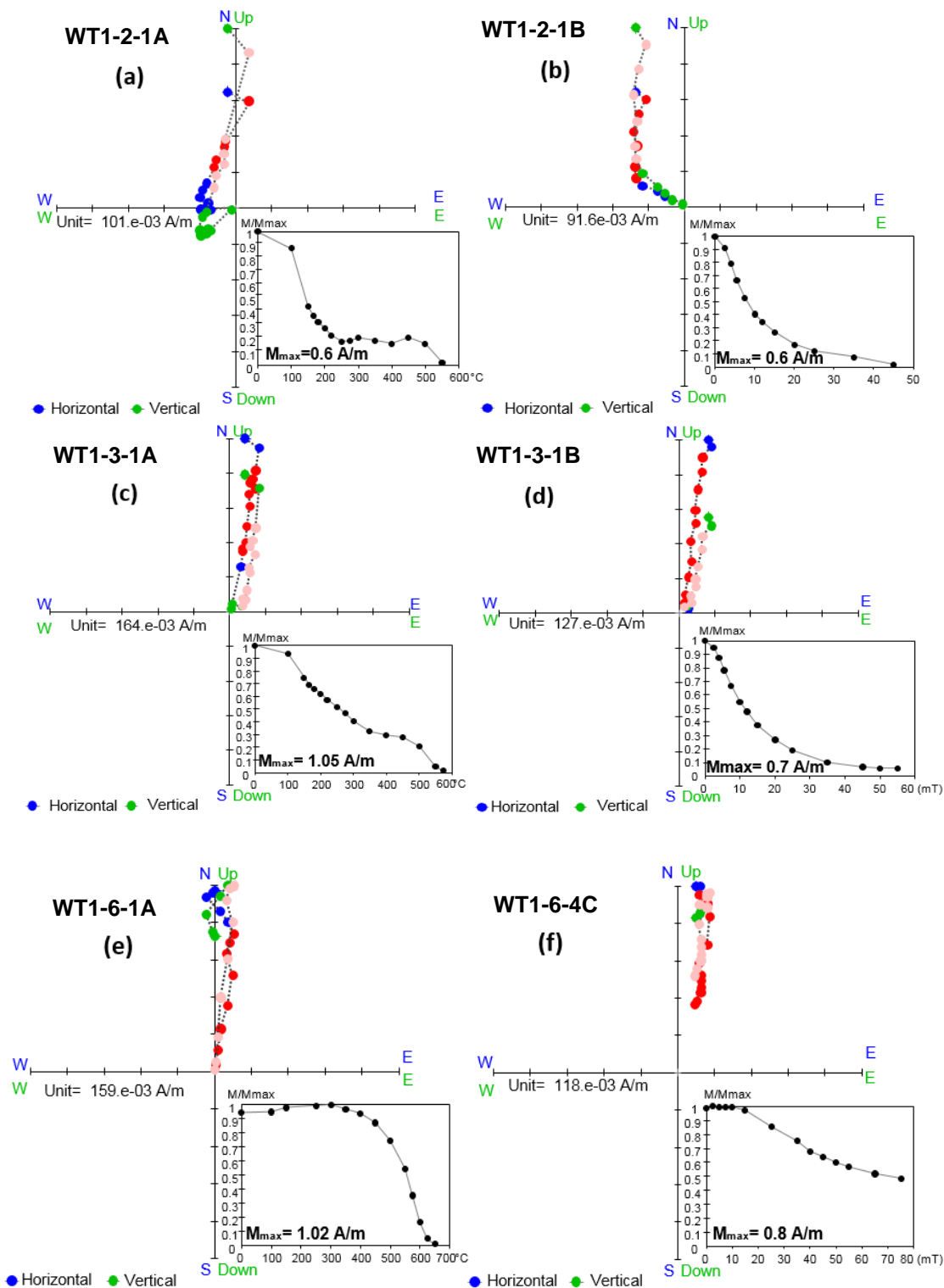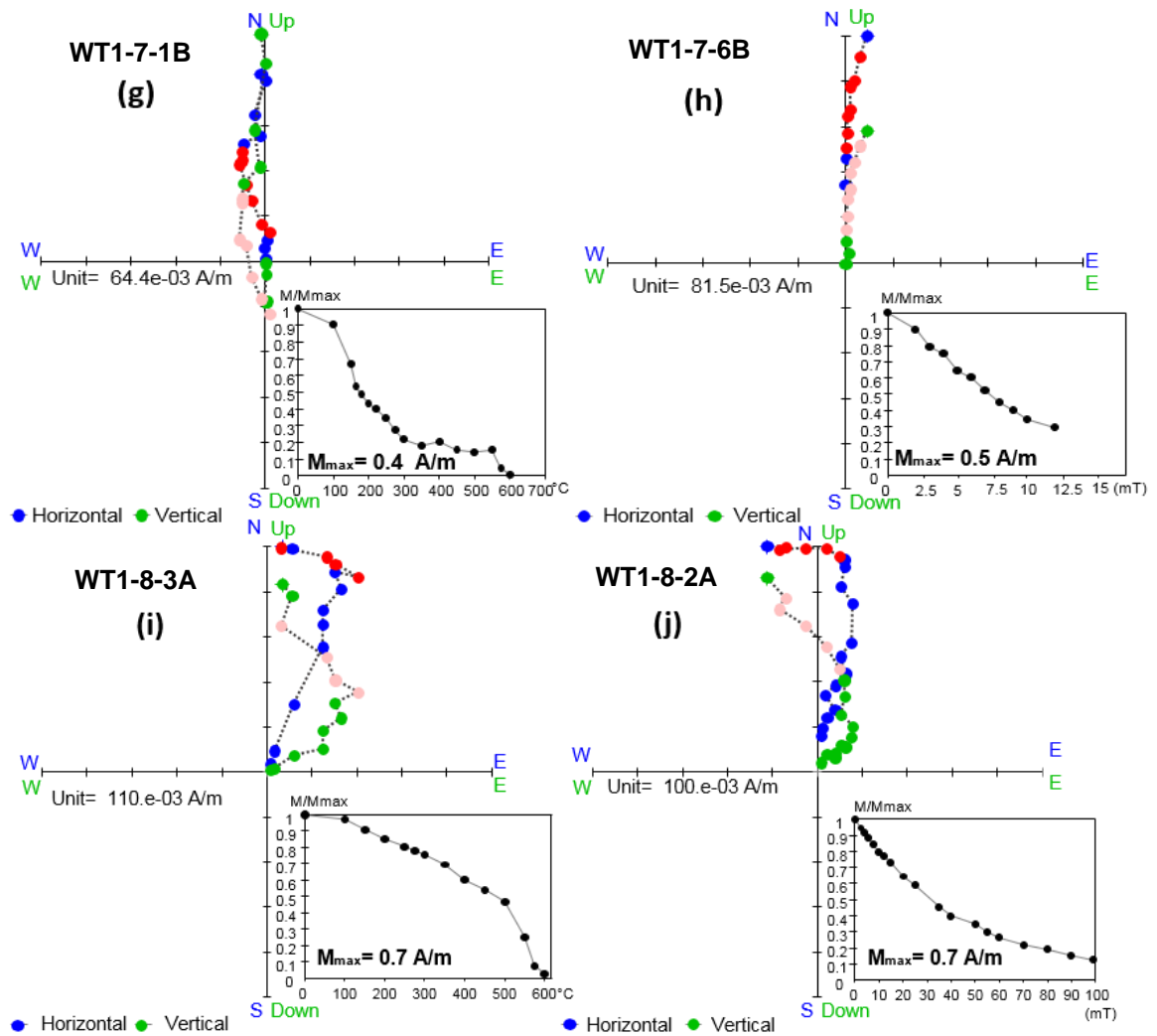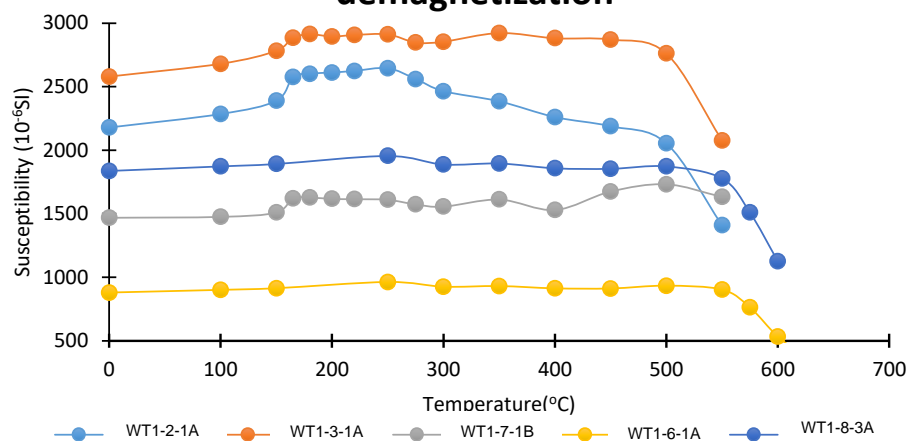
Figure 7.12. Demagnetization data of specimens from five hangi stones from site WT1. Left plots (a), (c), (e), (g) and (i) are the results of thermal demagnetization, right plots (b), (d), (f), (h) and (j) are results of AFD. Each figure includes Zijderveld plot and inset decay plot of specimen. Pink and red data points in Zijderveld plots show the data included for the calculation of magnetic vectors. (k) Shows magnetic susceptibility after each temperature step.

Table 7.6. Directional data of hangi site WT1, calculated from thermal (THD) and alternating field demagnetization (AFD). C1 high blocking temperature component, C2 low blocking temperature component of magnetization. THD (P) is directional data extracted from palaeointensity experiments. N is a number of stones and n is a number of specimens used for calculations. Calculations are done with Remasoft30 software. RT indicates room temperature. Only black coloured data is included in calculations of mean archaeodirections.

| Sample ID | Temp/field range | N or n | Dec (°) | Inc (°) | MAD/$\alpha_{95}$ (°) |
|---|---|---|---|---|---|
| WT1-2-1A (C1) | 350-550°C (THD) | 5 | 282.6 | 39.4 | 4.9 |
| WT1-2-1A (C2) | 100-220°C (THD) | 5 | 356.7 | -49.6 | 11.8 |
| WT1-2-1B (C1) | 15-45mT (AFD) | 5 | 298.6 | -34.1 | 3.4 |
| WT1-2-1B (C2) | 2.5-12mT (AFD) | 6 | 3.7 | -54.5 | 2.7 |
| WT1-2-2B(C1) | 15-30mT (AFD) | 4 | 323.9 | -18.2 | 3.6 |
| WT1-2-2B(C2) | 6.5-15mT (AFD) | 6 | 2.0 | -50.2 | 1.8 |
| WT1-2-3A(C1) | 15-45mT (AFD) | 5 | 309.9 | -36.8 | 2.8 |
| WT1-2-3A(C2) | 2.5-12mT (AFD) | 6 | 359.4 | -57.1 | 1.2 |
| WT1-2-4A(C1) | 15-30mT (AFD) | 4 | 326.8 | -50.8 | 1.3 |
| WT1-2-4A(C2) | 6.5-15mT (AFD) | 6 | 5.9 | -55.7 | 1.8 |
| **Mean WT1-2** | | **4** | **2.8** | **-54.4** | **3.8** |
| WT1-3-1A | 150-450°C (THD) | 9 | 7.8 | -40.6 | 3.7 |
| WT1-3-2A | RT-450°C (P) | 10 | 7.4 | -52.0 | 4.5 |
| WT1-3-3A | RT-350°C (P) | 8 | 6.8 | -47.9 | 6.6 |
| WT1-3-4A | 2.5-12.5mT (AFD) | 7 | 7.2 | -45.7 | 3.3 |
| WT1-3-5A | 0-15mT (AFD) | 8 | 7.9 | -51.0 | 3.9 |
| **Mean WT1-3** | | **3** | **7.3** | **-49.2** | **3.3** |
| WT1-6-1A | 350-650°C (THD) | 9 | 7.9 | -55.2 | 2.2 |
| WT1-6-4C | 5-75mT (AFD) | 12 | 11.5 | -49.2 | 4.2 |
| WT1-6-5A | 10-75mT (AFD) | 10 | 9.7 | -50.8 | 4.0 |
| WT1-6-5B | 200-525°C (P) | 7 | 11.8 | -53.5 | 3.3 |
| WT1-6-5C | 200-525°C (P) | 7 | 11.8 | -54.9 | 2.9 |
| **Mean WT1-6** | | **5** | **10.6** | **-52.7** | **2.7** |
| WT1-7-1A | 4-15mT (AFD) | 5 | 354.9 | -51.0 | 2.9 |
| WT1-7-1B (C1) | 450-575°C (THD) | 4 | 17.3 | -64.7 | 3.4 |
| WT1-7-1B (C2) | 250-400°C (THD) | 6 | 333.7 | -47.5 | 4.0 |
| WT1-7-4B | 0-7.5mT (AFD) | 5 | 357.2 | -55.6 | 4.0 |
| WT1-7-6B | 2.5-8.5mT (AFD) | 8 | 5.8 | -44.0 | 1.8 |
| **Mean WT1-7** | | **3** | **359.7** | **-50.3** | **10.6** |
| WT1-8-2A(C1) | 12-35mT(AFD) | 5 | 354.5 | -29.0 | 6.5 |
| WT1-8-2A(C2) | 2.5-10mT(AFD) | 5 | 279.7 | -49.7 | 4.8 |
| WT1-8-3A(C1) | 400-600°C (THD) | 6 | 20.9 | -10.7 | 4.8 |
| WT1-8-3A(C2) | 100-275°C (THD) | 5 | 293.5 | -45.7 | 8.1 |
| WT1-8-6A(C1) | 300-500°C (P) | 5 | 6.9 | -44.0 | 2.2 |
| WT1-8-6A(C2) | 150-300°C(P) | 6 | 285.5 | -65.5 | 1.0 |
| WT1-8-6B(C1) | 300-500°C (P) | 5 | 10.4 | -43.6 | 3.7 |
| WT1-8-6B(C2) | 150-300°C (P) | 6 | 297.1 | -61.4 | 0.9 |
| **Mean WT1-8 (C1)** | | **3** | **8.6** | **-32.3** | **21.3** |
| **Mean WT1-8 (C2)** | | **3** | **288.8** | **-55.8** | **11.9** |
| **Mean WT1-2,3,6&7** | | **n = 15,** | **6.3** | **-52.2** | **2.5** |
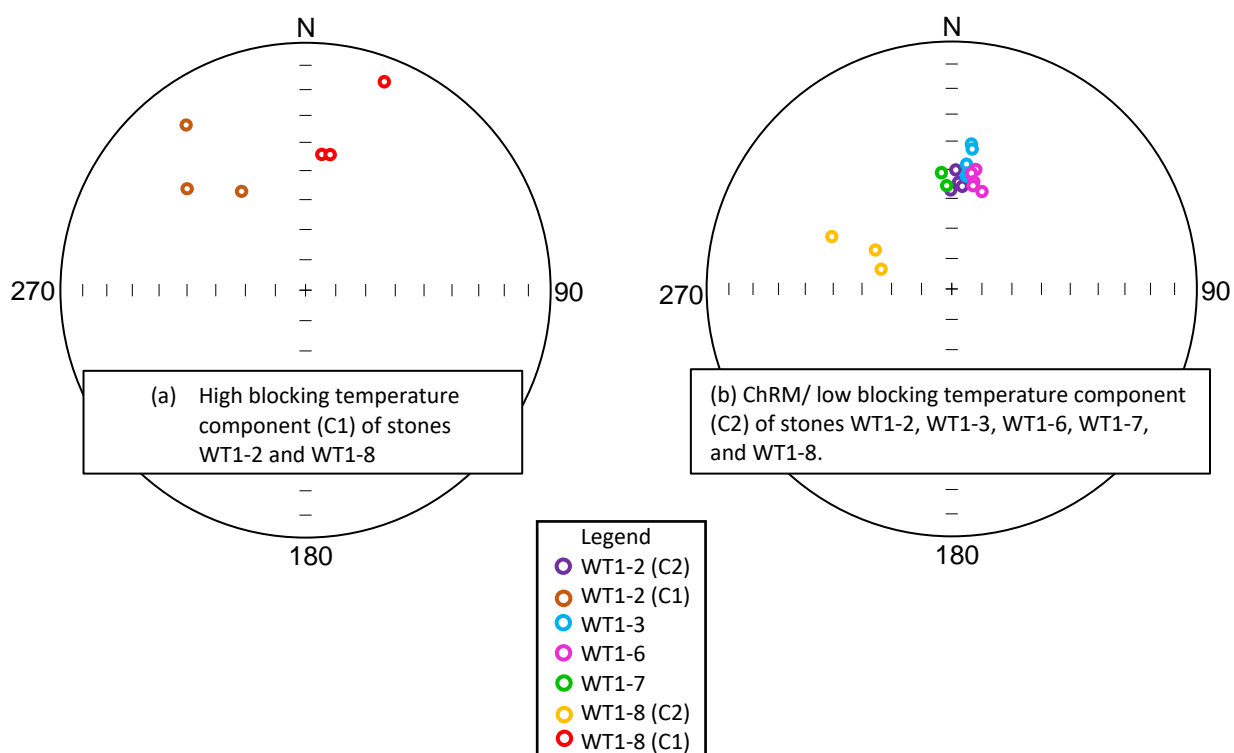
Figure 7.13. Stereographic projection of directional data of each specimen listed in Table 7.6. (a) High blocking temperature component (C1), (b) low blocking temperature component (C2).
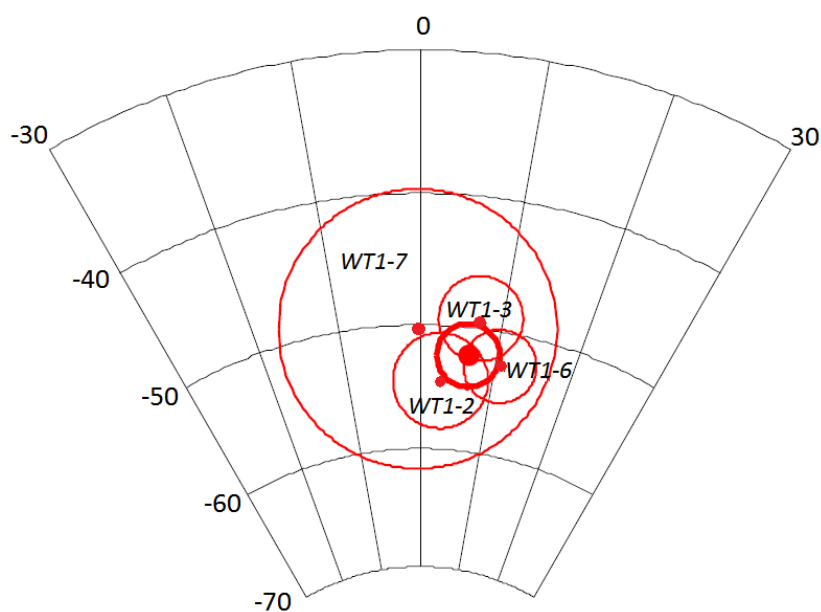


Figure 7.14. Stereoplot section (equal angle) of mean archaeodirections of stones WT1-2, WT1-3, WT1-6 and WT1-7, with $\alpha_{95}$'s. The bold red dot and circle are the overall site mean and its $\alpha_{95}$.

## 7.5.2. Hangi site WT2

The WT2 hangi stones have a stronger NRM than WT1 stones, in the range 1-10 A/m, and broader hysteresis loops, indicating a smaller magnetic grain size. Four specimens were thermally demagnetized, one from each of the four stones collected. The specimens lost little magnetization below a temperature of 400°C.  In specimen WT2-1-3A, the Zijderveld plot (Figure 7.15 (a)) shows two components of magnetization (removed from room temperature to 500°C, and from 500°C to 600°C). The magnetization increased in the initial steps by about 12% up to 500°C and then decayed 70% from 500-550°C. In WT2-2-3A (Figure 7.15 (b)), there are also two components of magnetization, the first removed from room temperature to 350°C and the second from 400-575°C. In specimens WT2-3-2B and WT2-4-3A, grains unblock above a temperature of 350°C (Figure 7.15 (c) & (d)), and the specimens lose their magnetization completely between temperatures of 550 and 600°C. The two components seen in both WT2-1-3A and WT2-2-3A indicate that the stones were disturbed during cooling at about 400-500°C.

The stones were not oriented in the field, so the projection of data points in the Zijderveld plots of Figure 7.15 is arbitrary, and an average site direction cannot be calculated. Figure 7.15 (e) shows that the susceptibilities of three of the specimens remain stable throughout the experiment, while in WT2-2-3A, susceptibility increases gradually above 300°C. The information provided by thermal demagnetization experiments was used to select suitable samples for palaeointensity experiments.
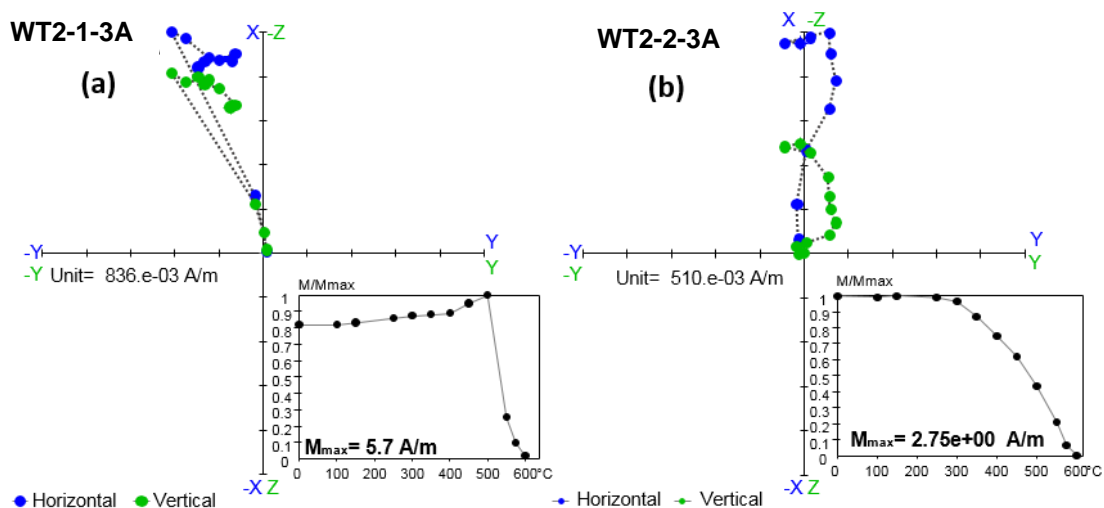
Figure 7.15. (a)-(d) Thermal demagnetization results of stones WT2-1, WT2-2, WT2-3 and WT2-4 from hangi site WT2. Each figure includes Zijderveld plot and inset decay plot of specimen. (e) Change in susceptibility of specimens with increase in temperature during stepwise progressive thermal demagnetization.

## 7.5.3. Hangi site WT3

The WT3 stones have NRMs in the range 0.1-2 A/m. Four specimens were thermally demagnetized, one from each of the stones collected. Specimen WT3-1-1B has a stable single component of magnetization trending towards the origin of the Zijderveld plot (Figure 7.16 (a)). Stones WT3-2, WT3-3 and WT3-4 are believed to have been disturbed during the cooling process or undergone reheating (up to lower temperature), as they show more than one component of magnetization. Specimens lose magnetization until

heated to 300-400°C and were completely demagnetized between temperatures of 575°C and 650°C.

In WT3-3-1B, three components of magnetization can be seen (Figure 7.16 (c)): the lowest blocking temperature component from 200-450°C, the second from 450-600°C, and the third from 600-650°C heading towards the origin. All specimens have lost 50-70% magnetization between 450°C to 550°C. The susceptibility did not change during the heating steps of thermal demagnetization up to 500°C, meaning there was no thermally-induced mineralogical alteration in the specimens. WT3 stones were non-oriented, so no absolute directional data was obtained.

**WT3: Change in susceptibility with temperature steps during demagnetization** (e)

Figure 7.16. (a-d) Thermal demagnetization results of stones WT3-1, WT3-2, WT3-3 and WT3-4 from hangi site WT3. Each figure includes Zijderveld plot and inset decay plot of specimen. (e) Change in susceptibility of specimens with increase in temperature during stepwise progressive thermal demagnetization.

## 7.5.4. Hangi site WT4

Thermal demagnetization experiments were performed on three specimens: WT4-1-3A, WT4-2-1A and WT4-4-5A. The results are shown in Figure 7.17 (a)-(c). The change in susceptibility of each specimen at all temperature steps is also shown in Figure 7.17 (d). These stones carry a stronger magnetization than the stones from the sites WT1, WT2 and WT3, with NRMs ranging from 3 to 4 A/m. A weak VRM component was removed below 150°C. All specimens have a stable single component of magnetization as can be clearly seen in Figure 7.17 (300-550°C for WT4-1-3A & WT4-2-1A; 450-550°C for WT4-4-5A), heading to the origin of the Zijderveld plots. There is no significant change in susceptibility up to 600°C, indicating no thermally-induced mineralogical alteration in the specimens. These stones were also not oriented, so directions are not consistent in Zijderveld plots and a site mean direction is not calculated.
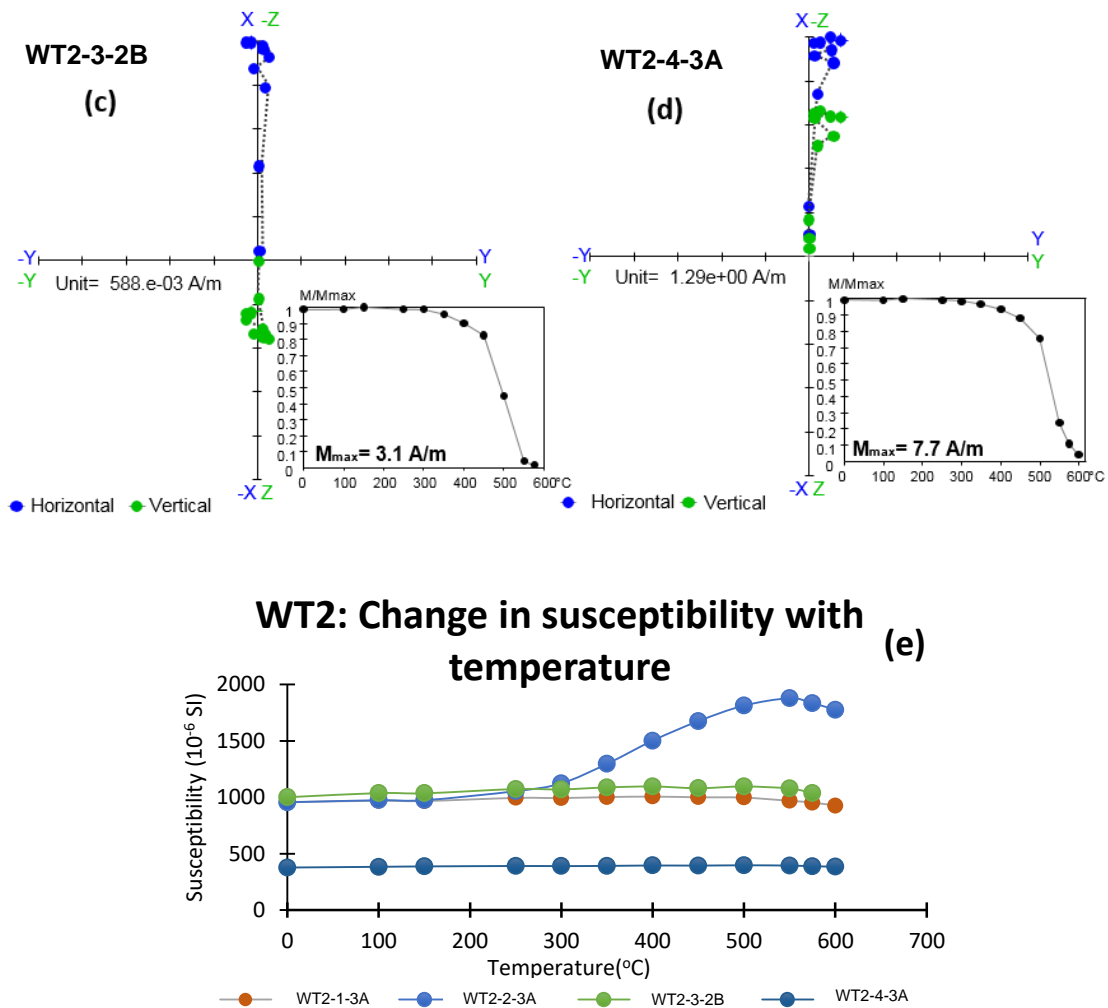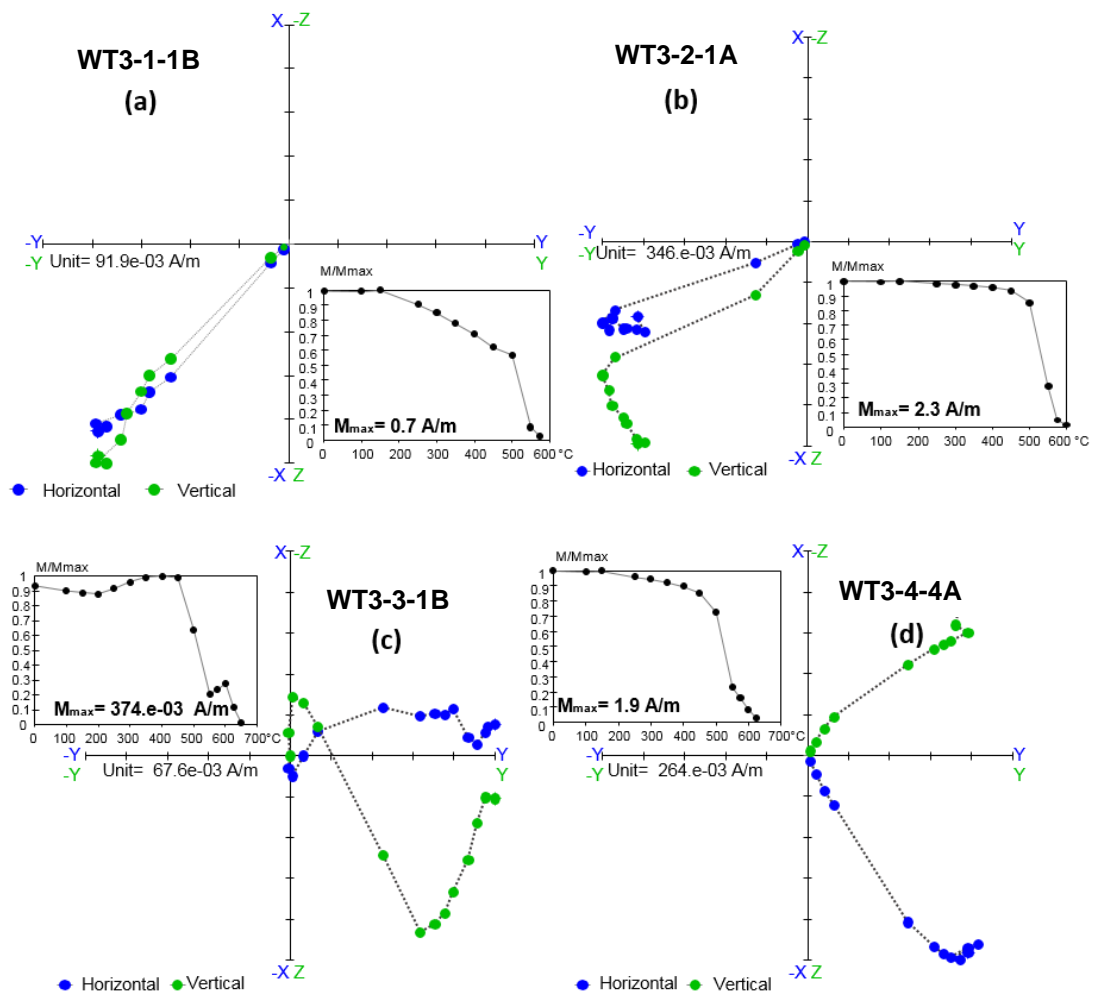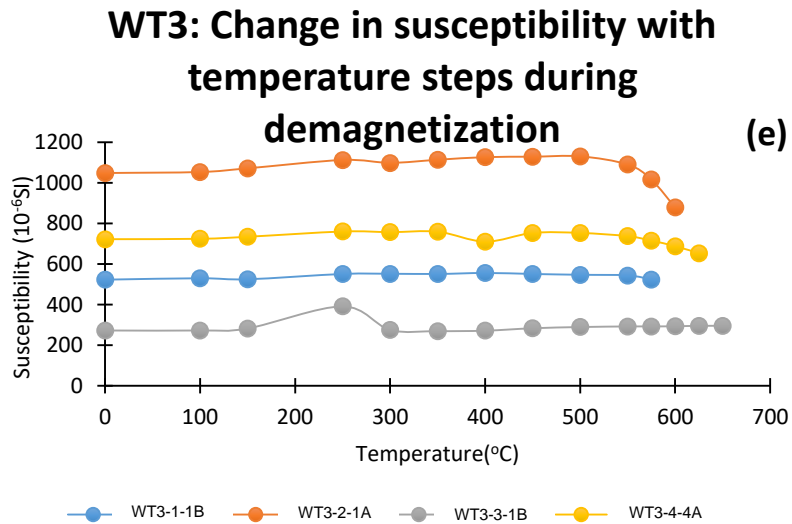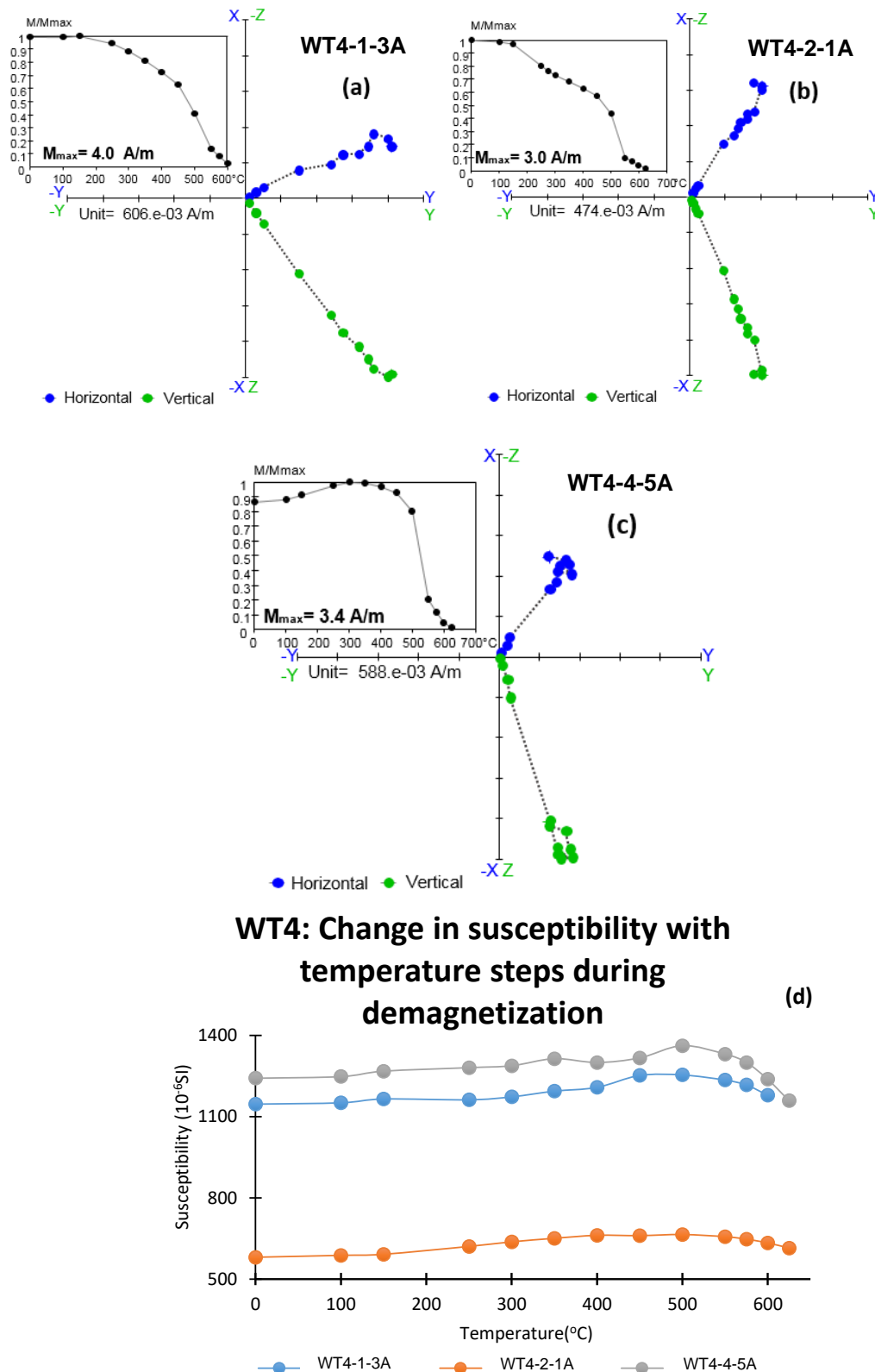
Figure 7.17. (a)-(d) Thermal demagnetization results of stones WT4-1, WT4-2 and WT4-4 from hangi site WT4. Each figure includes Zijderveld plot and inset decay plot of specimen. (d) Change in susceptibility of specimens with increase in temperature during stepwise progressive thermal demagnetization.

## 7.6. Archaeointensities

Archaeointensity experiments were performed on 22 specimens from the four WT sites, selected on the basis of the rock magnetic and thermal demagnetization data. This group of specimens included eight specimens from four of the WT1 stones (WT1-3, WT1-6, WT1-7, WT1-8), four specimens from two WT2 stones (WT2-3, WT2-4), four specimens from WT3 (WT3-1, WT3-4) and six specimens from three WT4 stones (WT4-1, WT4-2, WT4-4). All specimens were divided into two groups according to their blocking temperature spectrum. Samples with a stable single component of magnetization were preferred for intensity determination. The intensity data is summarized in Tables 7.7 & 7.8 and described in detail below.

### 7.6.1. WT1

The archaeointensity data from the WT1 specimens are shown in Figures 7.18 and 7.19. Only WT1-6 specimens were analyzed using Thellier Tool, as it was the only stone that carried a single component of magnetization (Figure 7.19). WT1-6-5C passed the TTB selection criteria. As already seen in demagnetization results, WT1-3, WT1-7 and WT1-8 carry multiple components of magnetization and so to calculate archaeointensities from the lower blocking temperature components only, Yu and Dunlop's method is used (Yu & Dunlop, 2002). From the Zijderveld plots, the temperature at which the components of magnetization separate can be clearly seen. The magnetization vector at this temperature (say at temperature $T_i$, where the components are separating) is subtracted from all magnetization vectors of temperature steps less than $T_i$ and Arai plots are plotted between magnetization calculated after subtraction and pTRM gained. The intensity values calculated using this method are given in Table 7.7. Intensities were also calculated by using Thellier Tool and selecting low blocking temperature components; these intensities were slightly weaker than the values calculated using multivectorial intensities method. In the case of WT1-3 and WT1-7, there are no sharp junctions visible, so the temperature point ($T_i$) has been chosen carefully after observing horizontal and vertical projections separately in Zijderveld plots. The directions are calculated by using Remasoft software. This method provided better values for

parameters of selection criteria as Thellier Tool does not calculate directional parameters when only a low temperature component is selected for the intensity calculation, results in high MADs, and lowers the quality of the results.
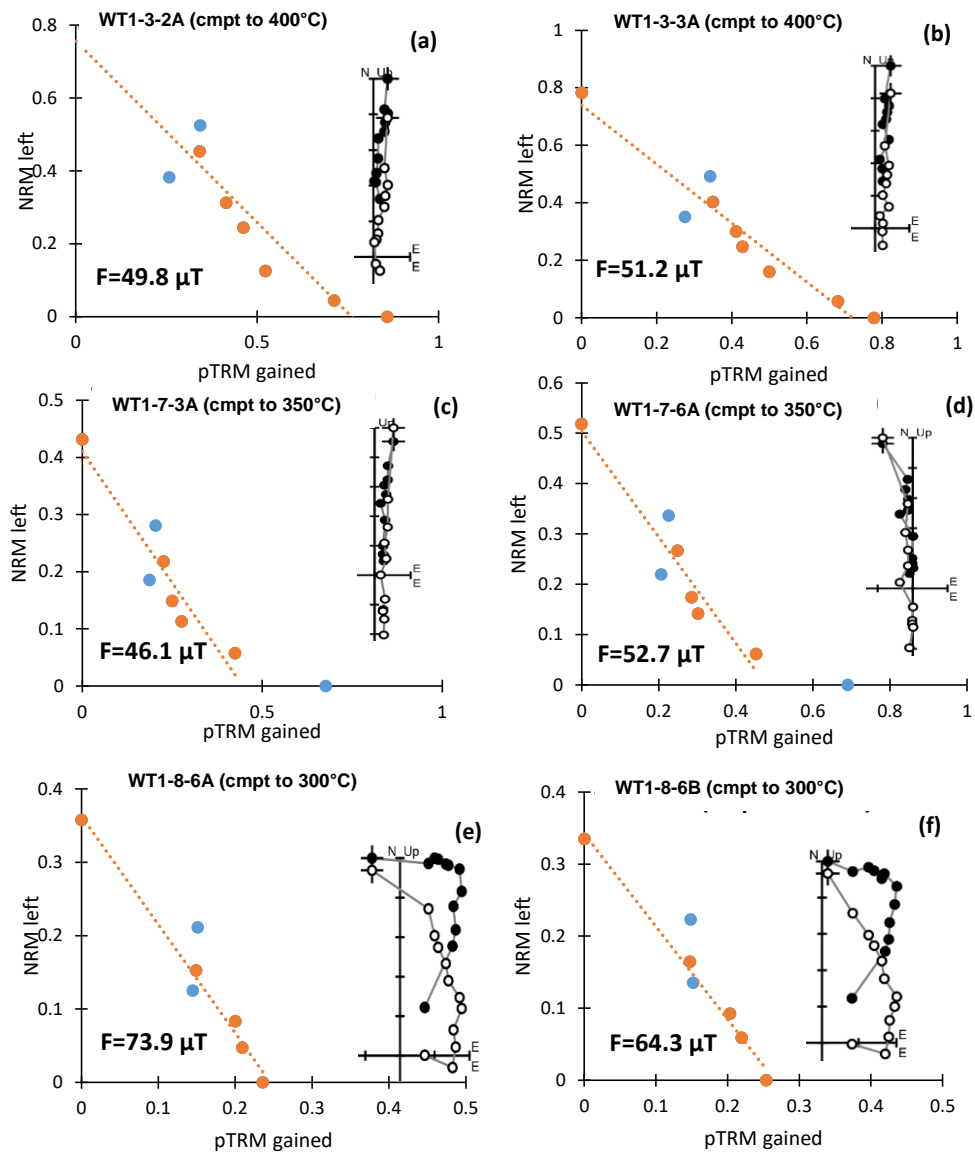


Figure 7.18. Arai diagrams obtained from specimens of stones WT1-3, WT1-7 and WT1-8 by doing manual calculations, Following Yu and Dunlop (2002). Zijderveld diagrams, plotted using Remasoft30 software, show demagnetization behaviour at each step.

The Curie temperature plots of Figure 7.8 show that thermal alteration took place in all WT1 samples above about 400°C, so it was not realistic to take archaeointensity experiments above this temperature. Hysteresis and IRM data show that the WT1 stones contain a high proportion of MD grains. These are the main reasons that most of the specimens did not pass the pTRM checks. WT1-6-5B did not meet the selection criteria as the pTRM and tail tests are lying in class TTC (Figure 7.19). However, WT1-6-5C meets quality criteria TTB and provides similar intensity value. Thus, these two specimens' data is also included in the site's mean intensity. WT1-8 specimens give higher intensity values and have a difference in the order of 10 microtesla. Furthermore, these results are not comparable with the archaeointensity values of other specimens of the site. Therefore, these are not included in the calculation of average intensity. The average archaeointensity of specimens WT1-3-2A, WT1-3-3A, WT1-6-5B, WT1-6-5C, WT1-7-3A and WT1-7-6A  is 47.7 ± 4.2 µT.
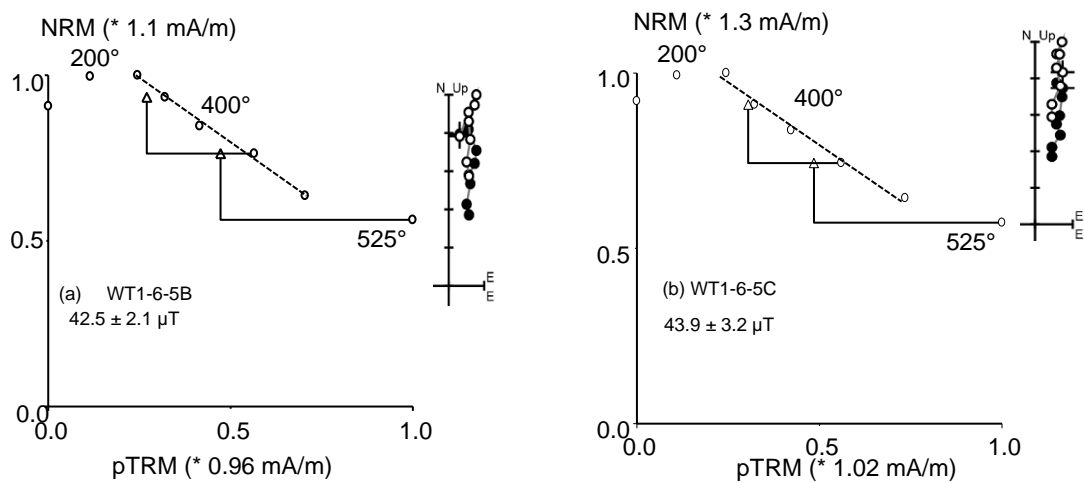


Figure 7.19. Arai plots of specimens WT1-6-5B and WT1-6-5C, produced using ThellierTool4.0.

Table 7.7. Archaeointensities of hangi stones from site WT1 determined using Multivectorial palaeointensity determination method (Yu and Dunlop, 2002) for specimens WT1-3, WT1-7 and WT1-8. Data of stone WT1-6 is calculated using Thellier Tool 4.0. Data presented in blue font is not included for calculation of average intensity. MAD (Anc.) is maximum angular deviation of the anchored directional fit to the palaeomagnetic vector on a vector component diagram (Kirschvink, 1980).

| Sample ID | Temp range (°C) | F±σ (µT) | N | β | f | q | MAD | $\delta_{CK}$ | $\delta_{pal}$ | $\delta_{TR}$ | $\delta_t$* | Class |
|---|---|---|---|---|---|---|---|---|---|---|---|---|
| Quality criteria | | | ≥5 ≥5 --- | ≤0.1 ≤0.15 --- | ≥0.35 ≥0.35 --- | ≥5 ≥0 --- | ≤6 ≤15 --- | ≤7 ≤9 --- | ≤10 ≤18 --- | ≤10 ≤20 --- | ≤99 ≤99 --- | TTA TTB TTC |
| WT1-3-2A | RT-400 | 49.8±3.2 | 9 | 0.02 | 1.0 | 50.7 | 3.7 | 11.2 | 3.0 | 3.8 | 10.5 | C |
| WT-3-3A | RT-400 | 51.2±1.7 | 9 | 0.01 | 1.0 | 66.8 | 2.6 | 13.0 | 8.5 | 1.7 | 15.3 | C |
| WT1-6-5B | 300-500 | 42.5±2.1 | 5 | 0.05 | 0.3 | 4.5 | 0.8 | 6.1 | 23.2 | 5.5 | 9.0 | C |
| WT1-6-5C | 300-500 | 43.9±3.2 | 5 | 0.07 | 0.3 | 3.1 | 1.3 | 4.7 | 16.6 | 3.1 | 9.1 | B |
| WT1-7-3A | RT-350 | 46.0±2.7 | 8 | 0.02 | 1.0 | 35.2 | 2.3 | 12.0 | 0.4 | 17.5 | 14.7 | C |
| WT1-7-6A | RT-350 | 52.7±2.1 | 9 | 0.02 | 1.0 | 34.7 | 5.7 | 11.8 | 2.02 | 16.2 | 18.2 | C |
| WT1-8-6A | RT-300 | 73.9±0.6 | 7 | 0.02 | 1.0 | 34.0 | 7.6 | 1.6 | 5.8 | 0.0 | 3.8 | A |
| WT1-8-6B | RT-300 | 64.3±0.6 | 7 | 0.02 | 1.0 | 39.8 | 4.1 | 0.1 | 0.4 | 0.0 | 3.9 | A |

## 7.6.2. WT2

Four specimens WT2-3-2A, WT2-3-3A, WT2-4-2A and WT2-4-2B, were used to determine palaeointensity. The specimens from these two stones have strong remanent magnetization but provided inconsistent values of palaeointensities. All specimens met the modified TTA or TTB selection criteria; Arai plots along with Zijderveld plots are shown in Figure 7.20. The palaeointensities of specimens from stone WT2-3-2A and WT3-3A differ by about 12µT and are also much smaller than the WT2-4 values of ca. 77 µT. The difference in intensity between the two stones could be due to the magnetization of the stones at different times. WT2 could be a cache of stones, containing stones from hangi sites of different ages. However, this cannot be the reason for the difference in intensities between specimens WT2-3-2A and WT2-3-3A. In Zijderveld plots of these specimens, it can be seen that magnetization vectors do not head straight to the origin and this may indicate a slight disturbance of the stones. Therefore, the intensity results of specimens from stone WT2-3 were rejected, and those of specimens from stones WT2-4 were accepted (Table 7.8). The average

palaeointensity of WT2-4-2A and WT2-4-2B is 77.3 ± 0.6 µT. Rock magnetic data have already shown that the mineral has PSD grains with the dominance of SD grains and also provided reliable palaeomagnetic results.



Figure 7.20. Arai diagrams obtained from specimens of stones WT2-3 and WT2-4 by using Thellier Tool 4.1. Arrows represent pTRM checks. Zijderveld diagrams, plotted using Remasoft30 software, show demagnetization behaviour at each step.

## 7.6.3. WT3

Arai plots of specimens WT3-1-1A, WT3-1-3B, WT3-4-2A and WT3-4-3A are shown in Figure 7.21 (a)-(d). The WT3-1-1A and WT3-1-3A data pass tail and pTRM-checks and meet TTA criteria (modified). In WT3-4-2A, β > 0.1 and WT3-4-3A, f < 0.35, so they both have q < 5 and fail TTA (Table 7.8). WT3-1-1A and WT3-1-3B show a linear trend in Arai

plots, whereas a curve is evident in WT3-4-2A and WT3-4-3A. This can be explained by values of remanence and coercivity ratios obtained from hysteresis and backfield experiments (Table 7.5). The measured intensities have a significant error due to the dominance of MD grains in the specimens, so the results of these specimens were rejected. The average palaeointensity of two specimens of stone WT3-1 is 60.3 ± 1.5 µT and is acceptable.



Figure 7.21. Arai plots obtained from specimens of stones WT3-1and WT3-4 using Thellier Tool 4.1. Arrows represent pTRM checks. Zijderveld diagrams, plotted using Remasoft30 software, show demagnetization behaviour at each step.

## 7.6.4. WT4

Six specimens, WT4-1-2B, WT4-1-4A, WT4-2-1B, WT4-2-2B, WT4-4-1A and WT4-4-3A, from three stones, WT4-1, WT4-2 and WT4-4, were used to determine the archaeointensity of site WT4 (Figure 7.22). The specimens of stone WT4-1 resulted in concave Arai plots and did not provide accurate results. These specimens also failed tail and pTRM checks due to thermochemical alterations (Table 7.8). Specimens from WT4-2 passed selection criteria at every step and did not show thermal alteration. The mean archaeointensity of WT4-2-1B and WT4-2-2B is 57.8 ± 0.8 μT. Specimens of stone WT4-4 provided inconsistent results and also failed pTRM-checks (Figure 7.22 (e) & (f)) and zero field tests at 525°C. The susceptibility of these specimens also started to decrease above 525°C, indicating a thermal alteration in the specimens. The archaeointensity experiments on these specimens did not proceed after 525°C.
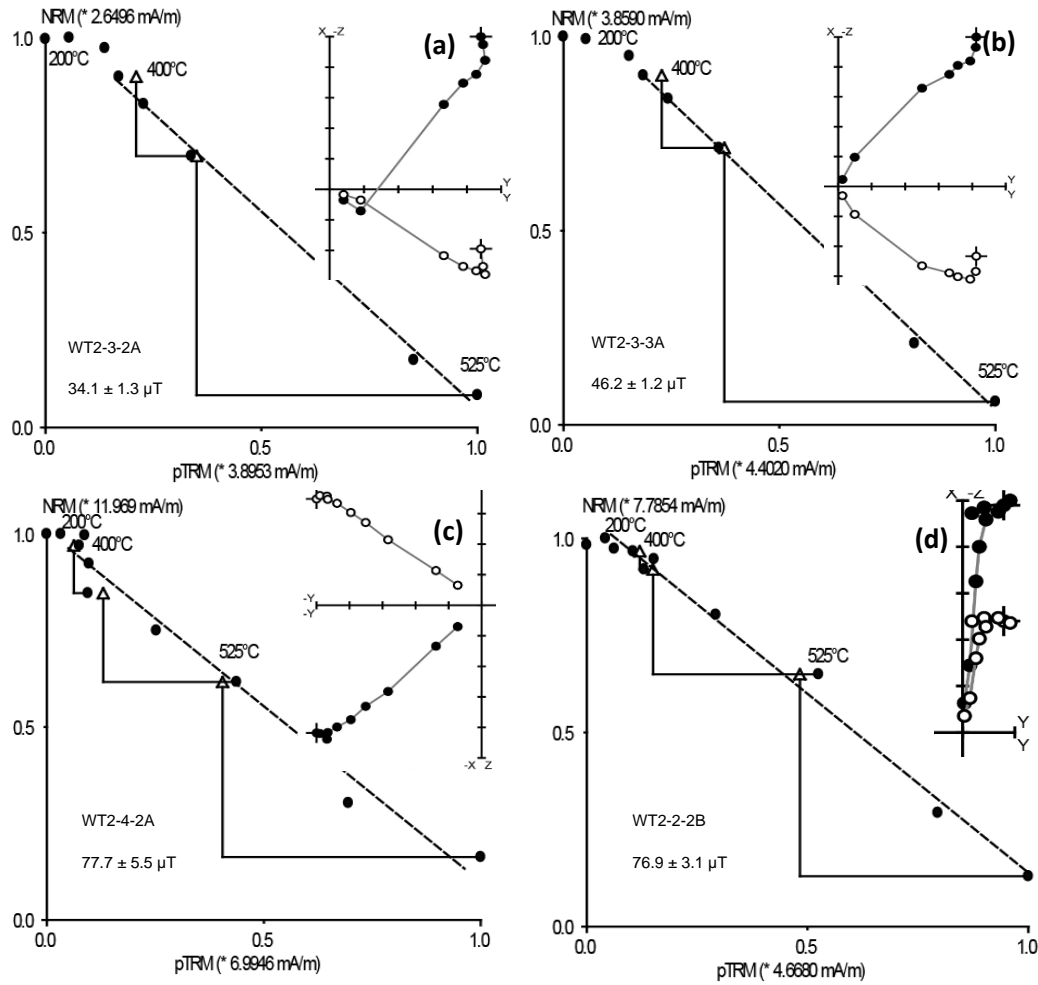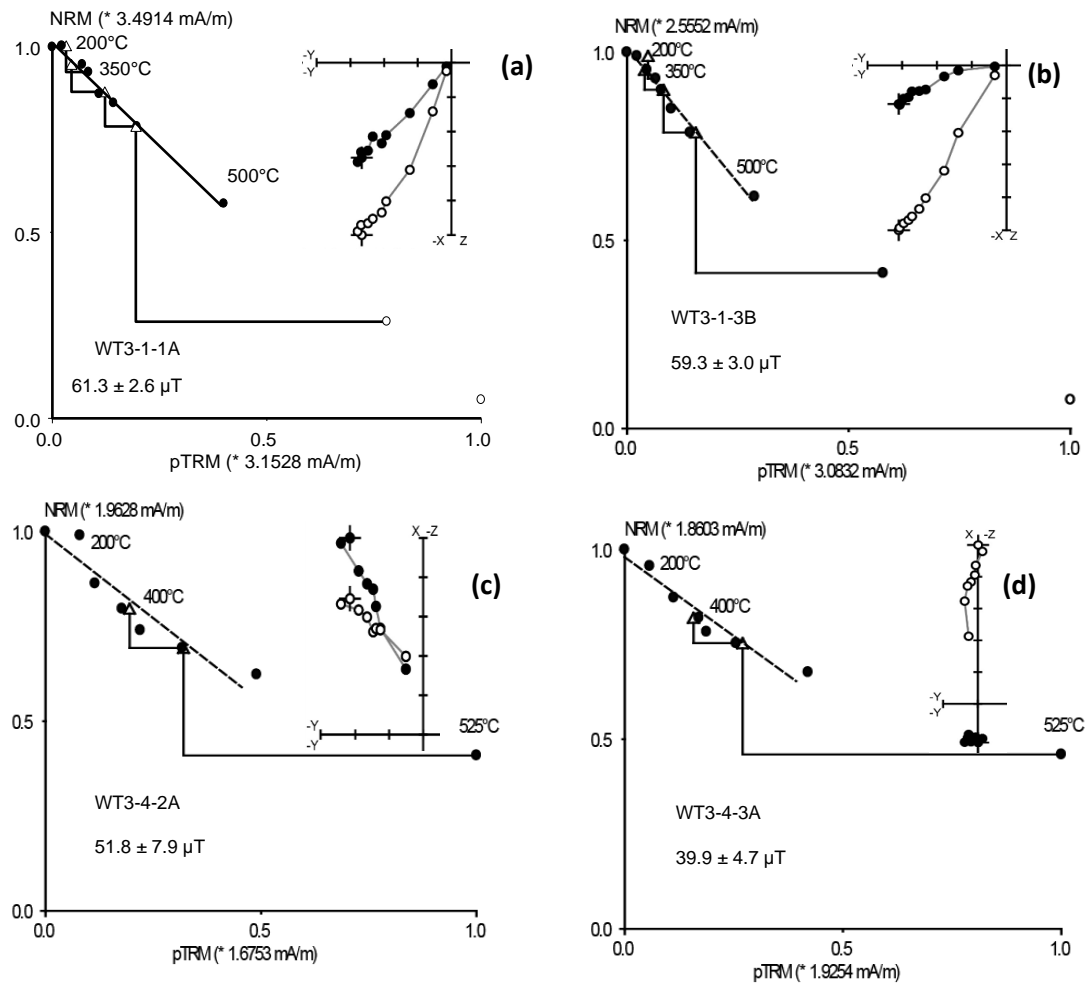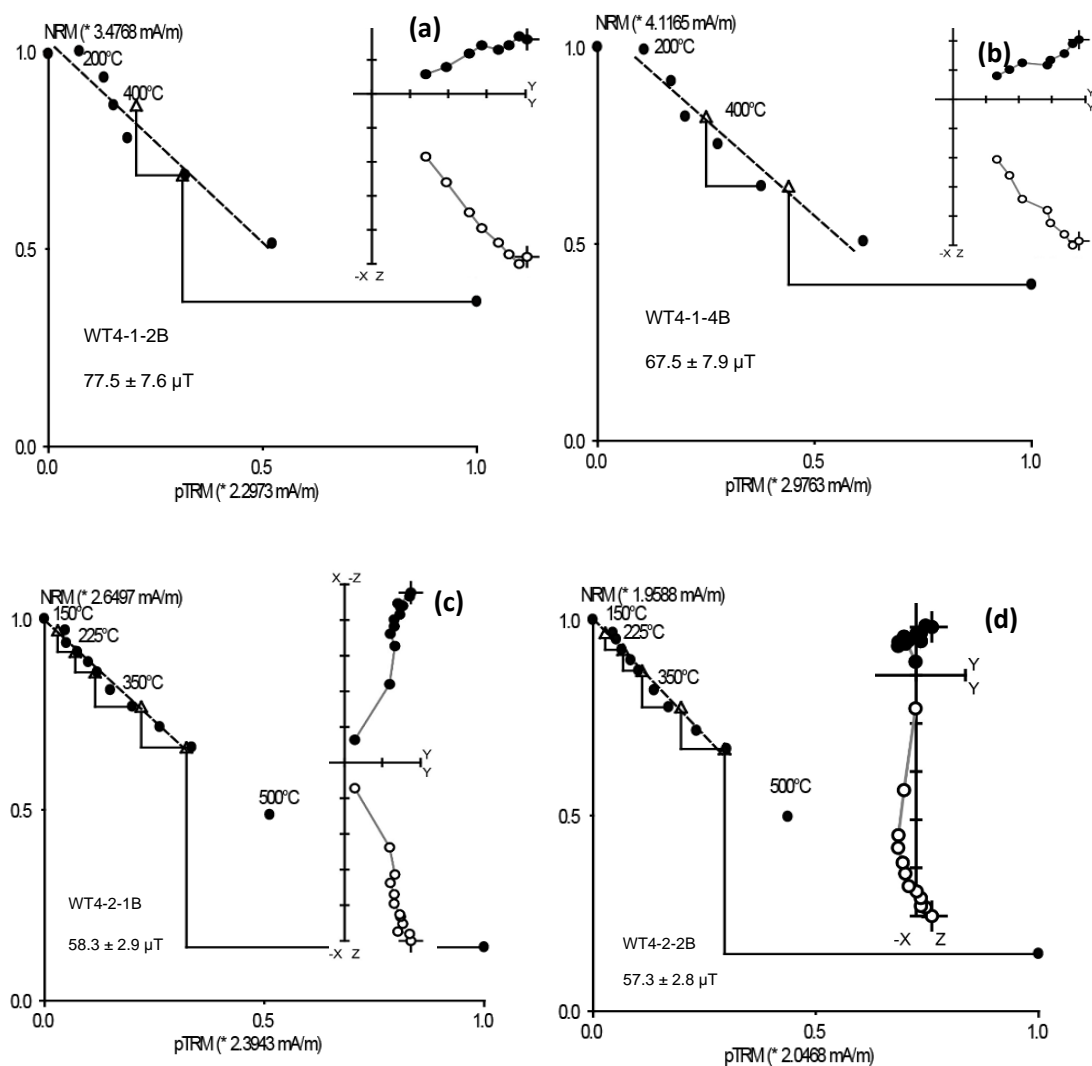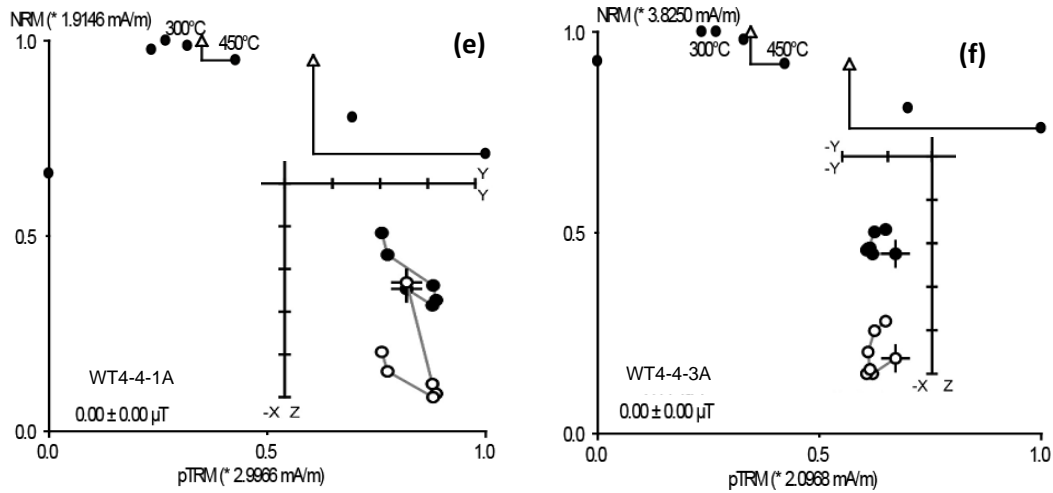
Figure 7.22. Arai diagrams obtained from specimens of stones WT4-1, WT4-2 and WT4-4 using Thellier Tool 4.1. Arrows represent pTRM checks. Zijderveld diagrams, plotted using Remasoft30 software, show demagnetization behaviour at each step.

Table 7.8. Archaeointensity results measured from four hangi sites at Whitianga. F are intensity results of individual specimens in µT. N is the number of data points included in a linear segment of Arai plot. β, f, q, $\delta_{CK}$, $\delta_{pal}$, α, MAD, $\delta_{TR}$ and $\delta_{t*}$ are statistical parameters defined in Chapter 2. Acceptable results are represented in black font.

| Sample ID | Temp range (°C) | F±σ (µT) | N | β | f | q | MAD | α | $\delta_{CK}$ | $\delta_{pal}$ | $\delta_{TR}$ | $\delta_t$* | Class |
|---|---|---|---|---|---|---|---|---|---|---|---|---|---|
| Quality criteria | | | ≥5 ≥5 --- | ≤0.1 ≤0.15 --- | ≥0.35 ≥0.35 --- | ≥5 ≥0 --- | ≤6 ≤15 --- | ≤15 ≤15 --- | ≤7 ≤9 --- | ≤10 ≤18 --- | ≤10 ≤20 --- | ≤99 ≤99 --- | TTA TTB TTC |
| WT2-3-2A | 350-525 | 34.1±1.3 | 5 | 0.04 | 0.8 | 12 | 7.4 | 7.7 | 3.8 | 3.4 | 1.4 | 2.3 | B |
| WT2-3-3A | 350-525 | 46.2±1.2 | 5 | 0.03 | 0.8 | 18 | 3.1 | 2.8 | 4.0 | 4.8 | 1.7 | 2.1 | A |
| WT2-4-2A | 300-575 | 77.7±5.5 | 8 | 0.07 | 0.8 | 8.9 | 0.9 | 0.9 | 3.1 | 2.2 | 2.9 | 4.2 | A |
| WT2-4-2B | 200-575 | 76.9±3.1 | 9 | 0.04 | 0.8 | 16 | 2.6 | 0.9 | 3.7 | 0.7 | 3.1 | 2.3 | A |
| WT3-1-1A | RT-500 | 61.3±2.6 | 8 | 0.04 | 0.4 | 7.2 | 2.3 | 6.3 | 2.7 | 1.5 | 2.0 | 4.1 | A |
| WT3-1-3B | 200-500 | 59.3±3.0 | 7 | 0.05 | 0.4 | 5.1 | 1.8 | 4.6 | 3.6 | 4.6 | 1.2 | 5.9 | A |
| WT3-4-2A | RT-500 | 51.8±7.9 | 7 | 0.15 | 0.4 | 2.2 | 3.1 | 7.8 | 1.7 | 4.3 | 1.8 | 6.7 | B |
| WT3-4-3A | RT-400 | 39.9±4.7 | 7 | 0.12 | 0.3 | 2.2 | 3.3 | 9.1 | 1.4 | 0.5 | 3.1 | 12.8 | B |
| WT4-1-2B | 200-500 | 81.5±9.0 | 7 | 0.11 | 0.5 | 3.1 | 1.2 | 0.8 | 5.3 | 10.5 | 2.0 | 22.1 | B |
| WT4-1-4A | 200-500 | 67.5±7.9 | 6 | 0.11 | 0.5 | 3.0 | 2.1 | 2.6 | 5.9 | 33.2 | 0.2 | 19.5 | C |
| WT4-2-1B | RT-450 | 58.1±2.9 | 10 | 0.05 | 0.4 | 6.1 | 1.4 | 4.4 | 2.0 | 6.4 | 1.1 | 4.6 | A |
| WT4-2-2B | RT-450 | 57.3±2.8 | 10 | 0.05 | 0.4 | 6.2 | 3.3 | 13.5 | 3.2 | 4.8 | 2.8 | 2.5 | A |

## 7.7. Discussion

Directional data was measured only for the stones from hangi site WT1; the stones from the other three locations, WT2, WT3, and WT4 were not oriented. For the specimens, which carried more than one component of magnetization, the lowest unblocking temperature component has been analyzed. The direction of magnetization is the result of the stones' final cooling in the hangi, and anything originating prior to this is not useful for determining ambient field directions, although it may still be useful for intensity experiments. Table 7.6 shows the mean direction from each specimen from WT1, and the average for all specimens that passed the selection criteria (MAD ≤ 5° and $\alpha_{95}$ ≤ 10°). Measured archaeointensities are listed in Table 7.7 and Table 7.8. The intensity results are reliable where their deviation is less than or equal to 7%. Twelve specimens provided successful archaeointensity results (Table 7.7 and Table 7.8) i.e. about 50% successful results; the intensity values are calculated from each specimen using ThellierTool4.0 (Leonhardt et al., 2004) and multi-vectorial palaeointensity method (Yu & Dunlop, 2002).

The directional data can be used for preliminary archaeomagnetic dating. The declination and inclination are compared with NZPSV1K (Turner et al., 2015) using the dating tool of Pavon-Carrasco et al., (2011). NZPSV1K includes data from the geomagnetic field model *gufm1* (Jackson et al., 2000), from 1590 to 1990AD, and lake sediment records from 1000 to 1590AD (Turner et al., 2015). Site WT1 was not dated by radiocarbon dating. Archaeomagnetic dating, however, suggests an age range of 1460 to 1545AD (Figure 7.23). This age range compares well with the ^{14}C date of 1427 to 1464AD given in Table 7.3 for site WT2. WT2 is stratigraphically above WT1; the data are compatible with both sites originating from ca. 1460AD. Comparison of the directional data of WT1 with lake sediment records suggests that the inclination values are around six degrees shallower than expected for the declination (Figure 7.23). In Figure 7.24 the mean archaeointensities of the sites WT1, WT2, and WT4 are compared with field intensities calculated from the global geomagnetic field model *gufm*1 (Jackson et al., 2000) at the location of Whitianga (latitude/longitude ~ 36.8°S/ 175°E). For site

WT1 the archaeomagnetic age has been used, while calibrated $^{14}$C ages have been used for WT2 and WT4.

WT2-3 specimens have provided a difference of about 12 µT in the intensity values calculated. On the other hand, WT2-4 specimens yielded consistent intensities. It can also be observed that statistical parameters of these specimens are lying in quality criteria TTA. Therefore, data of stone WT2-3 is not included in the calculation of the site's mean archaeointensity. Similarly, the specimens of stones WT3-1 and WT4-2 have shown nearly the same archaeointensity data, whereas WT3-4 and WT4-1 have demonstrated the variability of 12 µT and 14 µT respectively. This variability can be due to the inhomogeneity of the stones' mineralogy. Such data is therefore discarded for the calculation of the average intensity of the site. This data shows that between 1400 and 1500AD the geomagnetic field strength was frequently changing. Therefore, well dated and high-quality archaeomagnetic data from the Whitianga hangi sites is very useful in understanding the variation of the geomagnetic field at that historical time. More hangi stones belonging to other features of Whitianga archaeological site are available. These can be experimented on in future and their data help to extend the intensity curve to an earlier period.
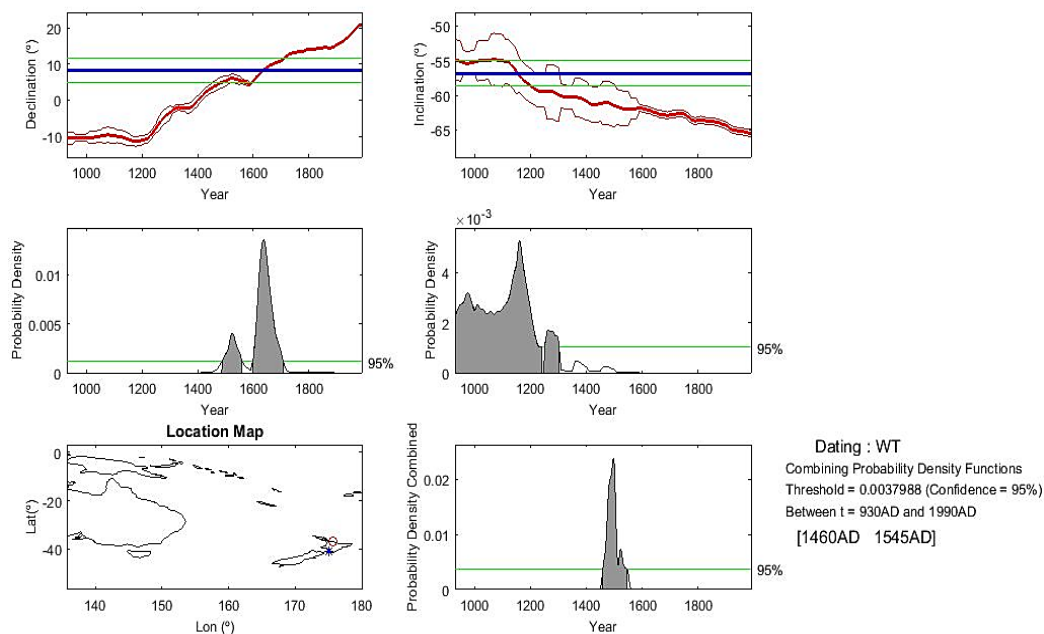


Figure 7.23. Archaeomagnetic dating of site WT1 by using directional data retrieved from hangi stones.

## 7.8. Conclusion

The WT1 directional data matches with NSPSV1K (Turner et al., 2015), and gives an archaeomagnetic date of 1460 to 1545AD that is consistent with ^{14}C dates on WT2 and WT4. Archaeointensity determinations on the WT hangi stones yielded a success rate of about 50% and has shown variability in intensity values. The reliable archaeointensities cover a large range (47.7 – 77.3 µT), and suggest that the field intensity varied greatly over a short period of around 100 years. Since WT intensity data precedes *gufm*1, there is no data available for direct comparison. The literature contains suggestions of significant variations in field strength in other parts of the world during the same period (archaeomagnetic jerks), which is still controversial (Gallet et al., 2003; Gallet et al., 2003; Stark, 2011).
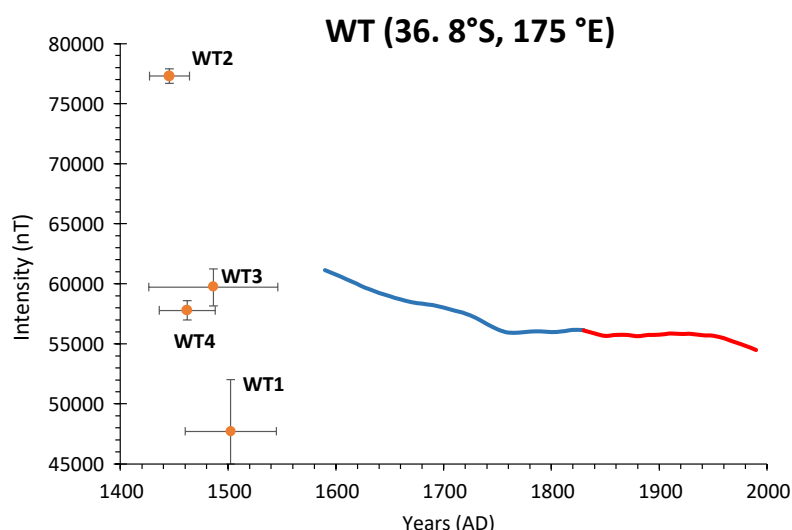


Figure 7.24. Geomagnetic field intensity at Whitianga (36.8°S /175°E) site for last 400 years calculated from *gufm1* (Jackson et al., 2000). Orange dots are the archaeointensities of sites WT1, WT2, WT3 and WT4 with 1σ error-bars.

# 8. Discussion and Conclusion

## 8.1 Reliability of data

Hangi stones are used as heat retainers, for the slow steaming of food in traditional Maori earth-covered ovens. They are naturally occurring rocks (in this study volcanic rocks and lithified sandstones). During the hangi process the magnetic mineralogy of the rocks is often enhanced and stabilized, making the stones good magnetic recorders for archaeomagnetic studies. Hangi stones from the archaeological sites studied here provided good-quality archaeomagnetic data with an overall success rate of more than 60%.

The archaeomagnetic results obtained from the ten hangi sites studied are summarized in Table 8.1.

Although oriented samples were collected from eight of the ten hangi sites, directional data could be retrieved from only five as the stones from the other sites were found to have been disturbed after cooling, possibly during rake-out. The directional data of such stones are not included in the calculation of site-mean directions. Stones which were disturbed during the cooling process have acquired more than one component of magnetization, and the lowest blocking temperature component may represent the field during the last cooling of the stone. The average direction for each stone is calculated from the specimens that provide consistent data (MAD < 15°). The site mean archaeodirection is then calculated from the stones that provide consistent directions ($\alpha_{95}$ < 5°).

High-quality archaeointensity results were obtained from most of the stones collected at the Great Mercury Island, Opihi River, Weld Pass, Riverlands, and Whitianga hangi sites. Intensity data were analyzed using ThellierTool4.0 (Leonhardt et al., 2004) and a specially written Excel spreadsheet. These delivered comparable results.

The magnetic mineralogy of some specimens had altered thermally during the palaeointensity experiments; these specimens did not pass tail/pTRM checks. However,

some such specimens have linear Arai plots and yield palaeointensities that compare well with high-quality data from the same site. These data were labelled Class C and included in site-mean archaeointensity calculations. Data points in the Arai plots used for the calculation of gradients have minimum scatter. More than 50% of the NRM has been used in each case. Most of the hangi sites have independent age control, obtained using dating of suitable charcoal fragments found amongst the stones. At other sites, contextual archaeological information can help constrain the age.

Table 8.1. Archaeomagnetic data from New Zealand hangi sites.

| Site Name | Lat (°) | Long (°) | ¹⁴C age range (AD years) | Dec (°) | Inc (°) | N | $\alpha_{95}$ (°) | F±σ (µT) | N for F | Dec relocated to 40°S 175°E (°) | Inc relocated to 40°S 175°E (°) | F relocated to 40°S 175°E (µT) | VADM ± δ ($10^{22}$Am²) | VDM ($10^{22}$A m²) | Archaeomagnetic age range (AD years) | Best age estimate (AD years) |
|---|---|---|---|---|---|---|---|---|---|---|---|---|---|---|---|---|
| GM1 | -36.6 | 175.8 | 1515-1542 (8.6%), 1625-1666 (86.3%) | 1.5 | -55.9 | 12 | 3.3 | 59.3±2.2 | 8 | 1.6 | -59.1 | 61.7 | 10.7±0.4 | 10.7 | 1380-1587 | 1516-1587 |
| GM2 | -36.6 | 175.8 | 1643-1673 (57.7%), 1743-1772 (16%), 1779-1797 (63%) | | | | | 54.1±2.2 | 11 | | | 56.3 | 9.7±0.4 | | | 1643-1797 |
| GM3 | -36.6 | 175.8 | 1650-1675 (31.6%), 1742-1798 (63%) | 6.1 | -57.3 | 8 | 2.4 | 59.1±2.1 | 7 | 6.4 | -60.4 | 61.5 | 10.6±0.4 | 10.5 | 1516-1647 | 1516-1650 |
| RL | -41.6 | 174.0 | 1161-1264 (88.1%) | 19.6 | -68.3 | 10 | 1.6 | 57.0±3.6 | 15 | 19.2 | -67.1 | 56.0 | 9.7±0.6 | 8.8 | 1938-1990 | 1938-1990 |
| WP | -41.6 | 174.1 | 1262-1301 (86.9%) | 15.1 | -61.8 | 25 | 2.6 | 59.9±3.3 | 26 | 14.7 | -60.3 | 58.4 | 10.2±0.5 | 10.0 | 1662-1859 | 1662-1859 |
| OP | -44.2 | 171.0 | 1465-1627 (95%) | | | | | 64.6±4.3 | 15 | | | 61.8 | 10.7±0.7 | | | 1465-1627 |
| WT1 | -36.8 | 175.7 | | 6.3 | -52.2 | 15 | 2.5 | 47.7±4.2 | 4 | 6.6 | -55.5 | 49.7 | 8.6±0.5 | 9.0 | 1460-1545 | 1460-1545 |
| WT2 | -36.8 | 175.7 | 1427-1464 (94.8%) | | | | | 77.3±0.6 | 2 | | | 80.3 | 13.9±0.1 | | | 1427-1464 |
| WT3 | -36.8 | 175.7 | | | | | | 60.3±1.5 | 2 | | | 62.6 | 10.8±0.3 | | | 1427-1545 |
| WT4 | -36.8 | 175.7 | 1436-1488 (95.2%) | | | | | 57.8±0.8 | 2 | | | 60.0 | 10.4±0.1 | | | 1436-1488 |

## 8.2 Comparison of data with other palaeomagnetic data and field models

The new archaeomagnetic directions and intensities obtained from the hangi were compared with direct observations of the magnetic field, palaeomagnetic records and field models for New Zealand covering the past 1000 years. All data has been relocated to a common location (40°S, 175°E) for comparison with other data (Figure 8.1a). Using virtual geomagnetic pole (VGP)-based relocation assumes that local differences in the field at any given time can be approximated to the differences in a (geocentric but tilted) dipole field. Calculations carried out using field values of various locations in New Zealand from the *gufm1* model show that errors associated with VGP relocation amount to less than 0.135°/100km for the New Zealand region (G. Turner pers. comm.). Figure 8.1b shows a stereo plot of the directional data of model NZPSV1K (Turner et al., 2014) and the New Zealand hangi archaeodirections. NZPSV1K includes field directions calculated from the *gufm*1 model (Jackson et al., 2000) from 1590 to 1990 AD, and a lake sediment composite record from 1000 to 1590 AD (Turner et al., 2015). Figure 8.1b shows that during the last 1000 years the declination has trended eastwards, from -10° to 22°, while the inclination has steepened from ~ -55° to ~ -66°.

Figure 8.1b shows that the archaeodirections of sites GM1, GM3, WP and RL are in very good agreement with the field model, and this correlation has been used to assign "archaeomagnetic ages" to the sites (Table 8.1). The inclination of hangi WT1, however, is some 6 ± 2° shallower than at any time in the historical record.

The intensity data is also compared with calculations of the global field model *gufm1* for the period 1590-1990 AD at 40°S 175°E (Figure 8.1c). The *gufm1* model gives fairly reliable values for the period 1838-1990 AD, as it is based on absolute intensity measurements (indicated by the red line in Figure 8.1c). Before 1838, however, there were no absolute intensity measurements, so *gufm*1 is based on the assumption that the Gauss coefficient $g_0^1$ can be extrapolated linearly over the preceding 200 years (Jackson et al., 2000) (indicated by the blue line in Figure 8.1c). According to *gufm*1, the intensity decays from ~ 64 μT to ~ 55 μT during the period 1590 AD-1990 AD. A similar

trend is followed by the archaeointensities of the hangi sites dated in this period (GM3, GM2, WP and RL) within uncertainties. Before 1590 AD, large intensity variations from ~ 80to 50 μT are seen in the Whitianga hangi data (WT1, WT2, WT3 & WT4). The value of 77.3 μT for WT2 is some 12-13 μT higher than any other archaeointensity obtained in the study.



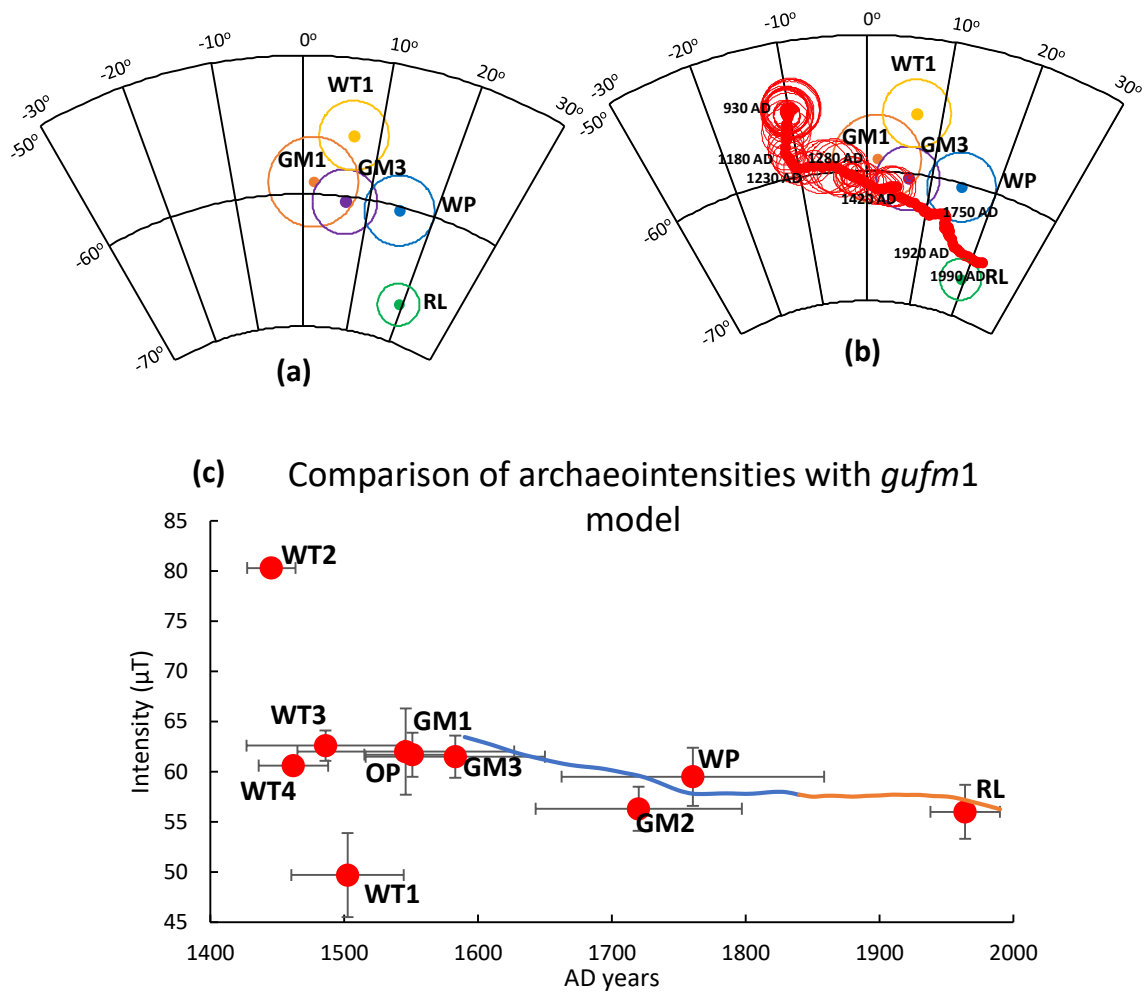Figure 8.1. (a) Archaeodirections (declination and inclination) of NZ hangi sites relocated to 40°S 175°E; (b) Comparison of NZPSV1K and NZ archaeodirections (all relocated to 40°S 175°E. Circles around coloured dots shows α95s. (c) Archaeointensities calculated from New Zealand hangi sites and *gufm1* model. Red dots are hangi data with error bars showing standard deviation and uncertainty in dates.

The new data are also compared with the global field model ARCH3K (Korte et al., 2009) after relocating all data to, and calculating the model field at, location 40°S 175°E (Figure 8.2). ARCH3K is a global geomagnetic field model constructed using archaeomagnetic data covering the past 3000 years. The model gives realistic information for the northern hemisphere, particularly for Europe, due to the availability of plentiful data from this region, while the model gives only sparse data from the southern hemisphere. Figure 8.2 displays changes in intensity, declination and inclination during the last 1000 years according to ARCH3K. The grey band around the black curve of the ARCH3K data is the 95% confidence interval, which is much larger before 1600 AD than after this date, when, like NZPSV1K, ARCH3K incorporates the direct observation-based *gufm1* model. The red dashed curves in all three plots indicate the NZPSV1K data and the blue dots the archaeomagnetic hangi data. The hangi data give five directional data points and ten intensity values covering the period 1400-2000 AD. In Figure 8.2 the values given by *gufm1* at this location are plotted in green. GAD (Geocentric Axial Dipole) directions and the present-day field at this location are shown as pink and blue lines. The geomagnetic field is generally thought to give a GAD if averaged over a long period of time (say 10,000-100,000 years), with all Gauss coefficients except $g_1^0$ averaging to zero (Merrill et al., 1998). However, over the past 1000 years the geomagnetic field at 40°S, 175°E does not average to the GAD direction. The present declination is ~22° east, and the inclination is ~6° steeper than the GAD value of 59.2°. It can be seen that all models from 1600-2000 AD overlap, due to *gufm*1 data being used for the last 400 years. At present, there is no intensity data in NZPSV1K. ARCH3K, however, gives intensity information before 1600 AD, while the archaeomagnetic data (blue dots), (except for points WT1 and WT2, follow the trend of both intensity and direction (declination and inclination) within the uncertainty range. GM2 lies below the curve and has a large age uncertainty (~ 77 years). The intensity value of the site is compatible with the curve when uncertainty bars of age and intensity data are considered together.
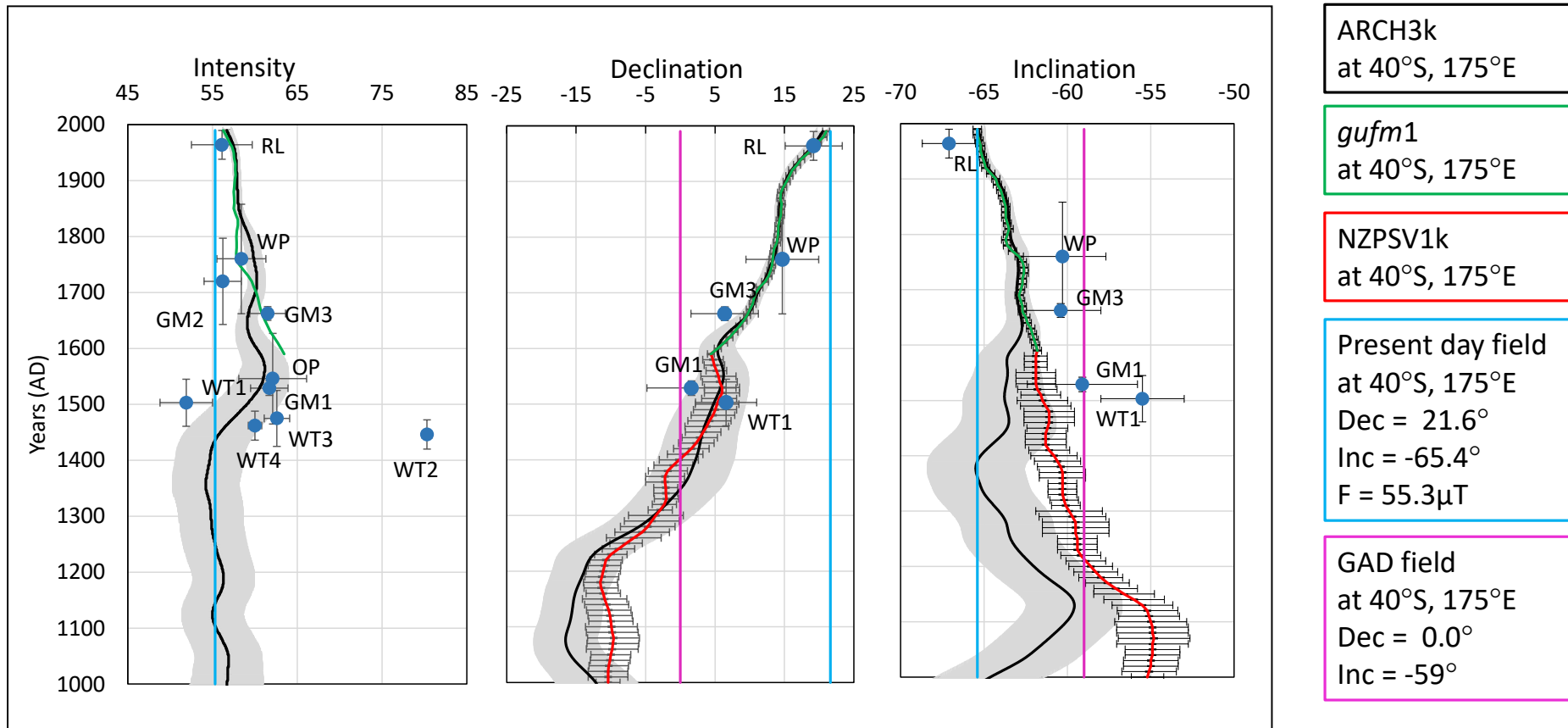
Figure 8.2. New Zealand's first archaeomagnetic data (blue dots). The red curve with 95% confidence bars is NZPSV1K (Turner et al., 2014), the black curve with grey cloud illustrates ARCH3K (Korte at al., 2009), with the green curve beneath the red curve indicating *gufm*1 (Jackson et al., 2000). All data curves are relocated to 40°S 175°E. Blue and pink lines represent the present day geomagnetic field in New Zealand at 40°S 175°E and GAD.

## 8.3 Comparison with SW Pacific data and geomagnetic field implications

Archaeointensity data from southeast Australia (Barbetti, 1977 and Barton & Barbetti, 1982) and SW Pacific Islands are shown in Figure 8.3 ( Figure 9.1(b) from Stark, 2011). The data displayed are relocated to Efate Island, Vanuatu (17.6°S 168.2°E), for comparison, and the sites have been $^{14}$C dated using marine shells and charcoal. It can be seen that the archaeointensities around 1000 AD and 1400 AD are lower and higher respectively than the values suggested by the ARCH3K and CALS3K models (Korte et al., 2009). Australian data shows maxima around 250 BC, whereas SWP data indicates minima around this period. In addition, another peak around 600 AD is displayed by Australian data. Moreover, the SWP data after 0 AD is in agreement with Australian data. However, this comparison is limited by the fact that due to large distances between the sites there may be regional field variations. Furthermore, there are also uncertainties in dates and a lack of data at several points for an appropriate comparison. Stark (2011) suggests that the sharp increase at about 1400 AD in Figure 8.3 may be the result of an "archaeomagnetic jerk" (Courtillot and Le Mouel, 1988). Gallet et al. (2003) introduced the idea of archaeomagnetic jerks and described them as points of "coincidence between sharp cusps in geomagnetic field direction and intensity maxima." Gallet et al. (2006) suggest that archaeomagnetic jerks may be associated with climate change, and the related sharp intensity peaks with the occurrence of cooling periods. The climate change over the time scales occurs possibly through the variation of cosmic flux interacting with the atmosphere due to the occurrence of jerks (Gallet et al., 2006). Archaeomagnetic jerks are also observed in archaeomagnetic data from Western Europe around 200 AD and 1400 AD (Figure 8.4 (a) & (b)). Although this intensity maximum in SW Pacific archaeomagnetic data around 1400 AD (Stark et al, 2011) do not have directional data for comparison, Figure 8.4 (c) shows a compilation of European archaeointensity data from 0 AD to present (Roberts and Turner, 2013). Between 1000 AD and the present, two main intensity peaks (~1300 and 1600 AD) are seen in the regional model SCHA.DIF.3K (Pavon-Carrasco et al., 2009) and one main peak (~1600 AD) in CALS3K (Korte et al., 2009). However, neither model shows a peak around 1400 AD.
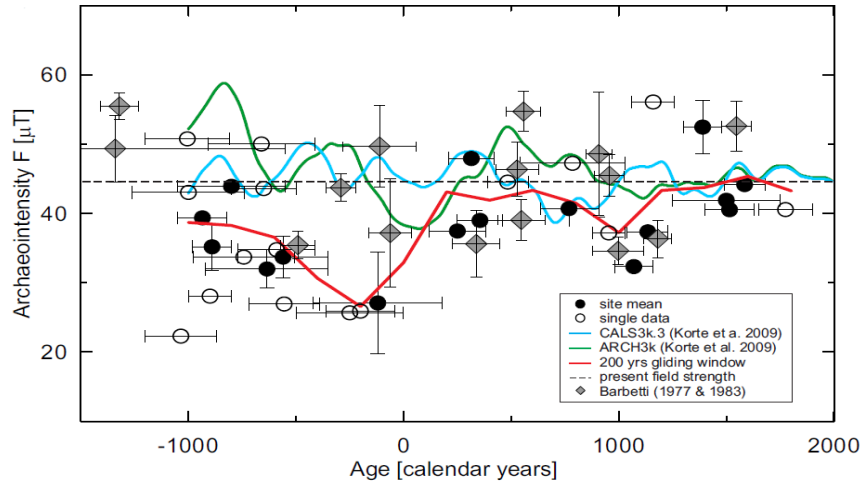
Figure 8.3. Comparison of archaeomagnetic data from Australia and SW Pacific Islands with geomagnetic field models for location of Island Efate (Figure 9.1 (b) from Stark, 2011).
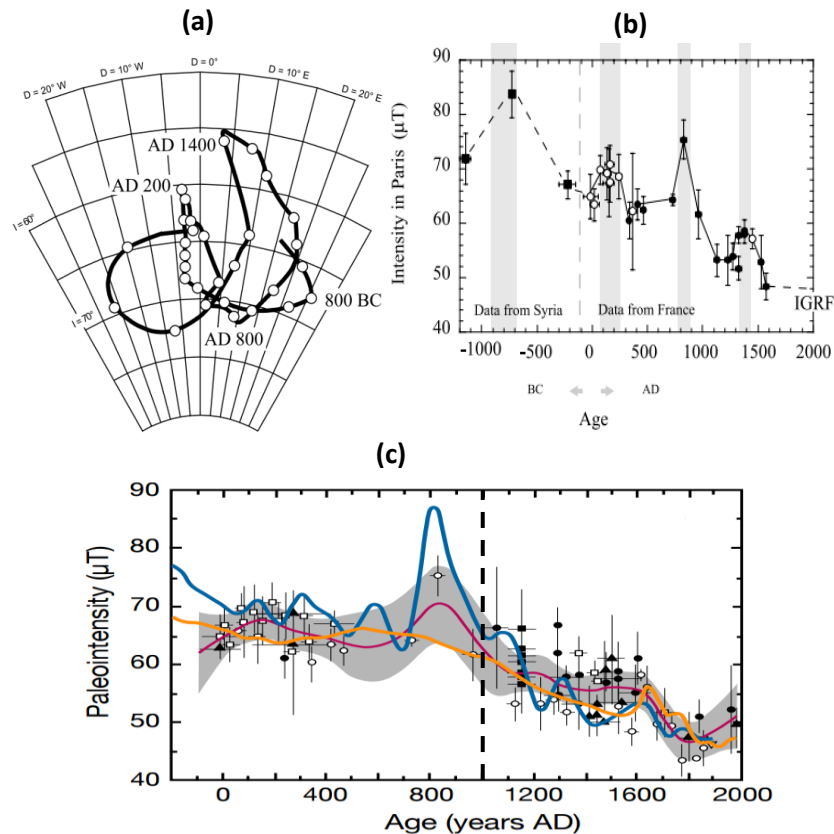


Figure 8.4. Archaeomagnetic jerks in European data. (a) Archaeomagnetic jerks in directional data from Syria and France from 1000 BC to present. (b) Intensity maxima correlated with directional cusps. (c) Archaeomagnetic secular variation records from Europe (Figure from Roberts & Turner, 2013) palaeointensity measurements are from France, Norway, and Denmark, all relocated to Paris (Go´mez-Paccard et al., 2008). The solid red line is mean data with shading showing 95% confidence interval. The blue and yellow lines are regional and global models SCHA.DIF.3K and CALS3K of Pavo´n-Carrasco et al., 2009 and Korte et al., 2009 respectively.

For a direct comparison of New Zealand archaeointensity data with the Australian and SW Pacific archaeomagnetic data, a virtual axial dipole moment (VADM) for each site has been calculated. Some stones could not be oriented and did not provide directional data. Therefore, it is assumed that the field is an axial dipole field and the virtual dipole moment (VDM) is not calculated for those sites. VDM is calculated using the following equation for the sites providing directional as well as intensity data (Roberts & Turner, 2013). In this equation, '$F$' is archaeointensity, '$\Theta_m$' is magnetic co-latitude (where $\theta_m = cot^{-1}(tan(I))$, r is the radius of Earth, and $\mu_o$ is the permeability of free space. VDM calculated for hangi sites varies between 8 and 10 x $10^{22}$ Am$^2$ (Table 8.1).

$$VDM = \frac{4\pi r^3}{\mu_o} \frac{F}{\sqrt{(1 + 3cos^2\theta_m)}}$$

The VADM can be calculated using the equation given further, where '$\Theta_s$' is the co-latitude of the site.

$$VADM = \frac{4\pi r^3}{\mu_o} \frac{F}{\sqrt{(1 + 3cos^2\theta_s)}}$$

The VADM data for the past 1000 years are shown in Figure 8.5, along with the global mean VADM curve of Knudsen at al., (2008), which is a least square fit to global (but largely northern hemisphere) VADM data. For the past 500 years, the New Zealand and SW Pacific data generally agree with each other to describe a VADM that has gradually decreased from about 10.5 to 9.5 x $10^{22}$ Am$^2$. For the period 1000-1200 AD, both Australian and SW Pacific values average about 8 x $10^{22}$ Am2, and are lower than the global mean values calculated by Knudsen et al., (2008, red curve) .   In the interim period from 1250 to about 1450 AD however, all three datasets include exceptionally high VADMs (12-14 x $10^{22}$ Am$^2$). The dashed green line shows the overall trend of VADM for the period of 1000 AD to present.

The anomalously high intensity value in the New Zealand data (WT2), dated between 1427 and 1464 AD, may coincide with the high intensities reported from the SW Pacific by Stark (2011), Australia (Barbetti, 1977; Barton & Barbetti, 1982) and Europe (Gallet et al., 2003) which have been classed as archaeomagnetic jerks (Figures 8.2, 8.3 & 8.4). However, no directional data is available from site WT2. In the directional data provided

by models NZPSV1K and ARCH3K, there are no sharp changes in directions. Hence, the availability of data is too small to say for certain that these intensity maxima fit Gallet et al.'s definition of archaeomagnetic jerks, or whether archaeomagnetic jerks are global or regional phenomena. More directional and intensity data are needed from this part of world for the period around 1400 AD to resolve this question. However, it is unlikely that the high intensity values of SW Pacific islands, New Zealand, Australia, and Europe are a coincidence. Such globally correlated high intensity values would imply coordinated changes in the pattern of fluid flow in Earth's outer core.
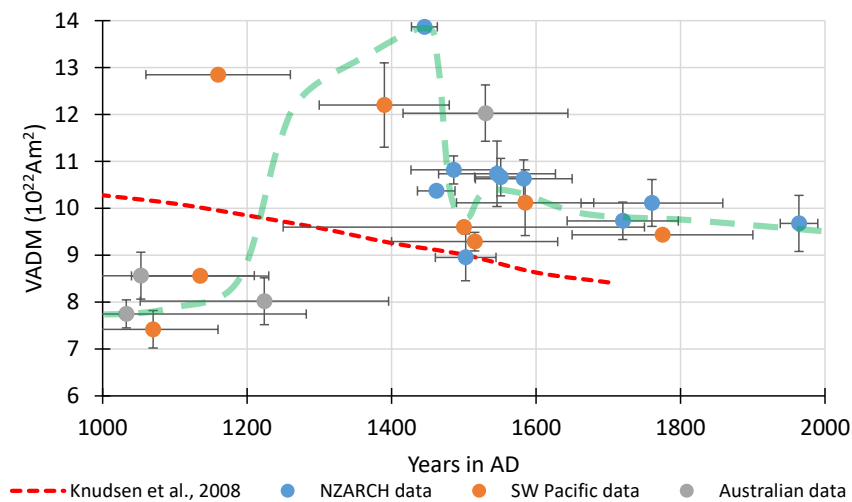


Figure 8.5. Variation of VADM over the past 1000 years: data from SW Pacific Islands (Stark, 2011), Australia ((Barbetti, 1977) and (Barton & Barbetti, 1982)) New Zealand (this study), and global average VADM (Knudsen et al., 2008).

## 8.4. Contribution to New Zealand archaeology

In earth ovens like hangis, stones are heated to a temperature above the Curie temperature of all naturally occurring magnetic minerals. Archaeomagnetic studies can provide important archaeological information about hangi sites. Thermomagnetic experiments may indicate whether or not the hangi stones have been heated sufficiently to have reached the end-point of thermal alteration, and repeated thermomagnetic experiments may indicate to what temperature the stones were heated. If the stones were heated to only a low temperature, there is a possibility that

the stones do not belong to a hangi but were heated for some other purpose, such as an open fire used for cooking once only, or some other purpose. Archaeomagnetic experiments may also identify the disturbance of stones during or after the cooling process.

Archaeointensity and directional data can be compared with geomagnetic field models or reference curves and an archaeomagnetic date for the site can thus be determined. This dating method is very useful when radiocarbon dating does not give a precise age due to, for example, the presence of ancient carbon in the sample or a lack of suitable dating material. Where both dating methods are possible, they can be combined to provide a best age estimate, which may be more precise than either method alone. In Figure 8.6, for example, radiocarbon dating gives an age range for site GM1 of 1516 AD-1666 AD, and archaeomagnetic dating gives an age range of 1380 AD-1587 AD, both with a 95% level of confidence. The probability distributions of the two dating methods can be combined, as shown in Figure 8.6, giving a shortened acceptable age range, or best age estimate, for GM1, in the overlapping area of distributions of 1516 AD to 1587 AD. Figure 8.6 has been created as an example of how probability densities can be multiplied to calculate a best age for a site.
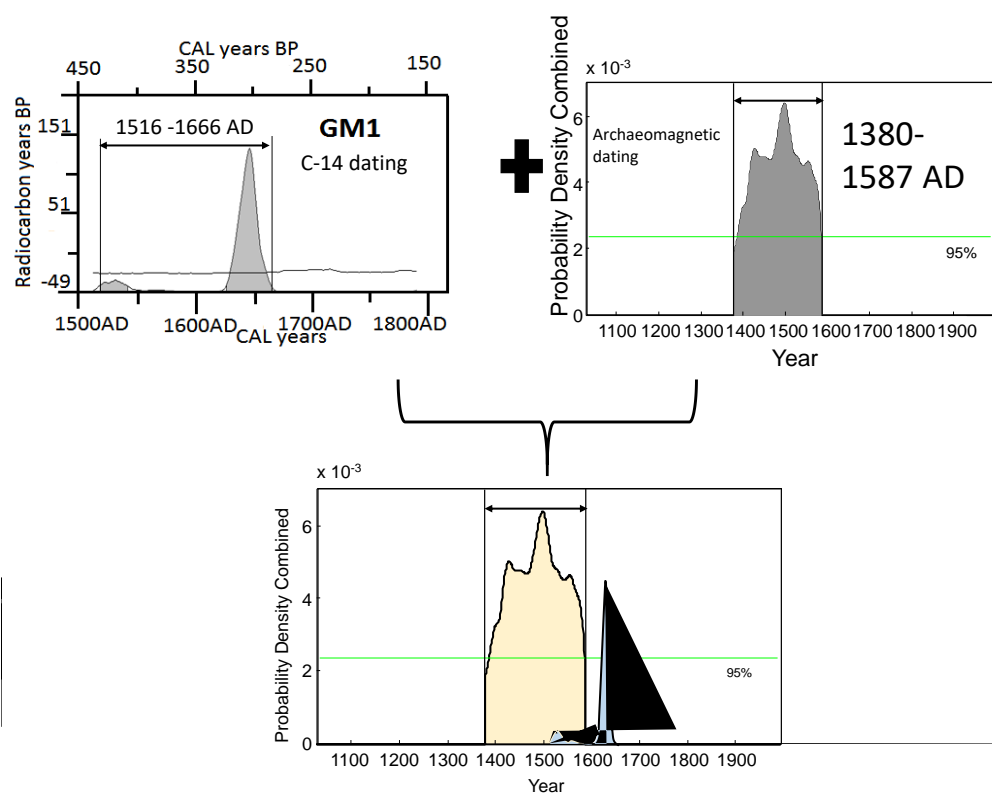
Figure 8.6. An example for estimation of the best age of hangi sites by combining the results of radiocarbon and archaeomagnetic dating.

## 8.5 Conclusions

Methods have been developed for the archaeomagnetic sampling of New Zealand hangi stones as well as for the preparation of specimens from the stones. Palaeomagnetic techniques have been modified for retrieving archaeomagnetic directions and intensities from them.

In total, ten archaeological sites were successfully sampled. Radiocarbon dating was applied to charcoal samples, and resulted in age estimates ranging from 1400 AD to 1990 AD.

Progressive demagnetization (thermal and/or alternating field) and Thellier-type palaeointensity methods were used to determine palaeo-directional and intensity data respectively. Of the ten five hangi sites sampled, five yielded successful archaeodirections, and all ten sites provided reliable archaeointensities. The declinations and inclinations of the archaeodirections range from 1.6° to 19° and -56° to -67° respectively, with     95 ≤ 5° in all cases. They lie on or close to the NZPSV1k reference curve, the gufm1 model and to observatory data of the past century. Archaeointensities fall between 50µT and 77µT, and have enabled the first archaeointensity record for New Zealand to be constructed. Over the past 400 years the archaeointensity record agrees well with intensities predicted by the global field model *gufm1*.

Virtual axial dipole moments were calculated from the New Zealand archaeointensities, and are in good agreement with those of archaeomagnetic studies in Australia and SW Pacific Islands that cover the same time period. Before 1600 AD, the archaeointensities include one unusually high value. This value, together with similarly high values from Fiji, Vanuatu (Stark, 2011) and Australia (Barbetti, 1983) suggests that there was a peak in intensity in the SW Pacific region between 1300 and 1400 AD. This peak may correspond to one of the "archaeomagnetic jerks" reported from Europe (Gallet et al., 2003).

The archaeomagnetic directions have been matched with the NZPSV1k declination and inclination reference curves, using the dating tool of Pavón Carrasco et al., (2011). The dating tool enables an "archaeomagnetic" date for each site to be estimated, which is independent of radiocarbon or other age controls. Five hangi sites could be archaeomagnetically dated in this way, which reduced age uncertainties to between 30 and 100 years.

Palaeomagnetic and rock magnetic measurements can also lead to an understanding of the thermal history of archaeological artefacts such as hangi stones. These measurements can help to distinguish between stones that have been reheated multiple times to a high temperature, as in a true hangi, from others that have been heated just once, or to a lower temperature in an open fireplace.

# References

Anderson, A., 1991. The chronology of colonization in New Zealand. Antiquity, 65(249), 767–795. doi.org/10.1017/S0003598X00080510

Barbetti, M., 1977. Measurements of recent geomagnetic secular variation in southeastern Australia and the question of dipole wobble. Earth and Planetary Science Letters, 36(1), 207–218. doi.org/10.1016/0012-821X(77)90200-X

Barton, C. E., & Barbetti, M., 1982. Geomagnetic secular variation from recent lake sediments, ancient fireplaces and historical measurements in southeastern Australia. Earth and Planetary Science Letters, 59(2), 375–387.doi.org/10.1016/0012-821X(82)90139-X

Biggin, A. J., Perrin, M., & Shaw, J., 2007. A comparison of a quasi-perpendicular method of absolute palaeointensity determination with other thermal and microwave techniques. Earth and Planetary Science Letters (Vol. 257). doi.org/10.1016/j.epsl.2007.03.016

Butler, R. F., 1992. Introduction to Geomagnetism. Paleomagnetism: Magnetic domains to geologic terranes. Blackwell Scientific Publications. doi.org/10.1016 /0031-9201(83)90056-0

Casas, L., Incoronato, A., 2007. Distribution analysis of errors due to relocation of geomagnetic data using the 'Conversion via Pole' (CVP) method: implications on archaeomagnetic data. Geophysical Journal International 169 (2), 448-454.

Cassidy, J. and Hill, M.J., 2009. Absolute palaeointensity study of the Mono Lake excursion recorded by New Zealand basalts. Physics of the Earth and Planetary Interiors, 172(3), 225-234.

Chadima, M., & Hrouda, F. 2006. Remasoft 3.0 a user-friendly paleomagnetic data browser and analyzer. Travaux Géophysiques, 27, 20–21.

Chulliat, A., S. Macmillan, P. Alken, C. Beggan, M. Nair, B. Hamilton, A. Woods, V. Ridley, S. Maus and A. Thomson, 2015, The US/UK World Magnetic Model for 2015-2020: Technical Report, National Geophysical Data Center, NOAA. doi: 10.7289/V5TB14V7

Coe, R. S., 1967. Paleo-intensities of the Earth's magnetic field determined from Tertiary and Quaternary rocks. Journal of Geophysical Research, 72(12), 3247–3262. doi.org/10.1029/JZ072i012p03247

Coe, R. S., Grommé, S., & Mankinen, E. A., 1978. Geomagnetic paleointensities from radiocarbon-dated lava flows on Hawaii and the question of the Pacific nondipole low. Journal of Geophysical Research: Solid Earth, 83(B4), 1740–1756. doi.org/10.1029/JB083iB04p01740

Constable, C., & McElhinny, M., 1985. Holocene geomagnetic secular variation records from north-eastern Australian lake sediments. Geophysical Journal.

Davidson, J., 1987. Prehistory of New Zealand. Longman Paul Ltd.

Day, R., Fuller, M., & Schmidt, V. A., 1977. Hysteresis properties of titanomagnetites: Grain-size and compositional dependence. Physics of the Earth and Planetary Interiors, 13(4), 260–267. doi.org/10.1016/0031-9201(77)90108-X

Dickin, A.P., 2005. Radiogenic isotope geology. Cambridge University Press.

Dunlop, D. J., 1979. On the use of Zijderveld vector diagrams in multicomponent paleomagnetic studies. Physics of the Earth and Planetary Interiors, 20(1), 12–24. doi.org/10.1016/0031-9201(79)90103-1

Dunlop, D. J., 2002a. Theory and application of the Day plot (M-rs/M-s versus H-cr/H-c) 1. Theoretical curves and tests using titanomagnetite data. Journal of Geophysical Research-Sol Ea, 107(B3), 2056. doi.org/10.1029/2001JB000486

Dunlop, D. J., 2002b. Theory and application of the Day plot ($M_{rs}/M_s$ versus $H_{cr}/H_c$) 2. Application to data for rocks, sediments, and soils. Journal of Geophysical Research, 107(B3), 1–15. doi.org/10.1029/2001JB000487

Dunlop, D. J., & Özdemir, O., 1997. Rock magnetism : fundamentals and frontiers. Cambridge University Press.

Ferk, A., Leonhardt, R., Hess, K.U. and Dingwell, D.B., 2011. Paleointensities on 8 ka obsidian from Mayor Island, New Zealand. Solid Earth, 2(2), 259.

Finlay, C.C., Maus, S., Beggan, C.D., Bondar, T.N., Chambodut, A., Chernova, T.A., Chulliat, A., Golovkov, V.P., Hamilton, B., Hamoudi, M. and Holme, R., 2010. International geomagnetic reference field: the eleventh generation. Geophysical Journal International, 183(3),1216-1230.

Fisher, R. A., 1953. Dispersion on a Sphere. Proceedings of the Royal Society of London, 217, 295–305.

Fisher, N. I., Lewis, T., & Embleton, B. J. J., 1987. Statistical Analysis of Spherical Data, 343. doi.org/10.1017/CBO9780511623059

Foner, S., 1959. Versatile and sensitive vibrating-sample magnetometer. Review of Scientific Instruments, 30(7), 548-557.

Force, E.R. and McFadgen, B.G., 2012. Influences of active tectonism on human development: a review and Neolithic example. Climates, Landscapes, and Civilizations, 195-202

Foster, D., 2014. Archaeological monitoring at Dashwood Pass road realignment, SH1, Marlborough. Monitoring report for Opus consultants.

Foster, D., 2015. Archaeological monitoring at Riverlands industrial estate, rear site expansion. Monitoring report for Wine Business Park Ltd.

Furey, L. and Fay, M., 2009. Description of Archaeological Deposits in Dunes, White Beach, Great Mercury Island (Ahuahu). Report to NZ Historic Places Trust and Michael Fay.

Gallet, Y., Genevey, A., & Courtillot, V., 2003. On the possible occurrence of "archaeomagnetic jerks" in the geomagnetic field over the past three millennia. Earth and Planetary Science Letters, 214(1), 237–242. doi.org/10.1016/S0012-821X(03)00362-5

Gallet, Y., Genevey, A., Le Goff, M., Fluteau, F., & Ali Eshraghi, S., 2006. Possible impact of the Earth's magnetic field on the history of ancient civilizations. Earth and Planetary Science Letters (Vol. 246). doi.org/10.1016/j.epsl.2006.04.001

Godwin, H., 1962. Half-life of Radiocarbon. Nature, 195(4845), 984–984. http://doi.org/10.1038/195984a0

Goff, J.R., Nichol, S. and Rouse, H.L. eds., 2003. The New Zealand Coast. Dunmore Press.

Golson, J., 1955. Dating New Zealand's Prehistory. The Journal of the Polynesian Society, *64*(1), 113-136.

Gómez-Paccard, M., McIntosh, G., Chauvin, A., Beamud, E., Pavón-Carrasco, F. J., & Thiriot, J., 2012. Archaeomagnetic and rock magnetic study of six kilns from North Africa (Tunisia and Morocco). Geophysical Journal International, 189(1), 169–186. doi.org/10.1111/j.1365-246X.2011.05335.x

Gose, W. A., 2000. Palaeomagnetic Studies of Burned Rocks. Journal of Archaeological Science, 27(5), 409–421. doi.org/10.1006/jasc.1999.0465

Hayward, B.W., 1976. Geology of the Whitianga Group, Great Mercury Island–Part I: Coroglen Subgroup stratigraphy. Tane, 22, 5-14.

Heslop, D., & Roberts, A. P., 2012. A method for unmixing magnetic hysteresis loops. Journal of Geophysical Research: Solid Earth, 117(3), 1–14. doi.org/10.1029/2011JB008859

Hill, M.J., Lanos, P., Chauvin, A., Vitali, D. and Laubenheimer, F., 2007. An archaeomagnetic investigation of a Roman amphorae workshop in Albinia (Italy). Geophysical Journal International, 169(2), 471-482.

Hoffman, K. A., & Day, R., 1978. Separation of multi-component NRM: A general method. Earth and Planetary Science Letters, 40(3), 433–438. doi.org/10.1016/0012-821X(78)90166-8

Hogg, A., Hua, Q., Blackwell, P. G., Niu, M., Buck, C. E., Guilderson, T. P., Heaton, T.T., Palmer, J.G., Reimer, R.W., and Turney, C.S.M., 2013. SHCal13 Southern Hemisphere Calibration, 0–50,000 Years cal BP. Radiocarbon, 55(4), 1889–1903. doi.org/10.2458/azu_js_rc.55.16783

Hopkinson, J., 1890. Magnetic Properties of Alloys of Nickel and Iron. Proceedings of the Royal Society of London, 48(292–295), 1–13. doi.org/10.1098/rspl.1890.0001

Hrouda, F., Müller, P., & Hanák, J., 2003. Repeated progressive heating in susceptibility vs. temperature investigation: a new palaeotemperature indicator. Physics and Chemistry of the Earth, Parts A/B/C, 28(16), 653–657. doi.org/10.1016/S14747065(03)00119-0

Irwin, G., & Walrond, C., 2012. When was New Zealand first settled? The date debate. Te Ara—the encyclopedia of New Zealand. Retrieved from http://www.teara. govt.nz/en/when-was-new-zealand-first-settled

Jackson, A., Jonkers, A. R. T., & Walker, M. R., 2000. Four centuries of geomagnetic secular variation from historical records. Philosophical Transactions of the Royal Society A: Mathematical, Physical and Engineering Sciences, 358(1768), 957–990. doi.org/10.1098/rsta.2000.0569

Jull, A. J. T., & Burr, G. S., 2015. Accelerator Mass Spectrometry (3–6). Springer Netherlands. doi.org/10.1007/978-94-007-6304-3_102

Keyes, I., 1970. Wairapa chert sources in prehistory. New Zealand Archaeological Association 13: 128-134.

Kissel, C., & Laj, C., 2004. Improvements in procedure and paleointensity selection criteria (PICRIT-03) for Thellier and Thellier determinations: application to Hawaiian basaltic long cores. Physics of the Earth and Planetary Interiors, 147(2), 155–169. doi.org/10.1016/j.pepi.2004.06.010

Knudsen, M.F., Riisager, P., Donadini, F., Snowball, I., Muscheler, R., Korhonen, K. and Pesonen, L.J., 2008. Variations in the geomagnetic dipole moment during the Holocene and the past 50 kyr. Earth and Planetary Science Letters, 272(1), 319-329.

Korte, M., Genevey, A., Constable, C.G., Frank, U. and Schnepp, E., 2005. Continuous geomagnetic field models for the past 7 millennia: 1. A new global data compilation. Geochemistry, Geophysics, Geosystems, 6(2).

Korte, M., Donadini, F., & Constable, C. G., 2009. Geomagnetic field for 0-3 ka: 2. A new series of time-varying global models. Geochemistry, Geophysics, Geosystems, 10(6). doi.org/10.1029/2008GC002297

Kostadinova, M., Jordanova, N., Jordanova, D. and Kovacheva, M., 2004. Preliminary study on the effect of water glass impregnation on the rock-magnetic properties of baked clay. Studia Geophysica et Geodaetica, 48(3), 637-646.

Krása, D., Petersen, K. and Petersen, N., 2007. Variable field translation balance. In Encyclopedia of Geomagnetism and Paleomagnetism, 977-979. Springer Netherlands.

Krijgsman, W. and Turner, G., 2015. Sediments, Terrestrial (Paleomagnetism). Springer Encyclopedia of Scientific Dating Methods, 752-760.

Leach, F., & Davidson, J., 2000. Pre-European catches of snapper (Pagrus auratus) in northern New Zealand. Journal of Archaeological Science.

Leach, H. M., 1982. Cooking without pots: aspects of prehistoric and traditional Polynesian cooking. New Zealand Journal of Archaeology.

Leonhardt, R., 2006. Analyzing rock magnetic measurements: The RockMagAnalyzer 1.0 software. Computers & Geosciences, 32(9), 1420–1431. doi.org/10.1016

/j.cageo.2006.01.006

Leonhardt, R., Heunemann, C., & Krása, D., 2004a. Analyzing absolute paleointensity determinations: Acceptance criteria and the software ThellierTool4.0. Geochemistry, Geophysics, Geosystems doi.org/10.1029/2004GC000807

Leonhardt, R., Krása, D., & Coe, R. S., 2004b. Multidomain behavior during Thellier paleointensity experiments: a phenomenological model. Physics of the Earth and Planetary Interiors, 147(2), 127–140. doi.org/10.1016/j.pepi.2004.01.009

Libby, W. F., 1955. Dosages from natural radioactivity and cosmic rays. Science, 122(3158), 57–58.

Lowe, D.J., 2008. Polynesian settlement of New Zealand and the impacts of volcanism on early Maori society: an update. Lowe, DJ, 142-147.

Lowrie, W., 2007. Fundamentals of geophysics. Cambridge University Press.

Mathews, P., 1995. Racing this time Marlborough. A Marlborough historical society publication No. 3.

McCulloch, B. A., & Trotter, M. M., 1971. Prehistoric rock art of New Zealand. Wellington: A H & AW Reed.

McFadgen, B., 2007. Hostile Shores: Catastrophic Events in Prehistoric New Zealand and Their Impact on Maori Coastal Communities. Auckland University Press.

McFadgen, B. G., Knox, F. B., & Cole, T. L., 1994. Radiocarbon calibration curve variations and their implications for the interpretation of New Zealand prehistory. Radiocarbon, 36(2), 221–236. doi.org/10.2458/AZU_JS_RC.36.1620

McFadgen, B. G., 1982. Dating New Zealand archaeology by radiocarbon. New Zealand Journal of Science, 25, 379–392.

Merrill, R.T., McElhinny, M.W., McFadden, P.L. and Banerjee, S.K., 1998. The Magnetic Field of the Earth: Paleomagnetism, the Core, and the Deep Mantle. Physics Today, 50, p.70.

Moskowitz, B. M., 1981. Methods for estimating Curie temperatures of titanomaghemites from experimentalJs-T data. Earth and Planetary Science Letters, 53(1), 84–88. doi.org/10.1016/0012-821X(81)90028-5

Nagata, T., 1943. 1. The Natural Remanent Magnetism of Volcanic Racks and Its Relation to Geomagnetic Phenomena. Earthquake Research Institute, Tokyo Imperial University.

Nagata, T., Momose, K., & Arai, Y., 1963. Secular variation of the geomagnetic total force during the last 5000 years. Journal of Geophysical Research , 68 (11), 5277–5281.

Néel, L., 1955. Some theoretical aspects of rock-magnetism. Advances in Physics, 4(14), 191–243. doi.org/10.1080/00018735500101204

Nicholas, J.L., 1817. Narrative of a voyage to New Zealand. Wilson and Horton.

Nilsson, A., Holme, R., Korte, M., Suttie, N., Hill, M., 2014. Reconstructing Holocene geomagnetic field variation: new methods, models and implications. Geophysical International Journal. 198 (1), 229–248. doi.org/10.1093/gji /ggu120.

O'Reilly, W., S, A., Akimoto S, K. T. and Y. M., Artman J O, M. J. C. and F. S., K, B. S., K, B. S., … N, Y., 1976. Magnetic minerals in the crust of the Earth. Reports on Progress in Physics, 39(9), 857–908. doi.org/10.1088/0034-4885/39/9/002

Parry, L. G., 1965. Magnetic properties of dispersed magnetite powders. Philosophical Magazine, 11(110), 303–312. doi.org/10.1080/14786436508221858

Parry, L. G., 1980. Shape-related factors in the magnetization of immobilized magnetite particles. Physics of the Earth and Planetary Interiors, 22(2), 144–154. doi.org/10.1016/0031-9201(80)90055-2

Paterson, G. A., Tauxe, L., Biggin, A. J., Shaar, R., & Jonestrask, L. C., 2014. On improving the selection of Thellier-type paleointensity data. Geochemistry, Geophysics, Geosystems, 15(4), 1180–1192. doi.org/10.1002/2013GC005135

Pavon-Carrasco, F. J., Rodriguez-Gonzalez, J., Osete, M. L., & Torta, J. M., 2011. A Matlab tool for archaeomagnetic dating. Journal of Archaeological Science, 38(2), 408–419. doi.org/10.1016/j.jas.2010.09.021

Petrovský, E., & Kapička, A., 2006. On determination of the Curie point from thermomagnetic curves. Journal of Geophysical Research: Solid Earth, 111(B12), doi.org/10.1029/2006JB004507

Prévot, M., Mankinen, E. A., Coe, R. S., & Grommé, C. S., 1985. The Steens Mountain (Oregon) geomagnetic polarity transition: 2. Field intensity variations and discussion of reversal models. Journal of Geophysical Research, 90(B12), 10417. doi.org/10.1029/JB090iB12p10417

Prior, C., 2012. A Carbon-14 Primer. Retrieved September 27, 2016, from https://issuu.com/halipublicationslimited/docs/forumcarbon14

Riisager, P., & Riisager, J., 2001. Detecting multidomain magnetic grains in Thellier palaeointensity experiments. Physics of the Earth and Planetary Interiors, 125(1–4), 111–117. doi.org/10.1016/S0031-9201(01)00236-9

Rikitake, T. and Honkura, Y., 1985. Solid earth geomagnetism. Advances in Earth and Planetary Sciences, 1. Elsevier Publishing.

Roberts, A. P., & Turner, G. M., 2013. Geomagnetic Excursions and Secular Variations. Encyclopedia of Quaternary Science (2nd ed., Vol. 1). Elsevier B.V. doi.org/10.1016 /B978-0-444-53643-3.00053-4

Schnepp, E. and Lanos, P., 2005. Archaeomagnetic secular variation in Germany during the past 2500 years. Geophysical Journal International,163(2), 479-490.

Schnepp, E., Worm, K., & Scholger, R., 2008. Improved sampling techniques for baked clay and soft sediments. Physics and Chemistry of the Earth, Parts, 407–413.

Selkin, P. A., & Tauxe, L., 2000. Long-term variations in palaeointensity. Philosophical Transactions of the Royal Society of London A: Mathematical, Physical and Engineering Sciences, 358(1768).

Shaar, R., Ben-Yosef, E., Ron, H., Tauxe, L., Agnon, A. and Kessel, R., 2011. Geomagnetic field intensity: How high can it get? How fast can it change? Constraints from Iron Age copper slag. Earth and Planetary Science Letters, 301(1), 297-306.

Skinner, W. H., 1912. Ancient Maori Canals, Marlborough. New Zealand Journal of Archaeology.

Sparks, R.J., and Manning, M.R. pers. com. WinscalX, version 5.1. GNS Science, 2011.

Stark, F., 2011. Secular variation of the Earth's magnetic field in the South West Pacific. (Doctoral dissertation, University of Liverpool).

Stark, F., Cassidy, J., Hill, M. J., Shaw, J., & Sheppard, P., 2010. Establishing a first archaeointensity record for the SW Pacific. Earth and Planetary Science Letters, 298(1–2), 113–124. doi.org/10.1016/j.epsl.2010.07.031

Stillinger, M., Feinberg, J., & Frahm, E., 2015. Refining the archaeomagnetic dating curve for the Near East: new intensity data from Bronze Age ceramics at Tell Mozan, Syria. Journal of Archaeological Science.

Tauxe, L., Pick, T., & Kok, Y., 1995. Relative paleointensity in sediments: a pseudo-Thellier approach. Geophysical Research Letters.

Tauxe, L., Mullender, T. A. T., Pick, T., 1996. Potbellies, wasp-waists, and Superparamagnetism in magnetic hysteresis. Journal of Geophysical Research-Solid Earth. 101 (B1), 571–583.

Tauxe, L., 1998. Paleomagnetic principles and practice. Kluwer Academic Publishers, London.

Tauxe, L., 2003. Paleomagnetic Principles and Practice. In Paleomagnetic Principles and Practice (pp. 83–120). Springer Netherlands. doi.org/10.1007/0-306-48128-6

Tauxe, L., 2007. Essentials of paleomagnetism. University of California Press.

Tauxe, L., Butler, R. F., Van der Voo, R. (Rob), & Banerjee, S. K., 2010. Essentials of paleomagnetism. University of California Press.

Thébault, E., Finlay, C.C., Beggan, C.D., Alken, P., Aubert, J., Barrois, O., Bertrand, F., Bondar, T., Boness, A., Brocco, L. and Canet, E., 2015. International geomagnetic reference field: the 12th generation. Earth, Planets and Space, 67(1), pp.1-19.

Thellier, E., 1959. Sur l'intensité du champ magnétique terrestre dans le passé historique et géologique. Ann. Geophys.

Trotter, M.M. and McCulloch, B., 1971. Prehistoric rock art of New Zealand (Vol.3). Raupo.

Turner, G.M., Thompson, R., 1981. Lake sediment record of the geomagnetic secular variations in Britain during Holocene times. Geophys. J. R. Astron. Soc. 65, 703–725.

Turner, G.M., Thompson, R., 1982. Detransformation of the British geomagnetic secular variation record for Holocene times. Geophys. J. R. Astron. Soc. 70, 789–792.

Turner, G.M., 1987. A 5000-year geomagnetic palaeosecular variation record from western Canada. Geophys. J. R. Astron. Soc. 91, 103–121.

Turner, G. M., & Lillis, D. A., 1994. A palaeomagnetic secular variation record for New Zealand during the past 2500 years. Physics of the Earth and Planetary Interiors, 83(3–4), 265–282. doi.org/10.1016/0031-9201(94)90093-0

Turner, G.M., McFadgen, B., Alfheid, M., and Ingham, M., 2013, December. Hangi magnetism: first archaeomagnetic results from New Zealand. In AGU Fall Meeting.

Turner, G.M., Greve, A., Kinger, R., de Gelder, G., Fitzsimons, S., Howarth, J.D., Hill, M.J., Nilsson, A. and Sheppard, P., 2014, December. Unlocking the Secrets of the Geodynamo: The Southwest Pacific Key. In AGU Fall Meeting (Vol. 1, p. 07).

Turner, G.M., Howarth, J.D., de Gelder, G.I.N.O., Greve, A., Kinger, R., Corkill, R., and Fitzsimons, S.J., 2015. NZPSV1K and NZPSV10K for New Zealand: Applications for dating and field modelling. AGU Joint Assembly, Montreal.

Turner, G., de Gelder, G. I. N. O., Howarth, J., Greve, A., Kinger, R., Corkill, R., & Nilsson, A., 2015. NZPSV1k and NZPSV10k: New palaeosecular v variation master records for New Zealand: Applications for dating and field modeling. AGU Fall Meeting.

Turner, G. M., Howarth, J. D., de Gelder, G. I. N. O., & Fitzsimons, S. J., 2015. A new high-resolution record of Holocene geomagnetic secular variation from New Zealand. Earth and Planetary Science Letters, 430, 296–307. doi.org/10.1016/j.epsl.2015.08.021

Verosub, K.L., 1977. Depositional and post depositional processes in the magnetization of sediments. Rev. Geophys. Space Phys. 15, 129–143.

Watson, G.S., 1956. A test for randomness of directions. Geophysical Supplements to the Monthly Notices of the Royal Astronomical Society,7(4), 160-161.

Wilmshurst, J. M., & Higham, T. F. G., 2004. Using rat-gnawed seeds to independently date the arrival of Pacific rats and humans in New Zealand. The Holocene, 14(6), 801–806. doi.org/10.1191/0959683604hl760ft

Wilmshurst, J. M., Anderson, A. J., Higham, T. F. G., & Worthy, T. H., 2008. Dating the late prehistoric dispersal of Polynesians to New Zealand using the commensal Pacific rat. Proceedings of the National Academy of Sciences, 105(22), 7676–7680. doi.org/10.1073/pnas.0801507105

Wilmshurst, J. M., Hunt, T. L., Lipo, C. P., & Anderson, A. J., 2011. High-precision radiocarbon dating shows recent and rapid initial human colonization of East

Polynesia, 108(5), 1815–1820. doi.org/10.1073/pnas.1015876108

Wilson, J., 2009. History - Māori arrival and settlement in Te Ara—the Encyclopedia of New Zealand. (2009).

Yang, T., Gao, J., Gu, Z., Dagva, B., & Tserenpil, B., 2013. Petrophysical properties (density and magnetization) of rocks from the Suhbaatar-Ulaanbaatar-Dalandzadgad geophysical profile in Mongolia and their implications. The Scientific World Journal, 2013, 791918. doi.org/10.1155/2013/791918

Yu, Y., & Dunlop, D. J., 2002. Multivectorial paleointensity determination from the Cordova Gabbro, southern Ontario. Earth and Planetary Science Letters, 203(3–4), 983–998. doi.org/10.1016/S0012-821X(02)00900-7

Zijderveld, J. D. A., 1967. AC demagnetization of rocks: Analysis of results: Methods in Palaeomagnetism. Elsevier Science.

Zutelija, B., 1976. Geology of the Whitianga Group, Great Mercury Island. Part II - Structures in the Minden Rhyolite of Southern Great Mercury Island. Tane, 22, 15–22.